CARBON- AND INORGANIC-BASED NANOSTRUCTURES FOR ENERGY APPLICATIONS

EDITED BY: Federico Cesano, M. Jasim Uddin, Yuanbing Mao and Muhammad N. Huda

PUBLISHED IN: Frontiers in Materials

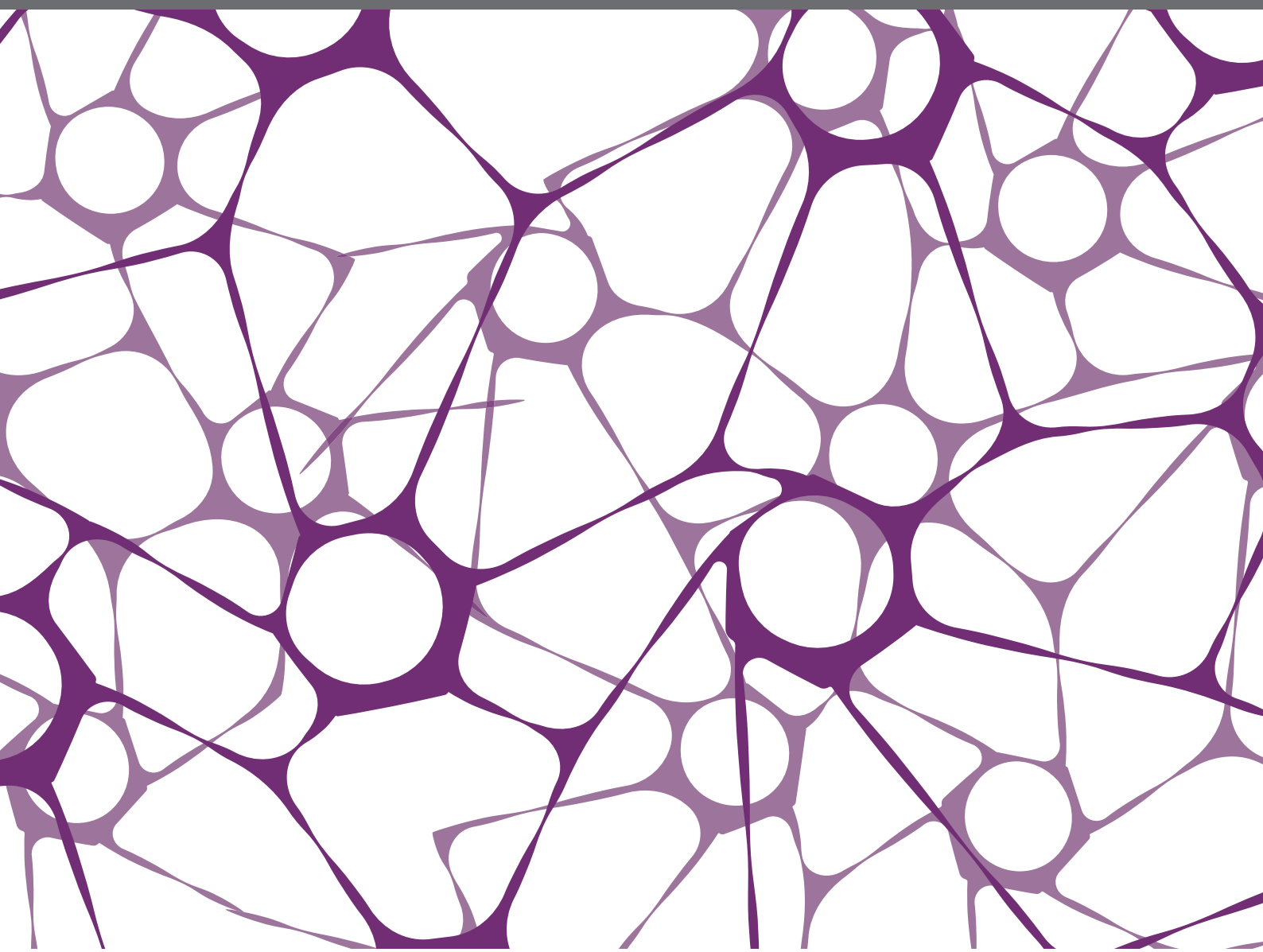

frontiers Research Topics

ISSN 1664-8714
ISBN 978-2-88966-331-6
DOI 10.3389/978-2-88966-331-6

About Frontiers

Frontiers is more than just an open-access publisher of scholarly articles: it is a pioneering approach to the world of academia, radically improving the way scholarly research is managed. The grand vision of Frontiers is a world where all people have an equal opportunity to seek, share and generate knowledge. Frontiers provides immediate and permanent online open access to all its publications, but this alone is not enough to realize our grand goals.

Frontiers Journal Series

The Frontiers Journal Series is a multi-tier and interdisciplinary set of open-access, online journals, promising a paradigm shift from the current review, selection and dissemination processes in academic publishing. All Frontiers journals are driven by researchers for researchers; therefore, they constitute a service to the scholarly community. At the same time, the Frontiers Journal Series operates on a revolutionary invention, the tiered publishing system, initially addressing specific communities of scholars, and gradually climbing up to broader public understanding, thus serving the interests of the lay society, too.

Dedication to Quality

Each Frontiers article is a landmark of the highest quality, thanks to genuinely collaborative interactions between authors and review editors, who include some of the world's best academicians. Research must be certified by peers before entering a stream of knowledge that may eventually reach the public - and shape society; therefore, Frontiers only applies the most rigorous and unbiased reviews.
Frontiers revolutionizes research publishing by freely delivering the most outstanding research, evaluated with no bias from both the academic and social point of view. By applying the most advanced information technologies, Frontiers is catapulting scholarly publishing into a new generation.

What are Frontiers Research Topics?

Frontiers Research Topics are very popular trademarks of the Frontiers Journals Series: they are collections of at least ten articles, all centered on a particular subject. With their unique mix of varied contributions from Original Research to Review Articles, Frontiers Research Topics unify the most influential researchers, the latest key findings and historical advances in a hot research area! Find out more on how to host your own Frontiers Research Topic or contribute to one as an author by contacting the Frontiers Editorial Office: researchtopics@frontiersin.org

CARBON- AND INORGANIC-BASED NANOSTRUCTURES FOR ENERGY APPLICATIONS

Topic Editors:
Federico Cesano, University of Turin, Italy
M. Jasim Uddin, The University of Texas Rio Grande Valley, United States
Yuanbing Mao, The University of Texas Rio Grande Valley, United States
Muhammad N. Huda, University of Texas at Arlington, United States

Citation: Cesano, F., Uddin, M. J., Mao, Y., Huda, M. N., eds. (2021). Carbon- and Inorganic-Based Nanostructures for Energy Applications.
Lausanne: Frontiers Media SA. doi: 10.3389/978-2-88966-331-6

Table of Contents

frontiers in Materials

EDITORIAL
published: 18 November 2020
doi: 10.3389/fmats.2020.609576

Editorial: Carbon- and Inorganic-Based Nanostructures for Energy Applications

Federico Cesano[1]*, *Mohammed Jasim Uddin*[2], *Yuanbing Mao*[3] and *Muhammad N. Huda*[4]

[1]Department of Chemistry, NIS (Nanostructured Interfaces and Surfaces) Interdepartmental Centre and INSTM Centro di Riferimento, University of Turin, Turin, Italy, [2]Photonics and Energy Research Laboratory, Department of Chemistry, The University of Texas Rio Grande Valley, Edinburg, TX, United States, [3]Department of Chemistry, Illinois Institute of Technology, Chicago, IL, United States, [4]Department of Physics, The University of Texas at Arlington, Arlington, TX, United States

Keywords: nanostructures, nanomaterials, nanocarbons, inorganic nanostructures, low-dimensional materials, energy materials

Editorial on the Research Topic

Carbon- and Inorganic-Based Nanostructures for Energy Applications

The transition from fossil fuels to sustainable energy sources needs more efficient materials and improved technologies. Traditional materials (either pristine or combined to form composites) are restricted by their low efficiency, low performance, short durability, environmental issues, high production costs, and narrow spectrum of applications. In recent years, the research in the field of materials for energy applications has been very active as documented by the number of scientific contributions that is trending with exponential growth (**Figure 1A**).

Furthermore, from a subject area standpoint, the field of "*energy materials*" is very broad and its relevant research is a multidisciplinary and multifaceted activity. For example, the subject area can range from the materials for nuclear reactors harnessing nuclear energy to the materials for chemical energy storage. Even, the safety materials for energy technologies can also be considered as "energy materials." Consequently, an issue on "*energy materials*" may include basic and fundamental scientific studies to more applicative contributions, which are comprised in a wide variety of applications (**Figure 1B**).

For this reason, it is quite difficult to provide a complete overview over the materials for energy. From the operational point of view, materials for energy conversion, transport and storage are typically included. Topics are manifold, multifaceted, and sometimes very diverse. For example, the field of the electrical energy storage is very far from fuel storage. In any case, a very wide and transversal viewpoint in a specific field can make available a remarkable innovation. As a rule, a look must always be directed towards new materials, fabricated experimentally (Uddin et al., 2014), or predicted theoretically (Sarker et al., 2013) and their properties (Zhang et al., 2019). For example, very recently the concept that uses the earth as a heat source and the night sky as a heat sink, known as thermoradiative photovoltaics, has been illustrated (Raman et al., 2019; Deppe and Munday, 2020). Materials for such devices will need a strong absorption and emission in the thermal radiation range, enough transparency to permit optical access to the night sky. Such materials have the potential to revolutionize the photovoltaics technology. Another look must always be oriented towards new characterization techniques and innovative investigation methods. For example, in the specific field of lithium (Li)-ion batteries, the machine learning assisted statistical analysis together with experiment-informed mathematical modelling have been shown very recently by Jiang et al. (2020). The authors have correlated the degree of particle detachment cathodes with the charging rate and particle sizes. Alternatively, X-ray nano-computed tomography dual-scan superimposition technique has been adopted by (Lu et al., 2020) to shed light on microstructural heterogeneities. The method has the potential to determine how the performance of the Li-ion batteries is affected under high rate conditions.

OPEN ACCESS

Edited by:
Emilia Morallon, University of Alicante, Spain

Reviewed by:
José Rodríguez-Mirasol, University of Malaga, Spain

***Correspondence:**
Federico Cesano
federico.cesano@unito.it

Specialty section:
This article was submitted to Carbon-Based Materials, a section of the journal Frontiers in Materials

Received: *23 September 2020*
Accepted: *23 October 2020*
Published: *18 November 2020*

Citation:
Cesano F, Uddin MJ, Mao Y and Huda MN (2020) Editorial: Carbon- and Inorganic-Based Nanostructures for Energy Applications. Front. Mater. 7:609576. doi: 10.3389/fmats.2020.609576

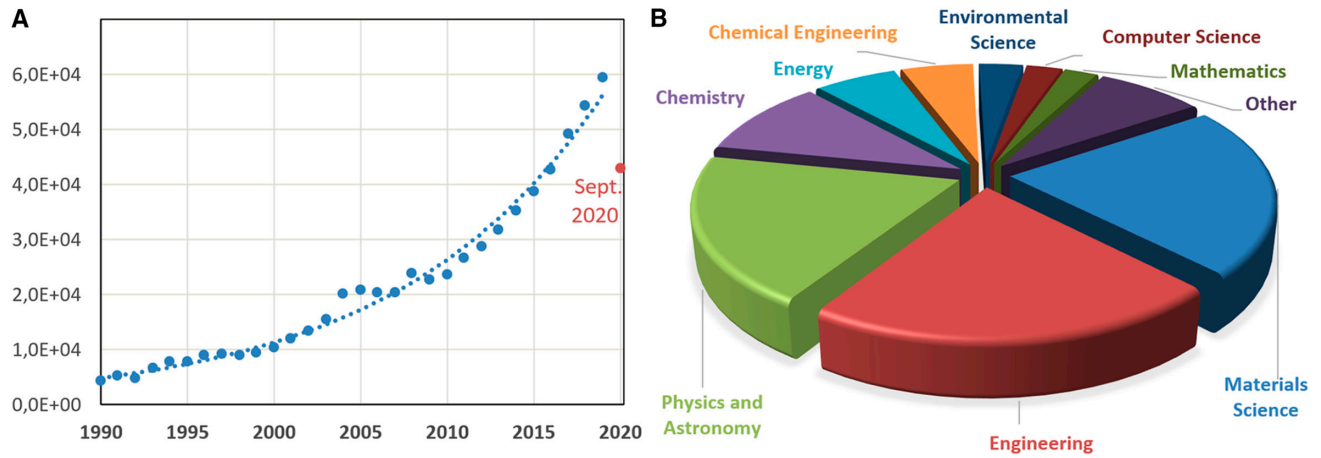

FIGURE 1 | Number of documents (keywords: Energy AND Materials, source: Scopus) published in the last 30 years **(A)**; Subject areas of scientific contributions dedicated to energy materials **(B)**.

The present article collection, composed of six research articles and three reviews, showcases some of the latest achievements and future perspectives in the field of the carbon-based and inorganic materials that are being designed to meet some of our energy challenges. In the present article collection, the attention to the environment is a common perspective, due to preparation methods adopted from natural resources, polymers and the attempt to minimize (or replace) metals for a more sustainable development of technologies. Cesano et al. reviewed the topic of *metal-free* conductors based on macrosized and nanoscale carbons (i.e., carbon fibers, carbon nanotubes, graphene) from the viewpoint of the electrical and thermal conductivity for electronic and electrical wiring applications. Specifically, CNTs and graphene can be assembled into macroscopic fibers, yarns and ropes to be used as conductors (Akia et al., 2017; Jang et al., 2020). From the perspective of replacing metals, which are present in nature with limited amounts, the role played by the chemistry in helping to exceed the electrical conductivity of metals by means of the molecular-level control and doping, is emphasized. The contribution helps to elucidate most recent results in the field, and envisages new directions and potential applications. Jangir et al. designed and fabricated a bio-hybrid electrode, which integrates Li, sulfur, and molybdenum in a nitrogen-doped reduced graphene oxide (NDRGO) matrix of biological origin. The obtained composite material works as an electrode, based on concepts of "*embedded redox couples*" and "*induced electron transfer*," behaving as a supercapacitor. Wu et al. reviewed MnO_2/carbon composites for supercapacitors from the viewpoints of the synthesis and of the electrochemical performance. Along with this broad theme, MnO_2 has emerged as one of the most promising electrode materials for its specific capacitance, wide potential range, high electrochemical activity, and environmental friendliness. In addition, due to their low electrical resistances, significant thermal stabilities, large specific surface areas, and porosities, carbons are ideal materials to be compounded with MnO_2. The authors show the latest findings on MnO_2/carbon supercapacitor electrodes, focusing on the fabrication strategies and the electrochemical performance influencing factors, with an outlook on the possible development directions in future for designing high-performance materials. Kulandaivalu et al. reviewed the subject of the layered double hydroxide (LDH)/carbon nanocomposites containing Ni^{2+} and $Co^{2+/3+}$ for supercapacitor applications. The combination of Ni-Co LDHs with carbon-based materials gives a remarkable improvement in the specific energy, specific capacitance, and specific power performance of supercapacitors. The authors explore important factors influencing the synthesis of LDHs and the correlation among morphology, structure, and electrochemical performances of the Ni-Co LDHs. Improvements needed to increase the performance of these new supercapacitors are also provided. Kumar et al. synthesized hexagonal copper phosphide (Cu_3P) platelets by chemical vapor deposition technique and incorporated it in the highly conducting 3D graphene scaffold, leading to the formation of Cu_3P/graphene hybrid to be used as supercapacitors with high Coulombic efficiency. The fabricated asymmetric supercapacitor using Cu_3P/graphene hybrid on graphite as cathode and activated carbon on graphite as anode showed high specific capacity, energy density, remarkable power density and an excellent cycle life. Li et al. fabricated spinel Li manganese oxide ($LiMn_2O_4$) in Li-ion battery. The authors observed improved stability even at elevated temperature with the addition of 1, 3-propane sultone working as an electrolyte additive compared to the cell without additive. On the other hand, Gouda et al. fabricated membrane electrode assembly in the proton exchange membrane fuel cells using graphene materials obtained from the thermal dissociation of polyethylene terephthalate, working as catalytic electrodes, and a ternary polymer blend (i.e., polyvinyl alcohol, polyethylene oxide, and polyvinyl pyrrolidone). The authors then investigated the effect of gas diffusion layers and the number of catalyst layers in three types of membrane electrode assemblies. Alternatively, semiconductor nanowires have the potential to reduce costs and

increase the efficiency of the devices. On this topic, Zayas-Bazán et al. prepared CdS nanowires utilizing the chemical vapor deposition technique and Bi nanoparticles working as a catalyst. The authors proposed a solar cell configuration, in which CdS nanowires operate as windows material (or even as absorber) in hybrid solar cells, like Quantum Dots Dye Sensitized Solar Cell, CdTe, or colloidal CdSeTe. Perovskite oxides are an important and effective class of mixed oxides which play a significant role in the fields of energy conversion, transport, and storage systems. For active electrocatalysts as water electrolysis to meet the demands of the sustainable energy-powered economy, they are fascinating alternatives to noble metals because of their catalytic activity and cost-effectiveness. Along this line, Mao et al. developed a series of Sr^{2+}-doped cobaltite perovskite $LaCoO_3$ particles as efficient catalysts for oxygen evolution reaction (OER).

Overall, the papers published in this issue cover materials for energy. The subject is manifold, multifaceted, and sometimes very different, but we can easily conclude that the theme will have significant developments in the coming years. We truly hope that contributions published within this article collection will contribute to help to increase the value of research articles in the field of energy materials, providing inspiration for new relevant publications.

AUTHOR CONTRIBUTIONS

All authors have made a substantial contribution to the work and they approved it for publication.

FUNDING

FC acknowledges support from MIUR (Ministero dell'Istruzione, dell'Università e della Ricerca), INSTM Consorzio and NIS (Nanostructured Interfaces and Surfaces) Inter-Departmental Centre of University of Turin. YM would like to thank the support from the Illinois Institute of Technology start-up funds. MNH was supported by the National Science Foundation Award No. 1609811. MU acknowledges the generous support from US Office of Naval Research.

ACKNOWLEDGMENTS

We thank all authors, reviewers, and editors who assisted in the article collection. We thank Dr. Alexander Stephens, Dr. Emily Young and all the editorial staff who assisted the Topic Editors.

REFERENCES

Akia, M., Cremar, L., Chipara, M., Munoz, E., Cortez, H., De Santiago, H., et al. (2017). *In Situ* production of graphene–fiber hybrid structures. *ACS Appl. Mater. Interf.* 9, 25474–25480. doi:10.1021/acsami.7b07509

Deppe, T., and Munday, J. N. (2020). Nighttime photovoltaic cells: electrical power generation by optically coupling with deep space. *ACS Photon.* 7, 1–9. doi:10.1021/acsphotonics.9b00679

Jang, Y., Kim, S. M., Spinks, G. M., and Kim, S. J. (2020). Carbon nanotube yarn: carbon nanotube yarn for fiber-shaped electrical sensors, actuators, and energy storage for smart systems. *Adv. Mater.* 32, 2070034. doi:10.1002/adma.202070034

Jiang, Z., Li, J., Yang, Y., Mu, L., Wei, C., Yu, X., et al. (2020). Machine-learning-revealed statistics of the particle-carbon/binder detachment in lithium-ion battery cathodes. *Nature Commun.* 11, 2310. doi:10.1038/s41467-020-16233-5

Lu, X., Bertei, A., Finegan, D. P., Tan, C., Daemi, S. R., Weaving, J. S., et al. (2020). 3D microstructure design of lithium-ion battery electrodes assisted by X-ray nano-computed tomography and modelling. *Nature Commun.* 11, 2079. doi:10.1038/s41467-020-15811-x

Raman, A. P., Li, W., and Fan, S. (2019). Generating light from darkness. *Joule* 3, 2679–2686. doi:10.1016/j.joule.2019.08.009

Sarker, P., Prasher, D., Gaillard, N., and Huda, M. N. (2013). Predicting a new photocatalyst and its electronic properties by density functional theory. *J. Appl. Phys.* 114, 133508. doi:10.1063/1.4821429

Uddin, M. J., Daramola, D. E., Velasquez, E., Dickens, T. J., Yan, J., Hammel, E., et al. (2014). A high efficiency 3D photovoltaic microwire with carbon nanotubes (CNT)-quantum dot (QD) hybrid interface. *Phys. Status Solidi RRL.* 8, 898–903. doi:10.1002/pssr.201409392

Zhang, L., Chen, Z., Su, J., and Li, J. (2019). Data mining new energy materials from structure databases. *Ren. Sustain. En. Rev.* 107, 554–567. doi:10.1016/j.rser.2019.03.036

Conflict of Interest: The authors declare that the research was conducted in the absence of any commercial or financial relationships that could be construed as a potential conflict of interest.

frontiers in Materials

ORIGINAL RESEARCH
published: 06 September 2019
doi: 10.3389/fmats.2019.00217

"Induced Electron Transfer" in Silk Cocoon Derived N-Doped Reduced Graphene Oxide-Mo-Li-S Electrode

Himanshi Jangir[1], Amarjeet Bhardwaj[2], Janakarajan Ramkumar[3], Sabyasachi Sarkar[4] and Mainak Das[5]**

[1] Design Program, Indian Institute of Technology Kanpur, Kanpur, India, [2] Department of Biological Sciences and Bioengineering, Indian Institute of Technology Kanpur, Kanpur, India, [3] Department of Mechanical Engineering, Indian Institute of Technology Kanpur, Kanpur, India, [4] Nano Science and Synthetic Leaf Laboratory at Downing Hall, Centre for Healthcare Science and Technology, Indian Institute of Engineering Science and Technology, Howrah, India, [5] Design Program and Biological Sciences & Bio-Engineering, Indian Institute of Technology Kanpur, Kanpur, India

Developing 'carbon lithium sulfide composite (C-Li_2S)' cathode is a promising strategy for Li-S battery. Quite interestingly, when Li and S are caged in a heavily nitrogen-doped reduced graphene oxide (NDRGO) matrix derived from Tassar silk cocoon, the composite (NDRGO-Li-S) electrode behaves like a supercapacitor. In this work, we first optimized the concentrations of sulfur and then introduced molybdenum in the NDRGO matrix to develop a stable NDRGO-Mo-Li-2S (where 2 stands for 2M) composite electrode. The electrode design process utilized the concepts of "embedded redox couples" and "induced electron transfer"; a putative strategy to alter internal electron-shuttling kinetics for applications in various charge storage devices; where a time of electron-shuttling is the key. In NDRGO-Mo-Li-2S composite the charge transport occurs via "induced electron transfer," where Li^+, is an *external oxidant*, provoking the inter atom electron transfer between Mo(VI), the *internal oxidant*, and S(-II), *the internal reductant* in Mo-S redox couple. This redox reaction is reversed using NDRGO, an *external reductant* inducing inter atom electron flow across [Mo(V)–(S2)] to complete the starting to product and back cycle. Such a redox cycle is competent for the flow of electrons in a lasting charge storage material through this unique bio-inorganic hybrid approach.

Keywords: induced electron transfer, silk cocoon, nitrogen doped reduced graphene oxide, lithium-sulfur battery, molybdenum, bio-hybrid electrode

OPEN ACCESS

Edited by:
Federico Cesano, University of Turin, Italy

Reviewed by:
Huan Pang, Yangzhou University, China
Qihui Wu, Jimei University, China
Liqiang Mai, Wuhan University of Technology, China

****Correspondence:***
Sabyasachi Sarkar
abya@iitk.ac.in
Mainak Das
mainakd@iitk.ac.in

Specialty section:
This article was submitted to Carbon-Based Materials, a section of the journal Frontiers in Materials

Received: *16 May 2019*
Accepted: *21 August 2019*
Published: *06 September 2019*

Citation:
Jangir H, Bhardwaj A, Ramkumar J, Sarkar S and Das M (2019) "Induced Electron Transfer" in Silk Cocoon Derived N-Doped Reduced Graphene Oxide-Mo-Li-S Electrode. Front. Mater. 6:217. doi: 10.3389/fmats.2019.00217

INTRODUCTION

A significant amount of research has undergone in Li-S battery; having sulfur as the cathode (positive electrode), lithium as the anode (negative electrode) and an aprotic organic solvent of lithium salt as an electrolyte (Rauh et al., 1979; Peled and Yamin, 1983; Peramunage and Licht, 1993; Shim et al., 2002; Armand and Tarascon, 2008; Aurbach et al., 2009). The major shortcomings of the Li-S battery are the following: (a) unstable nature of the sulfur cathode. (b) polysulfide shuttling problem. (c) challenges to select the appropriate electrolyte. (d) protecting the lithium anode or scouting for a more stable anode. These shortcomings have been dealt with in detail in recent reviews on the Li-S battery (Ely et al., 2018).

The present work involves the design and development of stable cathode material for Li-S battery. During the last decade, two major approaches have been attempted to improve the sulfur cathode. In the first approach, the sulfur cathode is being stabilized by forming a carbon-sulfur composite (Ji et al., 2009). While, in the second, Li_2S cathode is preferred over the sulfur cathode (Hassoun and Scrosati, 2010).

Li_2S suffers from poor electrical conductivity and sluggish electrochemical performance. Li_2S-carbon composite electrodes are currently being investigated to improve stability and electrochemical activity (Geng et al., 2018; Jangir et al., 2018; Li et al., 2018a,b,c; Luo et al., 2019; Shi et al., 2019; Zhou et al., 2019). In one of our earlier works, to improve the conductivity and stability of Li_2S, we developed a synthetic approach viz., we synthesized Li_2S in a conductivity cage of heavily nitrogen doped reduced graphene oxide (NDRGO) derived from the wild Tassar silk cocoon (Jangir et al., 2018). We sequentially entrapped equimolar lithium and sulfur in NDRGO, resulting in the formation of NDRGO-Li-S composite. While testing the electrochemical performance of the NDRGO-Li-S composite, to our surprise, we observe that the composite behaved as a better supercapacitor as compared to NDRGO (Jangir et al., 2018). This finding sets the tone for the present research and opens up a few **critical questions (a–c)**, that are enumerated below:

(a) In the earlier work, we used equimolar lithium and sulfur to develop the NDRGO-Li-S composite (Jangir et al., 2018). *If we vary the content of sulfur while keeping the concentration of lithium constant, how will it influence the electrochemical performance of the composite?*

(b) Since leaching of sulfur from both carbon-sulfur and Li_2S-carbon cathode is a persistent problem; *'how much sulfur can be optimally anchored in an NDRGO matrix, so that without any sulfur spillover, it retains stability and provides long term optimal electrochemical performance?'*

(c) *Exploring an alternative strategy to increase the stability of Li_2S-carbon composite?*

In the present work, we have addressed the **questions a** and **b**, by varying the concentration of sulfur and testing the electrochemical performance of the newly synthesized composites. The schematic of the strategy has been shown in **Figure 1**. While addressing **question c,** we drew our inspiration from two fundamental concepts: (i) electron shuttling through redox couples as observed in a biological membrane, (ii) induced electron transfer.

In the subsequent section, we will discuss each of these aspects and how these concepts assisted us in designing a stable Li_2S-carbon composite electrode.

(i) Electron shuttling in biological membranes is carried out by a series of embedded redox couples, mainly iron-sulfur (Fe-S), cytochromes, and copper proteins. These metalloproteins are used with different redox potentials to control the electron flow and sometimes the energy used in these steps are coupled to derive relevant biochemical reactions. The direction of electron flow is a function of the redox potential. The time an electron takes to travel from point A to point B in a chloroplast or mitochondrial membrane, though very fast, yet depends on the number of redox couples which it encounters during its journey. Thus, the capacitive discharge of such a membrane is a function of the number of redox couples present in the membrane (Stryer, 1999). Inspiration could be drawn from such biological membranes; to introduce redox couples in synthetic electrode membranes to make it more stable and vary the time of electron transfer. The specific question we ask, is the following: *could we stabilize sulfur by introducing an atom 'X' in the NDRGO matrix, so that sulfur forms redox couples with 'X' viz., S-X*. In such a situation, the electron kinetics will be altered, as well as sulfur will be stabilized as an internally embedded redox couple. We chose molybdenum (Mo) as our 'X' atom; with the assumption that it will form a two-dimensional MoS_2 structure on top of the NDRGO sheet, where MoS_2 will function as a redox couple, stabilizing the sulfur. So what we targeted, is to *develop an electrode matrix with an extended bond system having the key players as NDRGO, Mo, Li, and S*.

(ii) Quite interestingly, in such *extended bond systems*, transfer of electrons can be induced by different kinds of operations. This brings us to the least known concept, viz., "Induced electron transfer," introduced by Professor Henry Taube, through his famous book entitled "Electron Transfer Reactions of Complex Ions in Solution"; published in 1970 (Taube, 1970). Such an electron transfer across a central atom and an adjoining donor atom or ligand in a compound is induced by an external redox agent (either oxidant or reductant), that also participates in the said reaction. In such arrangement, the external redox system, say an oxidant provokes and initiates the electron transfer process across the central atom and ligand in the compound leading to a product, and the process is reversed by a second external reductant to bring back the product to starting compound (Taube, 1970; Sarkar and Ansari, 1986; Chandrasekaran et al., 1987; Ansari et al., 1988a,b,c; Miller and Min, 2009). The external oxidant and reductant, using such transitioning redox chemistry, maintained an interdependent two-ways electron shuttling arrangement necessary for storage devices. Such an approach could be exploited to control the time of electron transfer, which is the key for different kinds of charge storage electrodes viz., battery, supercapacitor, capattery.

Here, we have designed and engineered a bio-hybrid electrode by amalgamating these two above mentioned basic aspects of electron kinetics. The electrode consists of an embedded molybdenum-sulfur (Mo-S) redox couple; along with silk cocoon derived heavily nitrogen doped reduced graphene oxide (NDRGO) and lithium (Li), an electronegative and an electropositive species, respectively. This electrode exhibits "*induced electron transfer*"; where Li^+ acts as an external oxidant, providing the necessary driving force to provoke the inter atom electron transfer between Mo(VI), as internal oxidant, and S(-II), as internal reductant in Mo-S redox couple and NDRGO functions as external reductant assists in reversing the process and bringing the system back to its original configuration.

The work presented here is divided into three **sub-sections** as enumerated below:

Sub-section one: A detailed procedure has been discussed highlighting the design and engineering aspects of four different variants of the bio-hybrid electrode material. Further electrochemical characterization of these electrode materials have been carried out, and the results were compared to

FIGURE 1 | Overall experimental design and the strategies followed to develop a stable silk NDRGO, Li, S electrode. The heavily nitrogen doped reduced graphene oxide (NDRGO) derived from silk is used as a conductivity cage. Superscript 1 indicates NDRGO, a supercapacitor electrode. Superscript 2, stands for NDRGO-Li-S composite obtained from equimolar doping of Li and S on the NDRGO matrix. Superscript 3, stands for 1M Li and 2M S doping on the NDRGO matrix, i.e., NDRGO-Li-2S. Superscript 4, stands for 1M Li and 4M S doping on the NDRGO matrix, i.e., NDRGO-Li-4S. Superscript 5, stands for Mo, 1M Li and 2M S doping on the NDRGO matrix, i.e., MDRGO-Mo-Li-2S.

choose the best electrode configuration from the pool of four electrodes.

Sub-section two: Based on the comparative analysis in previous sub-section, a detailed structural analysis and life cycle studies were conducted for the NDRGO-Mo-Li-2S electrode configuration.

Sub-section three: A putative mechanism of electron transport on the electrode surface has been discussed on the basis of "induced electron transfer" and "shuttling of an electron through embedded redox couple" as observed in NDRGO-Mo-Li-2S electrode.

EXPERIMENTAL

Synthesis of Electrode Material and Electrochemical Characterization

Preparation of NDRGO

Tassar silk cocoon were obtained from the forest reserves of the state of Chhattisgarh in India as described in our previous work (Roy et al., 2014; Sahu et al., 2015; Dubey et al., 2018; Jangir et al., 2018). The dead pupae was removed and the Tassar silk cocoon was cut into small pieces and was then put into a crucible. The crucible was put into a furnace and the furnace was purged with argon for 45 min. Then the temperature of the furnace was slowly raised to 400 °C under argon atmosphere and that temperature was fixed to completely char the cocoon pieces for 4 h. The heating was then discontinued and the furnace was allowed to cool under argon till it attained room temperature. The bio-charred sample was removed from the crucible and was ground to form powdery fine particles using pestle and mortar. This sample was then packed and sealed into a Whatman filter paper to create a thimble-like package and the solid sample was placed inside and sealed to close the opening. That was repeatedly washed with acetone using a soxhlet extractor to remove any organic by-product formed under charring. The residual sample was allowed to dry and then oxidized using nitric acid. For this, 1 g of the washed sample was slowly added in portion into 30 ml of HNO_3 to control the exothermic reaction with the evolution of nitric dioxide fumes and when it is virtually subsided, the mixture was allowed to stand for 18–24 h at 40 °C. The acid was then removed under slow evaporation to solidify the mass which was then washed with water, methanol and acetone sequentially, and finally dried in a desiccator. This sample on analysis is found to be ∼15% nitrogen doped graphene oxide. This was then reduced using hydrazine hydrate. About 0.5 g of the above sample was treated in 30 ml of hydrazine hydrate at approximately 40 °C for 12 h. The insoluble reduced graphene oxide so formed was washed with water followed by methanol and acetone sequentially and dried in a desiccator. This sample is termed as nitrogen doped reduced graphene oxide (NDRGO) (Roy et al., 2014; Sahu et al., 2015; Dubey et al., 2018; Jangir et al., 2018).

Preparation of NDRGO-Li-S, NDRGO-Li-2S, NDRGO-Li-4S

Around 200 mg of NDRGO was added in previously argon purged 15 ml of dimethylformamide (DMF) and continuously stirred at 50 °C for 40 min under argon. Then, 21 mg of Li metal was added into it and stirred for 20 min. To this, 100, 200 and 400 mg of sulfur powder, respectively, added for NDRGO-Li-S, NDRGO-Li-2S, NDRGO-Li-4S compositions, respectively. In each case the final ternary mixture (NDRGO, Li and S) was stirred for 2 h, to obtain the final product. Then, DMF was removed by washing with benzene and the sample was stored in oxygen and moisture free chamber. Based on the sulfur ratio used, we got three products as NDRGO-Li-S, NDRGO-Li-2S, and NDRGO-Li-4S. NDRO-Li-S synthesis has been discussed in detail in one of our previous publications (Jangir et al., 2018).

Preparation of NDRGO-Mo-Li-2S

As mentioned in the preceding paragraph, around 200 mg of NDRGO was added in previously argon purged 15 ml of dimethylformamide (DMF) and stirred at 50 °C for 40 min under argon. Forty milligram ammonium molybdate tetra hydrate was added to this mixture and further stirred in an argon environment for 20 min, while maintaining a temperature of 50 °C. Following this, 21 mg Li was added. The reaction was allowed to progress for next 20 min and after this 200 mg S was added, and the reaction was continued for next 2 h. The final product was washed with benzene and stored for further use in vacuum desiccator.

Electrode Preparation, Electrolyte Preparation, and Electrochemical Characterization

(i) Electrode preparation: Electrode materials were coated on one side of the graphite sheet (current collector) of size 1.5 cm*1.5 cm. Only 5 mg of electrode material was coated.

(ii) Electrolyte preparation: 1 part of 1-butyl 3- methyl imidazolium tetrafluoroborate [BMIM]BF4 in 10 parts of acetonitrile (ACN) was used as electrolyte. This was prepared in argon atmosphere by gently dissolving in ACN for 30 min (Wang et al., 2012; Jangir et al., 2018).

(iii) Electrochemical characterization: Electrochemical analysis was performed using ZIVE SP1 single channel electrochemical workstation. We used three electrode configuration with platinum as counter electrode and a reference electrode. Two analyses were performed: cyclic voltammetry (CV) followed by charge-discharge study. CV was performed in the voltage range of −1.5 V to +1.5 V at a scan rate of 5 milliVolt per second (mV/s). Charge discharge analyses (CC/CC mode) were performed using a constant charging and discharging current of 5 milliampere (mA) in the voltage range of −1.5 V to +1.5 V. Long-term charge discharge analysis was performed for NDRGO-Mo-Li-2S at a constant charging and discharging current of 0.2 mA in a voltage range of −0.5 V to +1.0 V. In addition, for NDRGO-Mo-Li-2S, CV was performed at different scan rates of 100, 50, 5, and 1 mV/s. Also, charge discharge curves were recorded for 5, 1, and 0.2 mA constant current in a voltage window of −0.5 V to +1.0 V.

Electrode Material Characterization

Field emission gun scanning electron microscopy (FE-SEM) was performed using JSM-7100F (JEOL Ltd.). Transmission electron micrographs were obtained from FEI Technai 20 U Twin Transmission Electron Microscope (TEM). X-ray photoelectron spectroscopy (XPS) was done using PHI 5000 Versa probe II FEI Inc. instrument. X-ray diffraction (XRD) pattern was obtained using PANanlyticalX'Pert instrument.

RESULTS AND DISCUSSION

This results section has been divided into three subsections as discussed earlier in the "introduction."

Sub-section 1

Design principles and engineering of five different variants of bio-hybrid electrode material and the electrochemical characterization **(Figures 1–6)**.

The electrode designing process was initiated from a naturally derived material of biological origin viz., Tassar silk cocoon. Bio-charred silk cocoon is a rich source of heavily nitrogen (∼16%) doped reduced graphene oxide (NDRGO) matrix, exhibiting remarkable fluorescence, soft ferromagnetism, and supercapacitor properties (Roy et al., 2014; Sahu et al., 2015; Dubey et al., 2018; Jangir et al., 2018). We discovered that doping equimolar lithium and sulfur (NDRGO-Li-S) in NDRGO matrix improves supercapacitor properties (Jangir et al., 2018).

In the present work, we initially attempted to improve the electrochemical properties of NDRGO-Li-S complex, by increasing the S content from 1 to 2M and 4M, thus resulting in two new complexes NDRGO-Li-2S and NDRGO-Li-4S, respectively. The transmission electron micrographs of NDRGO-Li-S, NDRGO-Li-2S, and NDRGO-Li-4S composites are shown in **Figures 2a–c**. All the composites showed a 2-D sheets like geometry ascertaining the presence of NDRGO matrix. In our earlier works on NDRGO and NDRGO-Li-S, we observed similar results (Roy et al., 2014; Sahu et al., 2015; Dubey et al., 2018; Jangir et al., 2018). The distribution of the chemical moieties in these complexes were further verified by their XRD signatures as shown in **Figure 3**. The XRD traces highlight the elemental distribution of these electrode materials.

Next, we performed CV analysis for NDRGO, NDRGO-Li-S, NDRGO-Li-2S, and NDRGO-Li-4S (**Figure 4**). Since in our earlier work, NDRGO and NDRGO-Li-S showed superior supercapacitor properties, we tested supercapacitor properties of NDRGO-Li-2S and NDRGO-Li-4S. Initially CV analysis was performed using a typical super capacitor testing protocol viz., voltage range of −1.5 V to +1.5 V with a scan rate of 5 mV/s. We made two important observations at this stage of experimentation. CV analysis showed that NDRGO-Li-2S performs better than NDRGO, NDRGO-Li-S and NDRGO-Li-4S (**Figure 4A**). But for NDRGO-Li-4S composite, a significant amount of sulfur spillage took place in the electrolyte during electrochemical measurement, as observed by the change in the color of the electrolyte to yellow (**Figure 4B**). After running the

electrode for few cycles, we observed unstable recordings and detachment of electrode material from the graphite sheet (as can be observed at the bottom of the beaker shown in **Figure 4**).

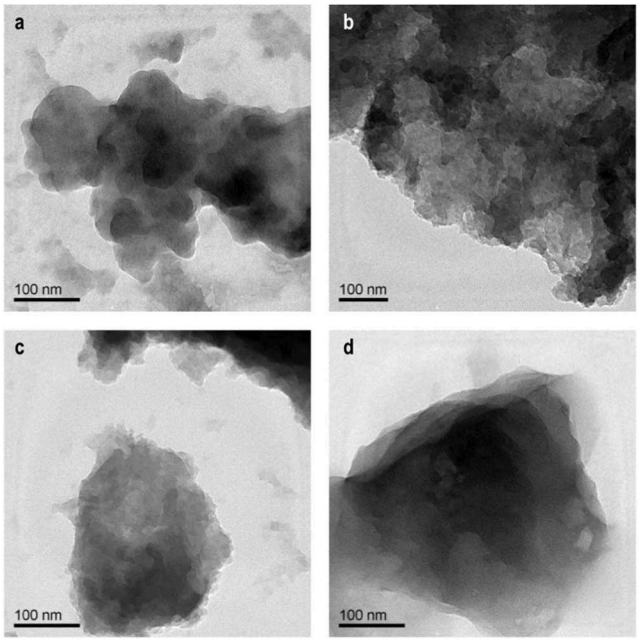

FIGURE 2 | Representative TEM images: **(a)** NDRGO-Li-S. **(b)** NDRGO-Li-2S. **(c)** NDRGO-Li-4S. **(d)** NDRGO-Mo-Li-2S.

In one of the earlier work, Medenbach et al. (2018) reported similar sulfur spillage. Due to unstable nature of the NDRGO-Li-4S composite, this composition was not included for further experiments. The material indeed showed initial promise but further work is needed to stabilize the composite. Followed by CV, we performed a charge discharge analysis for NDRGO-Li-S, NDRGO-Li-2S, and NDRGO-Li-4S and compared the results (**Figure 4C**). A constant charging and discharging current of 5 mA in the voltage range of −1.5 V to +1.5 V was used for analyzing the results viz., typically used for testing super capacitor (Stoller and Ruoff, 2010).

While NDRGO-Li-2S performed better than NDRGO-Li-S, but to our surprise, NDRGO-Li-4S completely deviated from super capacitor behavior. But the unstable nature of the complex prevented us from exploring it further. Based on CV and charge-discharge results, we proceeded with NDRGO-Li-2S composite.

We further tried to improve the stability and supercapacitive property which we observed in NDRGO-Li-2S complex. Without altering the structural conformation, viz., layered sheet-like structure of this complex, we plan to introduce another 2-D sheet like matrix (MoS_2) into it. Recently, to enhance the photo-catalytic activity of reduced graphene oxide (rGO), a similar approach has been reported, where a rGO-MoS_2 composite has been prepared by Cravanzola et al. (2016). In our present work, to achieve this, we chronologically introduced molybdenum into the NDRGO matrix before lithium and sulfur because of the following reasons (**Figure 1**):

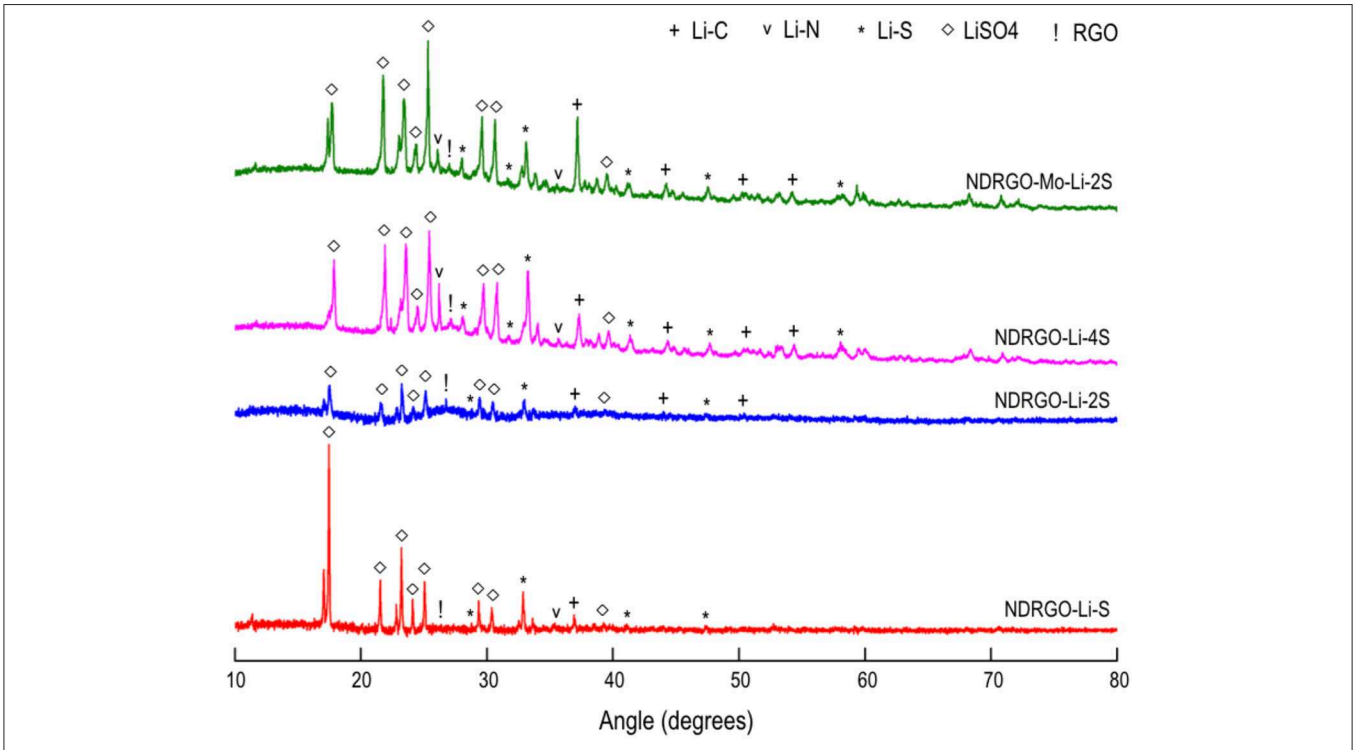

FIGURE 3 | XRD pattern of the synthesized composites.

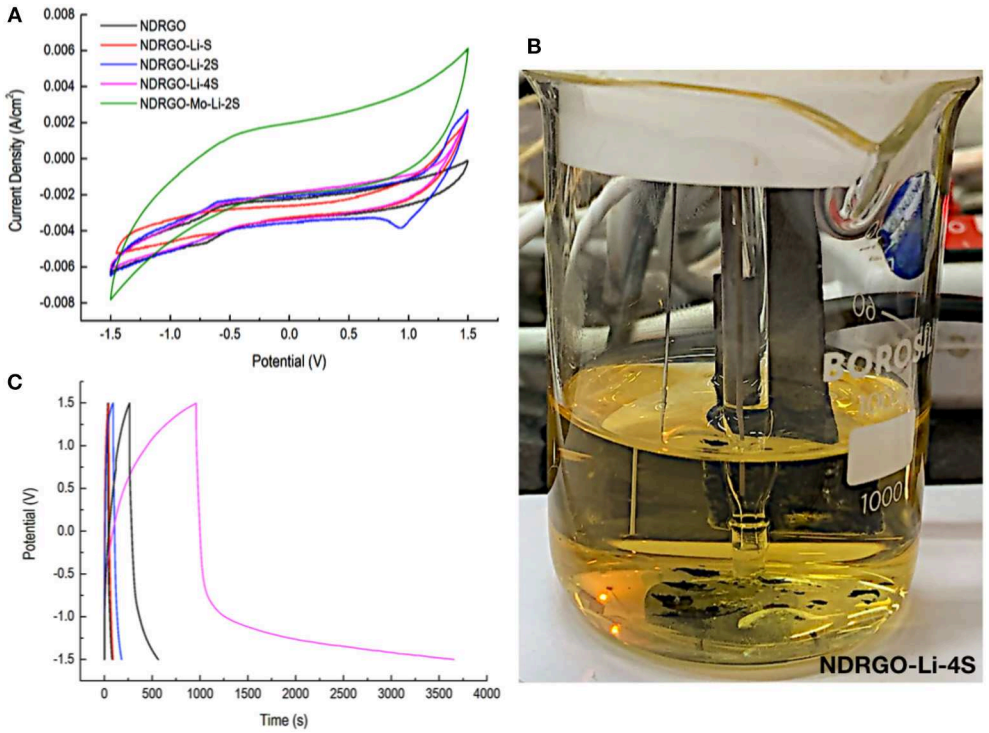

FIGURE 4 | Electrochemical characterization of all the composites. CV was performed in the voltage range of −1.5 V to +1.5 V at a scan rate of 5 millivolt (mV) per second. Charge discharge analyses (CC/CC mode) were performed using a constant charging and discharging current of 5 milliampere (mA) in the voltage range of −1.5 V to +1.5 V. **(A)** Cyclic voltammogram analysis. **(B)** *Sulfur spillage* in NDRGO-Li-4S composite. **(C)** Charge-discharge analysis.

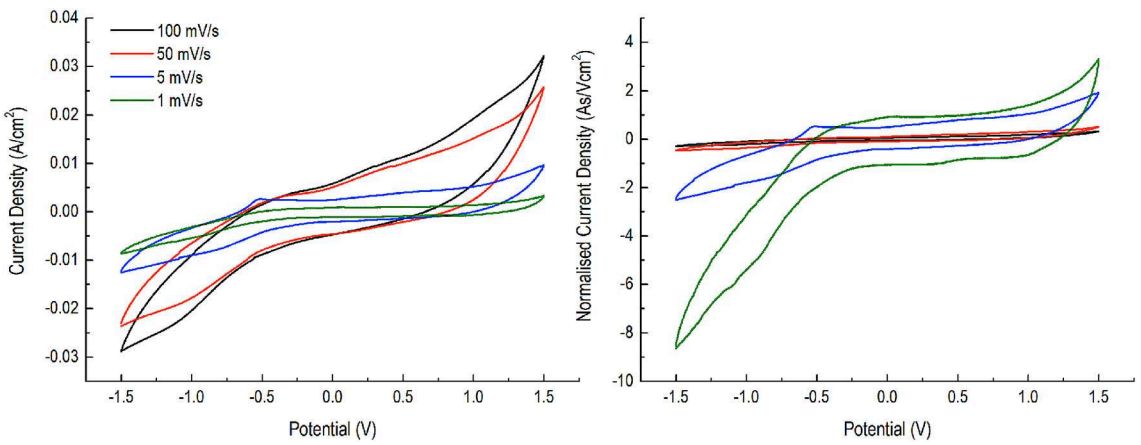

FIGURE 5 | CV analysis of NDRGO-Mo-Li-2S at 1, 5, 50, 100 mV/s and normalized current density (As/Vcm^2).

(a) *Assuming that the assembly of the atoms follows a layer by layer strategy, the larger size of Mo on top would have hampered the interaction of smaller Li and S atoms with the electrolyte.*
(b) *Mo being multi-valent would provide varied binding sites for upcoming Li and S atoms.*
(c) *By this strategy, Li is sandwiched between two multi-valent atoms viz., Mo and S.*
(d) *Introducing a larger Mo atom between NDRGO matrix and Li, increased the distance between highly electropositive Li and highly electronegative N.*

This newly synthesized NDRGO-Mo-Li-2S showed surprising deviation from super capacitor like properties in terms of cyclic voltammogram (**Figure 4A**) and charge-discharge characteristics (**Figure 4C**) than any of its siblings' like NDRGO, NDRGO-Li-S,

and NDRGO-Li-2S. What was even more surprising was the stability of this new composite viz., NDRGO-Mo-Li-2S. *Since NDRGO-Mo-Li-2S composite did not show any super capacitor like feature, we designed additional experiments to test its electrical nature.*

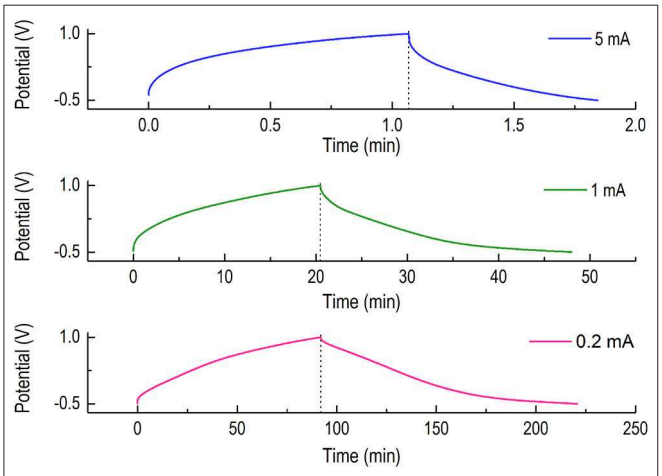

FIGURE 6 | Charge discharge analyses (CC/CC mode) were performed for NDRGO-Mo-Li-2S using a constant charging and discharging current of 5, 1, and 0.2 mA in the voltage range of −0.5 V to +1.0 V.

Next, we performed CV for NDRGO-Mo-Li-2S at different scan rate and further determined the normalized current density (**Figure 5**). Upon normalization of the current density, we observed certain striking differences viz., at 50 and 100 mV/s scan, one does not see any difference. But as we lower the scan rate to 5 mV/s and then further down to 1 mV/s, we started to see a complete deviation from higher scanning rates viz., 50 and 100 mV/s. Thus this critical information, indicated that the electrode material is more suitable for devices requiring slow charge kinetics viz., more like a battery electrode, or something between battery and supercapacitor (capattery) (Akinwolemiwa et al., 2015), the goal with which we initiated our research (a stable Li_2S-C composite).

In the light of this result (**Figure 5**), we performed a charge discharge analysis (CC/CC mode) of the material using a constant charging and discharging current of 5, 1, and 0.2 mA in the voltage range of −0.5 V to +1.0 V (**Figure 6**). The voltage window of 1.5 V was selected, since we observe that at low current, the electrode perform optimally at this range. As we lowered down the current, the material behaved typically like a battery material, a NDRGO-Mo-Li-2S cathode. What is most

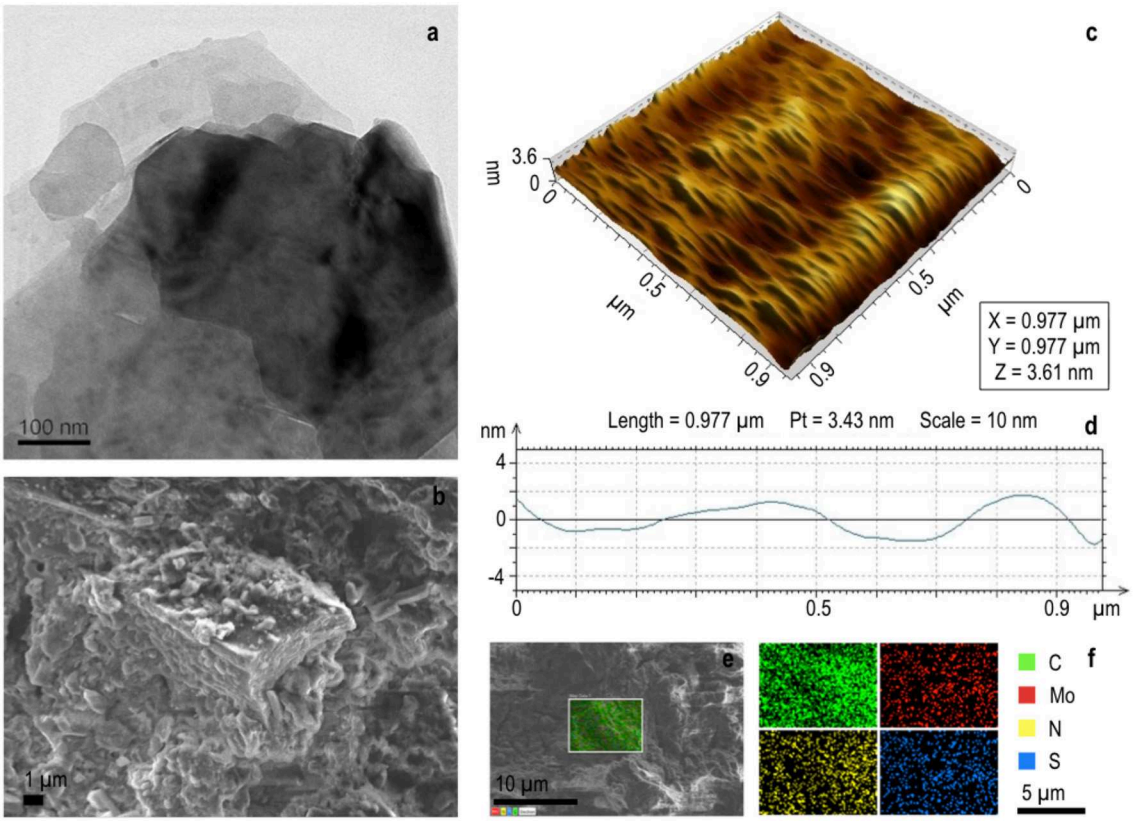

FIGURE 7 | Structural analysis of NDRGO-Mo-Li-2S. **(a)** Representative TEM image. **(b)** Representative FESEM image showing lamellar structure. **(c)** AFM image. **(d)** Height profile of the material in AFM. **(e)** Representative site used for elemental analysis. **(f)** Elemental analysis for C, N, Mo and S.

TABLE 1 | The binding energies obtained from the narrow spectra for each constituting elements of NDRGO-Mo-Li-2S.

Element	Bond type	Binding energy (eV)
C1s	C-C	284.0
	CH_3-Li	282.4
	C-S_2	287.0
	C_5H_5N/MoS_2	286.0
	C_6H_5CN	285.0
N1s	C_5H_5N	398.6
	Mo-N	397.95
	Li-N	396.5
	C_6H_4CNSSH	400.4
Mo3d	Mo(0)	226.23
	$Mo_{5/2}$(IV)	230.3
	Mo(V)	231.2
	$Mo_{3/2}$(IV)	233.9
	Mo(VI)	232.9
Li1s	Li	53.0
	Li-S	54.3
	Li-N	55.8
S2p	MoS_2	162.9
	C-S	161.7
	$(S_n)^{2-}$	166.2
	S-S	160.84
	$C_6H_5S(O)_2NH(C_4H_2N(S))C_6H_5$	168.00

interesting revelation is that, *it is feasible to engineer the charge-discharge kinetics with little molecular tweaking. Next challenging question for us was to explore the structure of NDRGO-Mo-Li-2S.*

Sub-section 2

Detailed structural analysis and life cycle studies of NDRGO-Mo-Li-2S electrode.

Based on the electrochemical results, we further explored the structural characteristics of NDRGO-Mo-Li-2S **(Figure 7)**. The key question we asked is "how introduction of Mo completely alters the stability and functional efficiency of the material?"

In NDRGO-Mo-Li-2S, a weak 002 peak appears at 26.5 °C in its XRD, indicating significant deoxygenation and the presence of the nitrogen atoms in the crystal lattice of graphene. This intercalation of nitrogen, resulted in increased distance between the graphite layers **(Figure 3)**. It showed 2D stacked sheet like morphology in TEM (**Figure 2d** and **Figure 7a**). Further, SEM images showed lamellar geometry **(Figures 7b,f)**. The depth profile of the matrix in AFM showed an average height of 3.6 nm **(Figure 7c)**. The presence of S, Mo, C, and N was further verified by elemental analysis.

In order to analyze the surface chemical features of NDRGO-Mo-Li-2S, we performed a detailed XPS. **Table 1** shows the binding energies corresponding to the bonds observed in NDRGO-Mo-Li-2S complex in the XPS spectra. The assignment of XPS peaks were validated with NIST X-ray photoelectron spectroscopy database (Naumkin et al., 2012).

The broad spectrum of XPS shows the presence N1s, C1s, Mo3d, S2p, Li1s **(Figure 8A)**. The narrow spectra of C1s, N1s, Mo3d, Li1s, S2p are shown in **Figures 8B–F**.

The initial hypothesis we laid out in the synthesis of NDRGO-Mo-Li-2S, to our satisfaction corroborates with its structural and bonding characteristics. The TEM, FESEM, and AFM showed extensive stacking of sheets, this is in line with the characteristics of NDRGO **(Figure 7**, **Table 1)** and MoS_2 as evident in **Figure 8F**, **Table 1**. Mo exists in elemental as well as in IV, V, VI oxidation states **(Figure 8D)**. Sandwiching of Mo between NDRGO and S is also observed **(Figure 8B)**. The integration of Mo into the NDRGO matrix is highly evident **(Figure 8F)**. Addition of Li after Mo has served to be advantageous as, Li being a smaller atom managed to percolate through the Mo sieve and bond with C and highly electronegative N atoms of NDRGO; it has also stayed above Mo and bonded with S **(Figure 8E)**. The role of Mo in the NDRGO-Mo-Li-2S complex, seems like that of an atomic ligand that holds the constituent atoms at a distance from each other. An analogy could be drawn where *Mo acts like a dielectric with carbon-nitrogen on one side and lithium-sulfur on the other side making a series of molecular capacitors within the NDRGO-Mo-Li-2S matrix.*

The multivalency and the proposed atomic coordinating ability of Mo in NDRGO-Mo-Li-2S complex led us to study the life of the material at a lower current. The charge discharge experiment was tried to match the real life conditions, where, the NDRGO-Mo-Li-2S electrode (in three cell electrode configuration) was maintained under argon atmosphere continuously for 23 days. The time course of the experiment is illustrated in **Table 2**. The experiment was done in eight sets (I-VIII) and a gap of around 12 h was given between each set. During this gap phase, the system was left idle. The gap was purposefully introduced in order to validate, whether system can restart from its original configuration after undergoing an idle phase. We obtained a total of 133 cycles of which representative traces of 7 cycles viz., 3rd, 23rd, 43rd, 63rd, 83rd, 103rd, 123rd cycles are shown in **Figures 9A–G**. A comparative profile of the charge-discharge curve for cycle number 2 and 133 is shown in **Figure 9H**. We observed that the system performed consistently throughout the experimentation process and the material maintained its original configuration. Such results prove the stability of NDRGO-Mo-Li-2S electrode.

One interesting aspect could be seen while carefully looking at the tendency of the charge discharge curves viz., the capacity decayed at the former cycle testing and increased at the latter cycle testing. It seems like the system is behaving like programmable matter in order to attain its most stable configuration. In this process, the entire quaternary mixture it slowly moving to a more stable and ordered state through several metastable states reflecting the transition from one type of electron transfer (supercapacitor like) to another kind of electron transfer (battery type). These transition classify the material into the range of cappatery like material.

Sub-section 3

A putative mechanism of electron transport on the electrode surface of NDRGO-Mo-Li-2S.

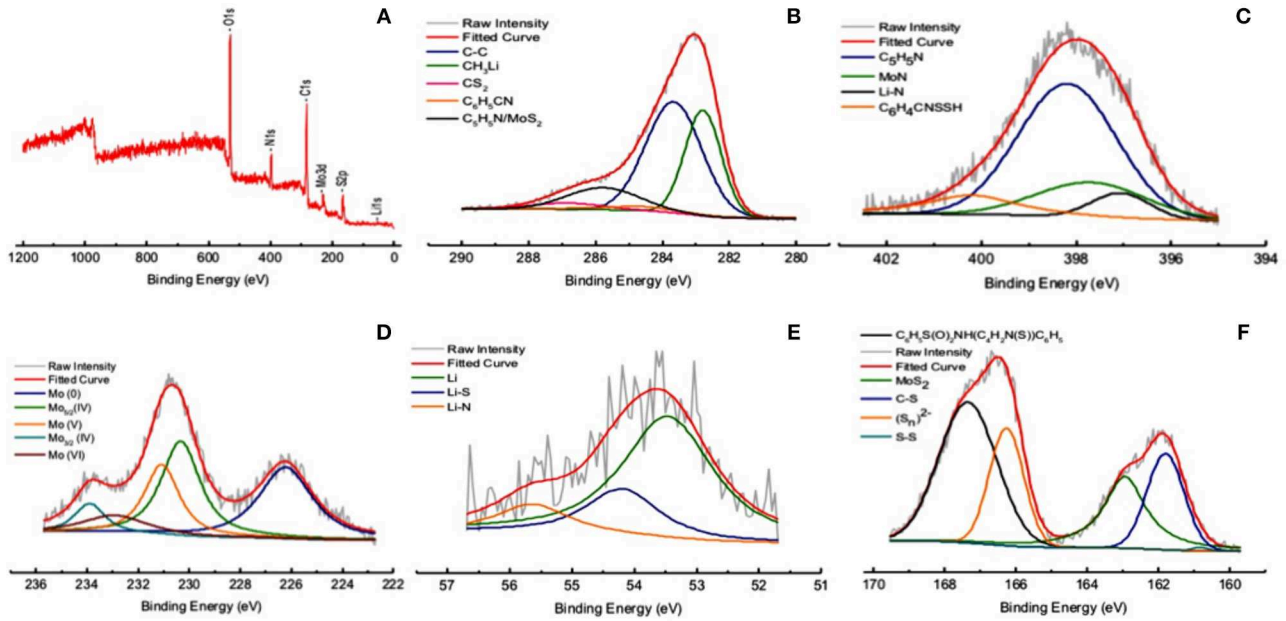

FIGURE 8 | XPS analysis of NDRGO-Mo-Li-2S. **(A)** Broad spectrum. Narrow spectra of **(B)** C1s. **(C)** N1s. **(D)** Mo3d. **(E)** Li1s. **(F)** S2p.

TABLE 2 | The time course of charge-discharge cycles for NDRGO-Mo-Li-2S at 0.2 mA in the potential window, +1 V to −0.5 V.

Set number	Number of cycles	Number of hours	Cycle number illustrated in Figure 9
I	18	∼65.0	A
II	39	∼130.0	B,C
III	7	∼19.4	D
IV	28	∼79.2	E
V	6	∼18	–
VI	22	∼72	F
VII	6	∼23	–
VIII	7	∼36	G

This interesting behavior of NDRGO-Mo-Li-2S, prompted us to propose a putative model of electron transfer, where we attempted to address the following question: How introduction Mo changed the charge-discharge time and area within CV curve? These properties may be related to the stability of the charge and electron release processes which could be explained by introducing very unique "induced electron transfer" reactions (Taube, 1970; Sarkar and Ansari, 1986; Chandrasekaran et al., 1987; Ansari et al., 1988a,b,c; Miller and Min, 2009). Here, the sustained electron flux is maintained by invoking the role of Li as an external oxidant, Li^+ (I). This provokes the intra-atom electron transfer across Mo(VI)-S(II) bond, where Mo(VI) is the internal oxidant and S(II), is the internal reductant. For electron book keeping, it can be presumed that two sulfide ions release two electrons getting self oxidized to disulfide (S_2) (II) anion. The released two electrons are shared one each by the external oxidant, Li^+ (I) to create Li and internal oxidant Mo(VI) to create Mo(V). Such redox reaction is reversed using NDRGO as external reductant (releasing electron) to induce intra-atom reverse electron flow across [Mo(V)-(S_2)] to regenerate the starting [Mo(VI)-S(II)] material to complete the cycle. Here NDRGO readily oscillates between its graphene oxide and reduced graphene oxide states. Interestingly all the oxidation states of these elements proposed in such electron transfers associated in this quaternary complex have been identified using XPS. Therefore, such redox cycle is competent for the flow of electrons in a lasting charge storage material through this unique bio-inorganic hybrid approach. In **Figure 10**, a putative mechanism of induced electron transfer in NDRGO-Mo-Li-2S is shown.

An important question which arises from this study is '*what kind of benefits 'induced electron transfer' could offer in development of lithium-sulfur batteries*?' It has been well-established that sulfur attached to metal plays varied electron transfer reaction. Sulfur has the unique distinction when S^{2-} (Sulfide anion) gets oxidized to elemental sulfur (S0) and in that situation S^{2-} and S0 combine to create S_2^{2-}. Interestingly if you add more S0 then there is a creation of S_3^{2-}. This is the polysulfide chemistry and can be extended to S_4^{2-} and further. Interestingly for species like S_4^{2-}, it dissociates to $2S_2^-$. Therefore, sulfide under electrochemical environment can display different species from neutral to anionic including free radical. Such chemistry has been exploited in induced electron transfer. For such special type of electron transfer for electron bookkeeping, if one assume the sulfide gets oxidized then the electron released can be shared by two different metal for example the chemistry of Li+ to Li must

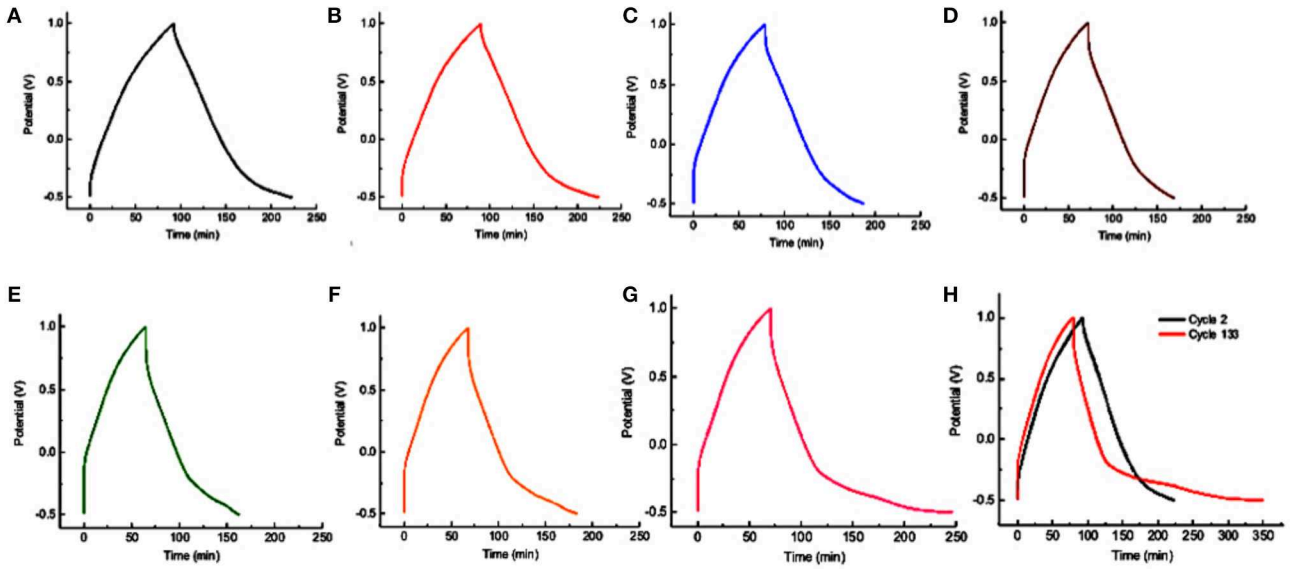

FIGURE 9 | Long-term charge-discharge cycles for NDRGO-Mo-Li-2S. **(A)** Cycle number 3. **(B)** Cycle number 23. **(C)** Cycle number 43. **(D)** Cycle number 63. **(E)** Cycle number 83. **(F)** Cycle number 103. **(G)** Cycle number 123. **(H)** Comparing the charge-discharge profile of cycle number 2 vs. cycle number 133.

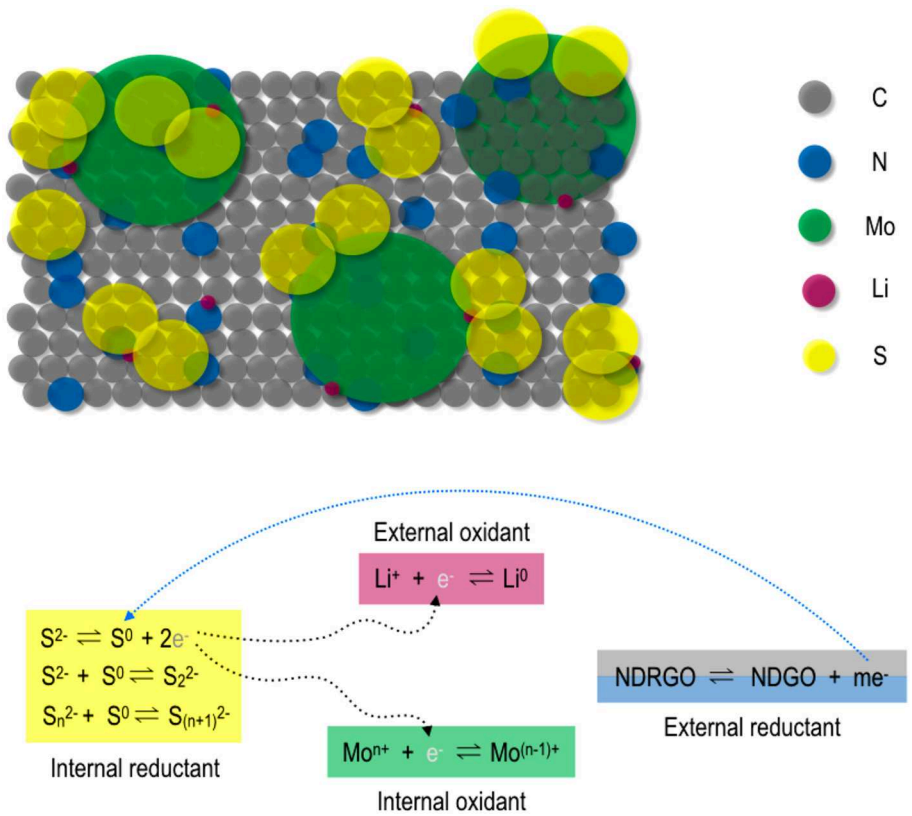

FIGURE 10 | Induced electron transfer in N-doped reduced graphene oxide-Mo-Li-S electrode; where m stands for number of electrons.

be compensated by involving one another electron capture by Mo in + state to produce in (N-1)+ state. These two together can control the two electrons released from say $2S^{2-}$ to create S_2^{2-} + 2 Electrons. So the question is the entire process is taking place if one can conceive the idea that in a molecule of lithium sulfide, if lithium ion is treated as external oxidant and sulfide as the

internal reductant; in this situation the extra electron generated can be shared by the used Mo ion. Here Mo act as internal oxidant. The reaction can be concerted if a ternary mixture like Li, S, Mo act in unison. Here the distinction of internal and external redox partner may not arise, but the shuttling of electron from sulfide to Li and Mo can effectively proceed. The entire electron transfer has different rate and where the rate of one half sulfur to Li may differ from Sulfur to Mo. Such a system can experience the electron transfer difference at different scan rate. A fine tuning of these ternary mixture can be made if there is nitrogen remain very near to these ternary system, which can affect the electron transfer. The nitrogen atom can do it readily because it has different oxidation state. However, there cannot be a fraction of electron that can participate moving from one atom to another and for that reason the delocalization of electron density of the entire system has to be taken into account. The measurement of such electron distribution is not straight forward because under the varied scan rate such overall electron density varies. For simple Li_2S cathode, such induced electron transfer may not be feasible because one has to maintain electron book keeping. So the concept of external oxidant and internal oxidant sharing electrons generated by internal reluctant and external reductant is not varied because for induced electron transfer concept there is the involvement of one internal oxidant and one external oxidant to share electron generated by the lone internal reductant. For conventional Li_2S cathode it is highly unlikely that one can invoke induced electron transfer process. Therefore to sustain such reaction in Li system other elements are nowadays routinely exploited for example the addition of iron, phosphate and further the transition metal-organic frame work (Geng et al., 2018; Jangir et al., 2018; Li et al., 2018a,b,c; Luo et al., 2019; Shi et al., 2019; Zhou et al., 2019).

Further with reference to NDRGO-Mo-Li-2S complex, we can see that the capacitor capacity has been greatly improved after adding Mo. Among them, the composition of sulfur has obtained the optimum result. Is it feasible to optimize the concentration of Mo? From atom conservation the extra addition of Mo will not enhance the electron transfer behavior. This is simple for the reason that Mo can play multi electron donor and acceptor and therefore an optimal stoichiometry like 1 unit of Mo in the system is expected.

Here it is worth highlighting the exceptional electrochemical stability of the heavily nitrogen doped carbon derived from a natural protein polymer (silk cocoon) and its transition metal sulfide composites; as stability of such composite always remained a challenge for different energy applications (Cravanzola et al., 2016; Dubey et al., 2018; Geng et al., 2018; Jangir et al., 2018; Li et al., 2018a,b,c; Luo et al., 2019; Shi et al., 2019; Zhou et al., 2019).

SUMMARY AND CONCLUSIONS

In summary, we have successfully designed and engineered a stable bio-hybrid electrode material which integrates lithium (Li), sulfur (S), and molybdenum (Mo) in a matrix of biological origin viz., silk cocoon derived heavily nitrogen (16%) doped reduced graphene oxide (NDRGO); thus resulting in NDRGO-Mo-Li-2S. The electron shuttling on this electrode is govern by a lesser explored route viz., "induced electron transfer" regulated by an electropositive Li, electronegative NDRGO and an embedded redox couple of Mo-S. We believe that such a bio-hybrid approach is a step toward developing sustainable, eco-friendly high energy electrode materials.

DATA AVAILABILITY

All datasets generated for this study are included in the manuscript/supplementary files.

AUTHOR CONTRIBUTIONS

This work is part of HJ's doctoral research. HJ and MD conceived the idea and designed the experiments. HJ developed the idea and conducted the synthesis, carried out the structural, chemical and electrochemical characterizations. AB conducted the synthesis and purification of the compounds. JR helped in TEM and AFM. SS and MD conceived the concept of electron transfer shuttle and role of Mo. HJ, SS, and MD wrote the manuscript.

FUNDING

HJ acknowledges Ministry of Human Resource and Development, Government of India for her doctoral fellowship research.

ACKNOWLEDGMENTS

Authors are thankful to the staff at Advance Centre for Material Science, Indian Institute of Technology Kanpur, India. We sincerely acknowledge the help offered to us by Mr. DD Pal for XPS, Mr. A Tiwari for XRD facility, and Mr. Mitesh for FESEM work. This work was an integral part of HJ's doctoral thesis.

REFERENCES

Akinwolemiwa, B., Peng, C., and Chen, G. Z. (2015). Redox electrolytes in supercapacitors. *J. Electrochem. Soc.* 162, A5054–A5059. doi: 10.1149/2.0111505jes

Ansari, M. A., Chandrasekaran, J., and Sarkar, S. (1988a). Sulfur mediated induced electron transfer reactions in tungsten-sulfur systems: synthesis and reactivity of bis (tetraethylammonium) bis (disulfido) dioxodi-m-sulfidodi tungstate. *Polyhedron* 7, 471–476. doi: 10.1016/S0277-5387(00)81193-6

Ansari, M. A., Chandrasekaran, J., and Sarkar, S. (1988b). Concealed induced internal electron transfer reaction in the synthesis of bis (diethyldithiocarbamato) (disulfido) oxotungsten from diethylammonium oxotrithiotungstate(2-) and carbon disulfide with oxygen. *Inorg. Chem.* 27, 763–764.

Ansari, M. A., Chandrasekaran, J., and Sarkar, S. (1988c). One pot synthesis of dinuclear tungsten(V) compounds containing [W2XY(μ -S)2]2+ (X = O, S; Y = O, S) cores by thermally induced internal electron-transfer processes. *Bull. Chem. Soc. Jpn.* 61, 2265–2267. doi: 10.1246/bcsj.61.2265

Armand, M., and Tarascon, J. M. (2008). Building better batteries. *Nature* 451, 652–657. doi: 10.1038/451652a

Aurbach, D., Pollak, E., Elazari, R., Salitra, G., Kelley, C. S., and Affinito, J. (2009). On the surface chemical aspects of very high energy density, rechargeable Li–Sulfur batteries. *J. Electrochem. Soc.* 156, A694–A702. doi: 10.1149/1.3148721

Chandrasekaran, J., Ansari, M. A., and Sarkar, S. (1987). Aging of ammonium tetrathiomolybdate (VI) in air: an example of induced electron transfer by external oxidant. *J. Less Common Met.* 134, L23–L25. doi: 10.1016/0022-5088(87)90570-4

Cravanzola, S., Cesano, F., Magnacca, G., Zecchina, A., and Scarano, D. (2016). Designing rGO/MoS2 hybrid nanostructures for photocatalytic applications. *RSC Adv.* 6, 59001–59008. doi: 10.1039/C6RA08633K

Dubey, A., Jangir, H., Verma, S., Saxena, M., Sarkar, S., Philip, D., et al. (2018). A green route for production of 'carbon based charge storage nanomaterials'. *Mater. Renew. Sustain Energy*. 7:20. doi: 10.1007/s40243-018-0127-7

Ely, T. O., Kamzabek, D., Chakraborty, D., and Doherty, M. F. (2018). Lithium–sulfur batteries: state of the art and future directions. *ACS Appl. Energy Mater.* 1, 1783–1814. doi: 10.1021/acsaem.7b00153

Geng, P., Zheng, S., Tang, H., Zhu, R., Zhang, L., Cao, S., et al. (2018). Transition metal sulfides based on graphene for electrochemical energy storage. *Adv. Energy Mater.* 8:1703259. doi: 10.1002/aenm.201703259

Hassoun, J., and Scrosati, B. (2010). A high-performance polymer tin sulfur lithium ion battery. *Angew Chem. Int. Ed. Engl.* 49, 2371–2374. doi: 10.1002/anie.200907324

Jangir, H., Pandey, M., Jha, R., Dubey, A., Verma, S., Philip, D., et al. (2018). Sequential entrapping of Li and S in a conductivity cage of N-doped reduced graphene oxide supercapacitor derived from silk cocoon: a hybrid Li–S-silk supercapacitor. *Appl. Nanosci.* 8, 379–393. doi: 10.1007/s13204-018-0641-z

Ji, X., Lee, K. T., and Nazar, L. F. (2009). A highly ordered nanostructured carbon–sulphur cathode for lithium–sulphur batteries. *Nat. Mater.* 8, 500–506. doi: 10.1038/nmat2460

Li, Q., Xu, Y., Zheng, S., Guo, X., Xue, H., and Pang, H. (2018a). Recent progress in some amorphous materials for supercapacitors. *Small* 14:1800426. doi: 10.1002/smll.201800426

Li, X., Zheng, S., Jin, L., Li, Y., Geng, P., Xue, H., et al. (2018b). Metal-organic framework-derived carbons for battery applications. *Adv. Energy Mater.* 8:1800716. doi: 10.1002/aenm.201800716

Li, Z., He, Q., Xu, X., Zhao, Y., Liu, X., Zhou, C., et al. (2018c). A 3D nitrogen-doped graphene/TiN nanowires composite as a strong polysulfide anchor for lithium-sulfur batteries with enhanced rate performance and high areal capacity. *Adv. Mater.* 30:e1804089. doi: 10.1002/adma.201804089

Luo, Y., Yan, Y., Zheng, S., Xue, H., and Pang, H. (2019). Graphitic carbon nitride based materials for electrochemical energy storage. *J. Mater. Chem. A* 7, 901–924. doi: 10.1039/C8TA08464E

Medenbach, L., Escher, I., Köwitsch, N., Armbrüster, M., Zedler, L., Dietzek, B., et al. (2018). Sulfur spillover on carbon materials and possible impacts on metal-sulfur batteries. *Angew. Chem. Int. Ed.* 57, 13666–13670. doi: 10.1002/anie.201807295

Miller, J. S., and Min, K. L. (2009). Oxidation leading to reduction: redox-induced electron transfer (RIET). *Angew Chem. Int. Ed. Engl.* 48, 262–272. doi: 10.1002/anie.200705138

Naumkin, A. V., Kraut-Vass, A., Gaarenstroom, S. W., and Powell, C. J. (2012). *Compiled and Evaluated NIST X-Ray Photoelectron Spectroscopy Database* (NIST standard reference database 20, Version 4.1). Gaithersburg, MD: National Institute of Standards and Technology. doi: 10.18434/T4T88K

Peled, E., and Yamin, H. (1983). Electrochemistry of a nonaqueous lithium/sulfur cell. *J. Power Sources* 9, 281–287. doi: 10.1016/0378-7753(83)87029-3

Peramunage, D., and Licht, S. (1993). A solid sulfur cathode for aqueous batteries. *Science* 261, 1029–1032. doi: 10.1126/science.261.5124.1029

Rauh, R. D., Abraham, K. M., Pearson, G. F., Surprenant, J. K., and Brummer, S. B. (1979). A lithium/dissolved sulfur battery with an organic electrolyte. *J. Electrochem. Soc.* 126, 523–527. doi: 10.1149/1.2129079

Roy, M. K., Kusurkar, T. S., Maurya, S. K., Meena, S. K., Singh, S. K., Sethy, N., et al. (2014). Graphene oxide from silk cocoon: a novel magnetic fluorophore for multi-photon imaging. *3 Biotech* 4, 67–75. doi: 10.1007/s13205-013-0128-2

Sahu, V., Grover, S., Tulachan, B., Sharma, M., Srivastava, G., Roy, M., et al. (2015). Heavily nitrogen doped, graphene supercapacitor from silk cocoon. *Electrochim. Acta* 160, 244–253. doi: 10.1016/j.electacta.2015.02.019

Sarkar, S., and Ansari, M. A. (1986). Conversion of W(VI)OS32- into [W(V)2O2(μ-S)2(S2)2]2- and vice-versa by internal redox processes induced by iodine and Sx2-Sabyasachi Sarkar, Mohammad A. Ansari. *J. Chem. Soc. Chem. Commun.* 324–325. doi: 10.1039/C39860000324

Shi, H., Zhao, X., Wu, Z.-S., Dong, Y., Lu, P., Chen, J., et al. (2019). Free-standing integrated cathode derived from 3D graphene/carbon nanotube aerogels serving as binder-free sulfur host and interlayer for ultrahigh volumetric-energy-density lithiumsulfur batteries. *Nano Energy* 60, 743–751. doi: 10.1016/j.nanoen.2019.04.006

Shim, J., Stribel, K. A., and Cairns, E. J. (2002). The lithium/sulfur rechargeable cell effects of electrode composition and solvent on cell performance. *J. Electrochem. Soc.* 149, A1321–A1325. doi: 10.1149/1.1503076

Stoller, M. D., and Ruoff, R. (2010). Best practice methods for determining an electrode material's performance for ultracapacitor. *Energy Environ. Sci.* 3, 1294–1301. doi: 10.1039/c0ee00074d

Stryer, L. (1999). *Biochemistry*. New York, NY: W. H. Freeman and Co. Ltd., (1727), ASIN:B01MZ56QSC.

Taube, H. (1970). *Electron-Transfer Reactions of Complex Ions in Solution*. Orlando, FL: Academic Press, ISBN: 978-0-12-683850-3.

Wang, H., Liu, S., Huang, K., Yin, X., Liu, Y.-N., and Peng, S. (2012). BMIMBF4 ionic liquid mixtures electrolyte for Li-ion batteries. *Int. J. Electrochem. Sci.* 7, 1688–1698. Available online at: http://www.electrochemsci.org/papers/vol7/7021688.pdf

Zhou, H., Li, X., Li, Y., Zheng, M., and Pang, H. (2019). Applications of MxSey (M = Fe, Co, Ni) and their composites in electrochemical energy storage and conversion. *Nano Micro Lett.* 11:40. doi: 10.1007/s40820-019-0272-2

Conflict of Interest Statement: The authors declare that the research was conducted in the absence of any commercial or financial relationships that could be construed as a potential conflict of interest.

frontiers in Materials

ORIGINAL RESEARCH
published: 09 January 2020
doi: 10.3389/fmats.2019.00337

Green and Low-Cost Membrane Electrode Assembly for Proton Exchange Membrane Fuel Cells: Effect of Double-Layer Electrodes and Gas Diffusion Layer

M. H. Gouda[1], Mohamed Elnouby[2], Andrew N. Aziz[3], M. Elsayed Youssef[3], D. M. F. Santos[4] and Noha A. Elessawy[5]**

[1] Polymer Materials Research Department, Advanced Technology and New Materials Research Institute, City of Scientific Research and Technological Applications, New Borg El-Arab City, Egypt, [2] Nanomaterials and Composites Research Department, Advanced Technology and New Materials Research Institute, City of Scientific Research and Technological Applications, New Borg El-Arab City, Egypt, [3] Computer Based Engineering Applications Department, Informatics Research Institute IRI, City of Scientific Research and Technological Applications, New Borg Al-Arab City, Egypt, [4] Center of Physics and Engineering of Advanced Materials, Instituto Superior Técnico, Universidade de Lisboa, Lisbon, Portugal, [5] Advanced Technology and New Materials Research Institute, City of Scientific Research and Technological Applications, New Borg Al-Arab City, Egypt

OPEN ACCESS

Edited by:
M. Jasim Uddin, University of Texas Rio Grande Valley Edinburg, United States

Reviewed by:
Qihui Wu, Jimei University, China
Muhammad Zobayer Bin Mukhlish, Shahjalal University of Science and Technology, Bangladesh

***Correspondence:**
D. M. F. Santos
diogosantos@tecnico.ulisboa.pt
Noha A. Elessawy
nony_essawy@yahoo.com

Specialty section:
This article was submitted to Carbon-Based Materials, a section of the journal Frontiers in Materials

Received: *29 September 2019*
Accepted: *06 December 2019*
Published: *09 January 2020*

Citation:
Gouda MH, Elnouby M, Aziz AN, Youssef ME, Santos DMF and Elessawy NA (2020) Green and Low-Cost Membrane Electrode Assembly for Proton Exchange Membrane Fuel Cells: Effect of Double-Layer Electrodes and Gas Diffusion Layer. Front. Mater. 6:337. doi: 10.3389/fmats.2019.00337

The success of fuel cells depends on the proper design of the electrodes and membrane allowing easy access of oxygen and protons. Using non-precious catalyst electrodes based on recyclable carbon nanostructures is most important to produce clean energy and increase the ability to commercialize the fuel cells. Herein, reduced graphene oxide (rGO) and graphene/magnetic iron oxide nanocomposite (rGO/MIO) are successfully synthesized as anode and cathode, respectively, from polyethylene terephthalate (PET) waste bottles using easy steps in order to simplify the method and reducing the production cost. While, the membrane is prepared from low cost and eco-friendly ternary polymers blend which are polyvinyl alcohol (PVA), polyethylene oxide (PEO) and polyvinyl pyrrolidone (PVP) then doped with sulfonated graphene oxide. The prepared electrodes have characteristic high porosity and their electrocatalytic performances are evaluated using three-electrode cell electrochemical studies as cyclic voltammetry and linear scan voltammetry combined with rotating disk electrode. A new assembly of the membrane between two non-precious catalyst electrodes as a single polymer electrolyte membrane fuel cell (PEMFC) was developed using a catalyst-coated membrane technique. The membrane electrode assembly (MEA) design parameters which affect its performance in hydrogen fuel cells as number of used catalyst layers (CL) or using gas diffusion layer (GDL) were evaluated in a single cell set-up with H_2/O_2 operation and the results revealed that the performance MEA was enhanced with using GDL more than that of MEA without GDL by 66% at a current density of 0.8 A cm^{-2} while the performance with double CL was better than that of the conventional single CL by 30% at a current density of 0.98 mA cm^{-2}.

Keywords: graphene, graphene iron oxide composites, proton exchange membrane, membrane electrode assembly, hydrogen fuel cells

INTRODUCTION

As a result of the rapid urbanization since the beginning of the last century, the global growth of fossil fuel energy consumption has increased, leading to an increase in environmental pollution rate. Consequently, environmental pollution has shifted research attention to get clean energy conversion and storage systems. Fuel cells are known as one of the cleanest energy conversion systems due to their high energy density, high energy-conversion efficiency, environmental safety, and other outstanding features (Frey and Linardi, 2004).

Among different types of fuel cells, the polymer electrolyte membrane fuel cell (PEMFC) is a promising green energy conversion technology for both portable and stationary devices, as well as transportation applications. This is may be due to its economic, high efficiency, low-temperature operation, zero or low emission and rapid start-up (Gouda et al., 2019). The conversion process of chemical to electrical energy in PEMFCs depends on two chemical reactions at anode and cathode where oxygen reduction occurs at the cathode and hydrogen oxidation occurs at the anode (Liu et al., 2019a) and both reactions need catalysts to reduce the electrochemical over-potential and to increase the voltage output. The oxygen reduction reaction (ORR) at the cathode is a multistep reaction involved with multielectron, thus the ORR reaction consumes most of the catalyst material. Consequently, the development of low cost, high-performance electrocatalysts for improving ORR kinetics is essential to reduce the cost of PEMFCs (Liu et al., 2019b). Pt-based composites are considered as the most efficient cathode catalysts, but they have disadvantages as high cost, crossover poisoning and low stability especially in acidic media (Choi et al., 2015). However, high-performance non-precious metal catalysts (NPMCs) simultaneously active for the ORR at the cathode and the hydrogen oxidation reaction (HOR) at the anode are desperately needed to replace these precious metals and to solve the drawbacks (Gupta et al., 2016). Under these circumstances, transition metal oxides (Gao et al., 2017; Lai et al., 2017), hybrid inorganic nanocarbon materials (Su et al., 2014; Ye et al., 2017) and carbon-doped metal-free heteroatom nanomaterials (Dumont et al., 2019) were used to substitute platinum for constructing highly efficient non-precious metal catalysts. Where, the promoted activity of doped carbon materials may be attributed to the electron-donating or electron-accepting behavior between adjacent carbon atoms and the heteroatoms, which modify the charge allocation in the carbon plane (Shen et al., 2014).

In addition to catalyst electrodes, the polymeric proton exchange membrane is one of the most important components of PEMFCs. Thus, development of the proton exchange membrane using non-perfluorinated based polymers as new alternative membranes attracted many researchers with the aim of replacing benchmark Nafion® membranes to reduce the production cost and to be closer to commercialization (Bakangura et al., 2016; Pourzare et al., 2016). However, the non-perfluorinated based polymers are usually modified chemically with several treatments, such as polymers blending, incorporation of doping agents in the polymer matrix as carbon-based nanomaterials and polymers sulfonation to improving the membrane properties (Awang et al., 2015; Pourzare et al., 2016; Sedesheva et al., 2016; Pandey et al., 2017).

Recently, graphene (G) and graphene-based materials have received great interest as a promising material for fuel cell applications due to its remarkable advantages, such as; large specific surface area, mechanical flexibility, and good electrical conductivity. In particular, a significant improvement in the electrocatalytic activity of electrodes was observed with graphene or modified graphene as the catalyst support or as a metal-free catalyst (Iwan et al., 2015; Morales-Acosta et al., 2019). Moreover, the incorporation of graphene oxide (GO) or sulfonated graphene oxide (SGO) into a polymer matrix of the PEM (Li et al., 2017; Pandey et al., 2017; Qiu et al., 2017) enhance its ionic conductivity and improve its physicochemical properties (Beydaghi et al., 2014).

In recent years, many researchers have been interested in turning the membrane electrode assembly (MEA) prototypes into commercially valuable products by improving its overall efficiency, increase current density and decrease the cost of the membrane and catalytic materials used. However, the results show that the true performance of the MEA for PEMFC is not only depended on the properties of the individual components but also depend on the MEA production method and the operating conditions in the cell (Aziz et al., 2018) such as the composition of electrode inks, electrode pressing, percentage of humidification and applied pressure on both electrodes, gas diffusion layer (GDL) materials used and cell temperature (Frey and Linardi, 2004; Thanasilp and Hunsom, 2010; Kim et al., 2015).

Motivated by these observations, this research concerns the production of low-cost MEA for PEMFC using non-precious metal graphene-based materials as catalytic electrodes prepared from the thermal dissociation of plastic waste using simple, one-pot, environmentally-friendly, and applicable synthesis method. While the polymeric proton exchange membrane was produced based on an ecological and simple approach via polymer crosslinking and casting techniques using a ternary crosslinked polymer containing poly (vinyl alcohol), poly (ethylene oxide) and poly (vinyl pyrrolidone) (Gouda et al., 2019) instead of benchmark Nafion® membranes. The polymer matrix doped with sulfonated graphene oxide (SGO) was used to enhance its mechanical properties and water retention of the membrane, whereas the sulfonic groups allowed keeping the membrane in a well-hydrated condition, thus improving the proton conductivity (Ayyaru and Ahn, 2017). However, to develop low-cost high-performance MEA, the fabrication procedures were tested using three types of MEAs and performance comparison was done to study the effect of gas diffusion layers (GDL) and the number of catalyst layers.

MATERIALS AND METHODS

Preparation of Electrode Materials

Preparation of Reduced Graphene Oxide (rGO)

Plastic bottles waste as sources of polyethylene terephthalate (PET) were used to prepare reduced graphene oxide (rGO). The PET bottle waste was ready to use as mentioned in a

previous study (El Essawy et al., 2017). Two grams of waste were introduced into an enclosed autoclave container and placed inside the center of an electric furnace at 800°C for 1 h. The resulting dark products were collected and crushed.

Preparation of Reduced Graphene Oxide/Magnetic Iron Oxide Nanocomposite (rGO/MIO)

rGO/MIO nanocomposite was synthesized by using an inverse co-precipitation process based on the precursors of ferric chloride ($FeCl_3.6H_2O$), ferrous sulfate ($FeSO_4.7H_2O$), and the precipitator of ammonium hydroxide (NH_4OH) (Ma et al., 2018). Twenty mL 0.2 M NH_4OH aqueous solution and 0.5 g of reduced graphene oxide (rGO) were added into a 250 mL four-neck bottle under N_2 atmosphere for 30 min and 1.08 g $FeCl_3.6H_2O$ and 0.54 g $FeSO_4.7H_2O$ with a stoichiometric ratio $[Fe^{2+}]$:$[Fe^{3+}]$ equal to 1:2, corresponding to Fe_3O_4, were dispersed using an ultrasonic dispersion method into 60 mL 1:1 (volume ratio) water-ethanol mixed solvents. The mixture was then poured rapidly into a four-neck bottle under vigorous mechanical stirring for 10 min with N_2 bubbling throughout the reaction. The nanocomposites were separated magnetically, washed with deionized water until the throwdown solution became neutral then dried in a vacuum oven at 80°C for 24 h.

Characterization of Electrode Materials

X-ray Diffraction (XRD) data (Shimadzu-7000, U.S.A.) was collected with a CuKα radiation beam (λ = 0.154060 nm). An X-ray Photoelectron Spectroscopy (XPS) Phi 5300 ESCA system (Perkin-Elmer, U.S.A) with Mg (Kα) radiation (X-ray energy 1253.6 eV) was used. A Transmission Electron Microscope (TEM) (TECNAI G20, Netherland with EDX) was also used. The Brunauer-Emmett-Teller (BET) surface area and total pore volume were measured using Barret-Joyner-Halenda (BJH) adsorption methods.

Electrochemical Measurements of Electrodes

The catalytic activity of rGO and rGO/MIO nanocomposites were tested for ORR in 0.1 M KOH electrolyte. The sample inks were prepared by ultrasonicating a mixture containing 450 µl of 2-propanol and 50 µl of 10 wt % Nafion mixture solution with 2.5 mg of sample to form a homogeneous ink. Then a polished and clean glassy carbon (GC) disk electrode with 0.126 cm^2 geometric surface area was loaded with 10 µL of suspension. Potentiostat/Galvanostatic (VoltaLab 40 PGZ301) with software Voltamaster4 was used for all electrochemical experiments.

The three-electrode electrochemical cell was used to conduct the electrochemical measurements at room temperature using 0.1 M KOH solution as the electrolyte. A graphite rod was used as the counter electrode, Hg/HgO (1 M NaOH) as a reference electrode and the tested prepared electrode material supported on GC as the working electrode. As electrode potentials presented in the manuscript refer to the Hg/HgO reference electrode. The electrolyte was saturated with N_2 or O_2 for 30 min before each electrochemical test.

Cyclic voltammetry (CV) was used to check the electrochemical activity of rGO or rGO/MIO in N_2-saturated electrolyte solution for three cycles with −0.8 V to 0.2 V potential window at 100 mVs^{-1} scan rate. Furthermore, the CV was also recorded in O_2-saturated electrolyte for three cycles with −0.8 V to 0.2 V potential window at 100 mVs^{-1} scan rate to investigate the initial behavior of the electrode.

To study the electrochemical kinetics, linear scan voltammetry with rotating disk electrode technique (LSV-RDE) was used in O_2-saturated alkaline electrolyte solution in the 0.2 to −0.8 V potential window at a scan rate of 5 mVs^{-1} under several rotation speeds while keeping the O_2 flow on the surface of the solution during the measurements. Koutecky–Levich equation (K-L equation) was used to determine the number of electrons involved in the electrochemical reactions as illustrated in Equations (1) and (2).

$$(1/j) = (1/j_k) + (1/j_d) = (1/j_k) + 1/(B\omega^{1/2}) \quad (1)$$

B was determined from the slope of the Koutecky-Levich plot according to Equation (2) given below,

$$B = 0.62\, n\, F\, C_{O2}\, D_{O2}{}^{2/3} \upsilon^{-1/6} \quad (2)$$

where j is the measured current density, j_k and j_d are the kinetic and diffusion limiting currents densities; respectively, ω is the speed of rotation in rpm, when the rotation speed is expressed in rpm the value of 0.62 is used, F is the Faraday constant (96,485 C mol^{-1}), D_{O2} is the oxygen diffusion coefficient in the alkaline electrolyte solution (1.9 × 10^{-5} cm^2 s^{-1}), υ is the kinematic viscosity (0.01 cm^2 s^{-1}), and C_{O2} is the oxygen concentration (0.0012 mol L^{-1}). Koutecky-Levich plot between *(1/j)* and $(\omega^{-1/2})$ was plotted to obtain the number of electrons transferred *(n)* from the slope and the kinetic-limiting current j_k from the intercept of the plot.

To determine the ionic conductivity of the prepared membrane and electrodes, resistance measurements were carried out by electrochemical impedance spectroscopy (EIS) technique at 5 mV in the frequency range of 0.1 Hz−500 kHz. The resistance is represented by the high-frequency intercept on the

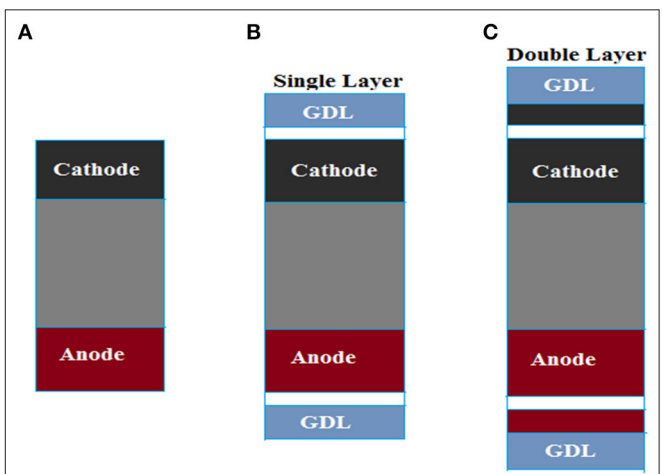

FIGURE 1 | Design of three membrane electrode assemblies (MEAs): **(A)** MEA 1, without GDL; **(B)** MEA 2, with single-layer electrodes; **(C)** MEA 3, with double-layer electrodes.

real axis of the complex impedance plot. The ionic conductivity was determined from resistance according to Equation (3),

$$\sigma = d/RA \quad (3)$$

where σ is the membrane ionic conductivity (S cm^{-1}), A is the geometric area (cm^2), d (cm) is the thickness and R (Ω) is the ohmic resistance.

Preparation and Characterization of PEM

The PVA/PEO/PVP blended polymers matrix named as PVA/PEO/PVP-SGO-3 was prepared and characterized as previously described (Gouda et al., 2019).

Preparation of Membrane Electrode Assembly

Spray method was used at the cathode and anode sides of the MEA. To identify an optimized fabrication concept, three types of MEAs were designed as depicted in **Figure 1** and the GDL used is carbon cloth (CeTech Carbon Cloth without MPL). The catalyst loading was adjusted to 0.4 mg cm^{-2} on anode and cathode. Both electrodes had an active surface area of 25 cm^2.

Cell Polarization Measurements

Polarization curves represent the trend of the losses affect PEM fuel cell performance. The single-cell was tested using Scribner Associates Model 850e test station. Fuel cell test station includes a computer-based control and data acquisition system based on advanced software for Electrochemical Research. The fuel cell polarization curves are obtained from this software whereas the voltage vs. current density of the fuel cell with model assumptions: an ideal mixture of reactant gasses, steady-state conditions, isothermal process, and fully hydrated system. In this study, polarization curves were monitored with potentiostatic mode for determining maximum and minimum potential and current values. After that polarization curves were recorded with galvanostatic mode (differential currents were chosen as 0.03 A at the low current region and 0.05 A at the high current region). In this way, most current values were obtained at the low current density. Humidified hydrogen and oxygen gases were fed to the fuel cell with the same flow rate of 250 sccm.

RESULTS AND DISCUSSION

Microscopic Visualization, Physical, and Chemical Characterizations of Electrodes Materials

As shown in **Figures 2A,B**, the TEM images of rGO and rGO/MIO nanocomposite demonstrate an exfoliated, crumpled and transparent flake-like morphology with several layers, in addition to entrapped iron oxide nanoparticles inside the graphene matrix for sample rGO/MIO and the EDX results implies presence of iron oxide in small ratio about 4% (atomic%) and that confirmed from the XPS results.

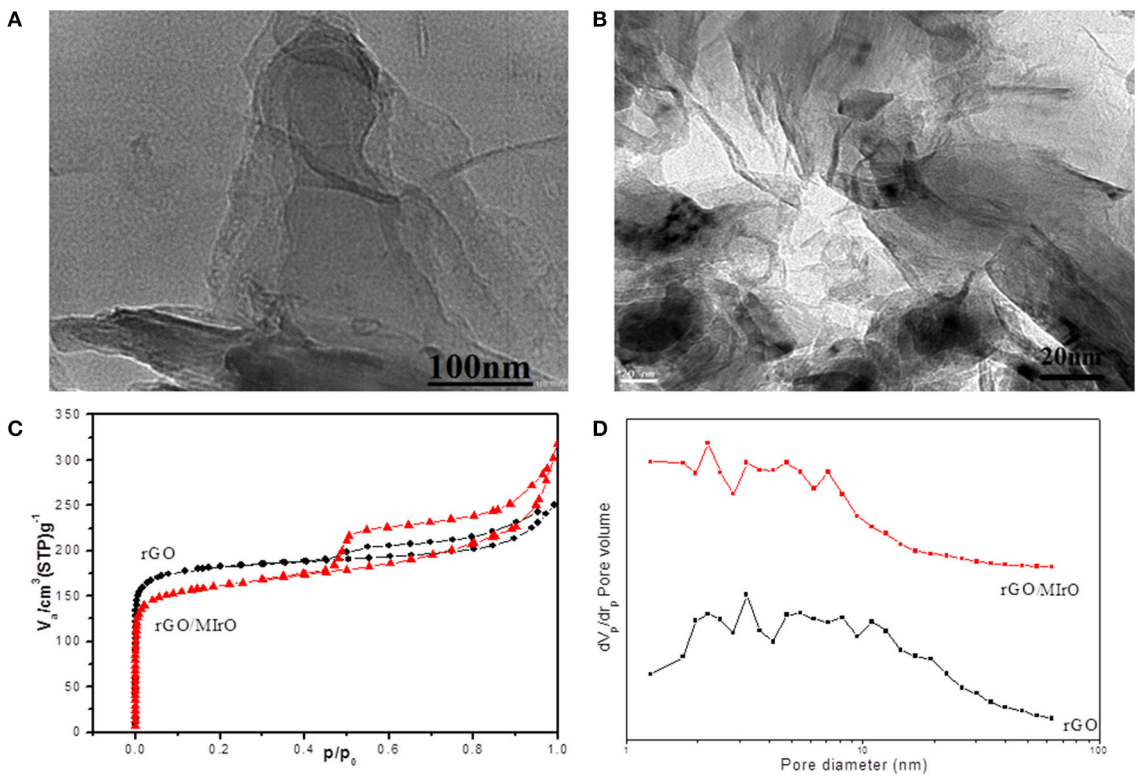

FIGURE 2 | TEM images for **(A)** rGO and **(B)** rGO/MIO samples. **(C)** N_2-adsorption-desorption isotherm and **(D)** BJH plot of rGO and rGO/MIO nanocomposite.

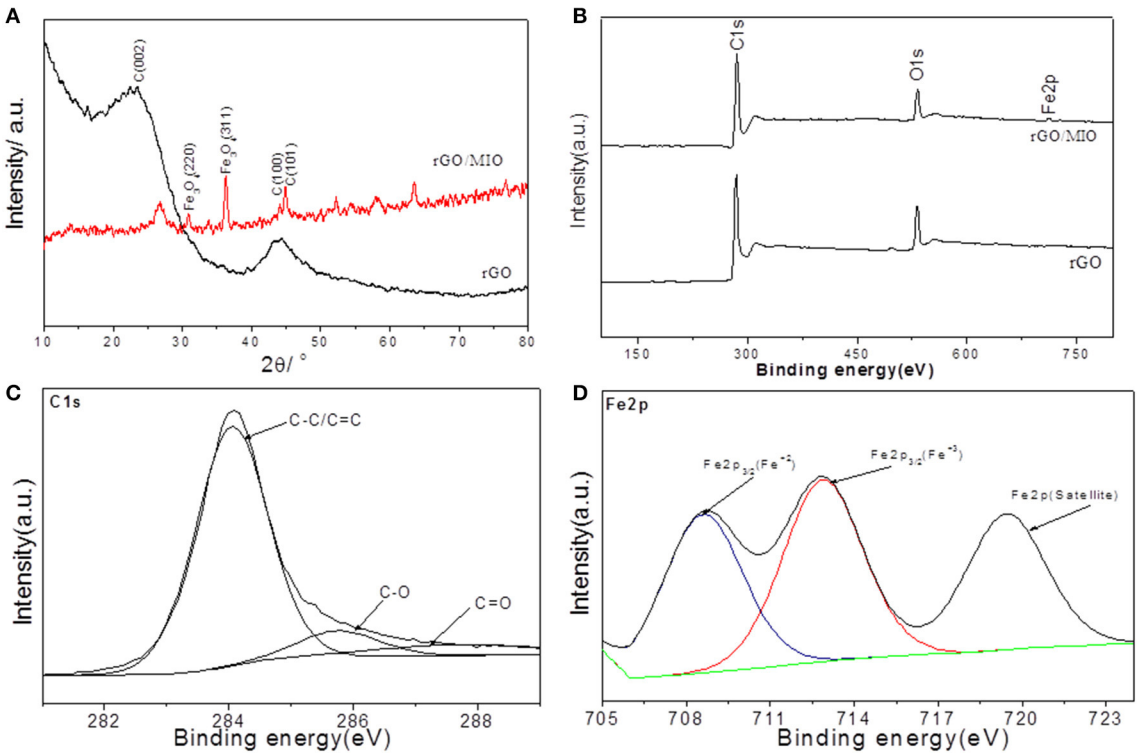

FIGURE 3 | (A) XRD patterns and **(B)** XPS survey spectra for rGO and rGO/MIO nanocomposite, together with high-resolution spectra of **(C)** C1s **(D)** Fe2p of rGO/MIO nanocomposite.

In order to investigate the surface porosity, an important factor affecting the mass transfer that affects the catalytic activity of the electrodes, the N_2 adsorption and desorption isotherm test at 77 K was performed. As can be seen in **Figure 2C**, rGO, and rGO/MIO nanocomposite samples presented isotherms with hysteresis loop of the Type IV, according to IUPAC classification, in the relative pressure range of 0.4–1.0, and capillary condensation, indicating the coexistence of microporous and mesoporous structure, as confirmed from BJH plot (**Figure 2D**) with mean pore diameter of 2.2 and 5.1 nm for rGO and rGO/MIO nanocomposite, respectively. However, it was noticed that the surface area and the pore size of rGO/MIO nanocomposite is higher than that of rGO indicating that, the introducing of iron oxide nanoparticles avoids the aggregation and restacking problems which led to an obvious increase in BET surface area and pore size and that is a valuable characteristic for electrocatalytic applications.

As can be seen in **Figure 3A** the XRD pattern of the rGO sample showed 2θ main peak at 26° and 44.3° which corresponds to the (002) and (100) reflections. For rGO/MIO sample, a slight shift for (002) plane was due to introducing of Fe_3O_4 nanoparticles between the rGO nanosheets thus increasing the interlayer spacing and that is beneficial to promote charge transfer in electrodes materials. However, the peaks at 2θ values of 30.28 (220) and 35.78 (311) are in good agreement with the inverse cubic spinel phase of Fe_3O_4 (ICDD card no.01-07-5088).

To explore the graphitic content and carbon speciation in rGO and rGO/MIO samples, X-ray photoelectron spectroscopy (XPS) was used. As shown in **Figure 3B**, the obtained material was formed with a high amount of carbon and a low amount of oxygen, in addition to traces of iron for rGO/MIO sample. The chemical bonding composition of rGO/MIO nanocomposite was investigated as shown in the high-resolution C1s and Fe2p spectra (**Figures 3C,D**). The peak in C1s at 284.19 eV corresponding to sp^2-hybridization (C-C bond and C=C), demonstrates that most of the C atoms are arranged in a honeycomb lattice, and the fitted peaks centered at 285.87 and 287.88 eV are assigned to C-O and C=O respectively. The Fe2p spectra reveal the presence of two components assigned to Fe^{2+} and Fe^{3+} oxides, where Fe^{3+} is the dominant component. Only $Fe2p_{3/2}$ is represented due to overlapping occurring between $2p_{3/2}$ and $2p_{1/2}$ edges (Otero et al., 2008; Molchan et al., 2015).

Half Cell Electrochemical Measurements

rGO and rGO/MIO samples were prepared from one-step thermal dissociation process of PET waste and have two-dimensional mesoporous structures with large surface area, pore volume, and pore size, being appropriate for electrocatalytic applications. To evaluate the ability of using prepared rGO and rGO/MIO as electrocatalysts in fuel cell application, the electrocatalytic activity of the prepared electrodes toward ORR was evaluated using cyclic voltammetry (CV), linear

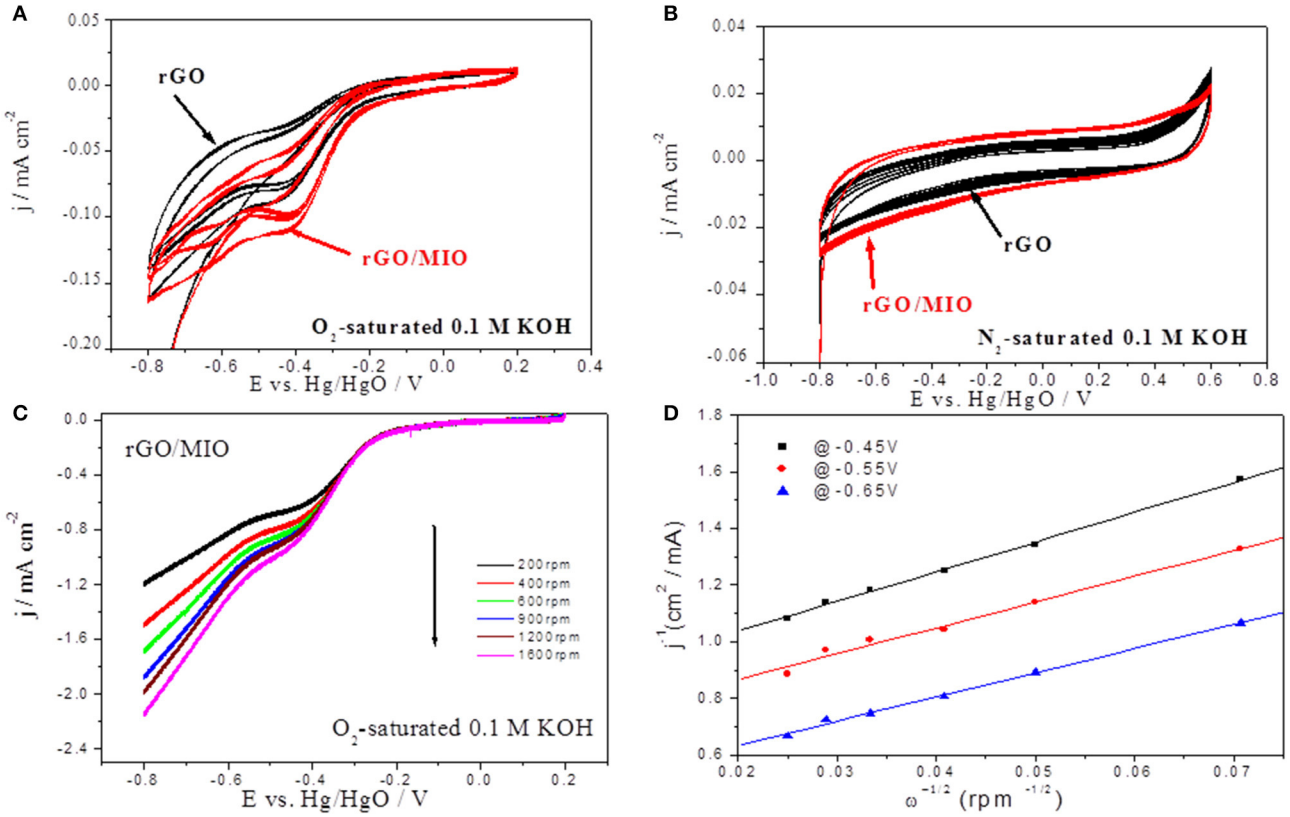

FIGURE 4 | CVs run at 100 mVs^{-1} with rGO and rGO/MIO electrodes in **(A)** O_2-saturated and **(B)** N_2-saturated 0.1 M KOH section. **(C)** Linear scan voltammograms recorded in O_2-saturated 0.1 M KOH at 5 mV s^{-1} and different rotation rates for ORR on rGO/MIO and **(D)** the corresponding Koutecky-Levich Plot obtained at three different potentials.

scan voltammetry (LSV) combined with rotating disk electrode (RDE) technique and electrochemical impedance spectroscopy (EIS).

The CV curves of both samples in O_2-saturated 0.1 M KOH electrolytes are shown in **Figure 4A**, where both samples showed cathodic current peaks. It is noticeable that the rGO/MIO sample has earlier onset potential than the rGO sample, in addition to higher reduction current density, suggesting higher ORR activity of rGO/MIO. **Figure 4B** shows the CVs of both samples in N_2 saturated 0.1M KOH electrolyte with the two samples showing similar behavior. From the previous CV survey, the prepared RGO material was selected to be used as the fuel cell anode and rGO/MIO was selected as the cathode material.

The ORR kinetics of the prepared rGO/MIO catalyst electrode were further studied by the LSV-RDE technique in O_2- saturated 0.1 M KOH electrolyte at different rotation rates (200, 400, 600, 900, 1,200, 1,600 rpm). As shown in **Figure 4C**, LSV curves confirmed its electrocatalytic performance in almost one-step process with an onset potential of ca. −0.25 V and the diffusion current increased with the increasing of the rotation rate which confirm that the reaction is diffusion-controlled under the tested condition. Moreover, three regions of interest can be distinguished, namely, the diffusion-controlled region at potential $E < -0.3$ V, the mixed diffusion kinetic region at potential $-0.1 \geq E \geq -0.3$ V, and the kinetics controlled region at $E \geq -0.1$ V. To calculate the number of electrons transferred during ORR, the Koutecky–Levich plots (K-L plot) at different potentials (−0.45 V, −0.55 V, and −0.65 V) were plotted (**Figure 4D**) and the average electron number was calculated. A value of about four electrons was found, suggesting a direct four-electron pathway for ORR ($O_2 + 4H^+ + 4e^- \rightarrow 2H_2O$), being this path the preferred (and more favorable) for fuel cell processes (Zhang et al., 2015).

It is known that electrochemical impedance spectroscopy (EIS) allows estimating ionic and electric conductivity of different systems. It is accepted that the high-frequency region of an impedance spectrum is associated with the internal ohmic resistance and the contact capacitance in the granular electrode structure, whereas the medium and low-frequency regions represent the charge-transfer resistance and the mass transport resistance, respectively (Yuan et al., 2010).

As shown in **Figures 5A,C,E** the incomplete semicircle that is potential independent has been assigned to different features, namely to internal ohmic resistance (R_{ohm}), represented by high-frequency intersection of the semicircle with the x-axis, charge-transfer resistance (R_{ct}), represented by the diameter of the semicircle, and contact capacitance in the granular electrode structure, represented by straight line at the high-frequency end of the semicircle (Fischer et al., 1998). As for the incomplete semicircle, it refers to a distributed resistance effect (Paganin

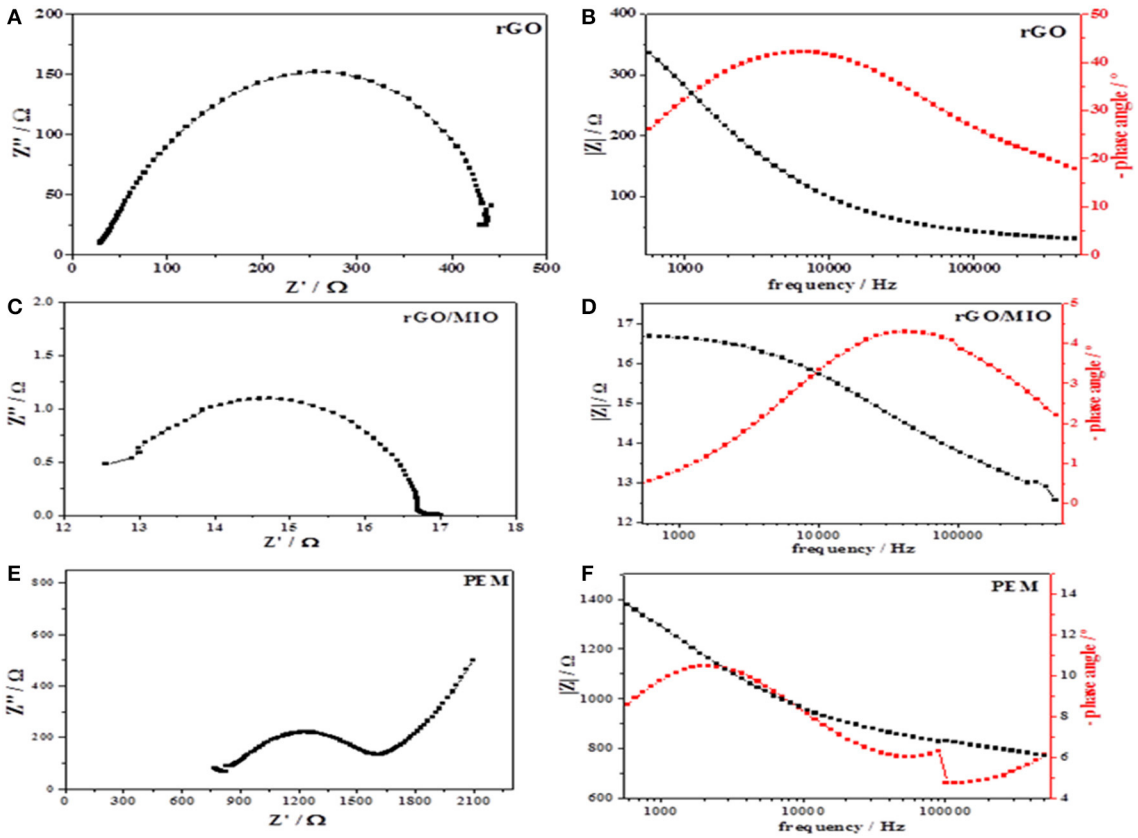

FIGURE 5 | Nyquist **(A,C,E)** and Bode **(B,D,F)** plots obtained for the rGO anode, the rGO/MIO cathode and for the PEM fuel cell.

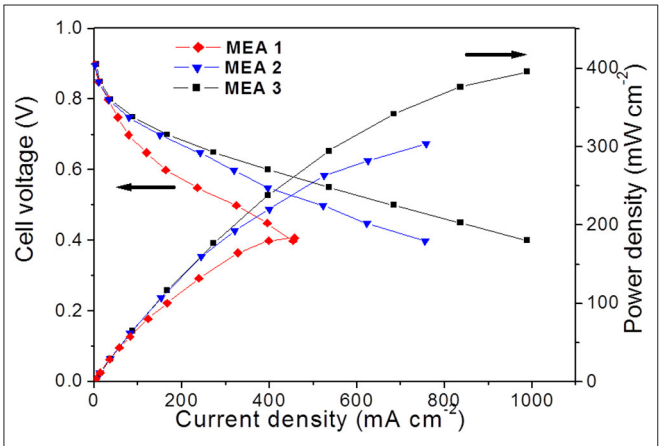

FIGURE 6 | Polarization **(Left)** and power density **(Right)** curves for the 3 designed MEAs. MEA1 contains single-layer electrodes without GDL, MEA2 contains single-layer electrodes with GDL and MEA3 contains double-layer electrodes.

et al., 1998). From Nyquist plots, the calculated ionic conductivity of anode (rGO), cathode (rGO/MIO) and PEM are 0.3, 7, and 0.07 mS cm^{-1} respectively. Furthermore, the Nyquist semicircle of the rGO/MIO sample is smaller than that of the rGO sample, indicating that it has lower resistance and better charge transfer. However, the main reasons for the higher conductivity (lower resistance) of rGO/MIO nanocomposite (than the original rGO sample) could be attributed to the following points: (i) the introduction of iron oxide nanoparticles slightly increased the degree of graphitization, which is beneficial for promoting the charge transfer (Liu et al., 2019a) (2) and (ii) iron oxide nanoparticles accelerate the electron transfer, which in turn enhances the conductivity of the rGO/MIO nanocomposite (Yang et al., 2017). In addition, the relaxation time peak from Bode plot (**Figures 5B,D**) is not well clear. However, this is favorable for the cathode material in fuel cells (Qayyum et al., 2016). On the other side, for rGO sample the Nyquist semicircle at low frequency characterized by higher polarization resistance more than rGO/MIO and that is a characteristic property for anode material (Siracusano et al., 2018). An incomplete semicircle ended with a straight line in the high-frequency range was detected for PEM as shown in **Figure 5E** and that attributed to the membrane characteristic property, however the Bode plot shown in **Figure 5F** exhibits two time constants at high frequencies and that is related to the membrane structure (Zhao-Luo et al., 2018).

Cell Performance

In general, MEA fabrication can come from two techniques. The first one is based on spraying the catalyst ink directly

onto the membrane, followed by a hot pressing step, while in the second technique the catalyst ink is directly sprayed onto the GDL and then hot-pressed onto the membrane (Frey and Linardi, 2004; Kim et al., 2015). The advantage of these techniques is that the catalyst loading can be adjusted by simply weighing the MEA or the GDL before and after coating with the catalyst ink but there is a risk of irregular catalyst transfer from the transfer film to the membrane. For that reason, an investigation on a cell performance of the developed MEA fabrication technique combining effect of using GDL and number of CLs was conducted using single-cell measurements with H_2/O_2 operation, however only easy steps were chosen in this preparation technique without using assembly hot pressing in order to simplify the method and reduce the production cost with regard to maximal performance in addition to, preventing a distortion in the pore structures of catalyst layers and gas diffusion layers.

Figure 6 shows the performance and power densities of the fabricated MEA 1, MEA 2 and MEA 3, whereas the lowest performance was for MEA 1, which was fabricated by using catalyst-coated membrane technique without GDL, compared to MEA 2, which was fabricated by using the same technique but using carbon cloth without a microporous layer as GDL. The addition of GDL to MEA facilitates the transport of interrupted gas and formed water through the electrochemically active areas of the MEA (Omrani and Shabani, 2017). It also prevents leakage of the electrode material throughout the MEA, thus leading to a performance enhancement of MEA 2 of 66% when compared to MEA 1.

The effect of the number of CLs also affects the performance of fabricated MEA 2 and MEA 3 examined and compared here. The electrode ink was sprayed onto the membrane only as in MEA 2 and onto the GDL and the membrane as in MEA 3. The results show that the highest power densities up to 395 $mWcm^{-2}$ at 988 mA cm^{-2} can be produced from MEA 3 with GDL and double-layered electrodes. Consequently, this result confirms the MEA performance depends on the electrode CLs number and morphology, and that could be referred to increasing the mass transport through the double layer electrodes, in addition to providing an effective path channel for water removal through the larger pores of the high porosity CL coated onto GDL.

CONCLUSIONS

This work contributes toward sustainable materials processing with upcycling technology to produce highly added-value products from reduced graphene oxide and reduced graphene oxide/magnetic iron oxide nanocomposite, produced from the thermal dissociation of plastic waste using simple, one-pot and applicable method. The prepared materials can be used as active catalyst electrodes with high durability for ORR in fuel cells, and hence get the benefits of simultaneous waste management and increasing the possibility for commercialization of low-temperature fuel cells by decreasing its production cost. Moreover, to develop high-performance MEAs and to identify the optimum fabrication conditions, three types of MEAs were designed. The optimum one is the MEA designed with a double-layer electrode involving an inner catalyst layer prepared by the catalyst-coated membrane (CCM) method and an outer catalyst layer directly coated on the gas diffusion layer to increase the catalyst utilization. Further investigations need to be carried out to elucidate the effect of using GDLs with a microporous layer on the performance of MEAs obtained in combination with the followed preparation technique.

DATA AVAILABILITY STATEMENT

All datasets generated for this study are included in the article.

AUTHOR CONTRIBUTIONS

MG fabricated the PEM and MEA. ME also participated in MEA fabrication, carried out CV and impedance measurements, and analyzed the experimental data. AA and MY performed and analyzed the data of fuel cell test station for fabricated MEAs. DS supervised and revised the manuscript. NE proposed the project, carried out electrodes preparation and characterization, and wrote the manuscript with input from the other coauthors.

FUNDING

DS would like to thank Fundação para a Ciência e a Tecnologia (FCT, Portugal) for contract no. IF/01084/2014/CP1214/CT0003 under IF2014 Programme.

REFERENCES

Awang, N., Ismail, A. F., Jaafar, J., Matsuura, T., Junoh, H., Othman, M. H. D., et al. (2015). Functionalization of polymeric materials as a high performance membrane for direct methanol fuel cell: a review. *React. Funct. Polym.* 86, 248–258. doi: 10.1016/j.reactfunctpolym.2014.09.019

Ayyaru, S., and Ahn, Y. (2017). Application of sulfonic acid group functionalized graphene oxide to improve hydrophilicity, permeability, and antifouling of PVDF nanocomposite ultrafiltration membranes. *J. Membr. Sci.* 525, 210–219. doi: 10.1016/j.memsci.2016.10.048

Aziz, A. N., Hassab, M. A., Elsayed Youssef, M., and El-Maghlany, W. M. (2018). "Performance analysis of DMFC and PEMFC numerically with models validation," in *International Journal of Advances in Electronics and Computer Science* 5, 14–17.

Bakangura, E., Wu, L., Ge, L., Yang, Z., and Xu, T. (2016). Mixed matrix proton exchange membranes for fuel cells: state of the art and perspectives. *Prog. Polym. Sci.* 57,103–152. doi: 10.1016/j.progpolymsci.2015.11.004

Beydaghi, H., Javanbakht, M., and Kowsari, E. (2014). Synthesis and characterization of poly (vinyl alcohol)/sulfonated graphene oxide nanocomposite membranes for use in proton exchange membrane fuel cells (PEMFCs). *Ind. Eng. Chem. Res.* 53, 16621–16632. doi: 10.1021/ie502491d

Choi, H., Kumar, N. A., and Baek, J. (2015). Graphene supported non-precious metal-macrocycle catalysts for oxygen reduction reaction in fuel cells. *Nanoscale* 7, 6991–6998. doi: 10.1039/C4NR06831A

Dumont, J. H., Martinez, U., Artyushkova, K., Purdy, G. M., Dattelbaum, A. M., Zelenay, P., et al. (2019). Nitrogen-doped graphene oxide electrocatalysts for the oxygen reduction reaction. *ACS Appl. Nano Mater.* 2, 1675–1682. doi: 10.1021/acsanm.8b02235

El Essawy, N. A., Konsowa, A. H., Elnouby, M., and Farag, H. A. (2017). A novel one-step synthesis for carbon-based nanomaterials from polyethylene

terephthalate (PET) bottles waste. *J. Air Waste Manage. Assoc*. 67, 358–370. doi: 10.1080/10962247.2016.1242517

Fischer, A., Jindra, J., and Wendt, H. (1998). Porosity and catalyst utilization of thin layer cathodes in air operated PEM-fuel cells. *J. Appl. Electrochem*. 28, 277–282. doi: 10.1023/A:1003259531775

Frey, T., and Linardi, M. (2004). Effects of membrane electrode assembly preparation on the polymer electrolyte membrane fuel cell performance. *Electrochim. Acta* 50, 99–105. doi: 10.1016/j.electacta.2004.07.017

Gao, S., Fan, B., Feng, R., Ye, C., Wei, X., Xu, J., et al. (2017). N-doped-carbon-coated Fe_3O_4 from metal-organic framework as efficient electrocatalyst for ORR. *Nano Energy* 40, 462–470. doi: 10.1016/j.nanoen.2017.08.044

Gouda, M. H., Gouveia, W., Afonso, M. L., Šljukić, B., El Essawy, N. A., Nassr, A. B. A. A., et al. (2019). Poly(vinyl alcohol)-based crosslinked ternary polymer blend doped with sulfonated graphene oxide as a sustainable composite membrane for direct borohydride fuel cells. *J. Power Sources* 432, 92–101. doi: 10.1016/j.jpowsour.2019.05.078

Gupta, S., Kellogg, W., Xu, H., Liu, X., Cho, J., and Wu, G. (2016). Bifunctional perovskite oxide catalysts for oxygen reduction and evolution in alkaline media. *Chem. Asian J.* 11, 10–21. doi: 10.1002/asia.201500640

Iwan, A., Malinowski, M., and Pasciak, G. (2015). Polymer fuel cell components modified by graphene: electrodes, electrolytes and bipolar plates. *Renew. Sustain. Energy Rev*. 49, 954–967. doi: 10.1016/j.rser.2015.04.093

Kim, G., Eom, K., Kim, M., Yoo, S., Jang, J., Kim, H., et al. (2015). Design of an advanced membrane electrode assembly employing a double-layered cathode for a PEM fuel cell. *ACS Appl. Mater. Interfaces* 7, 27581–27585. doi: 10.1021/acsami.5b07346

Lai, Q., Zheng, L., Liang, Y., He, J., Zhao, J., and Chen, J. (2017). Metal–organic-framework-derived Fe-N/C electrocatalyst with five-coordinated Fe-Nx sites for advanced oxygen reduction in acid media. *ACS Catal.* 7, 1655–1663. doi: 10.1021/acscatal.6b02966

Li, C., Xiao, L., Jiang, Z., Tian, X., Luo, L., Liu, W., et al. (2017). Sulfonic acid functionalized graphene oxide paper sandwiched in sulfonated poly(ether ether ketone): a proton exchange membrane with high performance for semipassive direct methanol fuel cells. *Int. J. Hydrog. Energy*. 42,16731–16740. doi: 10.1016/j.ijhydene.2017.05.126

Liu, M., Guo, X., Hu, L., Yuan, H., Wang, G., Dai, B., et al. (2019a). Fe_3O_4/Fe_3C@nitrogen-doped carbon for enhancing oxygen reduction reaction. *Chem. Nano. Mat*. 5:138. doi: 10.1002/cnma.201800594

Liu, M., Zhao, Z., Duan, X., and Huang, Y. (2019b). Nanoscale structure design for high-performance Pt-based ORR catalysts. *Adv. Mater*. 31:1802234. doi: 10.1002/adma.201802234

Ma, Y., Jin, P., Lei, W., La, P., Du, X., and Zhang, D. (2018). One-pot method fabrication of superparamagnetic sulfonated polystyrene/Fe_3O_4/graphene oxide micro-nano composites. *J Porous Mater*. 25, 1447–1453. doi: 10.1007/s10934-018-0557-8

Molchan, I. S., Thompson, G. E., Skeldon, P., Lindsay, R., Walton, J., Kouvelos, E., et al. (2015). Microscopic study of the corrosion behaviour of mild steel in ionic liquids for CO_2 capture applications. *RSC Adv*. 5, 35181–35194. doi: 10.1039/C5RA01097G

Morales-Acosta, D., Flores-Oyervides, J. D., Rodríguez-González, J. A., Sánchez-Padilla, N. M., Benavides, R., et al. (2019). Comparative methods for reduction and sulfonation of graphene oxide for fuel cell electrode applications. *Int. J. Hydrog. Energy* 44, 12356–12364. doi: 10.1016/j.ijhydene.2019.02.091

Omrani, R., and Shabani, B. (2017). Gas diffusion layer modifications and treatments for improving the performance of proton exchange membrane fuel cells and electrolysers: a review. *Int. J. Hydrog. Energy* 42, 28515–28536. doi.org/10.1016/j.ijhydene.2017.09.132

Otero, E., Wilks, R. G., Regier, T., Blyth, R. I., Moewes, A., and Urquhart, S. G. (2008). Substituent effects in the iron 2p and carbon 1s Edge Near-Edge X-ray Absorption Fine Structure (NEXAFS) spectroscopy of ferrocene compounds. *J. Phys. Chem. A* 112, 624–634. doi: 10.1021/jp074625w

Paganin,V. A., Oliveira, C. L. F., Ticianelli, E. A., Springer, T. E., and Gonzalez, E. R. (1998). Modelistic interpretation of the impedance response of a polymer electrolyte fuel cell. *Electrochim. Acta* 43, 3761–3766. doi: 10.1016/S0013-4686(98)00135-2

Pandey, R. P., Shukla, G., Manohar, M., and Shahi, V. K. (2017). Graphene oxide based nanohybrid proton exchange membranes for fuel cell applications: an overview. *Adv. Colloid Interface Sci*. 240, 15–30. doi: 10.1016/j.cis.2016.12.003

Pourzare, K., Mansourpanah, Y., and Farhadi, S. (2016). Advanced nanocomposite membranes for fuel cell applications: a comprehensive review. *Biofuel Res. J*. 12, 496–513. doi: 10.18331/BRJ2016.3.4.4

Qayyum, H., Tseng, C.-J., Huang, T.-W., and Chen, S.-Y. (2016). Pulsed laser deposition of platinum nanoparticles as a catalyst for high-performance PEM fuel cells. *Catalysts* 6:180. doi: 10.3390/catal6110180

Qiu, X., Dong, T., Ueda, M., Zhang, X., and Wang, L. (2017). Sulfonated reduced graphene oxide as a conductive layer in sulfonated poly(ether ether ketone) nanocomposite membranes. *J. Membr. Sci*. 524, 663–672. doi: 10.1016/j.memsci.2016.11.064

Sedesheva, Y. S., Ivanov, V. S., Wozniak, A. I., and Yegorov, A. S. (2016). Proton-exchange membranes based on sulfonated polymers, Orient. *J. Chem*. 32, 2283–2296. doi: 10.13005/ojc/320501

Shen, A., Zou, Y., Wang, Q., Dryfe, R. A. W., Huang, X., Dou, S., et al. (2014). Oxygen reduction reaction in a droplet on graphite: direct evidence that the edge is more active than the basal plane. *Angew. Chem. Int. Ed*. 53, 1–6. doi: 10.1002/anie.201406695

Siracusano, S., Trocino, S., Briguglio, N., Baglio, V., and Aricò, A. S. (2018). Electrochemical impedance spectroscopy as a diagnostic tool in polymer electrolyte membrane electrolysis. *Materials* 11:1368. doi: 10.3390/ma11081368

Su, Y., Jiang, H., Zhu, Y., Zou, W., Yang, X., Chen, J., et al. (2014). Hierarchical porous iron and nitrogen co-doped carbons as efficient oxygen reduction electrocatalysts in neutral media. *J. Power Source* 265, 246–253. doi: 10.1016/j.jpowsour.2014.04.140

Thanasilp, S., and Hunsom, M. (2010). Effect of MEA fabrication techniques on the cell performance of Pt–Pd/C electrocatalyst for oxygen reduction in PEM fuel cell. *Fuel* 89, 3847–3852. doi: 10.1016/j.fuel.2010.07.008

Yang, J., Hu, J., Weng, M., Tan, R., Tian, L., Yang, J., et al. (2017). Fe-cluster pushing electrons to n-doped graphitic layers with Fe_3C(Fe) hybrid nanostructure to enhance O_2 reduction catalysis of Zn-air batteries. *ACS Appl. Mater. Interfaces* 9, 4587–4596. doi: 10.1021/acsami.6b13166

Ye, L., Chai, G., and Wen, Z. (2017). Zn-MOF-74 derived N-doped mesoporous carbon as pH-universal electrocatalyst for oxygen reduction reaction. *Adv. Funct. Mater.* 27:1606190. doi: 10.1002/adfm.201606190

Yuan, X.-Z., Song, C., Wang, H., and Zhang, J. (2010). "EIS diagnosis for PEM fuel cell performance," in *Electrochemical Impedance Spectroscopy in PEM Fuel Cells* (London: Springer), 193–262. doi: 10.1007/978-1-84882-846-9

Zhang, J., Zhao, Z., Xia, Z., and Dai, L. (2015). A metal-free bifunctional electrocatalyst for oxygen reduction and oxygen evolution reactions. *Nat. Nanotechnol*. 10, 444–453. doi: 10.1038/nnano.2015.48

Zhao-Luo, Q., Huang, Q., Chen, Z., Yao, L., Fu, P., and Lin, Z. (2018). Polyvinylidene fluoride membranes probed by electrochemical impedance spectroscopy. *Mater. Res. Express* 5:065507. doi: 10.1088/2053-1591/aac7f2

Conflict of Interest: The authors declare that the research was conducted in the absence of any commercial or financial relationships that could be construed as a potential conflict of interest.

frontiers in Materials

REVIEW
published: 11 February 2020
doi: 10.3389/fmats.2020.00002

MnO_2/Carbon Composites for Supercapacitor: Synthesis and Electrochemical Performance

Dan Wu[1], Xiubo Xie[1], Yuping Zhang[1], Dongmei Zhang[2], Wei Du[1], Xiaoyu Zhang[1]* and Bing Wang[3]*

[1] School of Environment and Material Engineering, Yantai University, Yantai, China, [2] Shandong Institute for Food and Drug Control, Jinan, China, [3] CAS Key Laboratory for Biomedical Effects of Nanomaterials and Nanosafety, Institute of High Energy Physics, Chinese Academy of Sciences, Beijing, China

As an emerging energy storage device, the supercapacitor with high energy density, fast charging/discharging, and good cycle stability has aroused great interest. The performance of supercapacitors mainly depend on the electrode material. Manganese dioxide (MnO_2) has emerged as one of the most promising electrode materials for high theoretical specific capacitance, wide potential range, high electrochemical activity, and environmental friendliness. However, its deteriorated volume expansion and inherently low conductivity limit its development and application in supercapacitors. To circumvent the mentioned issues, the porous, thin film, or layered composite materials were prepared to enhance the electrical conductivity and specific surface area of MnO_2. Carbon materials are the ideal choice to compound with MnO_2 owing to their low electrical resistance, significant thermal stability, large specific surface area, and porosity. Up to now, several kinds of MnO_2/carbon composites as supercapacitor electrodes have been designed and fabricated. Herein, we give a concise review of the latest researches on MnO_2/carbon supercapacitor electrodes, focusing on the fabrication strategies and analyzing the influencing factors of electrochemical performance of MnO_2/carbon materials. An outlook on the possible development directions in future of designing high-performance MnO_2/carbon materials for the current challenges is also provided.

Keywords: MnO_2, carbon materials, composites, electrode material, supercapacitor

OPEN ACCESS

Edited by:
M. Jasim Uddin,
University of Texas Rio Grande Valley Edinburg, United States

Reviewed by:
Minshen Zhu,
Leibniz-Institut für Festkörper- und Werkstoffforschung (IFW Dresden), Germany
Aminur Rashid Chowdhury,
University of Texas at Austin, United States

****Correspondence:***
Wei Du
duwei@ytu.edu.cn
Xiaoyu Zhang
zhangxiaoyu@ytu.edu.cn

Specialty section:
This article was submitted to Carbon-Based Materials, a section of the journal Frontiers in Materials

Received: *28 September 2019*
Accepted: *06 January 2020*
Published: *11 February 2020*

Citation:
Wu D, Xie X, Zhang Y, Zhang D, Du W, Zhang X and Wang B (2020) MnO_2/Carbon Composites for Supercapacitor: Synthesis and Electrochemical Performance. Front. Mater. 7:2. doi: 10.3389/fmats.2020.00002

INTRODUCTION

Nowadays, with the excessive consumption of traditional energy sources such as coal, oil, and natural gas, the increasingly severe global climate and deteriorating ecological environment have caused a global crisis that endangers human survival. The development and utilization of eco-friendly renewable energy become an extremely imminent task all over the world. In the past decade, solar, hydro, wind, and tidal energy and other renewable energy sources have greatly alleviated serious problems in the energy and environmental fields (Yang et al., 2011; Xie X. et al., 2019). However, abundant and clean renewable energy mentioned above cannot be widely applied directly owing to the limitation of natural conditions and the poor tunability and stability of generating electricity. Therefore, reliable electrochemical energy storage (EES), including fuel cells, ion batteries, and supercapacitors, is extremely necessary to achieve efficient storage, conversion, and further utilization of the above energy sources (Palchoudhury et al., 2019). The Ragone plots

in **Figure 1** shows the relationship between power density and energy density for several typical EES systems (Wang J. G. et al., 2015). Among them, electrochemical capacitors, which are also known as supercapacitors, are considered to be a new generation of green energy storage device (Díaz-Delgado and Doherty, 2016), with greater capacitance than conventional capacitors and higher output power and longer life than lithium-ion batteries (Zhang Q. Z. et al., 2018). Combined with its simple structure, high power density, fast charging, and pollution-free effects in the production process, supercapacitors are widely applied in portable electronics, data backup, hybrid electric vehicle, aerospace, and other fields (Salinas-Torres et al., 2019).

According to the charge storage mechanism, supercapacitors are generally classified as electrochemical double-layer capacitors (EDLCs) and pseudocapacitors (Wang G. P. et al., 2012). Energy storage and conversion of EDLCs are accomplished by static charge separation in the Helmholtz layer. Common active materials with double-layer electrodes are mostly carbon materials, which can rapidly complete the charging and discharging process and remain stable, but their capacitance and energy density are relatively low (<10 Wh kg^{-1}) (Liang and Xin, 2015). The storage capacity of pseudocapacitors, compared with EDLCs, can be greatly improved owing to a series of reversible redox reactions on the surface/bulk phase of the electrode material (Conway, 1999). Transition metal oxides (Tajik et al., 2017) and conductive polymers (Snook et al., 2011) are commonly used as electrode materials for pseudocapacitors. The performance of supercapacitors is primarily dependent on the activity and kinetics of the electrode material. Therefore, it is very important to select suitable electrode materials, further optimize their structure, and improve their activity and kinetics to enhance the electrochemical properties of supercapacitors (Trudeau, 2013). Carbon materials and manganese dioxide (MnO_2), as the most representative materials of EDLCs and pseudocapacitors, respectively, show their unique advantages in energy storage.

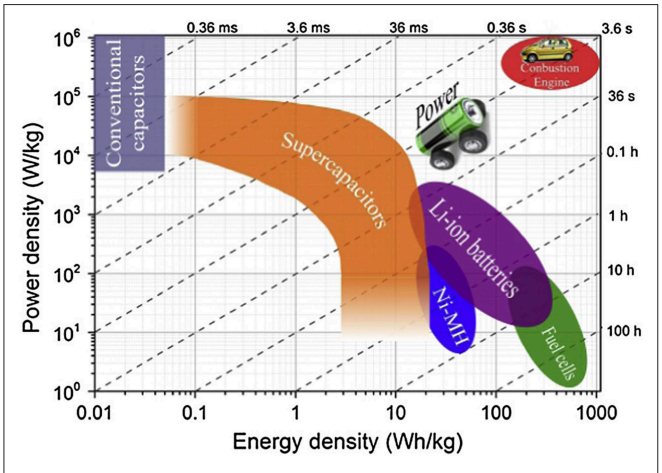

FIGURE 1 | Ragone plots of various electrochemical energy storage (EES) systems. Reproduced from (Wang J. G. et al., 2015), with permission from Pergamon.

Carbon is one of the most closely and important elements for humans in nature and plays an important role in our existing ecosystems (Candelaria et al., 2012). It has various electronic orbital properties of sp, sp^2, and sp^3 hybridization, and the anisotropy of sp^2 leads to various orientations of crystals and other arrays (Yu et al., 2018). Therefore, different kinds of carbon materials are formed by different chemical bonds. In particular, functional carbon materials considered to be ideal electrode materials for supercapacitors have attracted great attention owing to their low resistance, good electrical conductivity, high porosity, and large specific surface area (He et al., 2013; Borenstein et al., 2017). The EDLCs composed of carbon material form stable electric double layers by attracting mutually opposite charges at the electrode/electrolyte interface, which can achieve energy store through the physical electrostatic adsorption/desorption of charges. The energy storage mechanism is conducive to increasing the conductivity of the electrode to improve the specific capacity and energy density. Moreover, the carbon material can transform the structure and bonding mode of the composite material, thereby improving charging/discharging rate capability and cycle stability. For pure carbon materials, their specific capacitance and energy density (100∼300 F g^{-1}, 5∼7 Wh kg^{-1}) largely depends on specific surface area, porosity, and pore size distribution (Wang et al., 2019b). In recent years, a large number of functional carbon nanomaterials with related excellent properties, such as activated carbon (AC) (Faraji and Ani, 2015), graphene [including graphene oxide (GO) and reduced GO (rGO)] (Shi et al., 2018), carbon nanotubes (CNTs) (Qian et al., 2012), carbon nanofibers (CNFs) (Peng et al., 2016), and carbon aerogel (CA) (Hao et al., 2014) have emerged, which provide many favorable conditions for improving material properties. However, the specific capacitance and energy density of assembled EDLCs cannot compete with pseudocapacitors owing to their inherent electrostatic surface charging mechanism. Therefore, it is an effective way to prepare high-performance composite electrode materials by combining various functional carbon materials and typical metal oxides or conductive polymers.

Among many transition metal oxides, MnO_2 with abundant reserves, low toxicity, and simple preparation process, is widely used in oxidation catalyst materials, aqueous batteries, supercapacitors, and other fields (Zhu M. et al., 2018; Li F. et al., 2019; Luo et al., 2019; Wei et al., 2019). Especially in the case of supercapacitors, MnO_2 is considered to be one of the most promising electrode materials. Since Lee and Goodenough (1999) reported the pioneering work of amorphous MnO_2 electrodes with excellent pseudocapacitive behavior in KCl electrolytes, a large number of efforts have been made to develop high-performance MnO_2-based electrode materials. The reasons of the excellent performance of MnO_2 can be summed up in two aspects. From the perspective of electrochemical properties, MnO_2 displays outstanding characteristics of (a) a high theoretical capacity (1,370 F g^{-1}) referring to the single-electron redox reaction of each manganese atom; (b) a wide potential window (0.9–1.0 V) (Xie Y. et al., 2019); and (c) excellent electrochemical properties in neutral electrolyte, leading to low chemical corrosion of the collector. From the

perspective of environmental protection and economy, MnO_2 is abundant in earth, has low price, and is environmentally friendly (Wei et al., 2011). These unique advantages make MnO_2 an ideal choice for pseudocapacitor electrode materials. It is worth noting that MnO_2 contains a variety of crystal structures, including α-, β-, γ-, δ-, and λ-MnO_2; and its energy storage properties are determined by different crystal forms. Research has shown that the chain (Gao et al., 2017) or tunnel (Huang et al., 2019) structure of α-, β-, and γ-MnO_2 with large two-dimensional tunneling structure facilitates electron transfer to provide a relatively high capacitance value. The large surface area of δ-MnO_2 with a layered or sheet-like structure is more favorable for cation intercalation/deintercalation than the amorphous structure. The three-dimensional hinge structure of λ-MnO_2 can provide more active sites for better electrochemical properties (Prélot et al., 2003; Malak-Polaczyk et al., 2010). However, the further development of current MnO_2-based supercapacitors is limited by the drawbacks of MnO_2 electrode materials, such as low conductivity, poor ion diffusion constant, and poor structural stability (Wang J. G. et al., 2015). Therefore, the improvement of active materials mainly involves high reversible capacitance, structural stability, and rapid cation diffusion at high charge/discharge rates. A useful and direct approach is to uniformly modify MnO_2 materials onto layered porous conductive functional carbon materials to construct electrodes (Hu et al., 2018). The carbon materials can be served as a highly conductive and stable current collector, and its interconnection holes are beneficial for ion diffusion, whereas MnO_2 can shorten the transmission distance of ions to prepare a high-performance electrode material.

In recent years, a large amount of significant breakthroughs have been made in the design of high-performance MnO_2-based composite materials for application in supercapacitor devices. The number of research papers on MnO_2/carbon composites for supercapacitors recently published is shown in **Figure 2**. In **Figure 2a**, the number of research papers on carbon/MnO_2 composites has remained at a high level, which is still the research focus of electrode materials at present. And as shown in **Figure 2b**, recent work has shown that different types of carbon materials added to MnO_2 material are mainly in forms of graphene and CNTs. This paper summarizes the synthesis strategies of MnO_2/carbon materials with different morphologies and structures. The electrochemical properties and influencing factors of the electrode materials were further discussed. Finally, the remaining challenges of MnO_2/carbon composite supercapacitors are briefly generalized, and an outlook on the possible development directions in the future for designing high-performance MnO_2/carbon materials is also provided.

SYNTHESIS AND PROPERTIES OF MnO_2/CARBON COMPOSITES FOR SUPERCAPACITOR

MnO_2/Carbon Nanotube Composites

CNTs are one-dimensional quantum materials with a hollow tubular structure and excellent electrical conductivity, large specific surface area, and high chemical stability (Lu et al., 2019). From the perspective of the wall structure, it can be divided into single-walled CNTs (SWCNTs) and multi-walled CNTs (MWCNTs), both of which have been widely used in the energy storage. For SWCNTs, the specific surface area can reach 240–1,250 $m^2\ g^{-1}$, and pore size distribution is mostly in the wide range of 3 to 5 nm, with high specific capacitance of 180 F g^{-1}, power density of 20 kW kg^{-1}, and energy density of 6.5–7 Wh kg^{-1} (Fujiwara et al., 2001). And reduced electrode impedance and increased specific capacitance of SWCNTs can be obtained by the high-temperature heat treatment or addition of surfactants (Byl et al., 2005). For MWCNTs, the specific surface area (∼430 $m^2\ g^{-1}$), specific capacitance (∼180 F g^{-1}), power density (∼8 kW kg^{-1}), and energy density (∼0.56 Wh kg^{-1}) are slightly lower than those for SWCNTs (Fujiwara et al., 2001; Xie et al., 2017). In addition, carbon atoms in the CNTs are sp^2 hybridized, forming a hexagonal network with the surrounding three carbon atoms, and its *s* orbital composition is relatively large compared with sp^3 hybridization.

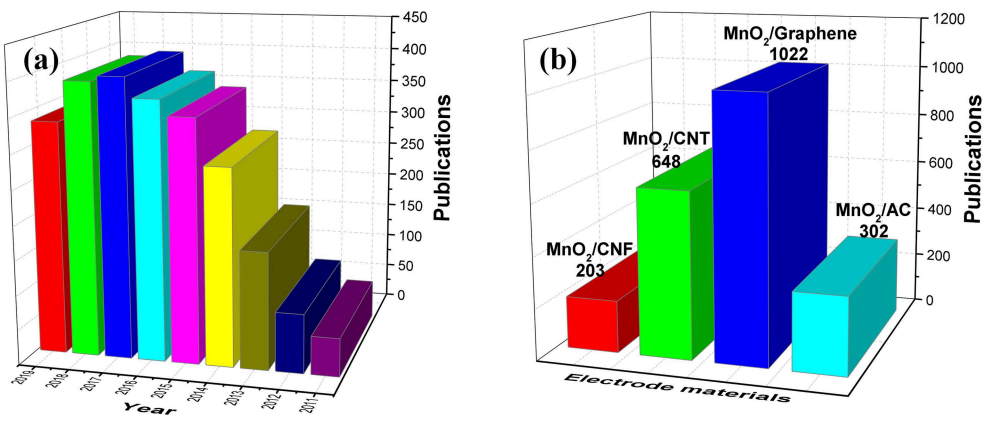

FIGURE 2 | Statistical survey of research papers on MnO_2/carbon composites for supercapacitors. **(a)** Total number of related reports from 2011 to 2019. **(b)** Literature statistics for different types of carbon materials/MnO_2 composites. Source: Web of Science. Search date: August 20, 2019.

The carbon atoms in the CNTs adopt sp^2 hybridization, and the surrounding three carbon atoms form a hexagonal network, which is larger than the sp^3 hybrid sulfur orbital composition. This contributed to the high mechanical strength, good flexibility, and excellent corrosion resistance and stability of CNTs that provide advantages for manufacturing flexible electrode. The introduction of carbon–carbon double bond, carboxyl group, hydroxyl group, hydrocarbon bond, and other functional groups on the surface of CNTs can improve their surface activity and help ions in electrolyte to enter into electrode materials. So far, the synthesis of CNTs has entered the commercial stage and production capacity of more than 1,000 tons (Xin and Wei, 2012). As a relatively mature nano-carbon material, the development of CNTs is of great scientific significance in the field of EES.

Considering that the specific capacitance of pure CNTs measuring 20–80 F g^{-1} (Dubey and Guruviah, 2019) is lower than that of other carbon materials (e.g., CNF is 120–370 F g^{-1} and AC is 100–300 F g^{-1}) and acts more like a scaffold (Zhang and Zhao, 2009), scientists wisely combined MnO_2 with CNTs to form nanocomposites. This composite material exerts a synergistic effect of electrical/mechanical benefits of CNTs and large pseudocapacitance of MnO_2, achieving expected high specific capacity and long cycle durability. The preparation of MnO_2/CNT composite electrode materials can be achieved by various synthetic methods such as electrodeposition techniques (Li Q. et al., 2014; Jeong et al., 2019), hydrothermal treatment (Ramesh et al., 2017), microwave-assisted methods (Yan et al., 2009; Li M. et al., 2017), chemical coprecipitation (Subramanian et al., 2006), and thermal decomposition (Liu et al., 2017; Bi et al., 2019). In 2006, amorphous δ-MnO_2 and SWCNT composite electrode materials were first studied. As shown in **Figures 3A,B**, Subramanian et al. (2006) successfully prepared a δ-MnO_2/SWCNT composite for supercapacitor electrodes using a simple precipitation method. Owing to the synergetic performance of double layer and pseudocapacitance, the δ-MnO_2/20 wt% SWCNT composite exhibits an excellent capacitance value of 110 F g^{-1} at 2 A g^{-1} and maintains 75% capacity over 750 cycles. Further studies have found that the CNT content has a significant effect on the cycle life of the material in **Figure 3C**, so the reasonable ratio of CNTs and MnO_2 is very critical for the electrochemical performance improvement of the composite. It is proved that the unique structure of CNTs is served as the conductive agent and support material, whereas MnO_2 used as a supplier of pseudocapacitors can significantly improve the electrochemical performance of MnO_2/CNT composites. This has led to a strong interest in MnO_2/CNT composite electrode materials. (Li L. et al., 2019) developed MnO_2-MWCNT by hydrothermal treatment directly on Ni foam for adhesive-free electrodes, as shown in **Figure 3D**. It can be seen from **Figure 3E** that ultrathin MnO_2 nanosheets were uniformly grown on forest-like MWCNTs, covering the surface of the foamed nickel. The areal density, specific capacitance, and capacitance retention of the binderless electrode material prepared in this manner reached 0.775 mg cm^{-2}, 1,350.42 F g^{-1} at 6.5 A g^{-1}, and 93.9%, respectively (see **Figure 3F**). This derives from the direct and strong contact between the MWCNT and the current collector that achieves low charge transfer and enhances the electrochemical properties of the composites, indicating that the binderless approach can significantly improve the conductivity of the electrode material. With the great advancement of science and technology and the improvement of people's living needs, flexible and lightweight flexible electronic devices have attracted widespread attention for their soft, deformable, and easy-to-wear properties. To meet these needs, it is necessary to develop an electrode with good flexibility and excellent electrochemical performance. Wang L. et al. (2017) synthesized SWCNTs by low-crystallization hydrothermal treatment, and then mixed they with MnO_2 to form an ordered network structure by vacuum filtration (see **Figure 3G**). The results show that the electrochemical properties of the materials can be improved by effectively regulating the regular fiber network structure. As is shown in **Figures 3H,I**, the area specific capacitance is 964 mF cm^{-2}, and the capacity retention rate is 81% of the composite. The assembled hybrid supercapacitors also provide high energy densities of 31.8 μWh cm^{-2} at a power density of 0.815 mW cm^{-2}, implying their great potential applications in flexible device. In addition, this review summarizes the electrochemical performance of some typical MnO_2/CNT electrode materials for comparison (see **Table 1**).

MnO_2/Graphene Composites

Graphene is a two-dimensional carbon nanomaterial composed of hexagonal carbon atoms in a honeycomb lattice (Huang et al., 2011; Bayle et al., 2015). With its excellent physical and chemical properties, it has shown broad application prospects in the field of energy storage and conversion (Chen P. et al., 2018; Lu et al., 2018). Interest in the study of graphene has not been attenuated after Novoselov and Geim prepared a single layer of graphene by mechanical stripping at room temperature, breaking the prediction that quasi-two-dimensional crystal materials could not exist alone at room temperature (Novoselov et al., 2004). A two-dimensional planar structure of graphene can be regarded as a building unit for constituting other dimensional carbon materials, such as zero-dimensional fullerene, one-dimensional CNTs, and three-dimensional graphite (Geim and Novoselov, 2007). In addition, the three-dimensional graphene structure can also be constructed by its self-assembling or in combination with other materials. Thanks to its two-dimensional sheet structure that can be used to construct three-dimensional electrode materials with controllable structure, it can meet the needs of no conductive agent and binder addition. The excellent electron migration rate can promote electron transport during charging/discharging to improve electrochemical performance of electrode materials. Due to the special structure of graphene, the theoretically excellent characteristics, such as large specific surface area (∼2,630 m^2 g^{-1}), excellent electrical conductivity, and excellent mechanical properties (resistance). Tensile strength of 130 GPa and stiffness of 1.5×10^8 psi, and good chemical and thermal stability (Ren et al., 2018) make it a considerable industrial material that most likely to achieves scale application in the short term for EES (Kannappan et al., 2018).

However, the volumetric energy density of most graphene-based electrode materials is very low, resulting in lower energy density of the electrodes. In order to make full use

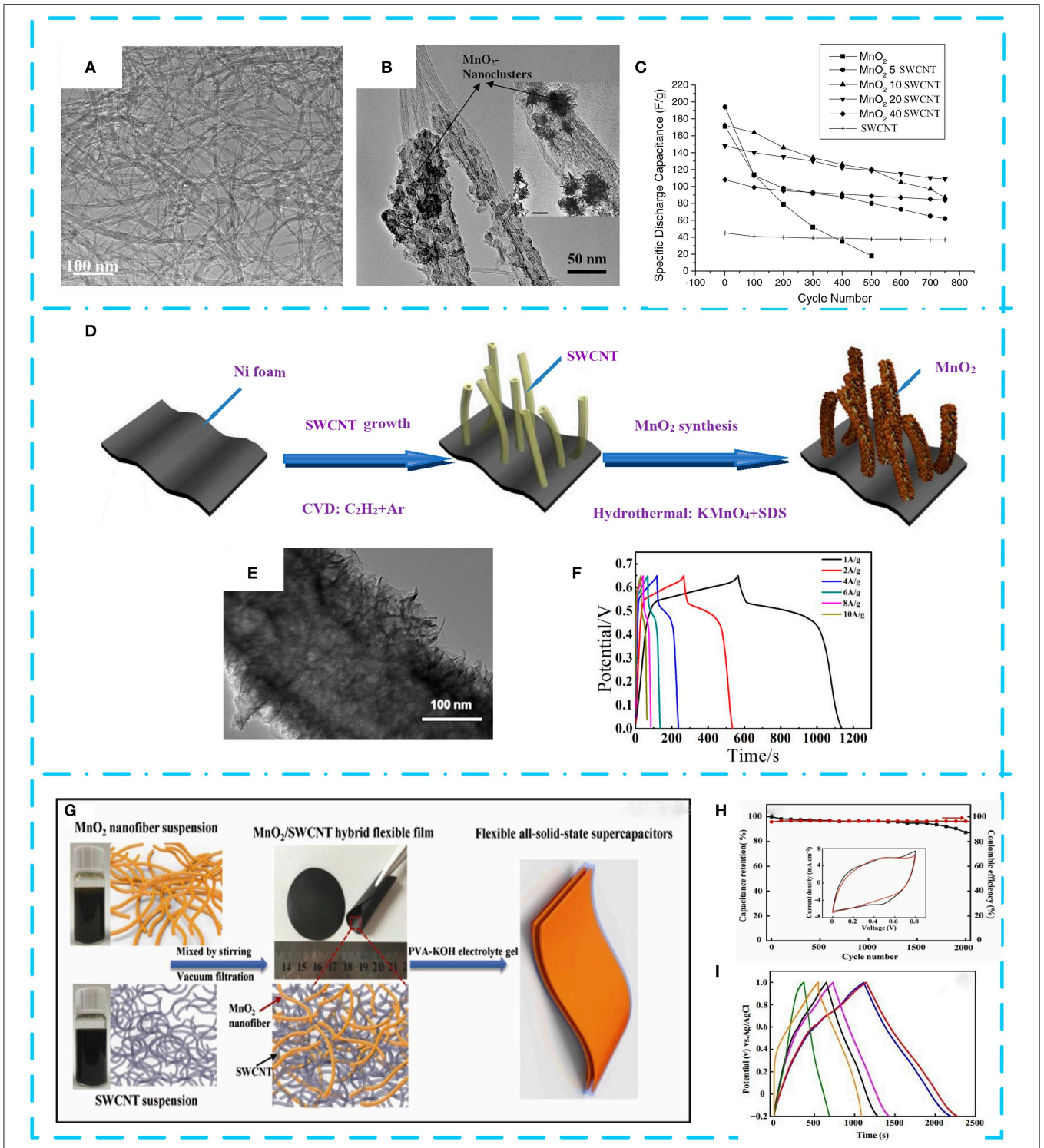

FIGURE 3 | Transmission electron microscopy (TEM) pictures. **(A)** Pure single-walled carbon nanotube (SWCNT). **(B)** MnO_2:20 wt% SWCNT composite. **(C)** Cyclic voltammograms of pure MnO_2, pure SWCNT, and MnO_2:20 wt% SWCNT composite at a scan rate of 2 mV s^{-1}. Adapted from Subramanian et al. (2006) with permission from Elsevier Inc. **(D)** Production process of MnO_2–multi-walled CNT (MWCNT)–Ni foam. **(E)** MnO_2 synthesized uniformly on MWCNTs. **(F)** Charge/discharge curves at different current densities of the MnO_2–MWCNT–Ni foam composite. Adapted from (Li L. et al., 2019) under the Creative Commons CC license. **(G)** Schematic preparation representation of the flexible all-solid-state δ-MnO_2/SWCNT hybrid supercapacitor. **(H)** Cyclic voltammetry curves from 5 to 100 mV s^{-1}. **(I)** Galvanostatic charge/discharge (GCD) curves of MnO_2/SWCNT composites at a current density of 0.1 mA cm^{-2} in a 1 M Na_2SO_4 electrolyte. Reproduced from Wang L. et al. (2017) with permission from the Royal Society of Chemistry.

TABLE 1 | Electrochemical performance of various MnO_2/CNT materials.

Material	Electrolyte	Specific capacitance/F g^{-1}	Rate capability/F g^{-1}	Stability (cycles)	References
MnO_2/CNT	0.2 M Na_2SO_4	642 (10 mV s^{-1})	370 (100 mV s^{-1})	∼70% (1,000)	Amade et al., 2011
MnO_2/MWCNT	0.5 M Na_2SO_4	276 (3 A g^{-1})	180.5 (9.5 A g^{-1})	91.6% (5,000)	Ramesh et al., 2017
MnO_2/CNT sponge	1 M Na_2SO_4	600 (1 A g^{-1})	430 (10 A g^{-1})	∼100% (1,000)	Liu et al., 2017
MnO_2/MWCNT	1 M KCl	251 (0.5 A g^{-1})	–	97% (1,000)	Subagio et al., 2019
MnO_2/CNT	1 M Na_2SO_4	740 (2 mV s^{-1})	503 (100 mV s^{-1})	92% (1,000)	Lv et al., 2012
MnO_2/CNT	0.5 M Na_2SO_4	793 (5 mV s^{-1})	659 (50 mV s^{-1})	97% (5,000)	Li Q. et al., 2014
MnO_2/CNT	1 M Na_2SO_4	740 (10 mV s^{-1})	578 (150 mV s^{-1})	99.5% (800)	Fan et al., 2008a
MWCNT/MnO_2	1 M Na_2SO_4	603.88 (10 mV s^{-1})	405.15 (100 mV s^{-1})	81% (1,000)	Li W. S. et al., 2019
γ-MnO_2/CNT	0.5 M Na_2SO_4	579 (10 mV s^{-1})	422 (150 mV s^{-1})	87.6% (5,000)	Fan et al., 2008b
MnO_2/CNT	0.5 M Na_2SO_4	442.9 (2 mV s^{-1})	180 (100 mV s^{-1})	–	Wang and Igor, 2009
MnO_2/CNT	0.5 M Na_2SO_4	164 (1 A g^{-1})	132 (10 A g^{-1})	–	Xiao et al., 2010
MnO_2/CNT	0.5 M Na_2SO_4	442.9 (2 mV s^{-1})	250 (100 mV s^{-1})	98.9% (1,000)	Zhang et al., 2012
MnO_2/CNT	0.1 M Na_2SO_4	290 (10 mV s^{-1})	145 (200 mV s^{-1})	88.4% (1,000)	Xin and Wei, 2012
MnO_2-doped PANI/CNT	1 M H_2SO_4	1,360 (5 mV s^{-1})	710 (100 mV s^{-1})	>82% (5,000)	Kaushal et al., 2019
MnO_2/SWCNT/SWCNF	0.5 M Na_2SO_4	276 (3 A g^{-1})	180.5 (9.5 A g^{-1})	91.6% (5,000)	Seung Woo et al., 2010
MnO_2/electrospun CNT	6 M KOH	141.7 (5 mV s^{-1})	67 (100 mV s^{-1})	84.9% (1,000)	Wang N. et al., 2011

CNT, carbon nanotube; MWCNT, multi-walled CNT; PANI, polyaniline; SWCNT, single-walled CNT; SWCNF, single-walled carbon nanofiber.

of the excellent properties of graphene, adding MnO_2 to graphene has become a popular choice for most researchers. This can effectively prevent graphene from agglomeration owing to strong van der Waals force by the introduction of MnO_2 between the sheets (Sheng et al., 2016). And the graphene can act as carbon skeleton that exerts an "elastic constraint" to prevent electrochemical dissolution of MnO_2. MnO_2/graphene composites prepared by microwave irradiation, low-temperature hydrothermal treatment, *in situ* reduction method, and electrospinning technology have stimulated their application potential in supercapacitors or other green energy devices. Yan et al. (2010) used a fast and simple microwave radiation method to deposit nanosized MnO_2 on the surface of graphene (see **Figures 4A,B**). The capacitance characteristics of the graphene–MnO_2 composite (78 wt% of MnO_2) show that the measured specific capacitance is 310 F g^{-1} at 2 mV s^{-1} (**Figure 4C**). This is almost three times better than that of pure graphene (104 F g^{-1}) and birnessite MnO_2 (103 F g^{-1}). Interestingly, the weight ratio of MnO_2 in the composite has a great influence on the capacitance performance. As the mass ratio increases from 20 to 78%, the specific capacitance value increases significantly. **Figure 4D** displays schematic preparation process of an ordered MnO_2-GO fiber composite supercapacitor electrode material by electrospinning (Saha et al., 2019). The MnO_2 particles with an average diameter of 260 nm uniformly distributed on the surface of graphene in **Figure 4E**, and the composite exhibited excellent electrochemical performance. The specific capacitance of the sample reached 863.0 F g^{-1} at a current density of 9 A g^{-1}, and the specific capacitance remained 88% of the initial value after 5,000 cycles (**Figure 4F**). By investigating the electrochemical properties, dielectric behavior, and impedance spectra of the samples, it was found that the ordered composites have higher diffusivity and charge mobility than the disordered MnO_2. It is concluded that changing the crystallinity of MnO_2 with increased electrical conductivity can improve the performance of GO/MnO_2 active materials. As the research progressed, ternary MnO_2 composites have been widely used. For example, Zhu G. et al. (2014) anchored MnO_2 nanoflakes on a graphene–CNT hybrid substrate to form a three-dimensional hybrid material without a binder (**Figures 4G,H**). The hybrid structure completely maintains high conductivity and high surface with increase of volume ratio of CNTs, exhibiting a capacitance value of 251 F g^{-1} at 1 A g^{-1} (see **Figure 4I**). A highly conductive MnO_2–CNT–graphene–Ni-foamed symmetrical supercapacitor delivers an energy density of 1,200 W kg^{-1} at a power density of 29 Wh kg^{-1}. It is worth noting that the crystallinity, micromorphology, and mass ratio of MnO_2 in nanocomposites have a significant effect on the electrochemical performance for supercapacitors. The friendly method under mild conditions is more conducive to the shape control of MnO_2/graphene and the feasibility of expanding production. Furthermore, the control of oxygen-containing functional groups and heteroatom doping of graphene is also a way to manufacture high-performance nanocomposites. The modified nanocomposite can effectively change the electronic properties of graphene and further improve the performance. In addition, this review summarizes the literature on the recently published MnO_2/graphene composites in **Table 2**.

MnO_2/Carbon Nanofiber Composites

CNFs are a type of carbon material that is internally composed of a layer of graphite carbon oriented along the fiber axis. According to different precursors of raw silk, CNFs are mainly divided into three classifications: polyacrylonitrile (PAN)-based carbon fiber, pitch-based carbon fiber, and rayon carbon fiber (Wazir and Kakakhel, 2009). Compared with AC materials, carbon fiber has obvious advantages in performance. The connection of the large, medium, and large number of small holes on the

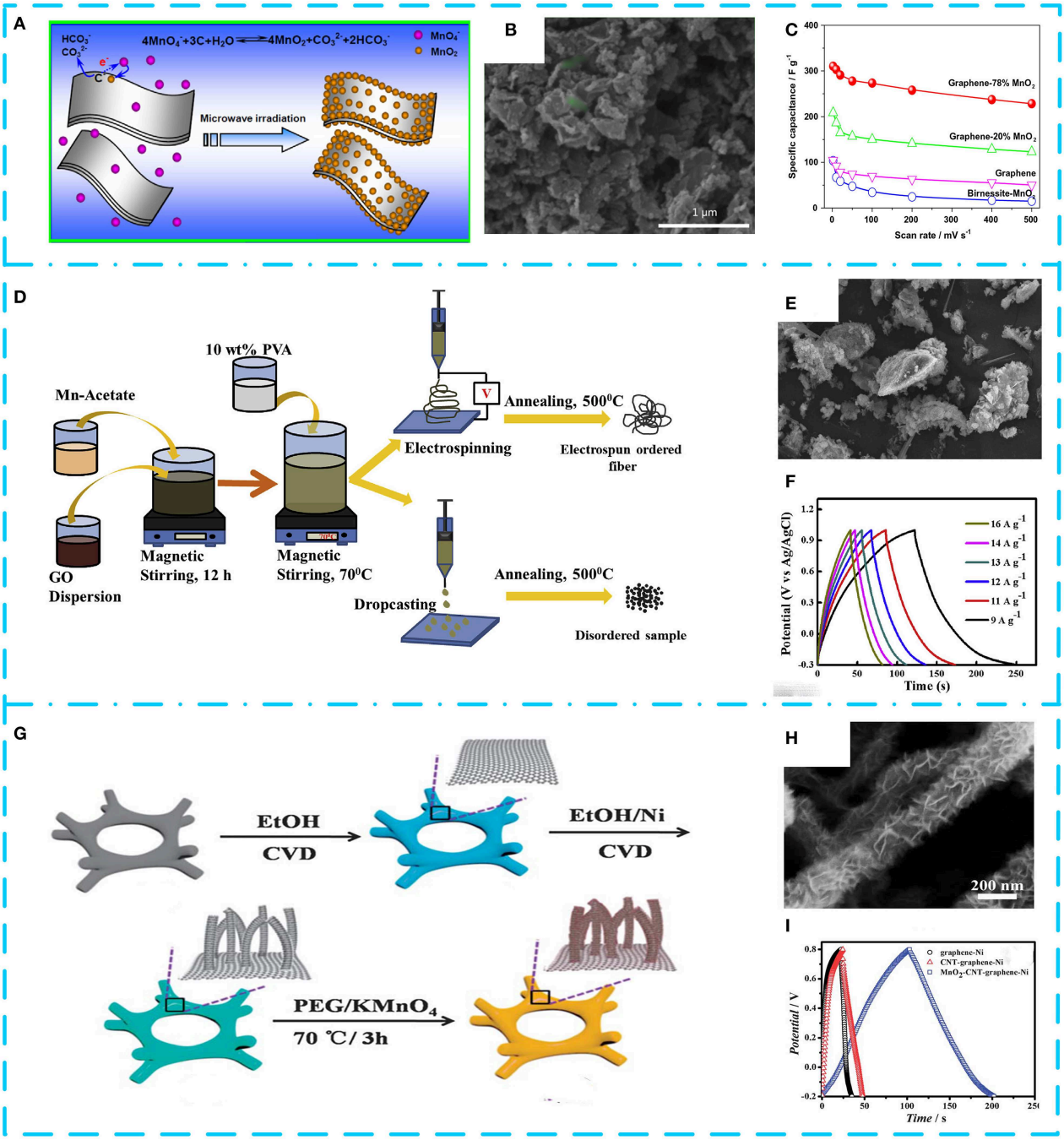

FIGURE 4 | (A) Schematic illustration of the synthesis and electrochemical performance of graphene–MnO_2 composite. **(B)** Low-magnification scanning electron microscopy (SEM) image of graphene−78% MnO_2, showing the preferred growth of MnO_2 near the edges of graphene. **(C)** Specific capacitance of composites at different scan rates of 2, 10, 20, 50, 100, 200, and 500 mV s^{-1}. Reproduced from Yan et al. (2010) with permission from Pergamon. **(D)** Schematic of synthesis procedure. **(E)** SEM image. **(F)** Galvanostatic charge/discharge (GCD) curves at different current densities of MnO_2/graphene−2D composites in 1 M of Na_2SO_4 solution. Adapted from Saha et al. (2019) with permission from Pergamon. **(G)** Schematic illustration. **(H)** SEM images of the fabricated 3D MnO_2-carbon nanotube (CNT)–graphene–Ni hybrids. **(I)** GCD curves of the graphene–Ni, CNT–graphene–Ni, and MnO_2–CNT–graphene–Ni hybrids. Adapted from Zhu G. et al. (2014) with permission from RSC Pub.

surface is very favorable for the transport of the electrolyte and the adsorption of the charges. Moreover, the excellent heat resistance, low thermal expansion, chemical stability, and good electrical conductivity make them very suitable as electrode materials for supercapacitors (Kim et al., 2019). Generally, CNFs can be prepared by chemical vapor deposition (CVD)

TABLE 2 | Electrochemical performance of various MnO_2/graphene materials.

Material	Electrolyte	Specific capacitance/F g^{-1}	Rate capability/F g^{-1}	Stability (cycles)	References
δ-MnO_2/graphene	1 M Na_2SO_4	270 (0.5 A g^{-1})	168 (15 A g^{-1})	90.12% (50,000)	Wang et al., 2019a
MnO_2/graphene	1 M KOH	342.8 (0.5 A g^{-1})	111.2 (20 A g^{-1})	90.3% (3,000)	Wang H. et al., 2019
N-doped graphene/MnO_2	1 M Na_2SO_4	411.5 (0.5 A g^{-1})	242 (20 A g^{-1})	88.3% (4,000)	Le et al., 2019
MnO_2/GO	1 M Na_2SO_4	315 (0.5 A g^{-1})	–	∼95% (5,000)	Wu et al., 2010
MnO_2/GO	1 M Na_2SO_4	360.3 (0.5 A g^{-1})	223.6 (5 A g^{-1})	>93% (1,000)	Dai et al., 2014
MnO_2/rGO	1 M Na_2SO_4	759 (2 A g^{-1})	196 (50 A g^{-1})	88% (3,000)	Jadhav et al., 2019
MnO_2/rGO	1 M Na_2SO_4	234.8 (0.1 A g^{-1})	136.9 (5 A g^{-1})	100% (10,000)	Chen Y. et al., 2018
MnO_2/graphene	1 M Na_2SO_4	255 (0.5 A g^{-1})	–	84.5% (10,000)	Zhang Q. et al., 2019
MnO_2/graphene	1 M Na_2SO_4	133 (10 mV s^{-1})	104 (150 mV s^{-1})	75% (10,000)	Amade et al., 2019
Graphene/MnO_2/CNTs	1 M Na_2SO_4	372 (0.5 A g^{-1})	194 (10 A g^{-1})	>90% (3,000)	Cheng et al., 2012
Sponge@rGO@MnO_2	1 M Na_2SO_4	205 (0.1 A g^{-1})	136.9 (5 A g^{-1})	90% (20,000)	Ge et al., 2013

GO, graphene oxide; rGO, reduced GO; CNTs, carbon nanotubes.

and spinning, using carbon ammonia compounds (including methyl, hexyl, ethyl, and carbon monoxide) as carbon precursors. The ammonium bicarbonate molecules are decomposed at high temperatures under the catalysis of metal catalysts such as iron, diamond, and ruthenium; and carbon atoms diffuse into the graphite layer to form a fibrous structure. The spinning method extrudes the precursor polymer into multiple continuous filaments through wet spinning, gel spinning, baking–melting, dry spinning, and electrostatic spinning, among which electrostatic spinning technology is the most widely applied (Zhang et al., 2015).

Owing to the compact structure, low porosity, and small specific surface area (<10 m^2 g^{-1}) of CNFs in practical applications (Sun et al., 2018), using pure CNFs as electrode materials leads to poor electrochemical performance. Therefore, they can be used as a substrate-carrying MnO_2 pseudocapacitor material to improve the electrochemical activity of the electrode, thereby preparing a high-performance composite electrode. Zhao H. et al. (2016) obtained bubble CNFs by exploding PAN at temperatures of 1,000°C in **Figure 5A**. The electrode after decoration with MnO_2 nanosheets has a capacitance value of 428 F g^{-1} at 1 A g^{-1} owing to the easy electron transport path of CNFs (**Figures 5B,C**). After 1,500 cycles, the specific capacitance of composites still remained 98.8%. Ma et al. (2016) used electrospun lignin-derived high-graphite electrospun CNF (ECNF; ∼200 nm in diameter and ∼583 m^2 g^{-1} of specific surface area) as the substrate and then decorated with MnO_2 nanowhiskers to obtain three kinds of nanocomposites with different weight percentages of MnO_2 (**Figure 5D**). The electrochemical performance of the sample with a mass ratio of ECNF and MnO_2 of 1:1 is optimal. The supercapacitor device prepared by using the composite as an electrode material has a specific capacitance of 83.3 F g^{-1}, an energy density of 84.3 Wh kg^{-1}, and a power density of 5.72 kW kg^{-1} (**Figures 5E,F**). As shown in **Figure 5G**, an effective solar technology was reported by Zhao C. et al. (2017). They successfully recovered regenerated carbon fiber (RCF) from carbon fiber-reinforced polymer (CFRP), and then the α-MnO_2 nanowires were uniformly grown on the surface of the high temperature-treated RCF. The MnO_2/RCF composite (MRCF) prepared by processing CNF at 150°C has an extremely large potential window (1.6 V) and excellent electrochemical performance (specific capacitance is 228.8 F g^{-1} at 1 A g^{-1}, and high cycle stability is ∼91.2% after 3,000 cycles) in **Figures 5H,I**. The asymmetric supercapacitor assembled with the composite as the positive electrode has an operating potential window of 2.0 V and exhibits a high energy density of 22.9 Wh kg^{-1}. There are relatively few studies on MnO_2/CNF, and some of the results are shown in **Table 3**. It is found that rationally designing the microstructure of MnO_2/CNF composites and enhancing the electrochemical utilization of MnO_2 can effectively improve EES.

MnO_2/Activated Carbon Composites

AC is a carbon material prepared by pyrolysis and activation of carbon-containing raw materials such as wood, coal, and petroleum coke. It has developed pore structure, large specific surface area, and abundant surface chemical groups (Abioye and Ani, 2015). According to the pore size, it can be classified into three types: macropores (≥50 nm), mesopores (2–50 nm), and micropores (≤2 nm) (Wei et al., 2016). In the energy storage mechanism, large pores are usually used as ion buffers, mesopores (transition pores) are used for efficient ion diffusion, and micropores are used to store charges. Owing to the rich pore structure of AC, its specific surface area can reach up to 3,000 m^2 g^{-1} (Barbieri et al., 2005), which creates favorable conditions for charge storage. AC possesses characteristics of stable chemical properties, abundant sources, wide operating temperature range, simple preparation process, large specific surface area, and environmental protection (Wang Y. et al., 2019). It has been considered to be the most extensive electric double-layer electrode active material in commercial applications. AC for electrodes of electric double-layer capacitors is usually derived from nature, such as charcoal, husks, and biomass, and can also be obtained by carbonized polymers. Generally, the synthesis process of AC is to carbonize a carbonaceous organic precursor in an inert atmosphere at a high temperature and then activate the carbon materials having a high specific surface area by physical or

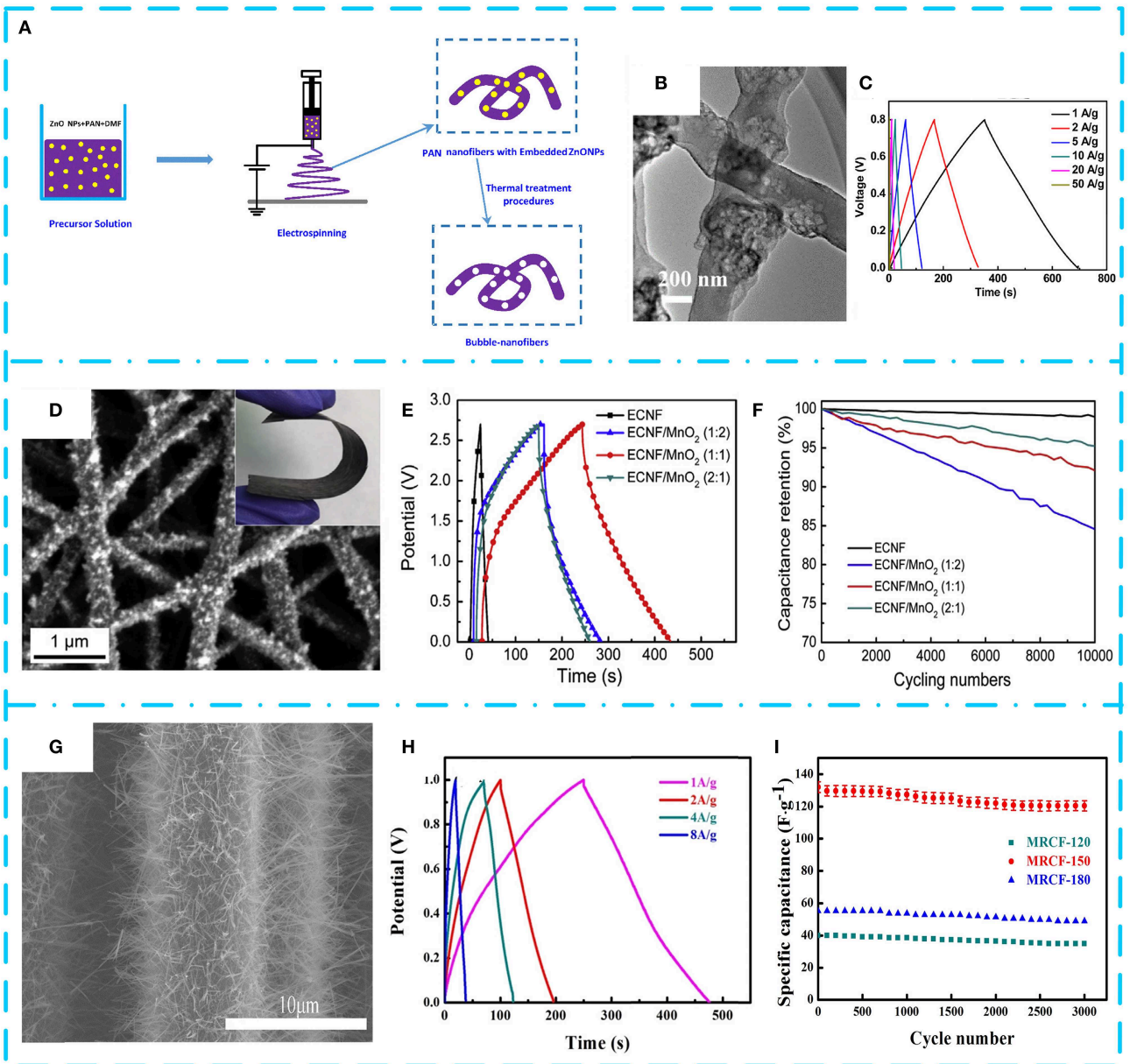

FIGURE 5 | (A) Schematic illustration of bubble carbon nanofibers (B-CNFs). **(B)** Transmission electron microscopy (TEM) image of B-CNF/MnO_2 composites with the B-CNFs calcined at 1,000°C. **(C)** Galvanostatic charge/discharge curves of B-CNFs/MnO_2 at different discharge current densities. Reproduced from Zhao H. et al. (2016) with permission from Pergamon. **(D)** Scanning electron microscopy (SEM) images of electrospun carbon nanofiber (ECNF)/MnO_2 (2:1). **(E)** Galvanostatic charge/discharge curves acquired from ECNF and three ECNF/MnO_2 mats/electrodes at current density of 250 mA g^{-1}. **(F)** Cycling stability/durability of the ECNF and three ECNF/MnO_2 mats/electrodes at high constant current density of 2,000 mA g^{-1}. Reproduced from Ma et al. (2016) with permission from Elsevier S.A. **(G)** SEM image of regenerated carbon fiber (RCF) prepared at 150°C. **(H)** Galvanostatic charge/discharge curves at different current densities of MnO_2/RCF (MRCF)-150 in 1 M of Na_2SO_4. **(I)** Cycle life of the MRCF-120, MRCF-150, and MRCF-180 electrodes at current density of 8 A g^{-1} in 1 M of Na_2SO_4 solution. Reproduced from Zhao C. et al. (2017) with permission from Pergamon.

chemical activation. Physical activation is usually performed by injecting CO_2 or water vapor at high temperatures to the system, followed by removing precursor uncarbonized substances and selective oxidation of carbides (López Ch et al., 2015). KOH, $ZnCl_2$, and H_3PO_4 are usually used as activators for chemical methods with carbonized substances to selectively react to form pores and increase specific surface (Abioye and Ani, 2015). According to the double-layer capacitance theory, the specific capacitance of AC is greatly affected by the specific surface area. The initial research hopes to increase specific capacitance by expanding specific surface area and pore volume of carbon materials. However, it is found that the capacitance of electrode

TABLE 3 | Electrochemical performance of various MnO_2/CNF material.

Material	Electrolyte	Specific capacitance/F g^{-1}	Rate capability/F g^{-1}	Stability (cycles)	References
CNF/MnO_2	1 M HCl	311 (2 mV s^{-1})	159 (200 mV s^{-1})	97.6% (1,000)	Zhi et al., 2012
CNF/MnO_2	6 M KOH	142 (10 mV s^{-1})	–	–	Nataraj et al., 2013
MnO_2/catalytically grown CNF	1 M Na_2SO_4	257 (5 mV s^{-1})	–	105% (1,000)	Zhou et al., 2017
CNFs/MnO_2	0.1 M Na_2SO_4	557 (1 A g^{-1})	186 (30 A g^{-1})	94% (1,500)	Wang J. G et al., 2011
CNFs/MnO_2	0.5 M Na_2SO_4	365 (1 A g^{-1})	–	95.3% (1,000)	Wang et al., 2013
MnO_2/CNF	0.1 M Na_2SO_4	374 (2 mV s^{-1})	198 (100 mV s^{-1})	94% (1,000)	Wang J. G. et al., 2012
CNT/CNF/MnO_2	1 M Na_2SO_4	517 (5 mV s^{-1})	–	75% (1,000)	Wang T. et al., 2015

CNF, carbon nanofiber.

materials is not linearly related to the specific surface area. Even if the specific surface area increases a lot, the increase of specific capacitance is still limited. Moreover, these shortcomings will in turn reduce the energy density and power density of AC electrode.

In order to further obtain high energy density and volume density, typical pseudocapacitive materials such as MnO_2 are increasingly anchored on AC to obtain ideal electrode materials. Chen M. D. et al. (2014) selected cotton stalk as carbon precursor and synthesized an amorphous AC material with 1,481 m^2 g^{-1} of specific surface area using H_3PO_4 as activator by one-step chemical activation. After that, electrolytic MnO_2/AC composites with different contents of MnO_2 were prepared, as shown in **Figure 6A**. The galvanostatic charge test confirmed that the composite with 5% MnO_2 (labeled as AC4) has optimum specific capacitance (169 F g^{-1}) and excellent cycle life (99.2% after 500 cycles), as shown in **Figures 6B,C**. With the deepening research, Zhang J. et al. (2019) proposed a novel high-voltage anode electrodeposition technique to deposit graded MnO_2 on AC cloth (**Figure 6D**). Interestingly, it was found that the AC cloth was activated to have a significant improvement in the conductivity and hydrophilicity of the composite electrode. It can be seen from **Figure 6E** that benefiting from the high conductivity of the closely contacted AC cloth/MnO_2 interface, the electrode exhibits a specific capacitance of 400 F g^{-1} in 1 M of Na_2SO_4 at 0.5 A g^{-1} in an asymmetric supercapacitor, and the impressive volumetric energy density reaches 3.82 mWh cm^{-3}. **Figure 6F** shows the good flexibility and mechanical properties of the composite. In **Figures 6G,H**, Li H. et al. (2019) combine AC fibers with MnO_2 to form electrodes with excellent flexibility and excellent capacitance properties. The area ratio of the composite material is as high as 410 mF cm^{-2}, delivering a high energy density of 36 μWh cm^{-2} and a high power density of 726 μW cm^{-2} (**Figure 6I**). Integrated devices with multiple electrodes can successfully illuminate light-emitting diodes, showing great potential applications. Finally, it is found that the perfect pore structure and proper surface modification that can function as a fast transfer ion and increase the wettability of the electrode surface are beneficial for suitable pore size distribution. Moreover, the presence of the AC can prevent agglomeration of MnO_2 and maximize the MnO_2 pseudocapacitance. **Table 4** summarizes the electrochemical performance of some representative MnO_2/AC composites. It shows that MnO_2/AC composites, as an environmentally friendly supercapacitor electrode material, have become a preferred choice for researchers.

SUMMARY AND OUTLOOK

This review summarizes the research achievements in synthesis methods and electrochemical performance of MnO_2/carbon composites for supercapacitors in recent years. In this system, MnO_2 provides a source of high specific capacitance and high energy density, while carbon materials ensure excellent cycle performance and high power density. Impressively, various functional carbon materials exhibit their own excellent physical and chemical properties in different dimensions, which provides feasibility to rationally optimize the microstructure and maximization of electrochemical properties of MnO_2/carbon electrode materials. Among these carbon substrates, one-dimensional carbon materials of CNTs and CNFs can provide high-speed diffusion and shorten ion diffusion paths owing to their high conductivity and good mechanical properties, becoming the preferred choice for flexible supercapacitors. Two-dimensional carbon materials represented by graphene are regarded as ideal conductive substrates for their high specific surface area, ultra-low density, and good electrical conductivity. Other AC materials with typical three-dimensional structure are widely used in preparing energy storage devices with high energy density due to their large number of microporous structures and rich functional groups. In general, carbon nanomaterial with excellent porous structure and high conductivity can maximize the electrochemical performance of MnO_2. Orderly and tidy channels (such as mesoporous carbon) can accelerate the transport of electrolyte ions and make it easier to enter MnO_2. Meanwhile, enhancing the degree of graphitization of carbon materials (such as CNTs and graphene) is conducive to the improvement of conductivity to ensure rapid transfer of charge. In recent years, numerous efforts have been made to explore high-performance MnO_2/carbon composites for supercapacitors, and exciting improvements have been achieved. However, there are still remaining several key drawbacks in those composites, such as the lack of ordered pore

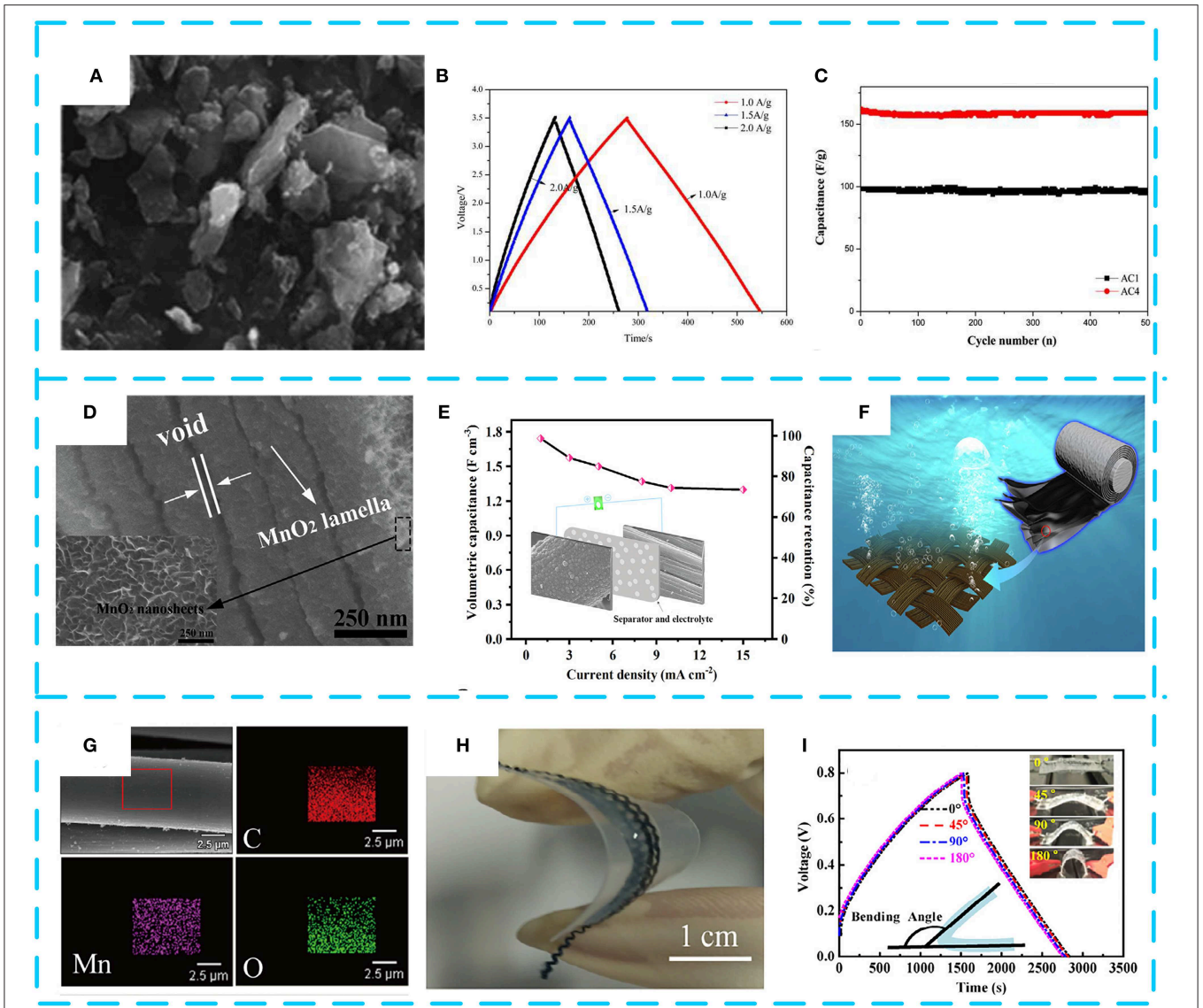

FIGURE 6 | (A) Scanning electron microscopy (SEM) images of AC4. **(B)** Galvanostatic charge/discharge curves of AC4 at 1.0 A g^{-1}. **(C)** Charge–discharge cycling stability of AC4 at current density of 2 A g^{-1}. Reproduced from Chen M. D. et al. (2014) with permission from Maney Publishing. **(D)** Cross-sectional SEM image of MnO_2/AC cloth-300. **(E)** Variations of the capacitance with current densities. **(F)** Schematic representation of the as-prepared electrode. Reproduced from (Zhang J. et al., 2019) with permission from Elsevier BV. **(G)** The corresponding energy-dispersive X-ray spectroscopy (EDS) elemental maps of Mn, O, and C. **(H)** Structure and electrochemical performance. **(I)** Charge–discharge curves at 0.1 mA cm^{-2} under different bending states of the MnO_2@ACF-6. Reproduced from (Li H. et al., 2019) with permission from Elsevier.

channels in the carbon substrate (Wang T. et al., 2015), the violent volume expansion and low electrochemical utilization rate of MnO_2 (Lei et al., 2012; Sun et al., 2017), and optimization of the composite structure (Zhang Q. Z. et al., 2018).

Faced with these practical challenges and obstacles, we believe that much more efforts should be focused on developing new-generation MnO_2/carbon composites that can better meet the energy storage requirements and standards of advanced supercapacitors in the future. Therefore, we suggest that future research trends may focus on the following aspects:

(1) For MnO_2/CNTs or CNFs, a carbon substrate with the optimal pore size distribution and specific surface area should be constructed to increase the specific capacity and power density of the supercapacitor; improve the poor surface wettability of CNTs by surface modification, ultrasound, and other treatments to ensure uniformity of MnO_2 deposition; and optimize the design of flexible and foldable CNF substrates that meet different requirements without sacrificing stable power output and long cycle stability.

(2) For MnO_2/AC, the low-mass load problem of MnO_2 should be improved without sacrificing the power of the

TABLE 4 | Electrochemical performance of various MnO_2/CNT material.

Material	Electrolyte	Specific capacitance/F g^{-1}	Rate capability/F g^{-1}	Stability (cycles)	References
AC/MnO_2	6 M KOH	193 (0.2 A g^{-1})	154 (2 A g^{-1})	77.8% (1,500)	Liu et al., 2015
Porous AC/MnO_2	6 M KOH	258 (1 A g^{-1})	235 (20 A g^{-1})	93.6% (10,000)	Kong et al., 2019
MnO_2/AC cloth	1 M Na_2SO_4	257 (5 mV s^{-1})	–	94.2% (5,000)	Shen et al., 2019
AC/MnO_2	1 M Na_2SO_4	297.8 (0.2 A g^{-1})	155 (20 A g^{-1})	94.8% (1,000)	Kim et al., 2015
AC/MnO_2	1 M Na_2SO_4	90.5 (5 mV s^{-1})	–	91.3% (1,000)	Kim et al., 2013
MnO_2/spherical AC	0.1 M Na_2SO_4	357 (1 A g^{-1})	–	93% (3,000)	Li Z. et al., 2014

CNF, carbon nanofiber; AC, activated carbon.

composite material to balance the overall performance, effectively exerting the coordination performance of MnO_2 and carbon materials.

(3) For MnO_2/graphene, MnO_2 should be deposited more uniformly on the surface of graphene and should establish an intimate connection by the new composite technology to prevent the damage of composite structure and improve the rate capability and cycle stability.

(4) MnO_2 should be combined with economical and green carbon materials to develop light, low-price, and environmentally friendly composite electrode materials.

AUTHOR CONTRIBUTIONS

All authors listed have made a substantial, direct and intellectual contribution to the work, and approved it for publication.

FUNDING

This work was supported by research program of the Key Laboratory for Biomedical Effects of Nanomaterials and Nanosafety, Chinese Academy of Sciences (NSKF201908).

REFERENCES

Abioye, A. M., and Ani, F. N. (2015). Recent development in the production of activated carbon electrodes from agricultural waste biomass for supercapacitors: a review. *Renew. Sust. Energ. Rev.* 52, 1282–1293. doi: 10.1016/j.rser.2015.07.129

Amade, R., Jover, E., Caglar, B., Mutlu, T., and Bertran, E. (2011). Optimization of MnO_2/vertically aligned carbon nanotube composite for supercapacitor application. *J. Power Sources* 196, 5779–5783. doi: 10.1016/j.jpowsour.2011.02.029

Amade, R., Muyshegyan-Avetisyan, A., González, J. M., Pino, A. P., György, E., Pascual, E., et al. (2019). Super-capacitive performance of manganese dioxide/graphene nano-walls electrodes deposited on stainless steel current collectors. *Materials* 12:483. doi: 10.3390/ma12030483

Barbieri, O., Hahn, M., Herzog, A., and Kötz, R. (2005). Capacitance limits of high surface area activated carbons for double layer capacitors. *Carbon* 43, 1303–1310. doi: 10.1016/j.carbon.2005.01.001

Bayle, M., Reckinger, N., Huntzinger, J. R., Felten, A., Bakaraki, A., Lan Landois, P., et al. (2015). Dependence of the Raman spectrum characteristics on the number of layers and stacking orientation in few-layer graphene. *Phys. Status Solidi* 252, 2375–2379. doi: 10.1002/pssb.201552204

Bi, T., Fang, H., Jiang, J., He, X., Zhen, X., Yang, H., et al. (2019). Enhance supercapacitive performance of MnO_2/3D carbon nanotubes-graphene as a binder-free electrode. *J. Alloys Compd.* 30, 759–766. doi: 10.1016/j.jallcom.2019.02.117

Borenstein, A., Hanna, O., Attias, R., Luski, S., Brousse, T., and Aurbach, D. (2017). Carbon-based composite materials for supercapacitor electrodes: a review. *J. Mater. Chem.* 5, 12653–12672. doi: 10.1039/C7TA00863E

Byl, O., Liu, J., and Yates, J. T. (2005). Etching of carbon nanotubes by ozone-a surface area study. *Langmuir* 21, 4200–4204. doi: 10.1021/la040132w

Candelaria, S. L., Shao, Y., Zhou, W., Li, X., Xiao, J., Zhang, J. G., et al. (2012). Nanostructured carbon for energy storage and conversion. *Nano Energy* 1, 195–220. doi: 10.1016/j.nanoen.2011.11.006

Chen, M. D., Wumaie, T., Li, W. L., Song, H. H., and Song, R. R. (2014). Electrochemical performance of cotton stalk based activated carbon electrodes modified by MnO_2 for supercapacitor. *Mater. Technol.* 30, A2–A7. doi: 10.1179/1753555714Y.0000000241

Chen, P., Yang, C., He, Z., and Guo, K. (2018). One-pot facile route to fabricate the precursor of sulfonated graphene/N-doped mesoporous carbons composites for supercapacitors. *J. Mater. Sci.* 54, 4180–4191. doi: 10.1007/s10853-018-3122-6

Chen, Y., Zhang, J., Li, M., Yang, C., Zhang, L., Wang, C., et al. (2018). Strong interface coupling and few-crystalline MnO_2/Reduced graphene oxide composites for supercapacitors with high cycle stability. *Electrochim. Acta* 292, 115–124. doi: 10.1016/j.electacta.2018.09.131

Cheng, Y., Lu, S., Zhang, H., Varanasi, C. V., and Liu, J. (2012). Synergistic effects from graphene and carbon nanotubes enable flexible and robust electrodes for high-performance supercapacitors. *Nano Lett.* 12, 4206–4211. doi: 10.1021/nl301804c

Conway, B. E. (1999). *Electrochemical Supercapacitors: Scientific Fundamentals and Technological Applications*. NewYork, NY: Springer. doi: 10.1007/978-1-4757-3058-6

Dai, K., Lu, L., Liang, C., Dai, J., Liu, Q., Zhang, Y., et al. (2014). *In situ* assembly of MnO_2 nanowires/graphene oxide nanosheets composite with high specific capacitance. *Electrochim. Acta* 116, 111–117. doi: 10.1016/j.electacta.2013.11.036

Díaz-Delgado, R., and Doherty, A. P. (2016). Carbons, ionic liquids, and quinones for electrochemical capacitors. *Front. Mater.* 3:18. doi: 10.3389/fmats.2016.00018

Dubey, R., and Guruviah, V. (2019). Review of carbon-based electrode materials for supercapacitor energy storage. *Ionics* 25, 1419–1445. doi: 10.1007/s11581-019-02874-0

Fan, Z., Chen, J., Zhang, B., Liu, B., Zhong, X., and Kuang, Y. (2008a). High dispersion of γ-MnO_2 on well-aligned carbon nanotube arrays and its application in supercapacitors. *Diamond Relat. Mater.* 17, 1943–1948. doi: 10.1016/j.diamond.2008.04.015

Fan, Z., Chen, J., Zhang, B., Sun, F., Liu, B., and Kuang, Y. (2008b). Electrochemically induced deposition method to prepare γ-MnO_2/multi-walled carbon nanotube composites as electrode material in supercapacitors. *Mater. Res. Bull.* 43, 2085–2091. doi: 10.1016/j.materresbull.2007.09.015

Faraji, S., and Ani, F. N. (2015). The development supercapacitor from activated carbon by electroless plating-A review. *Renew. Sust. Energ. Rev.* 42, 823–834. doi: 10.1016/j.rser.2014.10.068

Fujiwara, A., Ishii, K., Suematsu, H., Kataura, H., Maniwa, Y., Suzuki, S., et al. (2001). Gas adsorption in the inside and outside of single-walled carbon nanotubes. *Chem. Phys. Lett*. 336, 205–211. doi: 10.1016/S0009-2614(01)00111-7

Gao, F., Tang, X., Yi, H., Chao, C., Na, L., Li, J., et al. (2017). *In-situ* DRIFTS for the mechanistic studies of NO oxidation over α-MnO_2, β-MnO_2 and γ-MnO_2 catalysts. *Chem. Eng. J.* 322, 525–537. doi: 10.1016/j.cej.2017.04.006

Ge, J., Yao, H. B., Hu, W., Yu, X. F., Yan, Y. X., Mao, L. B., et al. (2013). Facile dip coating processed graphene/MnO_2 nanostructured sponges as high performance supercapacitor electrodes. *Nano Energy* 2, 505–513. doi: 10.1016/j.nanoen.2012.12.002

Geim, A. K., and Novoselov, K. S. (2007). The rise of graphene. *Nat. Mater.* 6, 183–191. doi: 10.1038/nmat1849

Hao, P., Zhao, Z., Tian, J., Li, H., Sang, Y., Yu, G., et al. (2014). Hierarchical porous carbon aerogel derived from bagasse for high performance supercapacitor electrode. *Nanoscale* 6, 12120–12129. doi: 10.1039/C4NR03574G

He, Y., Chen, W., Gao, C., Zhou, J., Li, X., and Xie, E. (2013). An overview of carbon materials for flexible electrochemical capacitors. *Nanoscale* 5, 8799–8820. doi: 10.1039/c3nr02157b

Hu, Y., Wu, Y., and Wang, J. (2018). Manganese-oxide-based electrode materials for energy storage applications: how close are we to the theoretical capacitance? *Adv. Mater.* 30:e1802569. doi: 10.1002/adma.201802569

Huang, J., Dai, Y., Singewald, K., Liu, C. C., Saxena, S., and Zhang, H. (2019). Effects of MnO_2 of different structures on activation of peroxymonosulfate for bisphenol A degradation under acidic conditions. *Chem. Eng. J.* 370, 906–915. doi: 10.1016/j.cej.2019.03.238

Huang, X., Yin, Z., Wu, S., Qi, X., He, Q., Zhang, Q., et al. (2011). Graphene-based materials: synthesis, characterization, properties, and applications. *Small* 7, 1876–1902. doi: 10.1002/smll.201002009

Jadhav, S., Kalubarme, R. S., Terashima, C., Kale, B. B., Godbole, V., Fujishima, A., et al. (2019). Manganese dioxide/reduced graphene oxide composite an electrode material for high-performance solid state supercapacitor. *Electrochim. Acta* 299, 34–44. doi: 10.1016/j.electacta.2018.12.182

Jeong, J. H., Park, J. W., Lee, D. W., Baughman, R. H., and Kim, S. J. (2019). Electrodeposition of α-MnO_2/γ-MnO_2 on carbon nanotube for yarn supercapacitor. *Sci. Rep.* 9:11271. doi: 10.1038/s41598-019-47744-x

Kannappan, S., Hao, Y., Kaliyappan, K., Manian, R. K., Pandian, A. S., Lee, Y. S., et al. (2018). Thiolated-graphene-based supercapacitors with high energy density and stable cycling performance. *Carbon* 134, 326–333. doi: 10.1016/j.carbon.2018.02.036

Kaushal, I., Sharma, A. K., Saharan, P., Sadasivuni, K. K., and Duhan, S. (2019). Superior architecture and electrochemical performance of MnO_2 doped PANI/CNT graphene fastened composite. *J. Porous Mat.* 26, 1287–1296. doi: 10.1007/s10934-019-00728-8

Kim, C. H., Yang, C. M., Kim, Y. A., and Yang, K. S. (2019). Pore engineering of nanoporous carbon nanofibers toward enhanced supercapacitor performance. *Appl. Surf. Sci.* 497:143693. doi: 10.1016/j.apsusc.2019.143693

Kim, M., Hwang, Y., Min, K., and Kim, J. (2013). Introduction of MnO_2 nanoneedles to activated carbon to fabricate high-performance electrodes as electrochemical supercapacitors. *Electrochim. Acta* 113, 322–331. doi: 10.1016/j.electacta.2013.09.058

Kim, S., Lee, J., Kang, J. S., Jo, K., Kim, S., Sung, Y. E., et al. (2015). Lithium recovery from brine using a k-MnO_2/activated carbon hybrid supercapacitor system. *Chemosphere* 125, 50–56. doi: 10.1016/j.chemosphere.2015.01.024

Kong, S., Jin, B., Quan, X., Zhang, G., Guo, X., Zhu, Q., et al. (2019). MnO_2 nanosheets decorated porous active carbon derived from wheat bran for high-performance asymmetric supercapacitor. *J. Electroanal. Chem.* 850:113412. doi: 10.1016/j.jelechem.2019.113412

Le, Q., Huang, M., Wang, T., Liu, X., Sun, L., Guo, X., et al. (2019). Biotemplate derived three dimensional nitrogen doped graphene@MnO_2 as bifunctional material for supercapacitor and oxygen reduction reaction catalyst. *J. Colloid Interface Sci.* 544, 155–163. doi: 10.1016/j.jcis.2019.02.089

Lee, H., and Goodenough, J. B. (1999). Supercapacitor behavior with KCl electrolyte. *J. Solid State Chem.* 144, 220–223. doi: 10.1006/jssc.1998.8128

Lei, Z., Shi, F., and Lu, L. (2012). Incorporation of MnO_2-coated carbon nanotubes between graphene sheets as supercapacitor electrode. *ACS Appl. Mater. Interfaces* 4, 1058–1064. doi: 10.1021/am2016848

Li, F., Wang, J., Liu, L., Qu, J., Li, Y., Bandari, V. K., et al. (2019). Self-assembled flexible and integratable 3D microtubular asymmetric supercapacitors. *Adv. Sci.* 6:1901051. doi: 10.1002/advs.201901051

Li, H., Liang, J., Li, H., Zheng, X., Tao, Y., Huang, Z. H., et al. (2019). Activated carbon fibers with manganese dioxide coating for flexible fiber supercapacitors with high capacitive performance. *J. Energy Chem.* 31, 95–100. doi: 10.1016/j.jechem.2018.05.008

Li, L., Chen, L., Qian, W., Xie, F., and Dong, C. (2019). Directly grown multiwall carbon nanotube and hydrothermal MnO_2 composite for high-performance supercapacitor electrodes. *Nanomaterials* 9:703. doi: 10.3390/nano9050703

Li, M., Chen, Q., and Zhan, H. (2017). Ultrathin manganese dioxide nanosheets grown on partially unzipped nitrogen-doped carbon nanotubes for high-performance asymmetric supercapacitors. *J. Alloys Compd.* 702, 236–243. doi: 10.1016/j.jallcom.2017.01.244

Li, Q., Lu, X. F., Xu, H., Tong, Y. X., and Li, G. R. (2014). Carbon/MnO_2 double-walled nanotube arrays with fast ion and electron transmission for high-performance supercapacitors. *ACS Appl. Mater. Interfaces* 6, 2726–2733. doi: 10.1021/am405271q

Li, W. S., Chang, M. L., Chuang, K. C., Li, Y. S., Luo, J. D., and Cheng, H. C. (2019). Electrochemical properties of CNT/MnO_2 hybrid nanostructure with low-temperature hydrothermal synthesis as high-performance supercapacitor. *J. Electrochem. Soc.* 166, A2194–A2198. doi: 10.1149/2.1551910jes

Li, Z., Liu, Z., Li, D., Li, B., Li, Q., Huang, Y., et al. (2014). Facile synthesis of α-MnO_2 nanowires/spherical activated carbon composite for supercapacitor application in aqueous neutral electrolyte. *J. Mater. Sci.-Mater. Electron.* 26, 353–359. doi: 10.1007/s10854-014-2407-z

Liang, M., and Xin, H. (2015). Microwave to terahertz: characterization of carbon-based nanomaterials. *IEEE Microw. Mag.* 15, 40–51. doi: 10.1109/MMM.2013.2288708

Liu, R., Liu, E., Ding, R., Liu, K., Teng, Y., Luo, Z., et al. (2015). Facile *in-situ* redox synthesis of hierarchical porous activated carbon@MnO_2 core/shell nanocomposite for supercapacitors. *Ceram. Int.* 41, 12734–12741. doi: 10.1016/j.ceramint.2015.06.106

Liu, Y., Zhou, X., Liu, R., Li, X., Bai, Y., and Yuan, G. (2017). Preparation of three-dimensional compressible MnO_2@carbon nanotube sponges with enhanced supercapacitor performance. *N. J. Chem.* 41, 14906–14913. doi: 10.1039/C7NJ03323K

López Ch, L. T., Chejne, F., and Bhatia, S. K. (2015). Effect of activating agents: flue gas and CO_2 on the preparation of activated carbon for methane storage. *Energy Fuels* 29, 6296–6305. doi: 10.1021/acs.energyfuels.5b01438

Lu, S., Guo, K. K., Xie, Y., and Ning, J. (2018). Ordered mesoporous carbons loading on sulfonated graphene by multi-components Co-assembly for supercapacitor applications. *Energy Technol.* 6, 1975–1985. doi: 10.1002/ente.201800116

Lu, Z., Raad, R., Safaei, F., Xi, J., Liu, Z., and Foroughi, J. (2019). Carbon nanotube based fiber supercapacitor as wearable energy storage. *Front. Mater.* 6:138. doi: 10.3389/fmats.2019.00138

Luo, S., Xie, L., Han, F., Wei, W., Huang, Y., Zhang, H., et al. (2019). Nanoscale parallel circuitry based on interpenetrating conductive sssembly for flexible and high-power zinc ion battery. *Adv. Funct. Mater.* 29:1901336. doi: 10.1002/adfm.201901336

Lv, P., Zhang, P., Feng, Y., Li, Y., and Feng, W. (2012). High-performance electrochemical capacitors using electrodeposited MnO_2 on carbon nanotube array grown on carbon fabric. *Electrochim. Acta* 78, 515–523. doi: 10.1016/j.electacta.2012.06.085

Ma, X., Kolla, P., Zhao, Y., Smirnova, A. L., and Fong, H. (2016). Electrospun lignin-derived carbon nanofiber mats surface-decorated with MnO_2 nanowhiskers as binder-free supercapacitor electrodes with high performance. *J. Power Sources* 325, 541–548. doi: 10.1016/j.jpowsour.2016.06.073

Malak-Polaczyk, A., Matei-Ghimbeu, C., Vix-Guterl, C., and Frackowiak, E. (2010). Carbon/λ-MnO_2 composites for supercapacitor electrodes. *J. Solid State Chem.* 183, 969–974. doi: 10.1016/j.jssc.2010.02.015

Nataraj, S. K., Song, Q., Al-Muhtaseb, S. A., Dutton, S. E., Zhang, Q., and Sivaniah, E. (2013). Thin, flexible supercapacitors made from carbon nanofiber

electrodes decorated at room temperature with manganese oxide nanosheets. *J. Nanomater.* 2013, 1–6. doi: 10.1155/2013/272093

Novoselov, K. S., Geim, A. K., Morozov, S. V., Jiang, D., Zhang, Y., Dubonos, S. V., et al. (2004). Electric field effect in atomically thin carbon films. *Science* 306, 666–669. doi: 10.1126/science.1102896

Palchoudhury, S., Ramasamy, K., Gupta, R. K., and Gupta, A. (2019). Flexible supercapacitors: a materials perspective. *Front. Mater.* 5:83. doi: 10.3389/fmats.2018.00083

Peng, S., Li, L., Yoong, J. L. K., Tian, L., Srinivasan, M., Adams, S., et al. (2016). Electrospun carbon nanofibers and their hybrid composites as advanced materials for energy conversion and storage. *Nano Energy* 22, 361–395. doi: 10.1016/j.nanoen.2016.02.001

Prélot, B., Poinsignon, C., Thomas, F., Schouller, E., and Villiéras, F. (2003). Structural-chemical disorder of manganese dioxides: 1. Influence on surface properties at the solid-electrolyte interface. *J. Colloid Interface Sci.* 257, 77–84. doi: 10.1016/S0021-9797(02)00013-9

Qian, W., Xu, G., Fei, W., Chao, Z., Cui, C., Zhao, M., et al. (2012). Carbon nanotubes for supercapacitors:consideration of cost and chemical vapor deposition techniques. *J. Energy Chem.* 21, 233–240. doi: 10.1016/S1003-9953(11)60358-7

Ramesh, S., Kim, H. S., Haldorai, Y., Han, Y. K., and Kim, J. H. (2017). Fabrication of nanostructured MnO_2/carbon nanotube composite from 3D precursor complex for high-performance supercapacitor. *Mater. Lett.* 196, 132–136. doi: 10.1016/j.matlet.2017.03.044

Ren, S., Rong, P., and Yu, Q. (2018). Preparations, properties and applications of graphene in functional devices: a concise review. *Ceram. Int.* 44, 11940–11955. doi: 10.1016/j.ceramint.2018.04.089

Saha, S., Maji, P., Pethsangave, D. A., Roy, A., Ray, A., Some, S., et al. (2019). Effect of morphological ordering on the electrochemical performance of MnO_2-graphene oxide composite. *Electrochim. Acta* 317, 199–210. doi: 10.1016/j.electacta.2019.05.148

Salinas-Torres, D., Ruiz-Rosas, R., Morallón, E., and Cazorla-Amorós, D. (2019). Strategies to enhance the performance of electrochemical capacitors based on carbon materials. *Front. Mater.* 6:115. doi: 10.3389/fmats.2019.00115

Seung Woo, L., Junhyung, K., Shuo, C., Hammond, P. T., and Yang, S. H. (2010). Carbon nanotube/manganese oxide ultrathin film electrodes for electrochemical capacitors. *ACS Nano* 4, 3889–3896. doi: 10.1021/nn100681d

Shen, H., Zhang, Y., Song, X., Liu, Y., Wang, H., Duan, H., et al. (2019). Facile hydrothermal synthesis of actiniaria-shaped α-MnO_2/activated carbon and its electrochemical performances of supercapacitor. *J. Alloys Compd.* 770, 926–933. doi: 10.1016/j.jallcom.2018.08.228

Sheng, L., Jiang, L., Wei, T., and Fan, Z. (2016). High volumetric energy density asymmetric supercapacitors based on well-balanced graphene and graphene-MnO_2 electrodes with densely stacked architectures. *Small* 12, 5217–5227. doi: 10.1002/smll.201601722

Shi, X., Zheng, S., Wu, Z. S., and Bao, X. (2018). Recent advances of graphene-based materials for high-performance and new-concept supercapacitors. *J. Energy Chem.* 27, 25–42. doi: 10.1016/j.jechem.2017.09.034

Snook, G. A., Kao, P., and Best, A. S. (2011). Conducting-polymer-based supercapacitor devices and electrodes. *J. Power Sources* 196, 1–12. doi: 10.1016/j.jpowsour.2010.06.084

Subagio, A., Hakim, Y. A., Ristiawan1, M. W., Kholil1, M. A., and Priyono (2019). Structural and morphological properties of MnO_2/MWCNT composite grown using the hydrothermal method for supercapacitor application. *J. Inorg. Organomet. Polym. Mater.* 14, 9936–9947. doi: 10.20964/2019.10.52

Subramanian, V., Zhu, H., and Wei, B. (2006). Synthesis and electrochemical characterizations of amorphous manganese oxide and single walled carbon nanotube composites as supercapacitor electrode materials. *Electrochem. Commun.* 8, 827–832. doi: 10.1016/j.elecom.2006.02.027

Sun, J., Cui, B., Chu, F., Yun, C., He, M., Li, L., et al. (2018). Printable Nanomaterials for the fabrication of high-performance supercapacitors. *Nanomaterials* 8:528. doi: 10.3390/nano8070528

Sun, P., Yi, H., Peng, T., Jing, Y., Wang, R., Wang, H., et al. (2017). Ultrathin MnO_2 nanoflakes deposited on carbon nanotube networks for symmetrical supercapacitors with enhanced performance. *J. Power Sources* 341, 27–35. doi: 10.1016/j.jpowsour.2016.11.112

Tajik, S., Dubal, D. P., Gomez-Romero, P., Yadegari, A., Rashidi, A., Nasernejad, B., et al. (2017). Nanostructured mixed transition metal oxides for high performance asymmetric supercapacitors: facile synthetic strategy. *Int. J. Hydrog. Energy* 42, 12384–12395. doi: 10.1016/j.ijhydene.2017.03.117

Trudeau, M. L. (2013). Advanced materials for energy storage. *MRS Bull.* 24, 23–26. doi: 10.1557/S0883769400053410

Wang, G. P., Zhang, L., and Zhang, J. J. (2012). A review of electrode materials for electrochemical supercapacitors. *Chem. Soc. Rev.* 41, 797–828. doi: 10.1039/C1CS15060J

Wang, H., Fu, Q., and Pan, C. (2019). Green mass synthesis of graphene oxide and its MnO_2 composite for high performance supercapacitor. *Electrochim. Acta* 312, 11–21. doi: 10.1016/j.electacta.2019.04.178

Wang, J. G., Kang, F., and Wei, B. (2015). Engineering of MnO_2-based nanocomposites for high-performance supercapacitors. *Prog. Mater. Sci.* 74, 51–124. doi: 10.1016/j.pmatsci.2015.04.003

Wang, J. G., Yang, Y., Huang, Z. H., and Kang, F. (2011). Coaxial carbon nanofibers/MnO_2 nanocomposites as freestanding electrodes for high-performance electrochemical capacitors. *Electrochim. Acta* 56, 9240–9247. doi: 10.1016/j.electacta.2011.07.140

Wang, J. G., Yang, Y., Huang, Z. H., and Kang, F. (2012). Synthesis and electrochemical performance of MnO_2/CNTs–embedded carbon nanofibers nanocomposites for supercapacitors. *Electrochim. Acta* 75, 213–219. doi: 10.1016/j.electacta.2012.04.088

Wang, J. G., Yang, Y., Huang, Z. H., and Kang, F. (2013). Effect of temperature on the pseudo-capacitive behavior of freestanding MnO_2@carbon nanofibers composites electrodes in mild electrolyte. *J. Power Sources* 224, 86–92. doi: 10.1016/j.jpowsour.2012.09.075

Wang, L., Huang, M., Chen, S., Kang, L., He, X., Lei, Z., et al. (2017). δ-MnO_2 nanofiber/single-walled carbon nanotube hybrid film for all-solid-state flexible supercapacitors with high performance. *J. Mater. Chem. A* 5, 19107–19115. doi: 10.1039/C7TA04712F

Wang, N., Wu, C., Li, J., Dong, G., and Guan, L. (2011). Binder-free manganese oxide/carbon nanomaterials thin film electrode for supercapacitors. *ACS Appl. Mater. Interfaces* 3, 4185–4189. doi: 10.1021/am201145k

Wang, T., Song, D., Zhao, H., Chen, J., Zhao, C., Chen, L., et al. (2015). Facilitated transport channels in carbon nanotube/carbon nanofiber hierarchical composites decorated with manganese dioxide for flexible supercapacitors. *J. Power Sources* 274, 709–717. doi: 10.1016/j.jpowsour.2014.10.102

Wang, X., Chen, L., Zhang, S., Chen, X., Li, Y., Liu, J., et al. (2019a). Compounding δ-MnO_2 with modified graphene nanosheets for highly stable asymmetric supercapacitors. *Colloid Surf.* 573, 57–66. doi: 10.1016/j.colsurfa.2019.04.040

Wang, X., Wu, D., Song, X., Du, W., Zhao, X., and Zhang, D. (2019b). Review on carbon/polyaniline hybrids: design and synthesis for supercapacitor. *Molecules* 24:2263. doi: 10.3390/molecules24122263

Wang, Y., and Igor, Z. (2009). Electrophoretic deposition of manganese dioxide-multiwalled carbon nanotube composites for electrochemical supercapacitors. *Langmuir* 25, 9684–9689. doi: 10.1021/la900937e

Wang, Y., Qu, Q., Gao, S., Tang, G., Liu, K., He, S., et al. (2019). Biomass derived carbon as binder-free electrode materials for supercapacitors. *Carbon* 155, 706–726. doi: 10.1016/j.carbon.2019.09.018

Wazir, A. H., and Kakakhel, L. (2009). Preparation and characterization of pitch-based carbon fibers. *N. Carbon Mater.* 24, 83–88. doi: 10.1016/S1872-5805(08)60039-6

Wei, H., Wang, X., Zhang, Y., Du, W., Sun, X., Jiang, F., et al. (2019). Facile synthesis of lotus seedpod-based 3D hollow porous activated carbon/manganese dioxide composite for supercapacitor electrode. *J. Electroanal. Chem.* 853:113561. doi: 10.1016/j.jelechem.2019.113561

Wei, L., Liu, J., and Zhao, D. (2016). Mesoporous materials for energy conversion and storage devices. *Nat. Rev. Mater.* 1:16023. doi: 10.1038/natrevmats.2016.23

Wei, W., Cui, X., Chen, W., and Ivey, D. G. (2011). Manganese oxide-based materials as electrochemical supercapacitor electrodes. *Chem. Soc. Rev.* 40, 1697–1721. doi: 10.1039/C0CS00127A

Wu, Z. S., Ren, W., Wang, D. W., Li, F., Liu, B., and Chen, H. M. (2010). High-energy MnO_2 nanowire/graphene and graphene asymmetric electrochemical capacitors. *ACS Nano* 4, 5835–5842. doi: 10.1021/nn101754k

Xiao, W., Xia, H., Fuh, J. Y. H., and Lu, L. (2010). Electrophoretic-deposited CNT/MnO_2 composites for high-power electrochemical

energy storage/conversion applications. *Phys. Scr.* 139:014008. doi: 10.1088/0031-8949/2010/T139/014008

Xie, S., Si, L., Cheng, F., and Lu, X. (2017). Recent advances for achieving high-performance carbon fiber materials for supercapacitors. *ChemElectroChem* 5, 571–582. doi: 10.1002/celc.201701020

Xie, X., Ni, C., Wang, B., Zhang, Y., Zhao, X., Liu, L., et al. (2019). Recent advances in hydrogen generation process via hydrolysis of Mg-based materials: a short review. *J. Alloys Compd.* 816:152634. doi: 10.1016/j.jallcom.2019.152634

Xie, Y., Yang, C., Chen, P., Yuan, D., and Guo, K. (2019). MnO_2-decorated hierarchical porous carbon composites for high-performance asymmetric supercapacitors. *J. Power Sources* 425, 1–9. doi: 10.1016/j.jpowsour.2019.03.122

Xin, L., and Wei, B. (2012). Facile synthesis and super capacitive behavior of SWNT/MnO_2 hybrid films. *Nano Energy* 1, 479–487. doi: 10.1016/j.nanoen.2012.02.011

Yan, J., Fan, Z., Wei, T., Cheng, J., Shao, B., Wang, K., et al. (2009). Carbon nanotube/MnO_2 composites synthesized by microwave-assisted method for supercapacitors with high power and energy densities. *J. Power Sources* 194, 1202–1207. doi: 10.1016/j.jpowsour.2009.06.006

Yan, J., Fan, Z., Wei, T., Qian, W., Zhang, M., and Wei, F. (2010). Fast and reversible surface redox reaction of graphene-MnO_2 composites as supercapacitor electrodes. *Carbon* 48, 3825–3833. doi: 10.1016/j.carbon.2010.06.047

Yang, Z., Zhang, J., Kintner-Meyer, M. C., Lu, X., Choi, D., Lemmon, J. P., et al. (2011). Electrochemical energy storage for green grid. *Chem. Rev.* 111, 3577–3613. doi: 10.1021/cr100290v

Yu, Z., Shang, J., Fu, W., Li, Z., and Cai, Y. (2018). A $sp^2 + sp^3$ hybridized carbon allotrope transformed from AB stacking graphyne and THD-graphene. *AIP Adv.* 8:015028. doi: 10.1063/1.5016387

Zhang, B., Kang, F., Tarascon, J. M., and Kim, J. K. (2015). Recent advances in electrospun carbon nanofibers and their application in electrochemical energy storage. *Prog. Mater. Sci.* 76, 319–380. doi: 10.1016/j.pmatsci.2015.08.002

Zhang, J., Sun, J., Shifa, T. A., Wang, D., Wu, X., and Cui, Y. (2019). Hierarchical MnO_2/activated carbon cloth electrode prepared by synchronized electrochemical activation and oxidation for flexible asymmetric supercapacitors. *Chem. Eng. J.* 372, 1047–1055. doi: 10.1016/j.cej.2019.04.202

Zhang, J., Wang, Y., Zang, J., Xin, G., Yuan, Y., and Qu, X. (2012). Electrophoretic deposition of MnO_2-coated carbon nanotubes on a graphite sheet as a flexible electrode for supercapacitors. *Carbon* 50, 5196–5202. doi: 10.1016/j.carbon.2012.07.002

Zhang, L. L., and Zhao, X. S. (2009). Carbon-based materials as supercapacitor electrodes. *Chem. Soc. Rev.* 38, 2520–2531. doi: 10.1039/b813846j

Zhang, Q., Wu, X., Zhang, Q., Yang, F., Dong, H., Sui, J., et al. (2019). One-step hydrothermal synthesis of MnO_2/graphene composite for electrochemical energy storage. *J. Electroanal. Chem.* 837, 108–115. doi: 10.1016/j.jelechem.2019.02.031

Zhang, Q. Z., Zhang, D., Miao, Z. C., Zhang, X. L., and Chou, S. L. (2018). Research progress in MnO_2-carbon based supercapacitor electrode materials. *Small* 14:1702883. doi: 10.1002/smll.201702883

Zhao, C., Ge, Z., Zhou, Y., Huang, Y., Wang, G., and Qian, X. (2017). Solar-assisting pyrolytically reclaimed carbon fiber and their hybrids of MnO_2/RCF for supercapacitor electrodes. *Carbon* 114, 230–241. doi: 10.1016/j.carbon.2016.12.025

Zhao, H., Han, W., Lan, W., Zhou, J., Zhang, Z., Fu, W., et al. (2016). Bubble Carbon-nanofibers decorated with MnO_2 nanosheets as high-performance supercapacitor electrode. *Electrochim. Acta* 222, 1931–1939. doi: 10.1016/j.electacta.2016.12.007

Zhi, M., Manivannan, A., Meng, F., and Wu, N. (2012). Highly conductive electrospun carbon nanofiber/MnO_2 coaxial nano-cables for high energy and power density supercapacitors. *J. Power Sources* 208, 345–353. doi: 10.1016/j.jpowsour.2012.02.048

Zhou, M., Gomez, J., Li, B., Jiang, Y. B., and Deng, S. (2017). Oil tea shell derived porous carbon with an extremely large specific surface area and modification with MnO_2 for high-performance supercapacitor electrodes. *Appl. Mater. Today* 7, 47–54. doi: 10.1016/j.apmt.2017.01.008

Zhu, G., He, Z., Chen, J., Zhao, J., Feng, X., Ma, Y., et al. (2014). Highly conductive three-dimensional MnO_2-carbon nanotube-graphene-Ni hybrid foam as a binder-free supercapacitor electrode. *Nanoscale* 6, 1079–1085. doi: 10.1039/C3NR04495E

Zhu, M., Wang, Z., Li, H., Yuan, X., and Zhi, C. (2018). Light-permeable, photoluminescent microbatteries embedded in the color filter of a screen. *Energy Environ. Sci.* 11, 2414–2422. doi: 10.1039/C8EE00590G

Conflict of Interest: The authors declare that the research was conducted in the absence of any commercial or financial relationships that could be construed as a potential conflict of interest.

NOMENCLATURE

Acronyms	Full name
AC	Activated carbon
B-CNFs	Bubble carbon nanofibers
CA	Carbon aerogel
CFRP	Carbon fiber-reinforced polymer
CNFs	Carbon nanofibers
CNTs	Carbon nanotubes
CVD	Chemical vapor deposition
ECNF	Electrospun carbon nanofiber
EDLCs	Electrochemical double-layer capacitors
EDS	Energy-dispersive X-ray spectroscopy
EES	Electrochemical energy storage
GO	Graphene oxide
MnO_2	Manganese dioxide
MRCF	MnO_2/regenerated carbon fiber
MWCNTs	Multi-walled carbon nanotubes
PAN	Polyacrylonitrile
PEG	Polyethylene glycol
PVA	Polyvinyl alcohol
RCF	Regenerated carbon fiber
rGO	Reduced graphene oxide
SDS	Sodium dodecyl sulfate
SWCNTs	Single-walled carbon nanotubes
ZnO NPs	ZnO nanoparticles

frontiers in Materials

ORIGINAL RESEARCH
published: 20 February 2020
doi: 10.3389/fmats.2020.00006

Bi Catalyzed CdS Nanowires With Temperature-Dependent Morphologies for Potential Applications in Solar Cells

*P. G. Zayas-Bazán[1], K. Gutierrez Z-B[1], O. de Melo[1,2,3], G. Santana[3], J. Sastré-Hernández[1], J. R. Aguilar-Hernández[1], M. Tufiño-Velázquez[1] and G. Contreras-Puente[1]**

[1] Escuela Superior de Física y Matemáticas, Instituto Politécnico Nacional, Mexico City, Mexico, [2] Physics Faculty, University of Havana, Colina Universitaria, Havana, Cuba, [3] Instituto de Investigación en Materiales, Universidad Nacional Autónoma de México, Cd. Universitaria, Coyoacán, Mexico

In this work, we present the preparation of CdS nanowires (CdS NWs) using the chemical vapor deposition technique and bismuth (Bi) nanoparticles as catalysts. The obtained nanowires were found to be in the hexagonal Greenockite structure according to XRD diffractograms and Raman spectroscopy measurements. Depending on the growth temperature, two kinds of morphologies were observed in SEM images. At low temperature (around 150°C), a high density and homogeneous population of thin and straight nanowires grown through the vapor–liquid–solid mechanism was observed. At higher temperature (around 270°C), thicker bunches of braided nanowires were observed. A quantitative analysis of the temperature-dependent photoluminescence spectra of the CdS NWs was carried out.

Keywords: solar cells, semiconductors, nanowires, photoluminescence, catalytic method

OPEN ACCESS

Edited by:
Federico Cesano, University of Turin, Italy

Reviewed by:
Oleg Dimitriev, National Academy of Sciences of Ukraine (NAN Ukraine), Ukraine
Aminur Rashid Chowdhury, University of Texas at Austin, United States

***Correspondence:**
G. Contreras-Puente
gscp1953@hotmail.com

Specialty section:
This article was submitted to Energy Materials, a section of the journal Frontiers in Materials

Received: *17 November 2019*
Accepted: *08 January 2020*
Published: *20 February 2020*

Citation:
Zayas-Bazán PG, Gutierrez Z-B K, de Melo O, Santana G, Sastré-Hernández J, Aguilar-Hernández JR, Tufiño-Velázquez M and Contreras-Puente G (2020) Bi Catalyzed CdS Nanowires With Temperature-Dependent Morphologies for Potential Applications in Solar Cells. Front. Mater. 7:6. doi: 10.3389/fmats.2020.00006

INTRODUCTION

Semiconductor nanowires have been the subject of intense research because of their novel properties and potential to be incorporated in advanced devices. They exhibit fast 1D growth rate with good crystalline quality, thus leading to advantages in efficiencies and costs (Cui and Lieber, 2001; Huang et al., 2001a; Lieber, 2003; Tang et al., 2011) in opto-electronic devices. CdS nanowires (CdS NWs) used as window material in p-n junction solar cells have the advantage of increasing the effective p-n interface, thus reducing the losses due to photo-carrier recombination and increasing light trapping as well (Liu et al., 2011). Taking this into account, we propose a solar cell with the configuration shown in **Figure 1**. On the other hand, this nanostructured CdS could be tested as windows material (or even as absorber) in hybrid solar cells, like Quantum Dots Dye Sensitized Solar Cell (QD-DSSC), CdTe, or colloidal CdSeTe. Our argument is supported by the fact that the space in between the nanowires could be embedded by an organic or inorganic photo-absorbent, or micro crystals (Wang et al., 2007; Lee et al., 2009; Grynko et al., 2015). Besides, the incorporation of CdS NWs could have the advantage of providing a direct path for the electrons to the anode, thus decreasing the recombination of photoexcited electrons with the electrolyte (Jasim, 2011; Pan et al., 2018) as a consequence of hopping between nanocrystals as occurs in DSSC cells. Other works carried out in recent years report the use of CdS NWs, combined with other materials such as ZnO, TiO_2, and Pt to produce photocatalytic hydrogen under visible light irradiation. In these cases, the CdS NWs showed an efficient charge separation, caused by fast diffusion of the generated

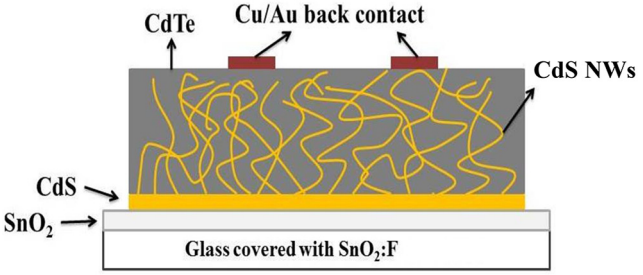

FIGURE 1 | Scheme of a prototype of solar cell using CdS nanowires.

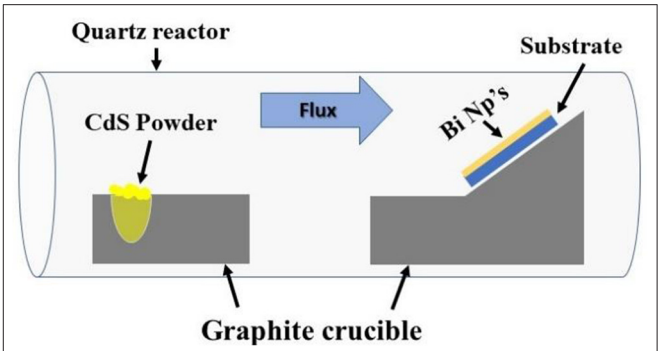

FIGURE 2 | Experimental setup used to grow CdS Nws. The source and substrate are located in two graphite crucibles inside a quartz reactor.

photoelectrons, becoming an excellent highly active photocatalyst for the production of hydrogen (Bao et al., 2006; Jang et al., 2008; Barpuzary et al., 2011).

Chemical vapor deposition (CVD) technique, assisted or not by metal catalysts (nanoparticles or very thin layers) is frequently used for preparing CdS NWs (Wang et al., 2002a; Ge and Li, 2004; Kwak et al., 2009). They are obtained by transport of the vapor species to the substrates covered with the catalyst. Different growth mechanisms have been found to be involved in the formation of nanostructures, the most characteristic being the vapor–liquid–solid (VLS) one (Givargizov, 1975; Kolasinski, 2006; Grynko et al., 2013). According to this mechanism, the metal catalyst forms a drop in which vapor species dissolve until oversaturation; then, the excess material precipitates and the nanowire forms with a drop at the tip.

Nanoparticles or very thin layers of gold are more frequently used as catalyst for the growth of nanowires (Huang et al., 2001b; Wang et al., 2002b; Fu et al., 2006; Ma et al., 2007; Zervos and Othonos, 2011). However, Au melting temperature or Au/Cd eutectic (1,064 and 500°C, respectively) are both quite high. In addition, Au has been found to form non-radiative recombination centers in CdS that degrade the optical properties of the nanowires (Schmidt et al., 2009). Bismuth appears to be a suitable catalyst candidate for the preparation of CdS NWs due to its low melting temperature of 271°C and because it forms a eutectic with Cd at 145°C (Keşlioglu et al., 2004). In the last few years, the preparation of nanostructures of several semiconductor materials using Bi as a catalytic metal has been reported (Wang et al., 2006; Ouyang et al., 2007; Sun and Buhro, 2008; Kwak et al., 2009, 2010). In these cases, the nanostructures were obtained using a thin layer of Bi; the solution–liquid–solid mechanism (SLS) has been verified. The use of a relatively large amount of chemicals in SLS growth, with the subsequent generation of by-products during the process, can work against the purity of the prepared material. In contrast, CVD CdS is characterized by a high degree of purity since only CdS vapor species and H_2 are present in the growth reactor.

In this work, we used Bi nanoparticles (NPs) to catalyze the growth of CdS NWs. Because of the low temperature of the Cd/Bi eutectic point, we obtained CdS NWs through the VLS mechanism in a CVD configuration at substrate temperatures as low as 145°C. After careful calibration experiments, the flux and the type of gas carrier were found to be determinant for obtaining the growth of nanowires in the VLS regime. Independent of the substrate temperature, two different kinds of morphologies were obtained, and their origin is discussed in relation with the growth parameters.

EXPERIMENTAL

Soda-lime glasses with a fluorine-doped tin oxide layer (TEC15, according to the manufacturer nomenclature, Pilkington, St Helens, United Kingdom) are covered using a triple-magnetron RF-Sputtering (model V3, Intercovamex, Mexico City, Mexico), with layers of sputtered undoped SnO_2 (35 nm) and CdS (60 nm) and were used as substrates. In a typical experiment, 10 μl of a suspension composed of 20 g of Bi nanoparticles (NPs) dispersed in 10 ml of methanol was spin-coated onto the substrate at 1,000 rpm for 30 s. Then, the substrate was heated at 70°C for 1 min, allowing the methanol to evaporate. CdS powder (Aldrich 99.999% purity) was located in a graphite boat in the highest temperature region (800°C) of a tubular furnace inside a quartz reactor. Initially, a nitrogen flow of 0.6 L/min was established to remove the air in the reactor. Afterwards, the system was flowed with forming gas (80% Ar/20% H_2) at atmospheric pressure at a rate of 0.1 L/min. Downstream, at a coldest region in the reactor (150 or 270°C for samples A and B, respectively), the substrate with the NPs was located (see **Figure 2**). The growth time was 10 min and, once the process was finished, the system was cooled down under N_2 flow.

Scanning electron microscopy (SEM) images and energy dispersed spectroscopy (EDS) were obtained with a JSM 7800F JEOL system (Kyoto, Japan) while TEM images were obtained with a JEM-ARM200CF microscope provided with a cold cathode electron gun (Cold Field Emission Gun, CFEG), a spherical aberration corrector CEOS. The x-ray diffractograms were taken with an X'Pert PRO PANalytical diffractometer (Almelo, Netherlands) in fixed grazing incidence angle at room temperature and using Cu-Kα radiation ($\lambda = 1.54056$ Å). Raman spectra were measured with a Labram HR800 (Horiba Jobin Yvon, Kyoto, Japan) equipment, with an excitation line of 633 nm with an output power of 10.7 μW and objective magnification of 50×. Photoluminescence (PL) spectra were obtained using a He–Cd laser with an excitation wavelength of 442 nm and output power of 16 mW at room temperature. A double monochromator SPEX-1403 was used to obtain the photoluminescence spectra and the signal was detected using a thermoelectrically cooled

photomultiplier RCA-C31034 that is coupled to a photon counter equipment. In other experiments, a 325-nm laser line was used as the excitation source and the sample emission was focused into a photomultiplier tube of an Acton SpectraPro 2500i spectrograph. All the spectra were corrected taking into account the spectral response of the system. No significant differences were found in the spectra that were taken with the two configurations.

RESULTS AND DISCUSSION

A secondary electron SEM image of the obtained nanowire forest observed in a typical region of the surface of the sample A is shown in **Figure 3A**. A high density and a homogeneous population of thin nanowires with straight morphology can be appreciated. In **Figure 4**, a low-resolution TEM image displays a nanowire around 50 nm thick, with a dark sphere at the tip, which we associate to a bismuth nanoparticle. At the left inset in **Figure 4**, a high-resolution TEM image allows one to appreciate the crystalline planes in the body of the nanowire. The measurement of the inter-planar distance of these planes indicates that the axial direction of the nanowire coincides with [100] crystalline direction, as frequently observed in CdS NWs (Fu et al., 2006). The nanowires are single crystals as can be observed in the corresponding Fast Fourier Transform in the right inset in **Figure 4**, which can be indexed as the [001] zone axis; thus, the nanowires grow with the [001] direction normal to the axis of the nanowires. **Figure 3B** shows an image obtained with the backscattered electron detector, which allows one to better resolve differences in chemical compositions. In this figure, small bright spots with spherical shape distributed throughout the sample surface and located at the tip of the nanowires can be appreciated. These bright spots were identified as Bi according to the EDS spectrum shown in the inset of **Figure 3B**. This is an indication that the VLS mechanism is responsible for the formation of the nanowires.

The nanowire morphology obtained at a higher substrate temperature of 270°C (sample B), is shown in **Figure 3C**. In this case, bunches of braided nanowires with diameters ranging between 100 and 300 nm are observed. Also, the nanowire density is smaller than that in sample A.

These morphology differences can be explained considering that, at the higher temperature of the sample B (near to the fusion point of Bi), several Bi nanoparticles can coalesce, forming larger particles and leading to the formation of more than one nanowire in the same catalyst particle.

In the x-ray diffractograms for both samples, shown in **Figure 5A**, the characteristic reflections of the CdS with Greenockite phase (PDF 41–1,049) are observed. The peaks marked with "+" come from the SnO_2 substrate layer with tetragonal phase (PDF 41–1,445), and the peaks around 40° correspond to the planes (104) and (110) of Bi with rhombohedral phase (PDF 44–1,246). The diffractogram of the substrate CdS layer was found to be very weak (see **Figure S1** in the supplementary material), which indicates that the main contribution of the diffractograms presented here comes from the CdS NWs.

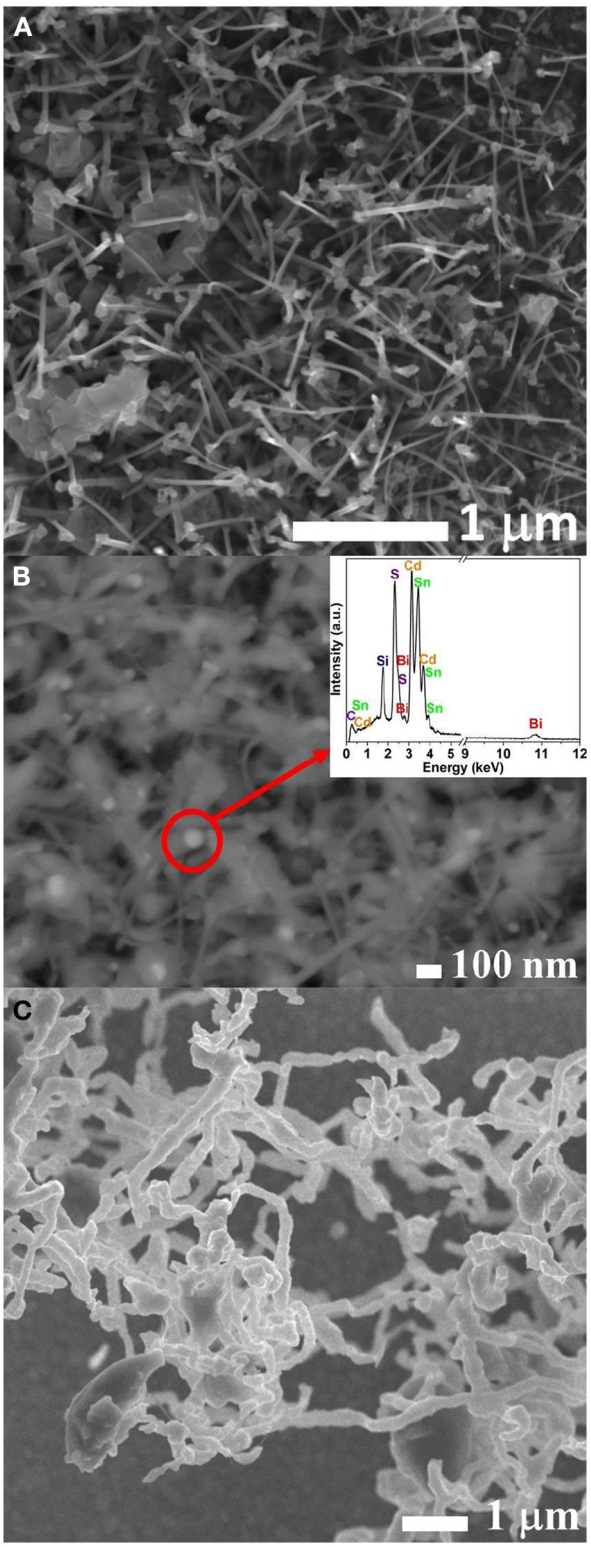

FIGURE 3 | (A) SEM images of the sample A showing a high density of CdS nanowires. **(B)** Backscattered electron image showing bright spots at the tip of the nanowires. In the inset, an EDS spectrum confirms the presence of Bi in the bright spots. **(C)** SEM images of the nanowires obtained in sample B with a substrate temperature of 270°C.

Raman spectra of samples A and B are shown in **Figure 5B** together with the spectrum of a target fabricated with the Bi nanoparticles. In the spectra, the characteristic emission of the longitudinal optical LO-mode of CdS with Greenockite phase at 300 cm^{-1} and its 2LO-first harmonic at 600 cm^{-1} can be appreciated (Nusimovici and Birman, 1967). This result confirms the indication of the x-ray diffraction analysis. The other emissions observed in the Raman spectrum of the nanowires are associated with the Bi nanoparticles: the peaks located around 97 and 185 cm^{-1} are the first- and second-order Raman scattering mode of bismuth in the rhombohedral structure (Lannin et al., 1975). The increase of the background intensity with increasing energy is associated to the fluorescence in the SnO_2 layer of the substrate (similar background was measured in samples with only the SnO_2 layer).

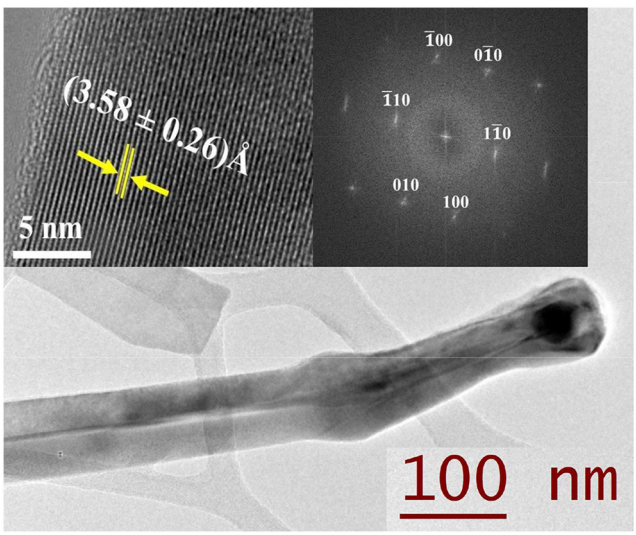

FIGURE 4 | TEM image of the nanowires at low resolution. The left inset shows a high-resolution TEM image in which it is possible to observe the crystalline planes. The Fast Fourier Transform is shown in the right inset, which can be indexed as the [001] zone axis.

Photoluminescence spectra for the samples at low temperature (12–20 K) and room temperature (300 K) are shown in **Figure 6**. The samples showed an intense and bright luminescence with a narrow peak around 2.5 eV at low temperature, which follows the behavior of near band gap emissions (NBE) (Yang et al., 2012). In fact, deconvolution of these spectra was carried out and the behavior of the intense peak with temperature was found to follow the Varshni equation $\left(E_g(T) = E_g(0) - \frac{\alpha T^2}{T+\beta}\right)$ as it can be observed in the insets, where E_0 is the low-temperature band gap and α and β are the Varshni constants (Varshni, 1967) (The complete set of spectra at different temperatures and the deconvolution of the spectra at low temperature can be seen in **Figure S2** and **Figure S3** in the supplementary material, respectively.). Following previous reports (Thomas and Hopfield, 1962), we assigned this peak to the emission of a bound exciton to a neutral acceptor (I_1). The NBE intense peak of sample B is much narrower than that detected for sample A and is slightly shifted. This suggests that the NBE luminescence of sample A is composed of other contributions probably related with defects. This is confirmed by the presence of an intense and wide band centered at around 2.05 eV, known as the "yellow band (YB)" of CdS that has been ascribed to donor–acceptor pairs related to relatively deep centers associated with Cd interstitial (Cd_i) or S vacancies (S_v) (Hong et al., 2000; Chandran et al., 2011). The YB has a tail at

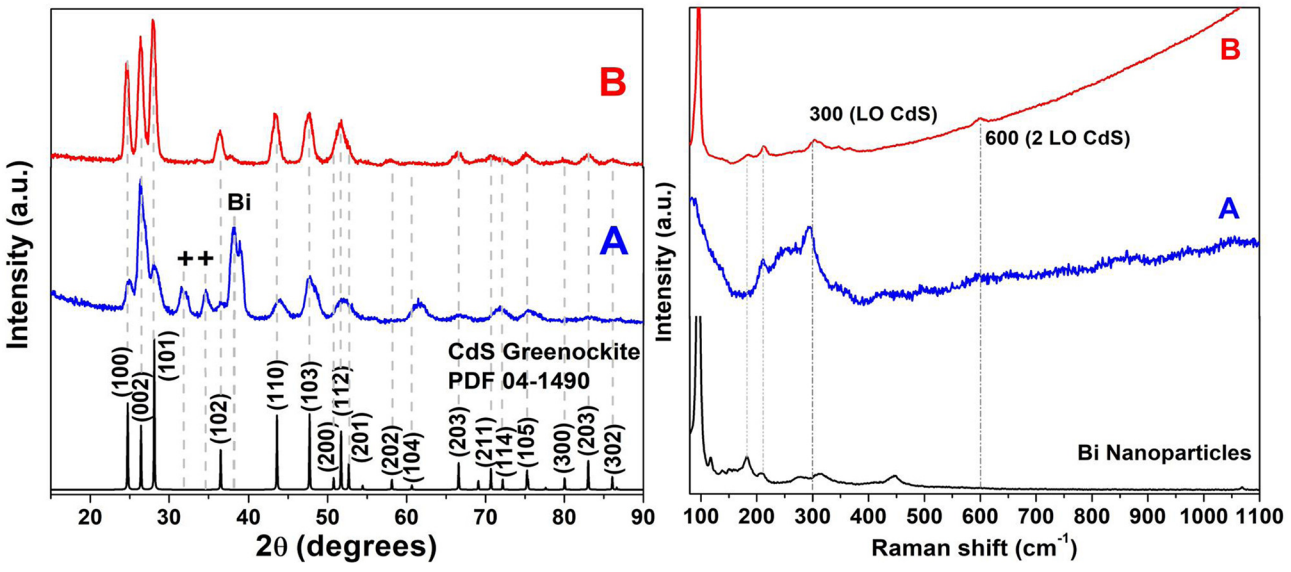

FIGURE 5 | (A) XRD diffractogram for samples A and B showing the characteristic peaks of the CdS with Greenockite phase (the peaks marked with + symbols come from the SnO_2 substrate). **(B)** Raman spectra of nanowires and nanoparticles. The vibrational modes 1LO and 2LO corresponding to CdS with Greenockite phase are observed.

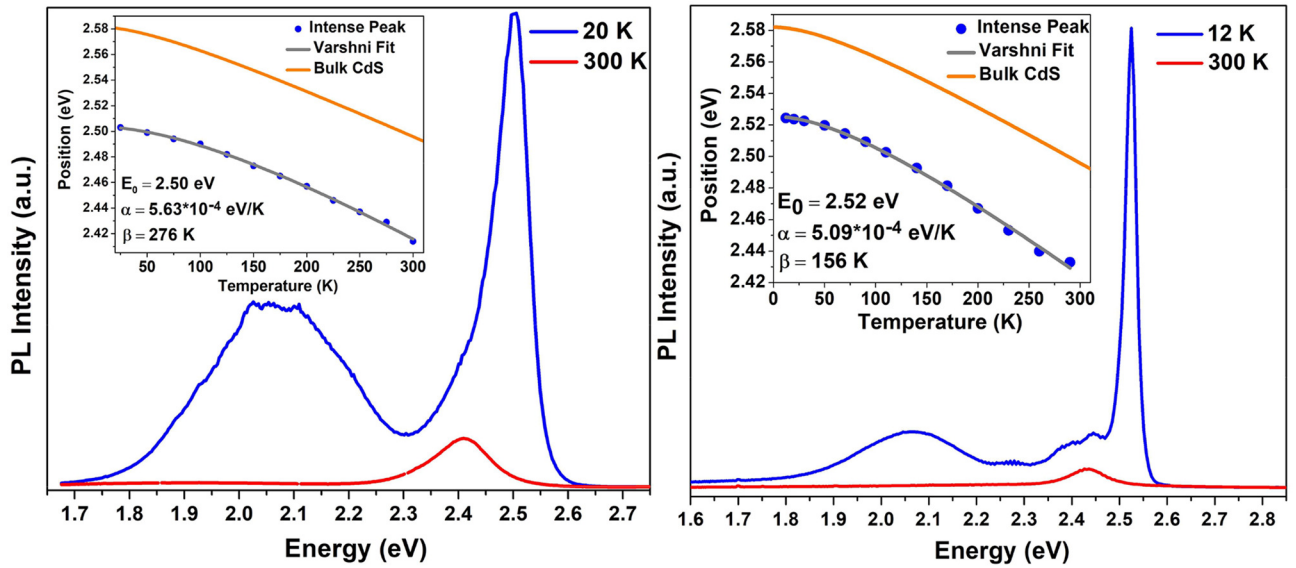

FIGURE 6 | Photoluminescence spectra at low and room temperature of **(A)** sample A and **(B)** sample B. In the inset, the fit of the NBE peak to the Varshni equation and the obtained parameters are presented.

near 1.9 eV, which can be ascribed to the red band (RB) usually related with surface defects (Shiraki et al., 1974). This combined defect band is more intense for sample A with respect to the NBE emission. At room temperature, spectra are dominated by the so-called "green band (GB)" with a high energy component peaking at near 2.4 eV, which has been related in the literature with a free to bound transition corresponding with the recombination of a free electron with a neutral acceptor (eA_0) (Colbow, 1966). The other two peaks present in the GB (resolved only in the spectra of sample B) having an energy separation near the CdS LO phonon (0.037 eV) (Marshall and Mitra, 1964) were considered as the typical phonon replicas of the 2.4-eV transition. According to the above PL analysis, CdS NWs in sample A seem to have a larger amount of defects. This is probably due to the larger surface-to-volume ratio (small diameter) for these nanowires. This can increase surface states as well as Cd vacancies. As a comparison, it is worth noting that the RT luminescence of CdS NWs grown by the SLS mechanism with Bi catalyst is dominated by the yellow band instead (Kwak et al., 2009).

It is important to consider that the bands, named YB, eA_0, or the unknown surface defect one, have charged state centers whose trapped charges can recombine and give place to the PL emission. The high density of trapped charge centers, originated from the non-crystalline nature of the material, is deleterious for the operation of II–VI solar cells. However, its presence is not completely unavoidable, and defects are always present in the materials, particularly when the surface-to-bulk ratio is high, like in NWs.

CONCLUSIONS

The CdS NWs were prepared using the catalytic method with Bi nanoparticles. X-ray diffractograms and Raman spectra verified the presence of CdS hexagonal phase. Depending on the growth temperature, the SEM images revealed two kinds of morphologies. At low temperature, a highly dense and homogeneous population of thin and straight nanowires with diameters <100 nm was obtained. The images obtained by backscattered electrons reveal bright spots with spherical shape at the nanowire tip, indicating a VLS mechanism. At higher temperatures, bunches of braided nanowires with diameters ranging between 100 and 300 nm were observed. These different morphologies can be explained as a consequence of the coalescence of Bi nanoparticles at higher substrate temperature. The study of the PL showed that thin nanowires obtained at low substrate temperature seem to have larger concentration of defects probably because of the large surface-to-volume ratio. CVD CdS NWs prepared with Bi nanoparticles could be used in CdS/CdTe third-generation solar cells with advantages with respect to gold-catalyzed ones. These CdS NWs have good crystalline quality, although defect bands could affect the efficiency of the solar cell. However, we consider it not significant because, at room temperature, this band is almost no appreciable.

DATA AVAILABILITY STATEMENT

The raw data supporting the conclusions of this article will be made available by the authors, without undue reservation, to any qualified researcher on request.

AUTHOR CONTRIBUTIONS

GC-P and OM contributed to the conception and design of the experiments and also to the analysis of the results. PZ-B and KGZ-B worked on the realization of the experiments, the characterization of the samples, and analysis of the results. GS,

JS-H, JA-H, and MT-V worked on the measurements of optical, structural, and morphological properties and also intervened in the analysis of the results. PG and OM wrote the original draft. All authors contributed to manuscript revision, read, and approved the submitted version.

ACKNOWLEDGMENTS

The authors gratefully acknowledge projects SIP-IPN-20190173, SIP-IPN-20196099, and COFAA-IPN for financial support in the paper publication and CONACyT support. OM thanks the support of UNAM/DGAPA/PREI program 2019. The experimental support of the CNMN-IPN in the realization of the presented works is recognized as well.

SUPPLEMENTARY MATERIAL

The Supplementary Material for this article can be found online at: https://www.frontiersin.org/articles/10.3389/fmats.2020.00006/full#supplementary-material

REFERENCES

Bao, N., Shen, L., Takata, T., Lu, D., and Domen, K. (2006). Highly ordered Pt-loaded CdS nanowire arrays for photocatalytic hydrogen production under visible light. *Chem. Lett.* 35, 318–319. doi: 10.1246/cl.2006.318

Barpuzary, D., Khan, Z., Vinothkumar, N., De, M., and Qureshi, M. (2011). Hierarchically grown urchinlike CdS@ ZnO and CdS@ Al2O3 heteroarrays for efficient visible-light-driven photocatalytic hydrogen generation. *J. Phys. Chem. C* 116, 150–156. doi: 10.1021/jp207452c

Chandran, A., Samuel, M., S., Koshy, J., and George, K. C. (2011). Correlated barrier hopping in CdS nanoparticles and nanowires. *J. Appl. Phys.* 109:084314. doi: 10.1063/1.3569744

Colbow, K. (1966). Free-to-bound and bound-to-bound transitions in CdS. *Phys. Rev.* 141:742. doi: 10.1103/PhysRev.141.742

Cui, Y., and Lieber, C. M. (2001). Functional nanoscale electronic devices assembled using silicon nanowire building blocks. *Science* 291, 851–853. doi: 10.1126/science.291.5505.851

Fu, X. L., Li, L. H., and Tang, W. H. (2006). Preparation and characterization of CdS/Si coaxial nanowires. *Solid State Commun.* 138, 139–142. doi: 10.1016/j.ssc.2006.02.015

Ge, J., and Li, Y. (2004). Selective atmospheric pressure chemical vapor deposition route to CdS arrays, nanowires, and nanocombs. *Adv. Funct. Mater.* 14, 157–162. doi: 10.1002/adfm.200305051

Givargizov, E. I. (1975). Fundamental aspects of VLS growth. *J. Cryst. Growth.* 31, 20–30. doi: 10.1016/0022-0248(75)90105-0

Grynko, D. A., Fedoryak, A. N., Dimitriev, O. P., Lin, A., Laghumavarapu, R. B., and Huffaker, D. L. (2013). Growth of CdS nanowire crystals: vapor–liquid–solid versus vapor–solid mechanisms. *Surf. Coat. Technol.* 230, 234–238. doi: 10.1016/j.surfcoat.2013.06.058

Grynko, D. O., Fedoryak, O. M., Smertenko, P. S., Ogurtsov, N. A., Pud, A. A., Noskov, Y. V., et al. (2015). Multifunctional role of nanostructured CdS interfacial layers in hybrid solar cells. *J. Nanosci. Nanotechnol.* 15, 752–758. doi: 10.1166/jnn.2015.9171

Hong, K. J., Jeong, T. S., Yoon, C. J., and Shin, Y. J. (2000). The optical properties of CdS crystal grown by the sublimation method. *J. Cryst. Growth.* 218, 19–26. doi: 10.1016/S0022-0248(00)00491-7

Huang, M. H., Mao, S., Feick, H., Yan, H., Wu, Y., Kind, H., et al. (2001a). Room-temperature ultraviolet nanowire nanolasers. *Science* 292, 1897–1899. doi: 10.1126/science.1060367

Huang, M. H., Wu, Y., Feick, H., Tran, N., Weber, E., and Yang, P. (2001b). Catalytic growth of zinc oxide nanowires by vapor transport. *Adv. Mater.* 13, 113–116. doi: 10.1002/1521-4095(200101)13:2<113::AID-ADMA113>3.0.CO;2-H

Jang, J. S., Kim, H. G., Joshi, U. A., Jang, J. W., and Lee, J. S. (2008). Fabrication of CdS nanowires decorated with TiO2 nanoparticles for photocatalytic hydrogen production under visible light irradiation. *Int. J. Hydr. Energy* 33, 5975–5980. doi: 10.1016/j.ijhydene.2008.07.105

Jasim, K. E. (2011). "Dye sensitized solar cells-working principles, challenges and opportunities," in *The Solar Cells-Dye Sensitized Devices,* ed L. A. Kosyachenko (Janeza Trdine; Rijeka: InTech), 172–204.

Keşlioglu, K., Erol, M., Maraşli, N., and Gündüz, M. (2004). Experimental determination of solid–liquid interfacial energy for solid Cd in Bi–Cd liquid solutions. *J. Alloy. Comp.* 385, 207–213. doi: 10.1016/j.jallcom.2004.05.010

Kolasinski, K. W. (2006). Catalytic growth of nanowires: vapor–liquid–solid, vapor–solid–solid, solution–liquid–solid and solid–liquid–solid growth. *Curr. Opin. Solid State Mater. Sci.* 10, 182–191. doi: 10.1016/j.cossms.2007.03.002

Kwak, W. C., Han, S. H., Kim, T. G., and Sung, Y. M. (2010). Electrodeposition of Cu (In, Ga) Se2 crystals on high-density CdS nanowire arrays for photovoltaic applications. *Cryst. Growth Des.* 10, 5297–5301. doi: 10.1021/cg101157a

Kwak, W. C., Kim, T. G., Lee, W., Han, S. H., and Sung, Y. M. (2009). Template-free liquid-phase synthesis of high-density CdS nanowire arrays on conductive glass. *J. Phys. Chem. C* 113, 1615–1619. doi: 10.1021/jp809365z

Lannin, J. S., Calleja, J. M., and Cardona, M. (1975). Second-order Raman scattering in the group-V b semimetals: Bi, Sb, and As. *Phys. Rev. B Condens. Matter.* 12:585. doi: 10.1103/PhysRevB.12.585

Lee, J. C., Lee, W., Han, S. H., Kim, T. G., and Sung, Y. M. (2009). Synthesis of hybrid solar cells using CdS nanowire array grown on conductive glass substrates. *Electrochem. Commun.* 11, 231–234. doi: 10.1016/j.elecom.2008.11.021

Lieber, C. M. (2003). Nanoscale science and technology: building a big future from small things. *MRS Bull.* 28, 486–491. doi: 10.1557/mrs2003.144

Liu, P., Singh, V. P., Jarro, C. A., and Rajaputra, S. (2011). Cadmium sulfide nanowires for the window semiconductor layer in thin film CdS–CdTe solar cells. *Nanotechnology* 22:145304. doi: 10.1088/0957-4484/22/14/145304

Ma, R. M., Wei, X. L., Dai, L., Huo, H. B., and Qin, G. G. (2007). Synthesis of CdS nanowire networks and their optical and electrical properties. *Nanotechnology* 18:205605. doi: 10.1088/0957-4484/18/20/205605

Marshall, R., and Mitra, S. S. (1964). Optically active phonon processes in CdS and ZnS. *Phys. Rev.* 134:A1019. doi: 10.1103/PhysRev.134.A1019

Nusimovici, M. A., and Birman, J. L. (1967). Lattice dynamics of wurtzite: CdS. *Phys. Rev.* 156:925. doi: 10.1103/PhysRev.156.925

Ouyang, L., Maher, K. N., Yu, C. L., McCarty, J., and Park, H. (2007). Catalyst-assisted solution– liquid– solid synthesis of CdS/CdSe nanorod heterostructures. *J. Am. Chem. Soc.* 129, 133–138. doi: 10.1021/ja066243u

Pan, Z., Rao, H., Mora-Seró, I., Bisquert, J., and Zhong, X. (2018). Quantum dot-sensitized solar cells. *Chem. Soc. Rev.* 47, 7659–7702. doi: 10.1039/C8CS00431E

Schmidt, V., Wittemann, J. V., Senz, S., and Gösele, U. (2009). Silicon nanowires: a review on aspects of their growth and their electrical properties. *Adv. Mater.* 21, 2681–2702. doi: 10.1002/adma.200803754

Shiraki, Y., Shimada, T., and Komatsubara, K. F. (1974). Optical studies of deep-center luminescence in CdS. *J. Appl Phys.* 45, 3554–3561. doi: 10.1063/1.1663817

Sun, J., and Buhro, W. E. (2008). The use of single-source precursors for the solution–liquid–solid growth of metal sulfide semiconductor nanowires. *Angew. Chem. Int. Ed.* 47, 3215–3218. doi: 10.1002/anie.200705142

Tang, J., Huo, Z., Brittman, S., Gao, H., and Yang, P. (2011). Solution-processed core–shell nanowires for efficient photovoltaic cells. *Nat. Nanotech.* 6:568. doi: 10.1038/nnano.2011.139

Thomas, D. G., and Hopfield, J. J. (1962). Optical properties of bound exciton complexes in cadmium sulfide. *Phys. Rev.* 128:2135. doi: 10.1103/PhysRev.128.2135

Varshni, Y. P. (1967). Temperature dependence of the energy gap in semiconductors. *Phys. A* 34, 149–154. doi: 10.1016/0031-8914(67)90062-6

Wang, F., Dong, A., Sun, J., Tang, R., Yu, H., and Buhro, W. E. (2006). Solution–liquid– solid growth of semiconductor nanowires. *Inorg. Chem.* 45, 7511–7521. doi: 10.1021/ic060498r

Wang, L., Liu, Y., Jiang, X., Qin, D., and Cao, Y. (2007). Enhancement of photovoltaic characteristics using a suitable solvent in hybrid polymer/multiarmed CdS nanorods solar cells. *J. Phys. Chem. C* 111, 9538–9542. doi: 10.1021/jp0715777

Wang, Y., Meng, G., Zhang, L., Liang, C., and Zhang, J. (2002a). Catalytic growth of large-scale single-crystal CdS nanowires by physical evaporation and their photoluminescence. *Chem. Mater.* 14, 1773–1777. doi: 10.1021/cm0115564

Wang, Y., Zhang, L., Liang, C., Wang, G., and Peng, X. (2002b). Catalytic growth and photoluminescence properties of semiconductor single-crystal ZnS nanowires. *Chem. Phys. Lett.* 357, 314–318. doi: 10.1016/S0009-2614(02)00530-4

Yang, Z. X., Zhong, W., Zhang, P., Xu, M. H., Deng, Y., Au, C. T., et al. (2012). Controllable synthesis, characterization and photoluminescence properties of morphology-tunable CdS nanomaterials generated in thermal evaporation processes. *Appl. Surf. Sci.* 258, 7343–7347. doi: 10.1016/j.apsusc.2012.04.010

Zervos, M., and Othonos, A. (2011). Gallium hydride vapor phase epitaxy of GaN nanowires. *Nanoscale Res. Lett.* 6:262. doi: 10.1186/1556-276X-6-262

Conflict of Interest: The authors declare that the research was conducted in the absence of any commercial or financial relationships that could be construed as a potential conflict of interest.

frontiers in Materials

ORIGINAL RESEARCH
published: 18 March 2020
doi: 10.3389/fmats.2020.00030

Three-Dimensional Graphene-Decorated Copper-Phosphide (Cu_3P@3DG) Heterostructure as an Effective Electrode for a Supercapacitor

Subodh Kumar[1†], S. K. Tarik Aziz[1†], Sushil Kumar[2†], Sk Riyajuddin[2], Gili Yaniv[3], Louisa Meshi[3], Gilbert D. Nessim[1]* and Kaushik Ghosh[2]**

[1] Department of Chemistry, Bar-Ilan Institute for Nanotechnology and Advanced Materials, Bar-Ilan University, Ramat Gan, Israel, [2] Institute of Nano Science & Technology, Mohali, India, [3] Department of Materials Engineering, Ben-Gurion University of the Negev, Beer-Sheva, Israel

Transition metal phosphides already emerged with great interest due to their energy storage capacitance, superior metalloid characteristics, and decent electrical conductivity. To achieve a commercially viable outcome, these electrodes are fabricated with interconnected carbonaceous materials. Herein, we have synthesized hexagonal copper phosphide (Cu_3P) platelets using chemical vapor deposition (CVD) and integrated it with highly conducting three-dimensional graphene (3DG), leading to a nanohybrid (Cu_3P@3DG) as a coulombic efficient supercapacitor. This nanohybrid has exhibited a specific capacitance (C_{sp}) of 1,095.85 F/g at 10 mV/s scan rate along with a cycling stability of 95% capacitive retention after 3,000 cycles at a current density of 8.97 A/g. The C_{sp} is almost four times higher and the stability is 1.2 times higher compared to the bare Cu_3P platelets. We have fabricated an asymmetric supercapacitor (ASC) using Cu_3P@3DG on graphite as cathode and activated carbon (AC) on graphite as anode (Cu_3P@3DG//AC) that has shown high specific capacity (108.78 F/g), energy density (8.23 Wh/kg), and power density (439.6 W/kg). Moreover, this ASC has exhibited an excellent life cycle (5,500 consecutive charge–discharge with 96% coulombic efficiency). Therefore, the proposed all-solid-state hybrid device can be considered as a route for next-generation high-performing energy storage devices.

Keywords: hexagonal copper phosphide platelets, chemical vapor deposition, red phosphorus, three-dimensional graphene (3DG), energy storage devices

OPEN ACCESS

Edited by:
Federico Cesano, University of Turin, Italy

Reviewed by:
David Aradilla, Commissariat à l'Energie Atomique et aux Energies Alternatives (CEA), France
Shuling Liu, Shaanxi University of Science and Technology, China

****Correspondence:***
Louisa Meshi
lmeshi.lm@gmail.com
Gilbert D. Nessim
Gilbert.Nessim@biu.ac.il
Kaushik Ghosh
kaushik@inst.ac.in

† These authors have contributed equally to this work

Specialty section:
This article was submitted to Energy Materials, a section of the journal Frontiers in Materials

Received: *28 October 2019*
Accepted: *28 January 2020*
Published: *18 March 2020*

Citation:
Kumar S, Aziz SKT, Kumar S, Riyajuddin S, Yaniv G, Meshi L, Nessim GD and Ghosh K (2020) Three-Dimensional Graphene-Decorated Copper-Phosphide (Cu_3P@3DG) Heterostructure as an Effective Electrode for a Supercapacitor. Front. Mater. 7:30. doi: 10.3389/fmats.2020.00030

INTRODUCTION

The relentless increase in energy demand and parallel steady reduction of fossil fuels drive the scientific and industrial need to develop renewable energy along with faster and compatible energy storage devices (Li et al., 2015, 2017; Zhang et al., 2019). Supercapacitors represent essential components that can bridge between stereotype capacitors and rechargeable batteries in terms of power and energy densities with a long cycle life (Wang et al., 2018; Cao et al., 2019;

Chen et al., 2019). In recent times, the synthesis of materials having semiconducting, metalloid, and energy storage properties has emerged at the forefront of research activities (Augustyn et al., 2014; López-Ortega et al., 2015; Sivula and Van De Krol, 2016). The transition metal phosphides are a fascinating class of materials because of their wide range of properties depending on their size and shape (Barry et al., 2008; Shao et al., 2017; Aziz and Islam, 2018). Metal phosphides have been tested and found to be active catalysts with their potential applications in electro-catalysis and photo-catalysis. In the last few years, several phosphides of nickel, cobalt, iron, molybdenum, tungsten, copper, and many more with different morphologies and crystallinity have been synthesized using different methods including phosphorization, electrodeposition, and ball milling (Brock et al., 2004; Henkes et al., 2007; Barry et al., 2008; Brock and Senevirathne, 2008; Wang et al., 2010). Metal phosphides with controlled nanostructures and elemental compositions have been designed and reported to provide significant enhancement in electrochemical activity (Wang et al., 2015a; Chen et al., 2016; Seo et al., 2016; Wu H. et al., 2016). Also, metal phosphides have metalloid properties and exhibit high specific capacitances (C_{sp}) and high volumetric and gravimetric capacities with lower intercalation potentials compared to commercial carbonaceous materials. Thus, they have attracted extensive interest to design novel electrode materials for supercapacitors rather than lithium-ion batteries (Li et al., 2017). Although transition metal hydroxides, metal oxides, and polymers (conducting) are commonly used electrode materials for lithium-ion batteries and pseudo-capacitors (Wang et al., 2015a,c; Zhu et al., 2015; Wu J. et al., 2016), however, these materials are kinetically slow for the fast electron transport and that invariably required for high-power density with moderate energy density (Li et al., 2017).

Copper phosphide (Cu_3P) is an air-stable, low-cost, environment-friendly material that exhibits high volumetric as well as comparable gravimetric capacity to that of graphite (Pfeiffer et al., 2004). Cu_3P have also been explored widely in the field of photo/electro-catalytic water splitting (Sun et al., 2015; Wei et al., 2016; Han et al., 2017; Hao et al., 2016). Recently, this material has been introduced in the energy storage sector to bridge the gap between electric double-layer capacitor (EDLC) and batteries (Chen et al., 2017; Zhang et al., 2019). It has been proved that the electrochemical activity of a material is strongly affected by its size, structure, and chemical composition. Cu_3P with different morphology and crystallinity have been synthesized and investigated for energy storage devices showing an improvement in electrochemical activities (Liu et al., 2012, 2016; Fan et al., 2016).

Carbonaceous matrices [e.g., graphene, carbon natotube (CNT), graphite, etc.] are simultaneously proved to be a promising choice of electrode material due to its high conductivity, large surface area, flexibility, and transparency which drags its attention toward large-scale applications in energy storage devices. Among various carbonaceous materials, three-dimensional graphene (3DG) is the promising choice as a backbone for electroactive materials for supercapacitor due to the random orientation of graphene flakes in three dimensions leading to the formation of micro/mesoporous structures (Mukherjee and Austeria, 2016; Singh et al., 2017; Xue et al., 2018). The 3DG provides high conductive channels for ion and electron transfer in charging–discharging cycles leading to a prominent improvement in overall capacitive performance of electroactive materials. Also, 3DG effectively minimizes the unwanted agglomeration of metal nanoparticles, thereby enhancing the chemical stability of the electroactive materials. In compliance to develop a novel approach for the synthesis of new hybrid materials (Kumar et al., 2017; Itzhak et al., 2018) herein, we report a facile, industrially scalable and easy method to produce a high yield of hexagonal Cu_3P by solid-state reaction at low temperature followed by the formation of nano-hybrid with 3DG matrix on graphite substrate. This nano-hybrid has demonstrated significantly high electrochemical performance at an optimized Cu_3P:3DG ratio with a tremendous C_{sp} of 1,095.85 F/g at a scan rate of 10 mV/s. The asymmetric device of Cu_3P@3DG electrode (positive) and activated carbon (AC) (negative electrodes) on graphite substrate reveals worthy performance in power densities, cycling stability, and excellent capacitive retention.

EXPERIMENTAL SECTION

Materials

The copper foil was purchased from Alfa-Aesar. Red phosphorus was purchased from Sigma Aldrich and was used without any further purification. A compressed cylinder tank of argon gas was procured from Gas Technologies with a purity of 99.999%. An atmospheric-pressure three-zone chemical vapor deposition (CVD) furnace, fitted with a quartz tube with an internal diameter of 22 mm, was used for the synthesis. The built-in furnace thermocouples measured the furnace temperatures, and the flow of argon was maintained using electronic mass flow controllers (MKS P4B with digital mass flows control unit model 247D). Graphite powder, H_2SO_4, ortho-phosphoric acid, potassium permanganate, H_2O_2 (30%), HCl, polyvinyl alcohol, potassium hydroxide, graphite sheet, nafion, and AC were purchased from TCI Chemicals India. Glassy carbon electrode was purchased from Sinsil International Pvt. Ltd.

Synthesis of Hexagonal Copper Phosphide Platelets

Usual techniques to synthesize transition metal phosphide is *via* plasma-enhanced CVD (PECVD) using PH_3 plasma (Liang et al., 2017) or multistep hydrothermal techniques (Zhou et al., 2015; Ding et al., 2019) *via* metal oxide/hydroxide intermediate followed by thermal annealing. Using the PECVD approach restricts the phosphorization on the material surface rather than bulk conversion. On the other hand, hydrothermal growth may lead to polycrystalline phosphides and oxide intermediates that are difficult to avoid, which may possibly be responsible for degrading the electrochemical performance.

CVD has been shown as a one-step process where hexagonal Cu_3P can be synthesized at an optimized temperature (Wei et al., 2016; Riyajuddin et al., 2019). In a typical experimental

procedure, 50 mg of red phosphorus is kept in a quartz boat and then covered with a 0.25-mm-thick copper foil (the native oxide layer on Cu-foil is removed by sonication with 4 M HCl for 20 min and washed with distilled water and isopropanol and then dried) as shown in **Supplementary Figure S1**. Initially, there is no direct physical contact between the red phosphorus and the copper foil, which is positioned above the red phosphorus-containing boat. This quartz boat is inserted in the quartz tube and positioned at the center of the furnace and heated at 450°C for 5 min under a flow of Ar (25 sccm) at an ambient pressure condition. In this process, phosphorus particles sublimate which are diffused into the copper and reacted with it to nucleate Cu_3P crystallites and then grow into hexagonal platelets. A layer of dark shining gray color is observed on the surface of the copper foil exposed to the red phosphorus environment.

The synthesis of Cu_3P experiments is performed by using the "fast-heat" technique in which the samples are initially positioned outside the heated zone of the furnace with a fan blowing on the exposed quartz tube surface to keep the sample at room temperature (Itzhak et al., 2018; Kumar et al., 2018). Once the set temperatures of furnaces have reached a stable value, then the quartz tube is shifted to position the sample in the growth zone to start the phosphorization process. Using this technique, the sample is placed immediately to the required growth temperature and avoided exposure during the ramping steps.

Synthesis of the Three-Dimensional Graphene Matrix

The modified hydrothermal reduction method has been used for the synthesis of 3DG on top of the graphite sheet as reported in our earlier work (Singh et al., 2017). Briefly, a piece of graphite sheet is dipped into 2 mg/ml aqueous dispersion of graphene oxide. This aqueous dispersed solution of the graphene along with graphite sheets is freeze-dried at −20°C for 12 h. After that, the solution temperature is allowed to reach room temperature followed by the addition of 0.6 ml of 2 M ascorbic acid to the graphene oxide aqueous dispersion, and the mixture is sealed in a Teflon-lined autoclave and heated in an oven at 120°C for 6 h. The as-grown material is thoroughly dried in a vacuum for the formation of a porous 3DG-coated graphite electrode.

Assembly of a Solid-State Asymmetric Supercapacitor Device

The ASC devices are assembled by utilizing the Cu_3P@3DG on graphite electrode as positive electrodes and AC on graphite as negative electrodes with polyvinyl alcohol (PVA)/KOH as gel electrolyte. The KOH/PVA gel electrolyte is prepared by mixing 5 g KOH and 4 g PVA in 50 ml distilled water with vigorous stirring at 90°C until the mixture solution becomes clear to form a semi gel state. Then, the prepared homogeneous 1 ml of each Cu_3P solution [∼0.3, 0.6, 0.91, 1.2, 1.5 mg/ml in Isopropyl alcohol (IPA)] is drop casted on top of 3DG-graphite electrodes (1 cm^2 × 1 cm^2) homogeneously and dried. Each electrode is covered with ∼1.1 mg of 3DG matrix. After that, the gel electrolyte is sandwiched between Cu_3P@3DG and AC electrodes, and the solid-state device is assembled successfully by moderate pressing to remove excess gel electrolytes and dried overnight. The active device area is 1 cm^2 × 1 cm^2, where longitudinally extended graphites are being used for making the connection for electrochemical measurement.

RESULTS AND DISCUSSION

In this work, hexagonal platelets were directly grown on copper foil by thermal annealing using a CVD system. A known amount of red phosphorus was kept in a quartz boat and covered with copper foil as shown in **Supplementary Figure S1**. Red phosphorus and copper foil were then heated at 450°C for 5 min under argon flow. A dark shiny gray color layer that formed on the red phosphorus-exposed side of the copper foil indicated the successful growth of Cu_3P. To investigate the effect of temperature on the morphology of Cu_3P on copper foil, the same experiment was repeated at 350, 450, 600, and 800°C. When the temperature was increased to 600°C, the material started losing its hexagonal morphology by condensing hexagonal platelets together. Upon further enhancement of the temperature up to 800°C, the entire hexagonal morphology was lost. On the other hand, lowering the temperature to 350°C, the hexagonal platelets did not nucleate, as shown in **Supplementary Figure S2**. These results confirmed that a specific temperature (450°C) was required for the growth of hexagonal platelets. HRSEM analysis of the synthesized Cu_3P revealed stacked platelets of hexagonal morphology with a lateral dimension in the range of micrometers and a thickness of a few nanometers, as shown in **Figure 1A**. HRSEM images and the corresponding elemental mapping patterns of Cu and P had demonstrated that the Cu and P elements were uniformly distributed on the hexagonal platelets (**Supplementary Figures S3c,d** in ESI). Transmission electron microscopy (TEM) analysis was performed for in-depth characterization. A low-magnification image, shown in **Figure 1B**, illustrated the nature of the hexagonal platelets. It was found that they consist of domains, although TEM sample preparation might influence the agglomeration (**Supplementary Figure S4**). The electron diffraction pattern taken from the agglomerate portion (**Supplementary Figure S4a**) was successfully indexed in terms of the hexagonal structure of the Cu_3P. It should be noted that the rings on the polycrystalline electron diffraction pattern indicated a large misorientation between the domains in the agglomerate. Using HRTEM, we studied small nano-sized domains constituting the agglomerate and did selected area electron diffraction (SAED), shown in **Figures 1C–D**. The SAED pattern was taken along [0001] orientation of one domain, and the corresponding HRTEM image is shown in **Supplementary Figure S4b**. In **Supplementary Figures S4b,c**, HRTEM image and SAED patterns were taken along [101 $^{-}$0] orientation of the domain fitting the atomic structure of Cu_3P, as reported by Olofsson (1972).

The phase content of the synthesized material was studied using X-ray diffraction (XRD) (**Figure 1E**). The XRD pattern exhibited strong, sharp peaks which were indexed in terms of hexagonal structure (P63cm) of the Cu_3P (JCPDS card no.

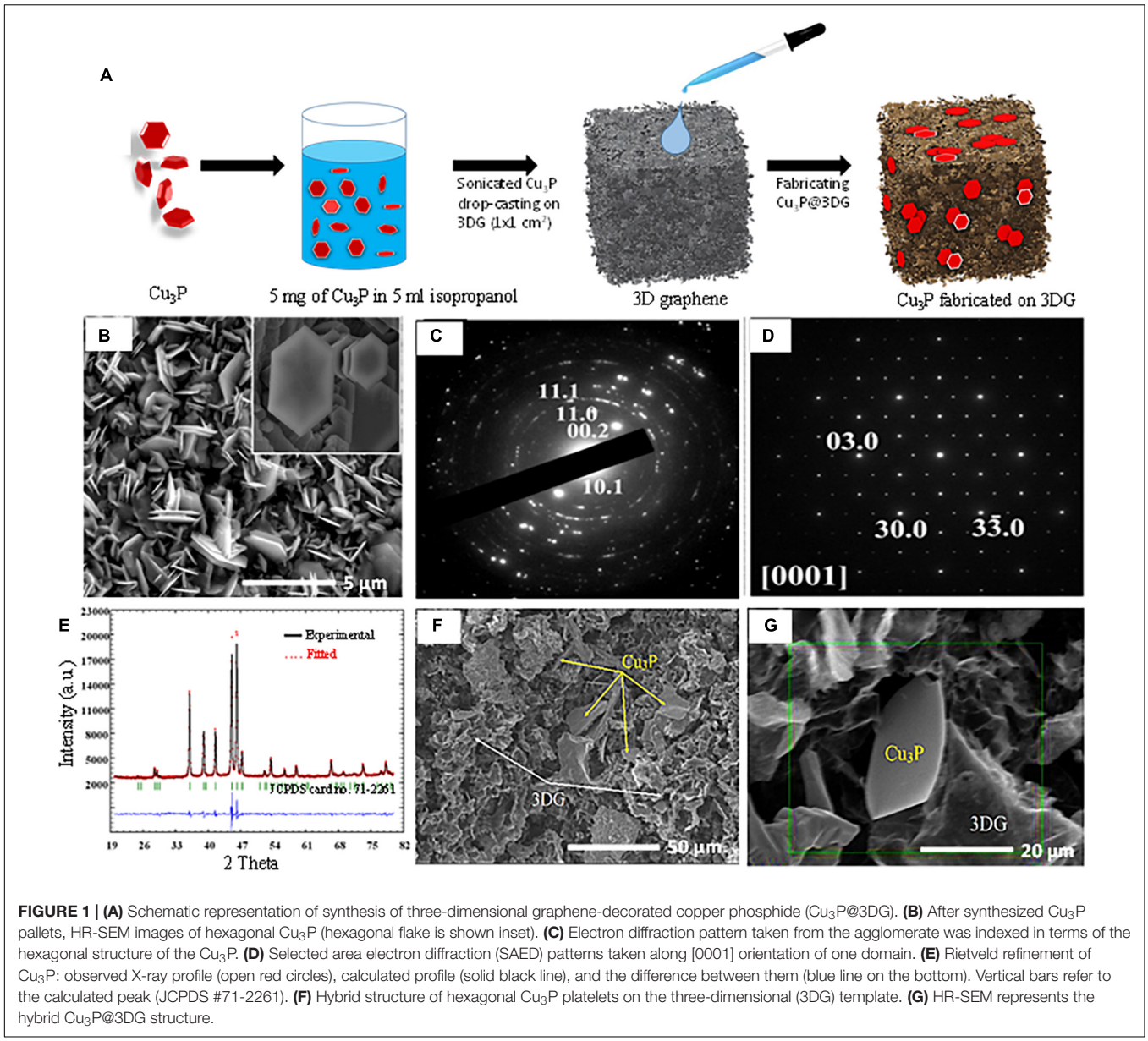

FIGURE 1 | (A) Schematic representation of synthesis of three-dimensional graphene-decorated copper phosphide (Cu_3P@3DG). **(B)** After synthesized Cu_3P pallets, HR-SEM images of hexagonal Cu_3P (hexagonal flake is shown inset). **(C)** Electron diffraction pattern taken from the agglomerate was indexed in terms of the hexagonal structure of the Cu_3P. **(D)** Selected area electron diffraction (SAED) patterns taken along [0001] orientation of one domain. **(E)** Rietveld refinement of Cu_3P: observed X-ray profile (open red circles), calculated profile (solid black line), and the difference between them (blue line on the bottom). Vertical bars refer to the calculated peak (JCPDS #71-2261). **(F)** Hybrid structure of hexagonal Cu_3P platelets on the three-dimensional (3DG) template. **(G)** HR-SEM represents the hybrid Cu_3P@3DG structure.

71-2261) (Hou et al., 2016). Rietveld refinement resulted in reliability factors: R_p = 2.3%, R_{wp} = 3.27%, R_{Bragg} = 1.05%, and R_{exp} = 1.73%. These low-reliability values excluded the possibility of the presence of impurities. It should be noted that atomic positions, occupancies, and thermal displacement parameters of the Cu_3P structure were not refined here, and the background was treated as linear. Lattice parameters were refined as a = 0.69673(1) nm and c = 0.71484(8) nm. The dependence of stoichiometry, temperature, and lattice parameters of the Cu_3P structure was discussed in the earlier report (Olofsson, 1972). Since the refined lattice parameters (i.e., a = 0.697, c = 0.7145 nm) were fitted well with reported parameters (Olofsson, 1972), thus the synthesized material was stoichiometric (or closely stoichiometric) as Cu_3P. To the best of our understanding, Rietveld refinement result of the as-synthesized sample was known to be the significant evidence for the formation of stoichiometric Cu_3P rather than the energy-dispersive X-ray spectroscopy (EDS) shown in **Supplementary Figure S3**. The presence of elements could be found in the EDS analysis. However, it was hard to estimate the stoichiometry *via* EDS since a large difference in atomic numbers of the constituents did not allow accurate standard in the EDS analysis. **Figure 1F** showed the formation of a hybrid porous structure made of hexagonal Cu_3P platelets along with 3DG. Careful observation indicated that the hexagonal Cu_3P platelets (shown by yellow arrows) were randomly scattered on the porous foamy 3DG architecture (shown by white arrows). A close-up view of these hybrid structures, shown in **Figure 1G**, revealed a single flake of Cu_3P trapped inside the 3DG matrix where a detailed EDS elemental mapping was performed to identify the

distribution of Cu, P, and C elements, respectively, shown in **Supplementary Figure S5**.

The X-ray photoelectron spectroscopy (XPS) analysis of Cu_3P elucidated the oxidation states and chemical interaction between Cu and red phosphorus (**Supplementary Figure S6**). The Cu, P, O, and C peaks appeared in the survey scan (shown in **Supplementary Figure S6a**). The presence of O1s peak indicated the superficial oxidation of Cu_3P, while the carbon peak was due to the background. The high-resolution XPS spectrum of Cu 2p (**Supplementary Figure S6b**) exhibited two peaks at 932.4 and 934.8 eV, which were attributed to phosphorized copper (Cu–P) and oxidized copper (Cu–O), respectively (Lin et al., 2016; Jin et al., 2017). **Supplementary Figure S6c** showed double peaks in the phosphorus region. The peak at 133.6 eV was due to the oxidized phosphorus in the form of phosphate (Li et al., 2016), and 129.7 eV was the binding energy of P in Cu_3P, which was lower than that of the binding energy of red phosphorus (130.2 eV), suggesting the conversion of copper to Cu_3P (Pfeiffer et al., 2005). The presence of Cu–O and POx was probably due to oxide layer formation on the surface of Cu_3P in ambient conditions.

To evaluate the as-grown nanomaterial as the promising electrode material, cyclic voltammetry (CV), galvanostatic charge–discharge (GCD), and electrochemical impendance spectroscopy (EIS) measurements were made to investigate the supercapacitive performance. The electrochemical window for CV and GCD measurements was kept in −0.5 to +0.5 V shown in **Figures 2A,B**. **Figure 2A** showed CV of the Cu_3P nanoplatelets under a three-electrode system in 1 M Na_2SO_4 electrolyte at a different scan rate from 10 to 200 mV/s. The broad shape of the asymmetric CV curves observed for Cu_3P nanoplatelets in the whole potential window indicated the presence of faradic behavior leading to pseudocapacitance along with electric double-layer capacitance (EDLC) existing simultaneously.

The appearance of two humps in between −0.5 and +0.5 V corresponding to cathodic and anodic maxima indicated that the Cu_3P platelets possess pseudocapacitive properties. These redox reactions attributed to the transition between metallic Cu(0) and Cu(I) species at an applied potential approximately −0.3 V vs. Ag/AgCl. While at the higher potential of 0.05 V vs. Ag/AgCl, the oxidation of Cu_3P platelets to Cu(II) species was observed due to aqueous interaction (**Figure 2A**). Further, the broad anodic peak nearly at 0.3 V could be attributed to the formation of a hydrous oxide of copper which originated from the hydrated cupric oxide (Jayalakshmi and Balasubramanian, 2008), and the corresponding chemical reaction was shown in equation (3). Here, the potential window had been fixed to 0.5 V to avoid the formation of Cu(III) species. So far, the identification of intermediate species was hard to find due to the chemical transformation of Cu_3P electrodes under electrochemical analysis, and the reaction mechanism was entirely unknown which required further detailed investigation. However, based on the available relevant literature, a possible

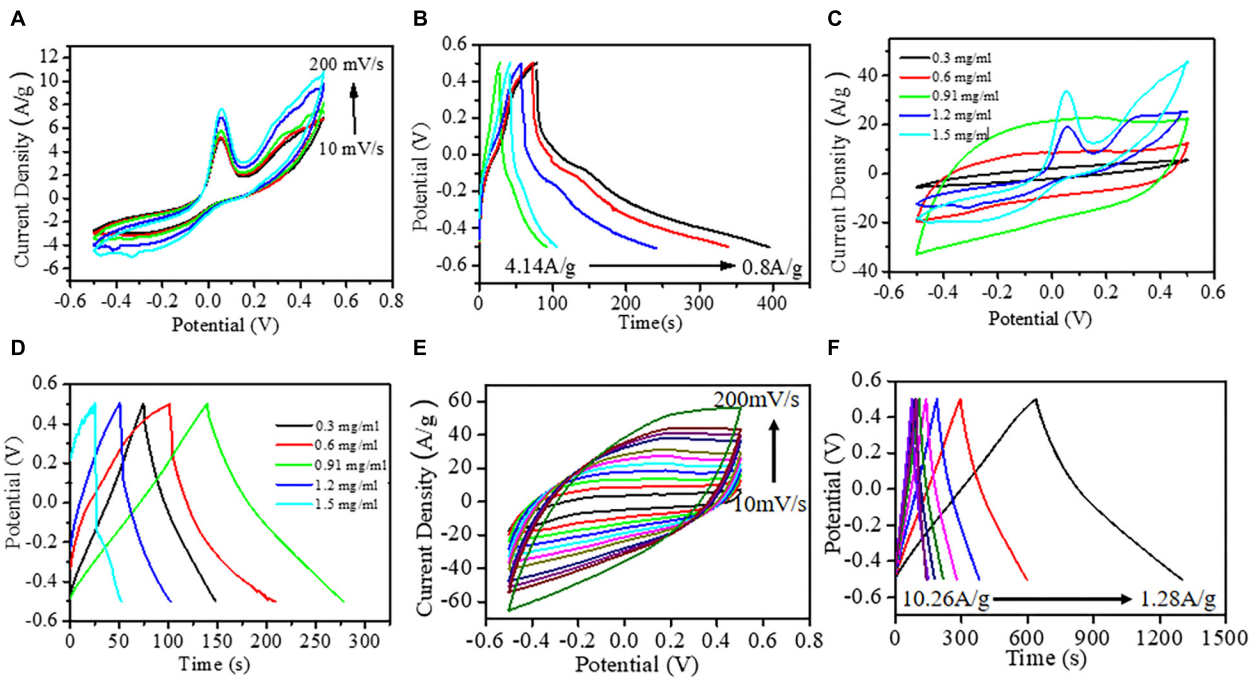

FIGURE 2 | Electrochemical characterization. **(A)** Typical cyclic voltammetry (CV) curves of hexagonal copper phosphide (Cu_3P) platelets on glassy carbon electrode at different scan rates (10, 50, 100, 150, and 200 mV/s). **(B)** Galvanostatic charge–discharge curves of Cu_3P platelets at various current densities. **(C)** CV curves at 50 mV/s scan rates for different rational compositions (0.3, 0.6, 0.91, 1.2, and 1.5 mg/ml) of Cu_3P on 3DG-graphite electrode. **(D)** Corresponding galvanostatic charge–discharge curves at 5.13 A/g current density. **(E)** Typical CV curves at different scan rates with the best weight ratio of 0.91 mg/ml of Cu_3P on graphite electrode (10–200 mV/s). **(F)** Corresponding galvanostatic charge–discharge curves at various current densities.

reaction mechanism had been proposed in the following equations (Poli et al., 2016; Chen et al., 2017).

$$Cu(I)_3P + xNa^+ + xe^- \rightarrow Na_x\{Cu(0)_xCu(I)_{3-x}\}P \quad (1)$$

$$Cu(I)_3P + H_2O \rightarrow Cu(II)_yO_yCu(I)_{3-y}P + 2_yH^+ + 2ye^- \quad (2)$$

$$CuO + H_2O \rightarrow Cu(OH)_2 \quad (3)$$

This mechanism could be attributed to redox reactions on the surface of Cu_3P platelets. Pfeiffer et al. (2004) had explained that all the elements of the first transition metal series have partially filled 3d shells, except copper and zinc. Nonetheless, only the copper has a complete 3d shell and a single 4 s electron. Hence, copper was the only element in the series to have M^{+1} state with filled D-orbital in Cu_3P platelets. The enhanced electrochemical performance might be attributed to the fact that the hexagonal Cu_3P platelets were composed of many small particles, which had significantly increased the specific surface area and provided more reaction sites on the surface evident from the SEM image shown in **Figures 1F,G**.

To further improve the Cu_3P electrode performance, we had designed a hybrid electrode with 3DG. The homogeneous distribution of Cu and P in hexagonal Cu_3P flake and carbon in the foamy graphitic matrix had confirmed the formation of Cu_3P@3DG hybrid network (shown in **Supplementary Figure S5**). For the development of effective electrode material, it was highly required to estimate the electrical conductivity of the proposed electrodes. The electrical conductivities of the Cu_3P@3DG and 3DG electrodes *via* 4PP configuration with the electrode spacing of 2 mm were calculated to be 1,076 S m^{-1} and 978 S m^{-1}, respectively. Here, the Cu_3P@3DG electrode exhibited better conductivity as compared to the bare 3DG electrode on graphite substrate. This could be due to the metalloid property of Cu_3P nanoparticles, shown in **Supplementary Figure S7**. To boost the kinetics of Cu_3P, Cu_3P@3DG had been elaborately designed, as schematically shown in **Figure 1A**. A systematic loading optimization of Cu_3P on a 3DG matrix had been performed for extracting the best capacitive performance of Cu_3P@3DG electrodes, as shown in **Figures 2C,D**. Here, the area under the CV curve was gradually increasing without any impressive redox peaks under the loading concentration of Cu_3P that varied from 0.3 to 0.91 mg/ml. Optimizing the weight% of Cu_3P in 3DG electrode, the redox probability of Cu_3P on the 3DG matrix had been controlled until 0.91 mg/ml loading. However, increasing the loading concentration to 1.2 mg/ml and above, the redox peaks appeared more prominent at the same potential as bare Cu_3P with increased current density due to the presence of the 3DG matrix. However, after a further increase in the concentration of Cu_3P until 1.5 mg/ml, the prominent redox peaks appeared. This loading concentration of Cu_3P on 3DG-graphite (0.91 mg/ml loading in 1 cm^2 × 1 cm^2) showed the best performance in galvanostatic charge–discharge curves at 5.13A/g current density (**Figure 2D**). For device fabrication as well as to evaluate the stability of the supercapacitor electrodes, the optimum loading concentration of Cu_3P had been fixed to 0.91 mg/ml. The electrochemical CV curves and GCD performance (with different scan rates) of 3DG and bare Cu_3P on graphite substrate are shown in **Supplementary Figure S8**. However, it had been observed that the C_{sp} value of Cu_3P on glassy carbon electrode (234.8 F/g) was slightly higher than that on graphite electrode (224 F/g) at a fixed current density of 1.28 A/g, which might be due to the interfacial interaction of electroactive material with the electrode substrate. The electrochemical analysis using this hybrid structure was carried out to evaluate its applicability toward energy storage devices. The C_{sp} of Cu_3P@3DG electrode was calculated to be 1,095.85, 901.50, 828.48, 778.70, 740.95, 706.66, 675.37, 590.95, 621.63, 597.45, 574.29, 495.97, and 421.65 F/g at the scan rate of 10, 20, 30, 40, 50, 60, 70, 80, 90, 100, 110, 150, and 200 mV/s, respectively from **Figure 2E**. Alternatively, the C_{sp} extracted from the GCD measurements (**Figure 2F**) of the Cu_3P@3DG electrode at various current density were calculated to be 849.81, 771.26, 734.35, 712.35, 692.39, 676.9, 659.98, and 644.75 F/g at 1.28, 2.56, 3.85, 5.13, 6.41, 7.69, 8.97, and 10.268 A/g, respectively (**Supplementary Figure S9**). The nearly isosceles triangular shape of the GCD (**Figure 2F**) implied excellent electron conductivity with tiny voltage drops at different current densities of Cu_3P@3DG electrode. The energy and power density extracted from the charge and discharge analysis were about 118.1, 107.1, 102.0, 99.0, 96.2, 94.1, 91.7, and 89.5 Wh/kg and 641.0, 1,282.0, 1,923.0, 2,564.1, 3,205.2, 3,846.2, 4,487.2, and 7,132.2 W/kg at 1.28, 2.56, 3.85, 5.13, 6.41, 7.69, 8.97, and 10.268 A/g current density, respectively.

The comparative CV curves of the electrodes made of three different electroactive nanomaterials: Cu_3P@3DG, 3DG, and bare Cu_3P were carried at a scan rate of 20 mV/s (**Figure 3A**). The C_{sp} of Cu_3P@3DG, 3DG, and Cu_3P electrodes were calculated to 901.5, 332.7, and 217.7 F/g (from CV curves), respectively, at a scan rate of 20 mV/s. Typically, the electrochemical properties like C_{sp} of Cu_3P@3DG were calculated to be nearly 2.5 times and four times enhanced as compared to bare 3DG and Cu_3P-based electroactive materials, respectively. The results implied that Cu_3P@3DG electrode referred to an excellent EDLC. The GCD measurements of the Cu_3P@3DG, 3DG, and bare Cu_3P on graphide electrodes at fixed current densities were performed with the potential window of 1.0 V (**Figure 3B**). The Cu_3P@3DG exhibited a high C_{sp} of 850 F/g (from GCD analysis) as compared to 3DG and bare Cu_3P of 336 F/g and 224 F/g, respectively, at a current density of 1.28 A/g. Even at a very high current density of 10.27 A/g, the C_{sp} reached up to 645 F/g which was about 76% of the capacitance retention compared to the current density of 1.28 A/g that invariably referred to the excellent stability of our electroactive material hetero-structure (shown in **Figure 2F**). The primary objective to incorporate 3DG along with Cu_3P platelets was to provide high conductive channels for ion and electron transfer in the charging–discharging process leading to the improvement of the overall performance of hybrid electrodes (An et al., 2014). This hybrid structure could effectively minimize the unwanted agglomeration of Cu_3P particles and simultaneously restricted the possibility of restacking of 3DG porous structure and thereby retaining the large surface area (**Supplementary Figure S10**), higher C_{sp}, better rate capability, and overall device stability.

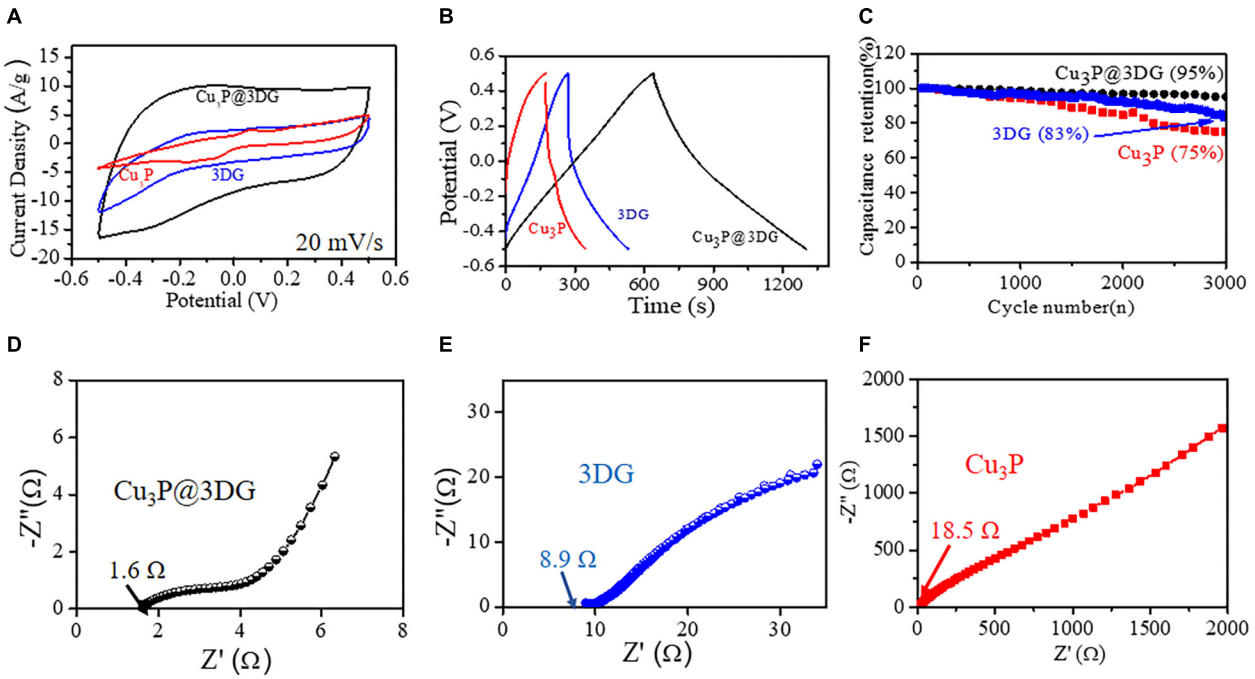

FIGURE 3 | (A) Cyclic voltammetry (CV) curves of the three-dimensional graphene-decorated copper phosphide (Cu_3P@3DG)-graphite (at 0.91 mg/ml), 3DG-graphite, and Cu_3P-graphite at 20 mV/s. **(B)** Galvanostatic charge–discharge curves collected at a fixed current density of 1.28 A/g for Cu_3P@3DG, 3DG, and Cu_3P on graphite electrodes. **(C)** Cycling performance of Cu_3P@3DG, 3DG, and Cu_3P on graphite electrodes at 1.28 A/g current density. **(D–F)** Impedance Nyquist plots of the Cu_3P@3DG, 3DG, and Cu_3P on graphite electrodes, respectively.

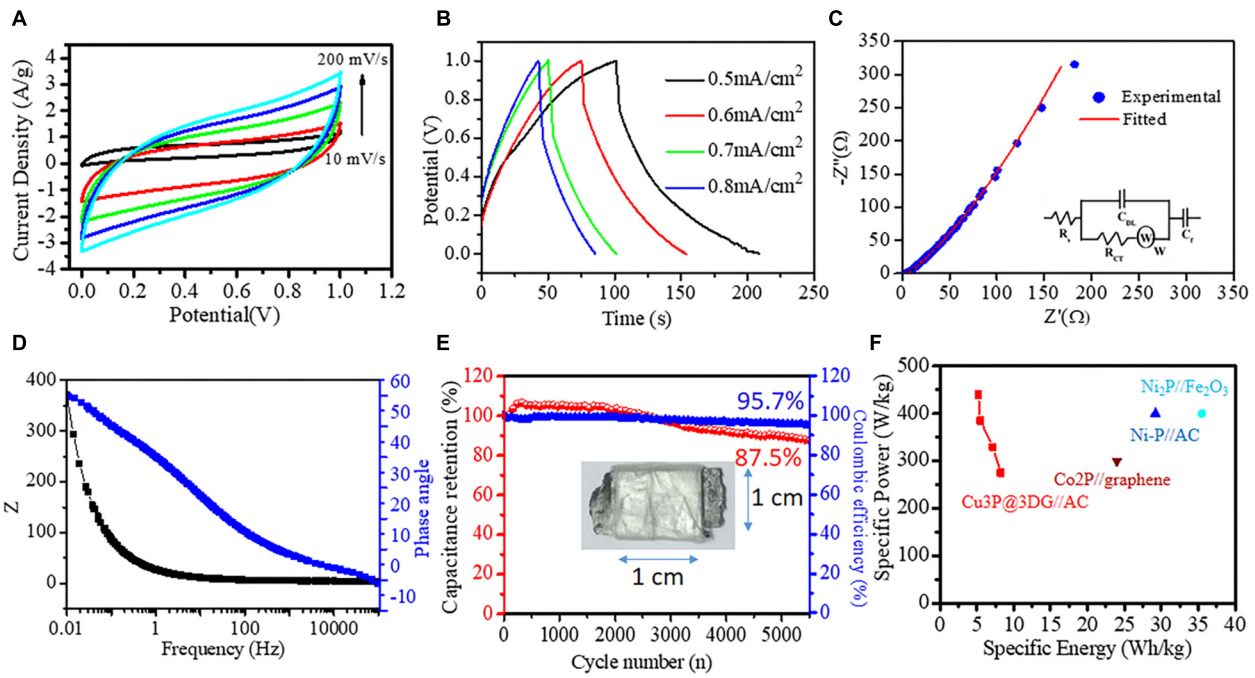

FIGURE 4 | Solid-state asymmetric supercapacitor (ASC). **(A)** Cyclic voltammetry (CV) curves obtained at different scan rates (10, 50, 100, 150, and 200 mV/s). **(B)** Galvanostatic charge–discharge curves obtained at different current densities (0.5, 0.6, 0.7, and 0.8 mA/cm^2). **(C)** Nyquist plot of the asymmetric device with the equivalent circuit as an inset. **(D)** Bode phase angle plot. **(E)** Capacitance retention (red ball-line) and coulombic efficiency (blue ball-line) of the assembled ASC device after 5,500 cycles; ASC device in the inset. **(F)** Ragone plots of ASC devices.

TABLE 1 | Comparison of capacitive performances of this work with those reported in relevant works.

Electrode material	Specific capacitance	Electrolyte	Cyclic stability	ASC device	ASC capacitance	Electrolyte	Energy, Power densities	ASC device stability	References
Ni_2P nanospheres	306.8 F/g at 1A/g	3 M KOH	62.7% retention after 5,000						Wu H. et al., 2016
Ni_2P nanorods	799.2 F/g at 1A/g	3 M KOH	68.4% retention after 5,000						Wu H. et al., 2016
Co_2P nanorods	284 F/g at 1 A/g	3 M KOH							Chen et al., 2016
Ni_2P/GS	1,912 F/g at 5 mA/cm^2	2 M KOH	77.1% retention after 2,300						An et al., 2014
Ni2P/rGO	2,266 F/g at 5 mA/cm^2	2 M KOH							An et al., 2014
Hexagonal copper phosphide (Cu_3P) platelets	224 F/g at 1.28 A/g	1 M Na_2 SO_4	75% retention after 3,000						Present Work
Ni_2P	843.25 F/g at 1 A/g	2 M KOH	96% retention after 1,000	$Ni_2P//Fe_2O_3$	100 F/g at 0.5 A g^{-1}	2 M KOH with one piece of cellulose paper as the separator	35.5 Wh kg^{-1}, 400 W kg^{-1}	96%, 1,000	Wang et al., 2015a
Ni_5P_4	801.5 F/g at 1 A/g	2 M KOH	87% retention after 1,000	$Ni_5P_4//Fe_2O_3$	88.3 F/g at 0.5 A g^{-1}	2 M KOH with one piece of cellulose paper as the separator		86%, 1,000	Wang et al., 2015a
Amorphous Ni-P	964 F/g at 4 A/g	2 M KOH	71.4% retention after 1,000	Ni-P//AC	105 F/g at 5 mV/s	2 mol L^{-1} KOH	29.2 Wh kg^{-1}, 400 W kg^{-1}	84.5% 1,000	Wang et al., 2015b
Co_2P nanoflowers	461 F/g at 1 A/g	6 M KOH		Co_2P//graphene	76.8 F/g at 0.4 A g^{-1}	6 M KOH	24 Wh kg^{-1}, 300 W kg^{-1}	97%, 6,000	Chen et al., 2016
Cu_3P nanotube	177.1 F/g at 3.5 mA/cm^2	1 M H_2SO_4		Cu_3P//CNT	142.8 F/g at 0.75 mA cm^{-2}	0.5 M H_2SO_4	44.6 Wh kg^{-1}, 17,045.7 W kg^{-1}	81.9% 5,000	Chen et al., 2017
Cu_3P@3DG	849.81 F/g at 1.28 A/g	1 M Na_2 SO_4	95% retention after 3,000	Cu_3P@3DG//AC	108.78 F/g at 10 mV/s	PVA KOH gel electrolyte	8.23 Wh kg^{-1}, 439.6 W/kg	82.5%, 5,500	Present Work

However, the bare 3DG (made of three-dimensionally oriented rGO with very low oxygen content shown in **Supplementary Figure S11**) is known to be acting as promising anode materials due to high electronegativity rather than effective cathode material where graphene is difficult to get oxidized under the operating potential window (Hossain et al., 2012). CV analysis of bare glassy carbon and Cu_3P decorated glassy carbon shown in **Supplementary Figure S12**.

The cycle stability had been evaluated for Cu_3P@3DG, 3DG, and hexagonal Cu_3P platelet-based electroactive materials on graphite substrate for its applicability in real phase energy storage devices. **Figure 3C** showed the variation of the C_{sp} retention (%) as a function of the cycle number of the galvanostatic charge–discharge curves of the Cu_3P@3DG, 3DG, and hexagonal Cu_3P platelets at a fixed current density of 1.28 A/g. Surprisingly, after 3,000 cycles, the capacitive retention of Cu_3P@3DG was found to be 95%, whereas that of 3DG was 83%. However, the stability degraded to 75% for bare Cu_3P platelets. This gave us a clear understanding that the 3DG matrix was protecting Cu_3P platelets from chemical degradation as well as agglomeration due to its high electrical and thermal conductivities. These excellent properties of 3DG in our nanohybrid materials had been further evaluated by characteristic electrochemical impedance study. **Figures 3D–F** showed the Nyquist plot of the Cu_3P@3DG, bare 3DG, and Cu_3P electrodes, respectively. In the spectrum, the equivalent series resistances of Cu_3P@3DG, 3DG, and bare Cu_3P on graphite electrodes were calculated to be 1.6, 8.9, and 18.5 **Ω**, respectively, which showed favorable conductivity (evident from the 4PP *I-V* characteristic, shown in **Supplementary Figure S7**) and very low internal resistance of Cu_3P@3DG hybrid for high specific power density.

The asymmetric supercapacitor (ASC) device was fabricated to investigate the potential application of Cu_3P@3DG nanohybrid as a positive electrode and AC as a negative electrode on a graphite substrate. The electrochemical performance of the ASC device was analyzed *via* CV at different scan rates, and GCD measurements were done at various current densities, as shown in **Figures 4A,B**. The potential window of the ASC Cu_3P@3DG and AC electrodes was fixed to be 0–1 V. **Figure 4A** displayed the CV curves of the ASC device at different scan rates with a constant potential window, which showed rectangular like CV curves without redox peaks. It indicated the excellent reversibility and kinetics for electrochemical reactions over the ASC electrode. The C_{sp} of the device was calculated to be 108.78, 61.65, 47.30, 39.86, and 35.09 F/g (217.56, 123.32, 94.61, 79.74, and 70.20 mF/cm^2) at the scan rate of 10, 50, 100, 150, and 200 mV/s respectively. Alternatively, the C_{sp} extracted from the GCD measurements of the device, as shown in **Figure 4B**, at various current densities were calculated to be 59.72, 51.82, 39.53, and 37.53 F/g (107.8, 94.33, 71.96, and 68.32 mF/cm^2) at 0.5, 0.6, 0.7, and 0.8 mA/cm^2 current densities, respectively. The energy and power densities were calculated to be 8.23, 7.2, 5.5, and 5.2 Wh/kg and 274.7, 329.7, 384.6, and 439.6 W/kg at 0.5, 0.6, 0.7, and 0.8 mA/cm^2 current densities, respectively. To further elucidate the origin of high electrochemical performance, the electrochemical impedance spectrum (EIS) was carried out to examine the Cu_3P@3DG//AC supercapacitor device. **Figure 4C** showed the Nyquist plot, the combined resistance Rs (the intrinsic, contact, and electrolyte resistance) of 4.24 **Ω**, the Cdl (the electric double layer capacitance) of 70.4 μF, and the Rct (the resistance of Faradic reaction) of 714 m**Ω**. The inclined line in the low-frequency region represented the Warburg impedance (W) of 19.2 mMho, and constant phase element (C_F) 81.1 mMho. Simultaneously, the apparent straight-line nature of the plot in a low-frequency region described the ideal capacitive behavior of this prototype ASC device. The corresponding equivalent circuit was drawn based on the complex non-linear least-squares fitting method, shown as an inset of **Figure 4C**. **Figure 4D** displayed the Bode phase angle plot of Cu_3P@3DG//AC. The absence of a horizontal segment in the Z-frequency plot at the low-frequency range revealed good charge-transfer behavior. Simultaneously, the high value of the phase angle curve manifested the great capacitive behavior of Cu_3P@3DG//AC at the low-frequency range. Moreover, the long-term cycling stability performance was examined by GCD analysis at a current density of 0.7 mA/cm^2. This supercapacitor device has demonstrated 82.5% capacitance retention after 5,500 cycles exhibiting outstanding cycling stability with 96% coulombic efficiency, as shown in **Figure 4E**. **Figure 4F** displayed the Ragone plot of ASC (Cu_3P@3DG//AC) device. All these observations indicated that the Cu_3P@3DG exhibited good electrochemical performance that could promote it to be an excellent material for its applicability in the next-generation energy storage device. In all the listed combination of metal phosphides, a direct comparison was not possible because of various factors like two-electrode experiment was performed in both solid and liquid state and the concentration and type of elecrolytes were different in all experimental conditions which had a prominent effect on the overall performance of the materials.

Table 1 depicts the transition metal phosphide-based active electrodes that so far had been tested as promising materials for supercapacitor devices. The synthesis of the metal phosphides with optimized nanostructures and composition was a real challenge. Although the reported specific capacitances of the active materials like Ni-P, Ni_2P, CoP, Co_2P, and Cu_3P with different morphologies were quite high, but the working potential and capacitance retention were significantly low. However, it was found to be quite challenging to expand the working potential of the electrodes for practical applications. Here, we offered a strategy to synthesize hexagonal Cu_3P platelets with 3DG as promising electrode materials for supercapacitors *via* controlling the directionality of the growth as well as engineering the facile interface between electrodes to electroactive materials which worked well in negative as well as positive working potentials.

CONCLUSION

In summary, the facile synthesis procedure of hexagonal Cu3P platelets and the fabrication of a heterostructure Cu_3P with interwoven 3DG on graphite electrode (1 cm^2 × 1 cm^2) shows a simple way to design a supercapacitor device for practical applications. The Cu_3P@3DG nanohybrid facilitates electron transfer and promotes kinetics with long cycling stability *via* lowering the internal resistance and providing electrochemical

stability of Cu_3P platelets. The high conductive channels for ions and electron transfer in the charging–discharging process leads to an enhancement of the overall device performance. The specific capacitance of the Cu_3P@3DG is 849.81 F/g at a current density of 1.28 A/g and also exhibits superior cycling performance, with 95% retention of capacitance after 3,000 cycles at a current density of 1.28 A/g. In contrast, the solid-state asymmetric device shows the C_{sp} of 109 F/g (from the CV) and 60 F/g (from GCD) with a capacitive retention of 82.5% and coulombic efficiency of 96% after 5,500 cycles, respectively. Due to the higher capacitance, lower cost, and excellent cycle stability of the Cu_3P@3DG, it is anticipated that the material has potential for next-generation energy storage applications.

DATA AVAILABILITY STATEMENT

All datasets generated for this study are included in the article/**Supplementary Material**.

AUTHOR CONTRIBUTIONS

SBK designed the work. SSK and SA performed the experiments and characterizations. SSK and SR prepared the electrodes assembly of the samples and analyzed the electrochemical data. KG and GN participated in interpreting and analyzing all data and finalized the manuscript. GY and LM helped to characterize HRTEM and TEM analysis. All authors read and approved the final manuscript.

FUNDING

KG is thankful for the financial support from Nano Mission, Department of Science & Technology, India [Grant No: SR/NM/NS-91/2016 (G)]. GN would also like to thank the Israel Science Foundation, VATAT, and the Israel Prime Minister's Office fuel alternative initiative for partial funding of this study under the Israel National Research Center for Electrochemical Propulsion (INREP).

ACKNOWLEDGMENTS

SBK would like to thank the Planning and Budgeting Committee of the Council for Higher Education for his PBC postdoctoral fellowship.

SUPPLEMENTARY MATERIAL

The Supplementary Material for this article can be found online at: https://www.frontiersin.org/articles/10.3389/fmats.2020.00030/full#supplementary-material

REFERENCES

An, C., Wang, Y., Li, L., Qiu, F., Xu, Y., Xu, C., et al. (2014). Effects of highly crumpled graphene nanosheets on the electrochemical performances of pseudocapacitor electrode materials. *Electrochim. Acta* 133, 180–187. doi: 10.1016/j.electacta.2014.04.056

Augustyn, V., Simon, P., and Dunn, B. (2014). Pseudocapacitive oxide materials for high-rate electrochemical energy storage. *Energy Environ. Sci.* 7, 1597–1614. doi: 10.1039/c3ee44164d

Aziz, S. T., and Islam, R. U. (2018). Polymer-supported Cu–nanoparticle as an efficient and recyclable catalyst for oxidative homocoupling of terminal alkynes. *Catal. Lett.* 148, 205–213. doi: 10.1007/s10562-017-2237-8

Barry, B. M., Gillan, E. G., and Mater, R. E. C. (2008). Low-temperature solvothermal synthesis of phosphorus-rich transition-metal phosphides. *Chem. Mater.* 20, 2618–2620. doi: 10.1021/cm703095z

Brock, S. L., Perera, S. C., and Stamm, K. L. (2004). Chemical routes for production of transition-metal phosphides on the nanoscale: implications for advanced magnetic and catalytic materials. *Chem. - A Eur. J.* 10, 3364–3371. doi: 10.1002/chem.200305775

Brock, S. L., and Senevirathne, K. (2008). Recent developments in synthetic approaches to transition metal phosphide nanoparticles for magnetic and catalytic applications. *J. Solid State Chem.* 181, 1552–1559. doi: 10.1016/j.jssc.2008.03.012

Cao, J., Lei, C., Yang, B., Li, Z., Lei, L., Hou, Y., et al. (2019). Zeolitic imidazolate framework-derived core-shell-structured CoS 2 /CoS2 -N-C supported on electrochemically exfoliated graphene foil for efficient oxygen evolution. *Batter. Supercaps* 2, 348–354. doi: 10.1002/batt.201800098

Chen, X., Cheng, M., Chen, D., and Wang, R. (2016). Shape-controlled synthesis of co2p nanostructures and their application in supercapacitors. *ACS Appl. Mater. Interfaces* 8, 3892–3900. doi: 10.1021/acsami.5b10785

Chen, Y., Zhang, W., Zhou, D., Tian, H., Su, D., Wang, C., et al. (2019). Co–Fe mixed metal phosphide nanocubes with highly interconnected-pore architecture as an efficient polysulfide mediator for lithium-sulfur batteries. *ACS Nano* 13, 4731–4741. doi: 10.1021/acsnano.9b01079

Chen, Y. C., Chen, Z. B., Lin, Y. G., and Hsu, Y. K. (2017). Synthesis of copper phosphide nanotube arrays as electrodes for asymmetric supercapacitors. *ACS Sustain. Chem. Eng.* 5, 3863–3870. doi: 10.1021/acssuschemeng.6b03006

Ding, L., Zhang, K., Chen, L., Yu, Z., Zhao, Y., Zhu, G., et al. (2019). Formation of three-dimensional hierarchical pompon-like cobalt phosphide hollow microspheres for asymmetric supercapacitor with improved energy density. *Electrochim. Acta* 299, 62–71. doi: 10.1016/j.electacta.2018.12.180

Fan, M., Chen, Y., Xie, Y., Yang, T., Shen, X., Xu, N., et al. (2016). Half-cell and full-cell applications of highly stable and binder-free sodium-ion batteries based on Cu3P nanowire anodes. *Adv. Funct. Mater.* 26, 5019–5027. doi: 10.1002/adfm.201601323

Han, A., Zhang, H., Yuan, R., Ji, H., and Du, P. (2017). Crystalline copper phosphide nanosheets as an efficient janus catalyst for overall water splitting. *ACS Appl. Mater. Interfaces* 9, 2240–2248. doi: 10.1021/acsami.6b10983

Hao, J., Yang, W., Huang, Z., and Zhang, C. (2016). Superhydrophilic and superaerophobic copper phosphide microsheets for efficient electrocatalytic hydrogen and oxygen evolution. *Adv. Mater. Interfaces* 3:1600236. doi: 10.1002/admi.201600236

Henkes, A. E., Vasquez, Y., and Schaak, R. E. (2007). Converting metals into phosphides: a general strategy for the synthesis of metal phosphide nanocrystals. *J. Am. Chem. Soc.* 129, 1896–1897. doi: 10.1021/ja068502l

Hossain, M. Z., Johns, J. E., Bevan, K. H., Karmel, H. J., Liang, Y. T., Yoshimoto, S., et al. (2012). Chemically homogeneous and thermally reversible oxidation of epitaxial graphene. *Nat. Chem.* 4, 305–309. doi: 10.1038/nchem.1269

Hou, C. C., Chen, Q. Q., Wang, C. J., Liang, F., Lin, Z., Fu, W. F., et al. (2016). Self-supported cedarlike semimetallic Cu3P nanoarrays as a 3D high-performance Janus electrode for both oxygen and hydrogen evolution under basic conditions. *ACS Appl. Mater. Interfaces* 8, 23037–23048. doi: 10.1021/acsami.6b06251

Itzhak, A., Teblum, E., Girshevitz, O., Okashy, S., Turkulets, Y., Burlaka, L., et al. (2018). Digenite (Cu9S5): layered p-type semiconductor grown by reactive

annealing of copper. *Chem. Mater.* 30, 2379–2388. doi: 10.1021/acs.chemmater.8b00191

Jayalakshmi, M., and Balasubramanian, K. (2008). Cyclic voltammetric behavior of copper powder immobilized on paraffin impregnated graphite electrode in dilute alkali solution. *Int. J. Electrochem. Sci.* 3, 1277–1287.

Jin, Y., Zhao, C., Wang, Y., Jiang, Q., Ji, C., and Jia, M. (2017). Large-scale production of Cu3P nanocrystals for ultrahigh-rate supercapacitor. *Ionics* 23, 3249–3254. doi: 10.1007/s11581-017-2267-7

Kumar, S., Aziz, S. T., Girshevitz, O., and Nessim, G. D. (2018). One-step synthesis of N-Doped graphene quantum dots from chitosan as a sole precursor using chemical vapor deposition. *J. Phys. Chem. C* 122, 2343–2349. doi: 10.1021/acs.jpcc.7b05494

Kumar, S., Gonen, S., Friedman, A., Elbaz, L., and Nessim, G. D. (2017). Doping and reduction of graphene oxide using chitosan-derived volatile N-heterocyclic compounds for metal-free oxygen reduction reaction. *Carbon N. Y.* 120, 419–426. doi: 10.1016/j.carbon.2017.05.071

Li, D., Baydoun, H., Verani, C. N., and Brock, S. L. (2016). Efficient water oxidation using CoMnP nanoparticles. *J. Am. Chem. Soc.* 138, 4006–4009. doi: 10.1021/jacs.6b01543

Li, X., Elshahawy, A. M., Guan, C., and John, W. (2017). Metal phosphides and phosphates-based electrodes for electrochemical supercapacitors. *Small* 13:1701530. doi: 10.1002/smll.201701530

Li, Z., Ding, J., and Mitlin, D. (2015). Tin and tin compounds for sodium-ion battery anodes: phase transformations and performance. *Acc. Chem. Res.* 48, 1657–1665. doi: 10.1021/acs.accounts.5b00114

Liang, H., Xia, C., Jiang, Q., Gandi, A. N., Schwingenschlögl, U., and Alshareef, H. N. (2017). Low-temperature synthesis of ternary metal phosphides using plasma for asymmetric supercapacitors. *Nano Energy* 35, 331–340. doi: 10.1016/j.nanoen.2017.04.007

Lin, Y.-G., Hsu, Y.-K., Lin, Y.-C., Chang, Y.-H., Chen, S.-Y., and Chen, Y.-C. (2016). Synthesis of Cu2O nanoparticle films at room temperature for solar water splitting. *J. Colloid Interface Sci.* 471, 76–80. doi: 10.1111/poms.12938

Liu, S., He, X., Zhu, J., Xu, L., and Tong, J. (2016). Cu3P/RGO nanocomposite as a new anode for lithium-ion batteries. *Sci. Rep.* 6, 1–10. doi: 10.1038/srep35189

Liu, S., Li, S., Wang, J., Shi, Q., and Li, M. (2012). Surfactant-assisted synthesis and electrochemical performances of Cu 3 P dendrites. *Mater. Res. Bull.* 47, 3352–3356. doi: 10.1016/j.materresbull.2012.07.026

López-Ortega, A., Lottini, E., Fernández, C. D. J., and Sangregorio, C. (2015). Exploring the magnetic properties of cobalt-ferrite nanoparticles for the development of a rare-earth-free permanent magnet. *Chem. Mater.* 27, 4048–4056. doi: 10.1021/acs.chemmater.5b01034

Mukherjee, D., and Austeria, M. (2016). Two-dimensional, few-layer for electrochemical hydrogen evolution over phosphochalcogenide, FePS3: a new catalyst wide pH range. *ACS Energy Lett.* 1, 367–372. doi: 10.1021/acsenergylett.6b00184

Olofsson, O. (1972). The crystal structure of Cu3P. *Acta Chem. Scand.* 26, 2777–2787. doi: 10.3891/acta.chem.scand.26-2777

Pfeiffer, H., Tancret, F., Bichat, M. P., Monconduit, L., Favier, F., and Brousse, T. (2004). Air stable copper phosphide (Cu3P): a possible negative electrode material for lithium batteries. *Electrochem. Commun.* 6, 263–267. doi: 10.1016/j.elecom.2003.12.012

Pfeiffer, H., Tancret, F., and Brousse, T. (2005). Synthesis, characterization and electrochemical properties of copper phosphide (Cu3P) thick films prepared by solid-state reaction at low temperature: a probable anode for lithium-ion batteries. *Electrochim. Acta* 50, 4763–4770. doi: 10.1016/j.electacta.2005.02.024

Poli, F., Wong, A., Kshetrimayum, J. S., Monconduit, L., and Letellier, M. (2016). In situ NMR insights into the electrochemical reaction of Cu3P electrodes in lithium batteries. *Chem. Mater.* 28, 1787–1793. doi: 10.1021/acs.chemmater.5b04802

Riyajuddin, S. K., Aziz, S. K. T., Kumar, S., Nessim, G. D., and Ghosh, K. (2019). 3D-graphene decorated with g-C_3N_4/Cu_3P composite: a noble metal-free bifunctional electrocatalyst for overall water splitting. *ChemCatChem*. doi: 10.1002/cctc.201902065

Seo, B., Baek, D. S., Sa, Y. J., and Joo, S. H. (2016). Shape effects of nickel phosphide nanocrystals on hydrogen evolution reaction. *CrystEngComm* 18, 6083–6089. doi: 10.1039/c6ce00985a

Shao, Y., Shi, X., and Pan, H. (2017). Electronic, magnetic, and catalytic properties of thermodynamically stable two-dimensional transition-metal phosphides. *Chem. Mater.* 29, 8892–8900. doi: 10.1021/acs.chemmater.7b03832

Singh, K., Kumar, S., Agarwal, K., Soni, K., Ramana Gedela, V., and Ghosh, K. (2017). Three-dimensional graphene with MoS 2 nanohybrid as potential energy storage/transfer device. *Sci. Rep.* 7:9458. doi: 10.1038/s41598-017-09266-2

Sivula, K., and Van De Krol, R. (2016). Semiconducting materials for photoelectrochemical energy conversion. *Nat. Rev. Mater* 1:15010. doi: 10.1038/natrevmats.2015.10

Sun, Z., Yue, Q., Li, J., Xu, J., Zheng, H., and Du, P. (2015). Copper phosphide modified cadmium sulfide nanorods as a novel p-n heterojunction for highly efficient visible-light-driven hydrogen production in water. *J. Mater. Chem. A* 3, 10243–10247. doi: 10.1039/c5ta02105g

Wang, D., Kong, L., Liu, M. C., Luo, Y. C., and Kang, L. (2015a). An approach to preparing Ni-P with different phases for use as supercapacitor electrode materials. *Chem. A Eur. J.* 21, 17897–17903. doi: 10.1002/chem.201502269

Wang, D., Kong, L., Liu, M., Zhang, W., and Luo, Y. (2015b). Amorphous Ni-P materials for high-performance pseudocapacitors. *J. Power Sources* 274, 1107–1113. doi: 10.1016/j.jpowsour.2014.10.179

Wang, X., Li, M., Chang, Z., Wang, Y., Chen, B., Zhang, L., et al. (2015c). Orientated Co 3 O 4 nanocrystals on MWCNTs as superior battery-type positive electrode material for a hybrid capacitor. *J. Electrochem. Soc.* 162, A1966–A1971. doi: 10.1149/2.0041511jes

Wang, J., Yang, Q., Zhang, Z., and Sun, S. (2010). Phase-controlled synthesis of transition-metal phosphide nanowires by ullmann-type reactions. *Chem. A Eur. J.* 16, 7916–7924. doi: 10.1002/chem.200902151

Wang, W., Zhang, L., Xu, G., Song, H., Yang, L., Zhang, C., et al. (2018). Structure-designed synthesis of CoP Microcubes from metal-organic frameworks with enhanced supercapacitor properties. *Inorg. Chem.* 57, 10287–10294. doi: 10.1021/acs.inorgchem.8b01524

Wei, S., Qi, K., Jin, Z., Cao, J., Zheng, W., Chen, H., et al. (2016). One-step synthesis of a self-supported copper phosphide nanobush for overall water splitting. *ACS Omega* 1, 1367–1373. doi: 10.1021/acsomega.6b00366

Wu, H., Ni, Y., Wang, M., and Lu, D. (2016). Shape-controlled synthesis and performance comparison of Ni2P nanostructures. *CrystEngComm* 18, 5155–5163. doi: 10.1039/c6ce00386a

Wu, J., Zhang, Q., Zhou, A., Huang, Z., Bai, H., and Li, L. (2016). Phase-separated polyaniline/graphene composite electrodes for high-rate electrochemical supercapacitors. *Adv. Mater.* 28, 10211–10216. doi: 10.1002/adma.201601153

Xue, S., Chen, L., Liu, Z., Cheng, H., and Ren, W. (2018). NiPS 3 nanosheet - graphene composites as highly efficient electrocatalysts for oxygen evolution reaction. *ACS Nano* 2018, 5297–5305. doi: 10.1021/acsnano.7b09146

Zhang, Y., Wang, G., Wang, L., Tang, L., Zhu, M., Wu, C., et al. (2019). Graphene-encapsulated CuP 2 : a promising anode material with high reversible capacity and superior rate-performance for sodium-ion batteries. *Nano Lett* 196, 2575–2582. doi: 10.1021/acs.nanolett.9b00342

Zhou, K., Zhou, W., Yang, L., Lu, J., Cheng, S., Mai, W., et al. (2015). Ultrahigh-performance pseudocapacitor electrodes based on transition metal phosphide nanosheets array via phosphorization: a general and effective approach. *Adv. Funct. Mater.* 25, 7530–7538. doi: 10.1002/adfm.201503662

Zhu, L., Wu, W., Zhu, Y., Tang, W., and Wu, Y. (2015). Composite of CoOOH nanoplates with multiwalled carbon nanotubes as superior cathode material for supercapacitors. *J. Phys. Chem. C* 119, 7069–7075. doi: 10.1021/acs.jpcc.5b01498

Conflict of Interest: The authors declare that the research was conducted in the absence of any commercial or financial relationships that could be construed as a potential conflict of interest.

frontiers in Materials

REVIEW
published: 30 June 2020
doi: 10.3389/fmats.2020.00147

Advances in Layered Double Hydroxide/Carbon Nanocomposites Containing Ni^{2+} and $Co^{2+/3+}$ for Supercapacitors

Shalini Kulandaivalu[1], *Nur Hawa Nabilah Azman*[1] *and Yusran Sulaiman*[1,2]*

[1] Department of Chemistry, Faculty of Science, Universiti Putra Malaysia, Serdang, Malaysia, [2] Functional Devices Laboratory, Institute of Advanced Technology, Universiti Putra Malaysia, Serdang, Malaysia

The exceptional characteristics and uniqueness of two-dimensional nickel-cobalt layered double hydroxides (Ni-Co LDHs) make them highly desirable material for supercapacitors. A combination of Ni-Co LDHs with carbon-based materials has given stupendous improvement to the performance of supercapacitors in terms of specific energy, specific capacitance, and specific power. Herein, a comprehensive insight into the recent progress of Ni-Co LDHs/carbon composites for supercapacitors is provided to the readers. Beginning with the description on the classification of supercapacitors and the detailed explanation on LDHs and carbon materials. The morphology, properties and electrochemical performances of the Ni-Co LDHs/carbon composites are well-elaborated in this review. The review also discusses the structural identification and important factors that influence the synthesis of LDHs.

Keywords: layered double hydroxides, supercapacitor, carbon materials, nickel, cobalt

OPEN ACCESS

Edited by:
Federico Cesano,
University of Turin, Italy

Reviewed by:
Cheng Jp,
Zhejiang University, China
Zan Gao,
University of Virginia, United States
David Aradilla,
Commissariat à l'Energie Atomique et aux Energies Alternatives (CEA), France

***Correspondence:**
Yusran Sulaiman
yusran@upm.edu.my

Specialty section:
This article was submitted to Energy Materials, a section of the journal Frontiers in Materials

Received: *19 December 2019*
Accepted: *27 April 2020*
Published: *30 June 2020*

Citation:
Kulandaivalu S, Azman NHN and Sulaiman Y (2020) Advances in Layered Double Hydroxide/Carbon Nanocomposites Containing Ni^{2+} and $Co^{2+/3+}$ for Supercapacitors. Front. Mater. 7:147. doi: 10.3389/fmats.2020.00147

INTRODUCTION

Abundant fossil fuels in the earth converted agricultural society to an industrial society, known as the industrial revolution. Since then, due to the growing need for energy to support economic growth and sustainable society, non-renewable fossil fuels are limited in supply. Based on the report provided in the British Petroleum (BP) Statistical Review of World Energy 2018 by the BP Company PLC, the growth of global primary energy consumption was estimated to increase in the rate of 2.2% as of 2017 and, the world set the highest fuel consumption record for natural gas (BP, 2018). Throughout industrialization, an alarming level of fossil fuel consumption is associated with environmental issues. The massive carbon dioxide emission from fossil fuel consumption has caused major climate change faced by today's world and this is also responsible for global warming and pollutions. This has triggered the quest for effective usage of renewable energy sources to replace fossil fuels. Despite the cost and efficiency, energy storage is the main hurdle in keeping up with renewable energies. Therefore, electrochemical energy storage systems are usually integrated with renewable energy sources to store and to deliver the energies efficiently. In that context, the development of nanotechnology, exploration for nano-sized materials, devices and systems has shed light on producing energy conversion and storage systems. Notably, in recent years, many significant efforts have been devoted to developing next-generation high-performance energy storage devices, particularly electrochemical supercapacitors. In 1957, General Electric had introduced the first double layer capacitor and patented the work (Becker, 1957). However, the outbreak of the era of supercapacitors is from Standard Oil of Ohio (SOHIO) when they

commercialized double layer supercapacitors as an official energy storage device (Pandolfo and Hollenkamp, 2006). Since then, it continues to tempt the attention of scientific communities as pointed by the number of articles published in supercapacitors (**Figures 1A,B**). To date, the devices exemplified as state-of-the-art for its impressive performance and also regarded as a highly promising electrochemical energy storage system among the available energy storage devices. It has unearthed profound impacts on today's world.

ELECTROCHEMICAL SUPERCAPACITOR

Electrochemical supercapacitors or more commonly known as supercapacitors differ from conventional capacitors in terms of performance. Generally, conventional capacitors and supercapacitors are governed by the same principals. Both systems are separated by a separator between the two conductive electrodes. However, the separator in the conventional capacitor is an insulating dielectric material, for instance, ceramic and glass. Contrarily, in supercapacitors, the two conductive electrodes are separated by a permeable insulating separator soaked in an electrolyte. Adding to this, the conductive electrodes of a supercapacitor mainly consists of highly porous electrodes with a high surface area instead of planar plates used in conventional capacitors. The permeable separator in supercapacitors allows ions from the electrolyte to move across the separator penetrating the material utilizing the porosity upon electrode polarization (**Figure 1C**). Whereas, when the electrodes are polarized in conventional capacitors, the charges will accumulate along the surface of dielectric material, creating electric fields as shown in **Figure 1D** (Kim et al., 2015). The superiority of supercapacitors accessing the porosity of electrodes makes it better performance than conventional capacitors.

The principles of supercapacitors have been widely reviewed in literature (Wang et al., 2012; Yu et al., 2015; Liu et al., 2018a). Briefly, supercapacitors are classified into two types, electrochemical double layer capacitors (EDLCs) and pseudocapacitors based on their charge storage mechanisms.

i. EDLCs stores energy by forming an electrochemical double layer at the interface of an electrode and electrolyte. An EDLC utilizes high-surface-area carbon-based materials as electrodes. It has excellent cycling stability that is able

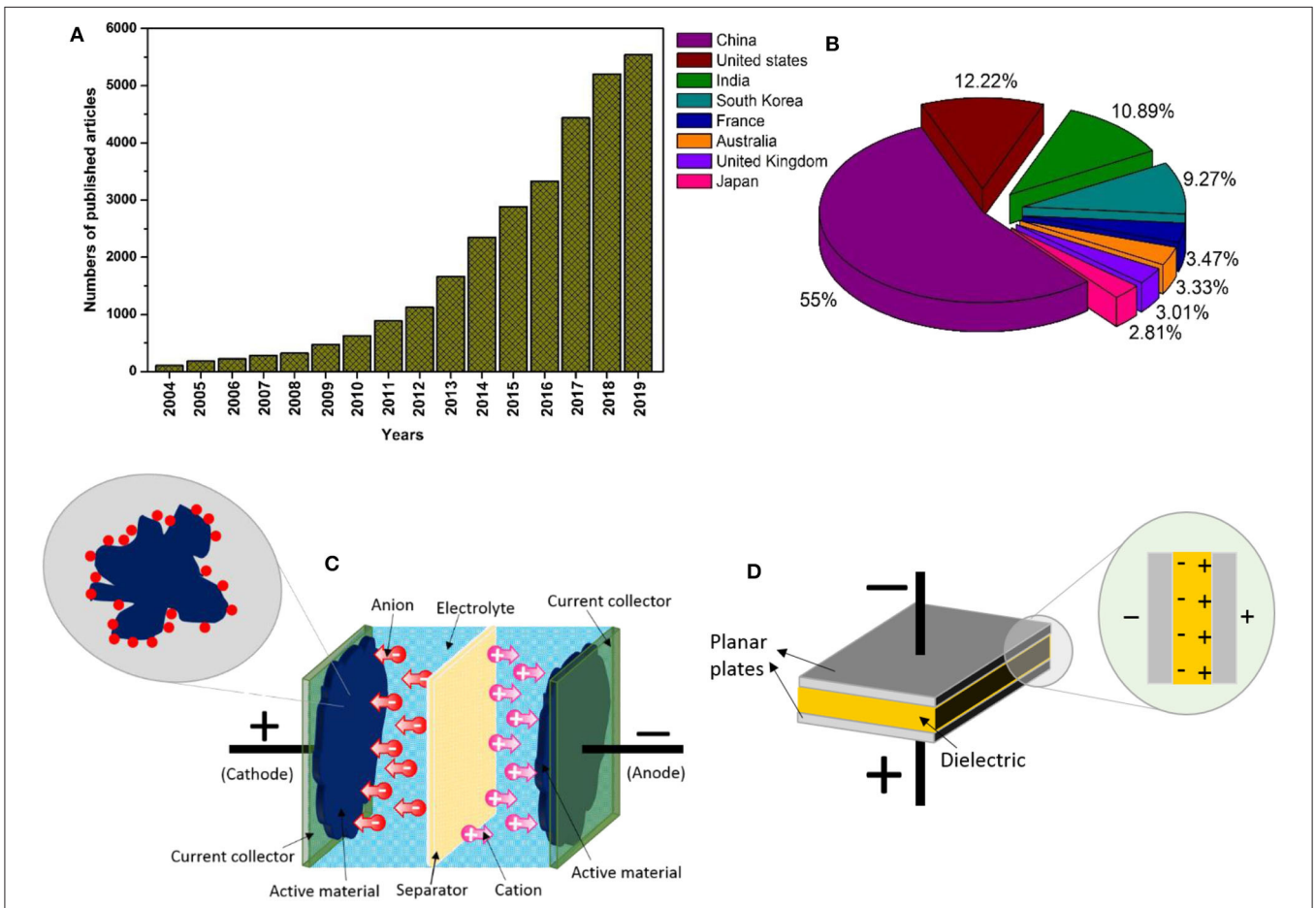

FIGURE 1 | (A) Trends in the number of articles published on supercapacitor, **(B)** proportions of overall publications by countries from 2004 to 2019 using the keyword "supercapacitor." (Data is collected from Scopus on 30 November 2019.), **(C)** schematic diagram of electrochemical supercapacitor, and **(D)** conventional capacitor.

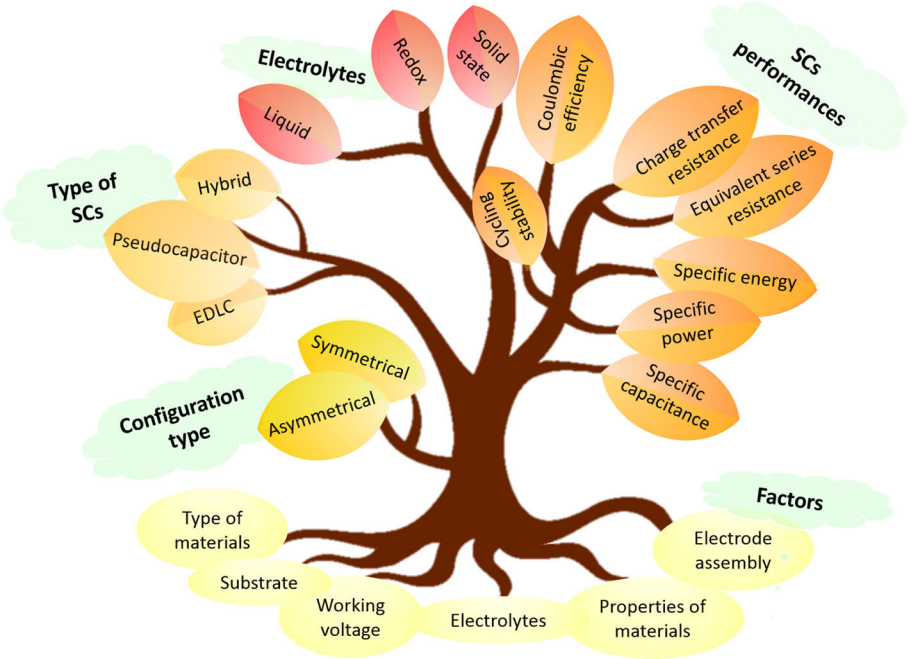

FIGURE 2 | Configuration, types, performance, and factor affecting electrochemical performance of supercapacitors.

to withstand a thousand continuous cycles without any significant changes in performance. However, EDLC has inadequate specific energy (Simon and Gogotsi, 2008).

ii. The charge storage of pseudocapacitors is based on the fast and reversible redox reactions of electroactive materials. Conducting polymers and transition metal oxides/hydroxides are common pseudocapacitive materials. In contrary to EDLC, pseudocapacitors have excellent specific capacitance. However, the poor cycling stability of pseudocapacitors due to the reversible oxidation-reduction reaction at/or near the electrode surface causing swelling and shrinkage of the materials. As a consequence, pseudocapacitors exhibit lower specific power performance than EDLC (Simon and Gogotsi, 2008).

By combining the energy storage mechanisms of EDLCs and pseudocapacitors, hybrid supercapacitors are produced. Hybrid supercapacitors were introduced as an effort to enhance the performance of the existing EDLCs and pseudocapacitors. It can be assembled symmetrically or asymmetrically depending on the configuration assembly (**Figure 2**). A symmetrical supercapacitor is configured with two similar electrode materials consisting of EDLC materials or pseudocapacitive materials (Sun et al., 2017). Whereas, an asymmetrical supercapacitor is made with different anode and cathode electrode materials (Fan et al., 2011). Theoretically, hybrid supercapacitors have better energy storage performances than EDLCs and pseudocapacitors (Kulandaivalu and Sulaiman, 2019). The alluring characteristics of electrochemical supercapacitors outperformed the lithium-ion batteries in terms of its high specific power (> 10 kW kg^{-1}), fast charging-discharging abilities (within few seconds) and long shelf life (>100,000 cycles) (Liu et al., 2016). However, it is still competing with lithium-ion batteries to achieve better specific energy.

Pointing on the specific energy and specific power, these two are the most imperative parameters comparing the performances of energy storage systems and it is commonly represented in a chart known as the Ragone plot. The specific energy (Wh kg^{-1}) typifies the energy capacity that the device is able to hold, whereas specific power (W kg^{-1}) represents the rate of the energy deliverable at a constant current density. This information is usually derived from galvanostatic charge-discharge (GCD) curves by the following equations:

$$Specific\ energy = \frac{0.5 \times (\Delta V^2) \times C_{sp}}{3.6} \quad (1)$$

$$Specific\ power = \frac{E \times 3600}{\Delta t} \quad (2)$$

where ΔV is cell operation potential, C_{sp} is specific capacitance, E is specific energy and Δt is the discharge time (Luan et al., 2013). Based on Equation (1), specific energy can be enhanced by increasing the specific capacitance and cell operation potential (Guo et al., 2019b). The ability of the materials to accommodate the charges is reflected by the specific capacitance. Hence, the electrode material is significantly important to enhance the specific capacitance. Selecting electrode materials should be placed equally on the porosity and surface area of the materials (Shi et al., 2011). However, it is worth to note, not all the surface area of the materials is accessible to the ions from the electrolytes (Lobato et al., 2017). Therefore, the effective surface area is the most accurate term to describe the influence

of the surface area of materials on the specific capacitance enhancement. Notably, pore size playing a crucial role for the electrolyte ion accessibilities within the materials utilizing the surface area, and thus increases the specific capacitance. Young et al. (2018) reported that the pore size of materials should be larger than the size of electrolyte ions for ions penetration. However, the best or suitable material pore size is still in disagreements (Largeot et al., 2008); thus, the authors concluded that each electrode material has its own critical pore size for ion penetration. Additionally, the electrode materials should also possess good electrical conductivity and satisfactory stability for high-performance supercapacitors. Apart from this, an alternative approach to increase the specific capacitance is by widening the cell operation potential. The operating potential of a supercapacitor relies on electrolyte (Pandolfo and Hollenkamp, 2006). The selection of electrolytes is based on (i) type of electrolyte, (ii) compatibility of electrolyte with the electrode material, (iii) the size of electrolyte ions and (iv) contacts between electrolyte and electrode material. As reviewed by Zhong et al. (2015), the electrolyte can be classified into liquid electrolyte comprising aqueous electrolyte (acid, alkaline and neutral) and non-aqueous electrolyte (organic electrolyte and ionic liquids), solid-state electrolyte (dry solid polymer electrolyte, gel polymer electrolyte and inorganic electrolyte) and redox active electrolyte (aqueous electrolyte, organic electrolyte, ionic liquid, and gel polymer electrolyte). Each electrolyte has its own advantages and disadvantages. For example, non-aqueous electrolytes have a wider cell operating potential window compared to aqueous electrolytes (Haas and Cairns, 1999). However, the aqueous electrolyte has greater specific capacitance and conductivity than non-aqueous electrolytes. Therefore, a careful selection of electrolyte is a must to obtain high performance supercapacitors. Another way to maximize the cell potential is by assembling asymmetrical supercapacitors. Asymmetrical supercapacitors with different positive and negative electrodes are able to extend the potential window compared to symmetrical assembly.

There is so much fascinating information on supercapacitors and a single review article is not enough to cover all of it. In the pursuit of producing high performing supercapacitors, a variety of materials have been explored. In light of this, conducting polymers, carbon-based materials and transition metal oxides/hydroxides are the most prospected electrode materials (Kulandaivalu et al., 2018; Mohd Abdah et al., 2018a,b). In recent times, the research is directed toward the development of composites to impede the demerits of these single constituents and to produce high-performance nanostructured materials. Over the last decades, we have seen tremendous improvement in the supercapacitors by designing new nanocomposite electrode materials. The attraction of electrode material for supercapacitor should be based on the following criteria:

a) low cost and easy to prepare.
b) high electronic conductivity to ease the ion transport within the electrode materials. Therefore, will increase the specific capacitance, specific energy, specific power and rate capability.
c) the high surface area with desirable pore size to increase the specific capacitance.
d) high mechanical and chemical stability to withstand the long charge-discharge cycles

The utilization of carbon-based materials in the fabrication of active materials for hybrid supercapacitors is a common practice. This is because of the versatility of carbon-based materials serve as a backbone due to their high mechanical strength, high hardness and excellent thermal properties. In most instances, carbonaceous materials often introduced with pseudocapacitive materials to enhance the supercapacitive performance, such as stability during charge-discharge cycles, the electrical conductivity of the composites and reduce the volume expansion of the composites. In recent years, metal hydroxides including layered double hydroxides (LDHs) have been explored widely as active materials for their multiple oxidation states. Herein, we highlight the advances in the investigation of LDHs containing Ni^{2+} and $Co^{2+/3+}$ with carbon-based materials as electrode materials for supercapacitors. There are several reviews on LDHs that disclose valuable insights on the LDHs and its related composites on their structures, preparation methods, applications and functionalities as summarized in **Table 1**. However, to the best of our knowledge, an extensive review of Ni-Co LDH/carbon nanocomposites for supercapacitors has not been previously reported. This review is intended to provide broad insight into the fundamental understanding of LDHs as well as Ni-Co LDH and Ni-Co LDH/carbon nanocomposites as electrode materials for supercapacitors.

LAYERED DOUBLE HYDROXIDES

LDHs are one of the most captivating 2D inorganic materials that have been applied in various fields, such as anticancer nanomedicine (Kim et al., 2018), photocatalysts (Shao et al., 2015), electrocatalysts (Long et al., 2014), and electrodes in energy storage and conversion technologies (Wang et al., 2018a; Kulandaivalu et al., 2019). The breakthrough of LDHs began with the amazing discovery of hydrotalcite minerals as synthetic materials in the 1940s by Feitknecht and Gerber (1942). However, when it was first described in 1842 by Hochstetter (1842), it was not widely acknowledged by the world as hydrotalcite but rather as mixed hydroxides, magnesium–aluminum hydroxycarbonate with the composition of $Mg_6Al_2(OH)_{16}CO_3{\cdot}4H_2O$. In addition, it is also the first natural occurring hydrotalcite reported in history. Yet, it was not until the 1960s after the discovery of hydrotalcite minerals that the detailed structure analysis on these minerals was fully outlined by Allmann and Taylor using the single crystal X-ray diffraction technique and identified it as the LDHs (Allmann, 1968; Taylor, 2018).

The LDHs are ionic lamellar compounds and better known as hydrotalcite-like clay materials. The name hydrotalcite is due to the similarities to the talc and high water content. Generally, the hydrotalcite-like clay materials can be classified into two types; cationic clays and anionic clays. The naturally occurring hydrotalcites are referred to as cationic clays. They have a stacking of negatively charged layers that have cations within the interlayer regions (**Figure 3**). The layers contain octahedral

TABLE 1 | The recent reviews on layered double hydroxide for supercapacitors.

Title	Summary	References
Research progress of Ni-Mn layered double hydroxide for supercapacitor	This review covers Ni-Mn LDHs as electrode materials for supercapacitors. A brief discussion on the synthesis method of Ni-Mn LDHs and the detailed research developments of Ni-Mn LDHs and its composites in asymmetrical supercapacitors were also discussed	Yan et al., 2018
Recent advances in layered double hydroxide as electrode materials for high-performance electrochemical energy storage devices	In this review, the author discussed the direct and indirect preparation method of various LDHs in detail. Adding to it, the authors also disclose the significant progress on the LDHs in electrochemical energy storage systems including supercapacitors and batteries	Sarfraz and Shakir, 2017
Layered double hydroxides toward high performance supercapacitor	In this review, the authors summarize the recent works of various LDHs as electrode materials for supercapacitors. Moreover, the composition adjustment of LDHs comprising the interlayer anions and host layer metal ions also discussed in detail	Li et al., 2017c
Chemical power source based on layered double hydroxides	The authors highlighted the recent progress of various LDHs in supercapacitors, fuel cells, metal-air batteries, lithium-ion batteries	Wang et al., 2015
Layered Double Hydroxide/Graphene Composites and Their Applications for Energy Storage and Conversion	The synthesis of LDHs/graphene-based composites was discussed in this article. Their performances in supercapacitors and electrochemical oxygen evolution reaction catalysis were also addressed	Hai-Yan Wang, 2018
Layered double hydroxide-graphene-based hierarchical nanocomposites: Synthetic strategies and promising applications in energy conversion and conservation	Methods in designing LDHs/graphene-based composites, and their applications as electrode materials in supercapacitors and as electrochemical or solar energy-driven photocatalytic water oxidation catalysts were addressed in detail	Varadwaj and Nyamori, 2016
Graphene/layered double hydroxides nanocomposites: review of recent progress in synthesis and application	This review covers the recent developments of LDHs/graphene-based composites along with their synthesis methods in various applications including oxygen evolution reaction, supercapacitors, hybrid sensors, adsorption, catalysis, water purification and flame retardant materials	Daud et al., 2016
Recent progress in layered double hydroxide based materials for electrochemical capacitors: Design, synthesis and performance	This review focuses on the broad aspect of LDHs and their composites with carbon materials, metals, metal oxides, metal sulfides, metal phosphides and polymers and further reviewing their performances for supercapacitors	Zhao et al., 2017

sheets in between the tetrahedral sheets, where typically cations in the tetrahedral sheets are silicon ion (Si^{4+}) and aluminum ion (Al^{3+}), whereas in octahedral are Al^{3+}, ferric ion (Fe^{3+}), and magnesium ion (Mg^{2+}) (Vaccari, 1998).

Unlike cationic clays, the anionic clays are commonly referred to LDHs that stacking brucite-like layers. Typically, the mirror image of cationic clays is the anionic clays. Instead of cations as in cationic clays, the anionic clays consist of anions in the positively charged interlayers (Abellán et al., 2020). In order to understand the structure of LDHs, the insights on the structure of brucite, $Mg(OH)_2$ is very crucial. In brucite, the hydroxyl ions are placed in the six vertices of the octahedral surrounding the divalent Mg^{2+} ion, which are located in the middle (**Figure 4A**). Each individual octahedral unit shares its edges with each other forming electrically neutral infinite layers. These layers are stacked one on top of another and bonded through hydrogen bonds, forming the brucite. The hydroxyl ions in these layers are closely packed giving 2D triangle symmetrical geometry. Then, the positive charges are introduced in the layers by partially replacing the Mg^{2+} ions with Al^{3+} forming the Mg-Al LDHs. The layers are then neutralized by the anions that intercalated in the interlayer region (in between the successive layers of layered double hydroxides). Water molecules also present in between the layers that bound with the hydroxide ions through hydrogen bonds (Sun et al., 2015). Various combinations of metal ions in LDHs also synthesized in a similar manner which can be expressed by the general formula:

$$[Me^{2+}{}_{1-\chi}Me^{3+}{}_{\chi}(OH)_2]^{\chi+}(A^{\alpha-})_{\chi/\alpha}.yH_2O$$

where, Me^{2+} is divalent metal cations (Zn^{2+}, Ni^{2+}, Co^{2+}, Ca^{2+}, etc.) and Me^{3+} is trivalent cations (Al^{3+}, $Cr^{3}+$, Fe^{3+} etc) as shown in **Figure 4A**. $A^{\alpha-}$ is abbreviated for anions with negative charges (Cl^-, CO_3^{2-}, NO_3^-, etc). A broad range of χ values have been reported in the preparation of LDHs, however, there is still disagreement is fixing the limit of the values. Nevertheless, in the preparation of pure LDHs, the χ values are fall in the range of $0.2 \leq \chi \leq 0.33$ (Walton, 2018).

The wide compositional and structural diversities in the LDHs system such as tunability of metal cations in the layers, easy adjustment of the molar ratio of metal cations and exchangeability of interlayer anions bestow various types of LDHs with unique architectures leading to incomparable physical and chemical properties. Adding to this, the variable oxidation states of metal cations in the LDHs and substitution of metal cations in the layers which provide high dispersion of metals boost the exploitation of metals cations of LDHs. Thus, these properties aid in enhancing the capacitive performances of LDHs as active materials particularly in supercapacitors as summarized in

Figure 4B. Indeed, over the last decades, there are ever-growing publications related to the LDHs as electrode materials for supercapacitors (**Figure 4C**).

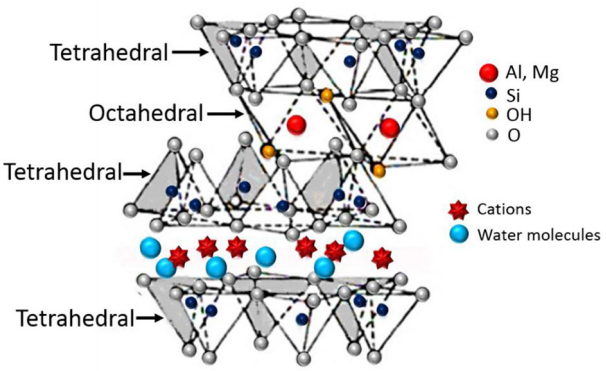

FIGURE 3 | Schematic illustration of cationic clay (Ghadiri et al., 2015).

STRUCTURAL IDENTIFICATION OF LDHs

One must be aware that X-ray diffraction (XRD) is a primary technique to analyze the crystalline phases, degree of crystallinity, and crystallite sizes of layered compounds (Cullity, 1957). Practically, in order to develop the layered compounds involving intercalation, knowledge on its crystalline structure is a must.

Prior to the XRD measurements, it is crucial to obtain a good Me^{2+}/Me^{3+} stoichiometry (the χ values) based on the molarity of species in LDHs. As mentioned earlier, the often reported χ values to fall between $0.2 \leq \chi \leq 0.33$, where the Me^{2+}/Me^{3+} ratio is between 2 and 4. The χ value is obtained using the following formula:

$$\chi = \frac{Me^{3+}}{Me^{3+} + Me^{2+}} \tag{3}$$

There are some arguments on the purity and structures of the compound formed if the χ values fall beyond the above-mentioned range. If the χ value is above 0.33, most likely Me^{3+}-O–Me^{3+} linkages will occur causing the electrostatic

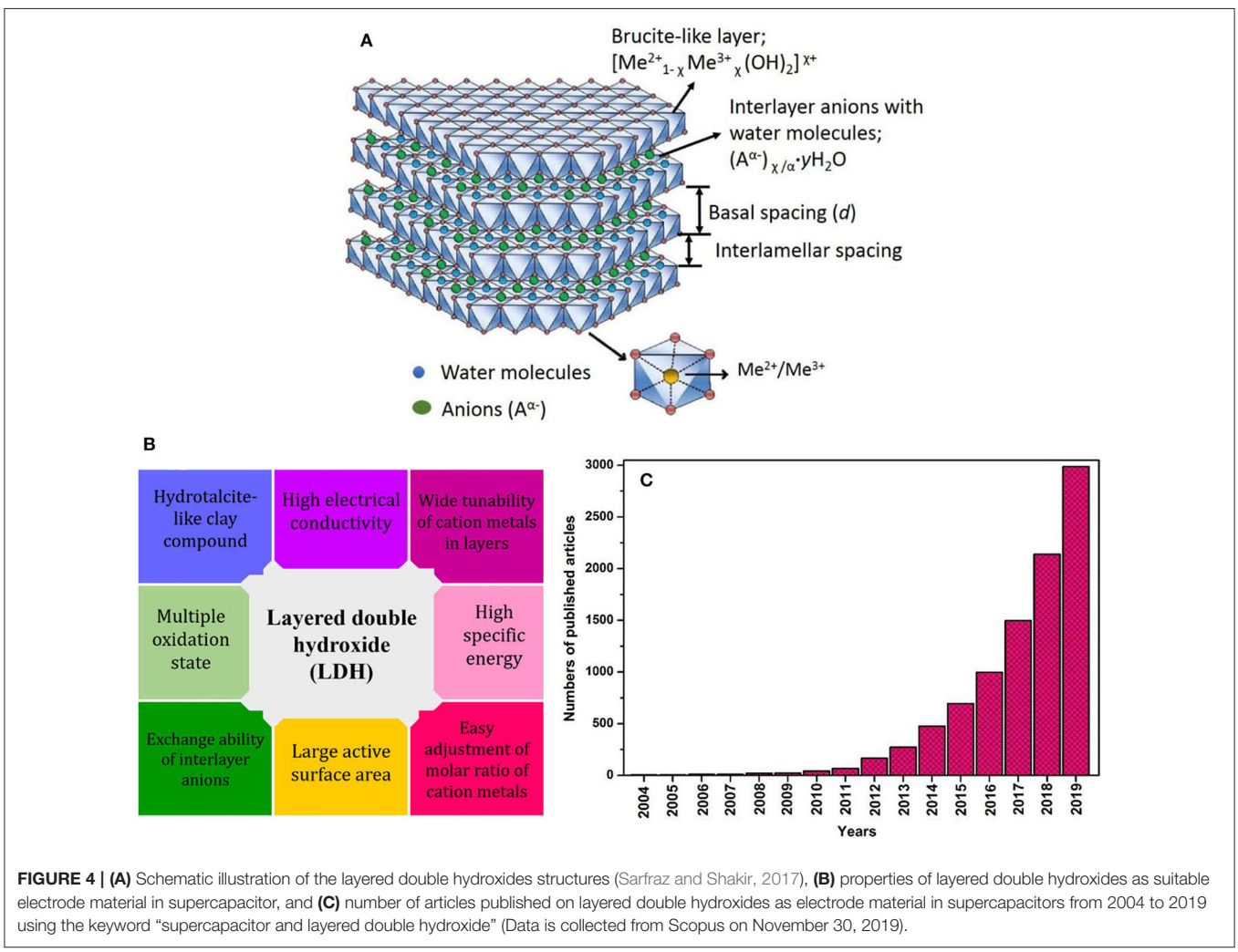

FIGURE 4 | (A) Schematic illustration of the layered double hydroxides structures (Sarfraz and Shakir, 2017), **(B)** properties of layered double hydroxides as suitable electrode material in supercapacitor, and **(C)** number of articles published on layered double hydroxides as electrode material in supercapacitors from 2004 to 2019 using the keyword "supercapacitor and layered double hydroxide" (Data is collected from Scopus on November 30, 2019).

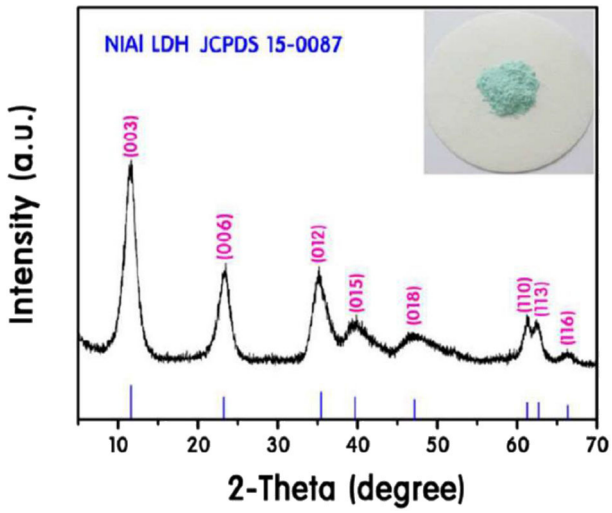

FIGURE 5 | XRD pattern of NiAl (Li et al., 2017a).

repulsion which eventually disturbs the lattice position. This phenomenon is termed as the cation avoidance rule. This rule defines from the secondary coordination sphere's point of view, where a 3+ metal cation could not contain another 3+ metal cation (Forano et al., 2006; Wang et al., 2013b). However, in a rare occurrence, χ values more than 0.33 are found, but it is believed this might be due to the experimental errors such as the presence of hydroxide compounds with amorphous phases that undetectable by the XRD or anions intercalated outside the hydrated layer galleries (Arias et al., 2013). On the other hand, if the $\chi < 0.33$ (which means Me^{2+}/Me^{3+} ratio is below 2) it will cause damages to the structure of LDHs due to the substitution of large Me^{3+} in LDHs (Wang et al., 2013b). Also, unusually very low or very high range of stoichiometry will result in the formation of LDHs with a mixture of other hydroxide compounds, $Me^{2+}(OH)_2$ or $Me^{2+}(OH)_3$ or $Me^{3+}OOH$ that provide inaccurate results. Therefore, stoichiometry is very important to produce pure LDHs.

The molar ratio of Me^{2+}/Me^{3+} is also equally important in the particle size of the resultant LDHs. LDHs prepared with a molar ratio between 1 and 3 provide a highly monodispersed particle size distribution (Chang et al., 2013). Yet, it is also expected that the LDHs might grow in disordered orientation when the molar ratio is approaching 1 (Cavani et al., 1991). Still, the root cause for the disordered phase could not be centered solely on the molar ratio. The preparation criteria, e.g., temperature, pressure, choice of precursors, and co-precipitation pH is also responsible for this formation (Pausch et al., 1986). However, when the molar ratio exceeds 3, noticeable enlargement in the particle size is normally observed due to agglomeration (Sun et al., 2015).

XRD is an important method in evaluating the LDHs formation. The confirmation of LDHs formation is accomplished by the presence of basal reflections (00*l*), at lower degrees ($2\theta = 10$ to 35°). The basal reflections indexed as (003) and (006) appear as strong/sharp, narrow and symmetrical diffraction peaks (**Figure 5**). These peaks designate to the basal reflection of intercalated anions (e.g., Cl^-, NO_3^-, SO_4^{2-}) in the galleries and ordered stacking sequence of LDHs (Mahjoubi et al., 2017; Richetta et al., 2018). Moreover, it is an indication of the formation of highly crystalline LDHs. The first basal reflection (003), more commonly appears with higher intensity than the second basal reflection, (006). However, in certain cases, the (006) reflection emerges more intense than the reflection of (003) which is related to the presence of complex metal anion in the interlayer of LDHs which increases the electron density in the midplane (Boclair et al., 1999; Beaudot et al., 2004).

The basal spacing is another important aspect of the LDHs and it can be calculated from the XRD pattern using the Bragg law:

$$n\lambda = 2d_{hkl}\sin\theta \tag{4}$$

where n is the diffraction order (an integer), λ is the wavelength of the X-rays (nm), d is the basal spacing (Å) and θ is the diffraction angle. Basal spacing is defined as the distance from the plane of a layer with its adjoining layer as shown in **Figure 4A**. The value of basal spacing is determined from the reflections of basal peaks (00*l)* and in some cases from the reflections of non-basal peaks ($hk \neq 0$). Of course, when preparing the LDHs, the basal spacing will arise differently depending on the preparation condition as mentioned earlier. Nevertheless, the molecular symmetry, charge, structure, size, type and orientations of anions used in the preparation of LDHs have a great influence on the basal spacing (Albiston et al., 1996; Kameda et al., 2006). Adding to this, intercalation and removal of water molecules into/from the interlayers also have an impact on the basal spacing (Li et al., 2017b).

Another essential step in analyzing the LDHs structure is determining the unit cell parameters. The basal spacing of reflection (003) defines unit cell parameter c or known as an interlayer distance along the c-axis and it represents the thickness of one brucite-like layer and one interlamellar space (Li et al., 2004). Note that, the c parameter would appear larger if there is a presence of impurities in the interlamellar space. Additionally, by assuming the thickness of the brucite-like layer to 4.769 Å as reported by Miyata (1975), the value interlamellar spacing can be deduced. Whereas, the basal spacing of reflection (110) defines the unit cell parameter a which reflecting the distance between the two metal cations within the layers. These values could be obtained using the expression, $c = 3d_{(003)}$ and $a = 2d_{(110)}$.

Ni-Co LAYERED DOUBLE HYDROXIDES

As it has been described earlier, redox active materials such as transition metal-based hydroxides and oxides have been used as active materials over a long period of time in supercapacitors due to their extraordinary properties such as high theoretical specific capacitance, multiple oxidation states and easy modification (Liu et al., 2018b; Qiu et al., 2018). Particularly, ruthenium oxides with high proton conductivity and high reversible oxidation-reduction process inevitably stand as a promising active material for supercapacitors. Nevertheless, this material is also known

for its high toxicity, high-priced and rareness in nature obstruct its wide applicability (Kim and Kim, 2006; Vellacheri et al., 2012). Apart from ruthenium oxides, nickel-based redox active materials and cobalt-based redox active materials are considered as promising active materials. In that context, to date, nickel hydroxides, $Ni(OH)_2$ and cobalt hydroxides, $Co(OH)_2$ are the most notably explored single metal hydroxides particularly in supercapacitors.

$Ni(OH)_2$ is extensively studied due to its low toxicity, abundance in nature, inexpensive and environmental friendliness. Nevertheless, it exhibits a low electrical conductivity ranges from 10^{-13} to 10^{-17} S cm^{-1} which consequently decreases the rate capability and life span (Motori et al., 1994). Moreover, slow ion diffusion rates and volume expansion during the charge-discharge cycles also restraining its electrochemical storage applications. α and β-$Ni(OH)_2$ have a high theoretical capacitance of 2,081 F g^{-1} within the potential window of 0.5 V (Wang et al., 2018c). α-$Ni(OH)_2$ is thermodynamically less stable than β-$Ni(OH)_2$ and easily converted to β-phase material by aging in alkaline solution or during continuous charge-discharge process. However, the former has a higher specific capacitance and good ionic conductivity than the latter due to high charge capacity and electrochemical reversibility (Meng and Deng, 2016). Additionally, despite the fact that both α-$Ni(OH)_2$ and β-$Ni(OH)_2$ contain close-stacked 2D $Ni(OH)_2$ layers, only α-$Ni(OH)_2$ comprises intercalated species (anions and water molecules). Thereby, resulting in differences in the electrochemical properties (Bastakoti et al., 2012).

$Co(OH)_2$ also possesses merits similar to $Ni(OH)_2$ such as low cost, environmental compatibility and high reversibility. $Co(OH)_2$ also exists in two polymorphs, α and β-$Co(OH)_2$. Compared to β-$Co(OH)_2$, α-$Co(OH)_2$ has higher electrochemical activity due to its larger interlayer spacing. The α-$Co(OH)_2$ with hydrotalcite structure is highly unstable structure and easily convert into brucite-like β-$Co(OH)_2$ (Cui et al., 2013). Additionally, this single hydroxide material also has a high theoretical capacitance of ∼3,460 F g^{-1} in a potential window of 0.6 V (Cao et al., 2004).

Undoubtedly, both of these materials exhibit exceptional properties. The great feasibility of these layered materials with large interlayer spacing endows effective accommodation of ions from the electrolyte in interlayers (Cui et al., 2013). Hence, the specific capacitance and rate capability can be enhanced significantly. Therefore, by combining these materials in the formation of Ni-Co LDHs can improve the overall performances in supercapacitors in terms of specific capacitance, cycling stability and rate capability. Incorporating nickel into the $Co(OH)_2$ system and vice versa gains benefits from the other and overcomes the drawbacks. The presence of nickel help in strengthening the electrochemical performances, while cobalt increases the electrical conductivity of the LDHs system (Windisch et al., 2001). It is reported that the formation of γ-NiOOH from $Ni(OH)_2$ is responsible for the volume expansion. Therefore, by incorporating cobalt into the $Ni(OH)_2$ the formation of γ-NiOOH can be surpassed as it can improve the oxygen over potential. While, during the charge-discharge process, the oxidation of Co^{2+} to highly conductive CoOOH improves the overall conductivity of the electrode material (Chen et al., 1999).

The performance of Ni-Co LDHs depends on the faradaic redox reaction of cobalt and nickel hydroxides. The charge storage of Ni-Co LDHs is related to chemical state changes of Ni^{2+}/Ni^{3+} and $Co^{2+}/Co^{3+}/Co^{4+}$, which refers to the adsorption of ions onto the surface of active materials during the redox reaction. The charge storage mechanism of Ni-Co LDHs during electrochemical measurements in the aqueous electrolyte is shown in the Equations 3–5 (Xie et al., 2012):

$$Ni(OH)_2 + OH^- \rightarrow NiOOH + H_2O + e^- \quad (5)$$

$$Co(OH)_2 + OH^- \rightarrow CoOOH + H_2O + e^- \quad (6)$$

$$CoOOH + OH^- \rightarrow CoO_2 + H_2O + e^- \quad (7)$$

FACTORS INFLUENCING THE FORMATION OF Ni-Co LDHS

Ni-Co LDHs have been an ideal candidate for supercapacitors for their distinctive layered structures, flexible tunability of anions/cations, and multiple oxidation states. In recent years, researchers have done astounding works on Ni-Co LDHs and they have focussed mainly on the composition, morphology, particle size and surface area of the LDHs in order to obtain high performance materials. It should be noted that the effectiveness of the charge storage of Ni-Co LDHs in supercapacitor varies with the properties of this active material. Morphologies, crystallinity, electrical conductivity and surface area of LDHs are very important to determine the electrochemical performances. Therefore, the factors influencing these factors will be reviewed in this section.

pH

Among the different fabrication routes for the LDHs, the co-precipitation method at a constant pH is commonly used. The pH value has a pivotal role in the formation of LDHs, particularly on the structure of LDHs. Typically, an alkaline solution (precipitant) added into the mixed metal salt solution to control the pH at a selected value has resulted in the co-precipitation of metals. Various type of alkaline solution is utilized to control the pH. With regard to Ni-Co LDHs, Li et al. (2016c) and Wang et al. (2018b) have chosen pH 8 as the optimal value to prepare the Ni-Co LDHs. Whereas, Cheng et al. (2013) and Mehrabimatin et al. (2019) have synthesized the LDHs by adjusting the pH at 9 through the addition of ammonium hydroxide solution. While, Shen et al. (2019) have used sodium hydroxide to maintain the pH to 9. On the contrary, pH 10 was also reported as the optimum medium to prepare the Ni-Co LDHs (Cao et al., 2019). In this study, the author used L-ascorbic acid and ammonia to control the pH. The precipitation pH value of 7.34 has also been reported using 2-methylimidazole (Wang et al., 2017b). The rule of thumb in this whole synthesis process is the pH value should exceed 4.0 and the pH range from 7 to 10 is commonly used to synthesize the Ni-Co LDHs. This is due to the fact that in the acidic condition the brucite-like layer in the LDHs will collapse. It also greatly argued that at lower pH

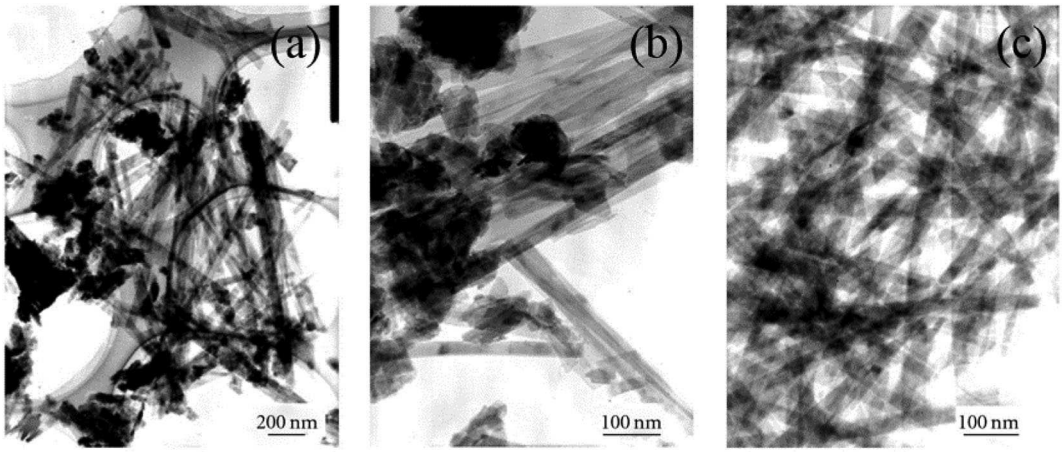

FIGURE 6 | TEM images for Ni/Al LDHs synthesized at different pH values. **(a)** 5.5, **(b)** 8.5, **(c)** 10.0 (Zhao et al., 2011).

values, an amorphous compound is produced, while at higher pH values, the brucite-like layer of LDHs with high crystallinity will evolve. However, there is no extensive works have been carried out to prove this statement. Furthermore, the addition of precipitant in the synthesis of LDHs produces hydroxide ions which involve in the redox reaction and eventually increase the crystallinity and hydrophilicity of the LDHs (Wang et al., 2013a). Thus, the charge transport and ion movement will be reinforced. Additionally, the basic growth condition also encourages the fast and uniform growth of LDHs whether in the form of nanoparticles or flower-like structure or flakes-like morphologies (Wang et al., 2013a). Talking about morphology, pH has a great impact on the morphology of LDHs which indirectly reflects the surface area (**Figure 6**). One must notice that different pH values resulted in different morphologies, such as nanorods, nanosheets, 3D nanoparticles, etc. (Zhao et al., 2011; Li et al., 2016c). However, there are little references which have been reported on the effect of pH on the morphology of Ni-Co LDHs. Nevertheless, the selection of pH for the formation of LDHs should be suitable for both metal ions (in the case of LDHs with two types of metals) to precipitate simultaneously. Therefore, it is always preferred to choose a pH value higher or equal to the precipitation pH value of a respective metal hydroxide considering their solubility equilibrium constants. In contrast with the usual basic condition, a study reported pH 6, as the optimal pH to prepare the Ni-Co LDHs using electrodeposition method (Chen et al., 2014c). The author claimed that at pH $\geq$ 7, pre-precipitation of hydroxides occurs causing higher rate of $Co(OH)_2$ formation than LDHs due to its low solubility at this pH. Whereas, at pH 6, the rate of nickel and cobalt hydroxides formation in LDHs is equal. Adding to this, a significant variation in values of specific capacitance is also noted when the pH is varied. When deciding the value of pH for LDHs synthesis, a fair consideration need to place on the type and nature of anions of the LDHs. This is due to the solubility of anions (e.g., Cl^-, NO_3^-, SO_4^{2-}) which differ from each other. Therefore, the amount of anions intercalated in the LDHs and the size of LDHs nanoparticles are also vary (Li et al., 2010). Moreover, the stability of LDHs is determined by the stability of intercalated anions. For example, Ni-Co LDHs containing chloride anion in the interlayer are stable in the pH ranging from 3.8 to 8.9 (Sun et al., 2013).

In general, Ni-Co LDHs can be synthesized in basic aqueous solution and mild acidic or near a neutral aqueous solution. Nevertheless, the selection of pH is not solely relied on one particular factor but other criteria for instance concentration of metals salts, the ratio of Me^{2+}/Me^{3+} ions, type of anions and preparation method which need to be taken into consideration.

Ratio

The optimization of the Me^{2+}/Me^{3+} ratio in LDHs is pivotal in the morphology, phase structure and capacitive behavior. Pointing to Ni-Co LDHs, plenty of work has been performed on the optimization of Ni^{2+}/Co^{2+} ratio (Wang et al., 2017b, 2019a). Synthesizing the Ni-Co LDHs by varying the metal ion ratios may result in variation in growth rates, nanostructures and pore size/size distribution (**Table 2**). Sun et al. (2013) studied the changes in the structure of Ni-Co LDHs when the metal ion ratios are altered. From the morphological point of view, when the ratio of cobalt is increased with respect to nickel (Ni:Co), changes from flower-like nanosheets (1:0) to nanosheets (1:1), nanospheres enclosed in nanoplates (1:2), highly porous 1D nanorods (1:4) and nanoparticles (0:1) is noticed. Interestingly, the Ni-Co LDHs (1:4) with 1D nanorods exhibited excellent electrochemical performances regardless of their average specific surface area than the ratio of 1:2. It was deduced that the broad pore size distribution (2 to 15 nm) in the former sample compared with other metal ratios reduces the charge transfer resistance and promotes the movement of electrolyte. In contrast with this finding, Kulkarni et al. (2013) demonstrated nanoflakes morphology for all Ni-Co LDHs (1:0, 0.75:0.25, 0.5:0.5, 0.4:0.6, 0.25:0.75, and 0:1), however, they showed variation in flakes size, pore size/distribution and the number of layers. The authors claimed that the amount of nickel in the layer is the

TABLE 2 | Summary of preparation condition, morphology, and specific capacitance of Ni-Co LDHs as supercapacitor electrode.

Method	pH	Ni/Co ratio	Temperature (°C)/ Reaction time (hour)	Capacitance	Nanostructure	References
Solvothermal	7.34	1:1	120/14	2,242.9 F g^{-1} at 1 A g^{-1}	Nanosheets	Wang et al., 2017b
Solvothermal	–	2:3	160/6	2,158.7 F g^{-1} at 1 A g^{-1}	3D hydrangea-like microspheres	Yan et al., 2015
Hydrothermal	–	2:1	100/10	293.9 C g^{-1} at 1 mA cm^{-1}	Nanowires	Zhang et al., 2019
Hydrothermal	–	9:1	100/48	808.4 C g^{-1} at 1 A g^{-1}	3D sea urchin-like nanosheets	Hou et al., 2019
Co-precipitation	8.72	6:4	55/15	2,228 F g^{-1} at 1 A g^{-1}	3D flower-like nanosheets	Li et al., 2016c
Electrodeposition	–	1:1	–	~0.8 F cm^{-2} at 2 mA cm^{-2}	Nanosheets	Wang et al., 2019c
Microwave-assisted hydrothermal	–	3:2	200/2	1,720 F g^{-1} at 3 A g^{-1}	Flower-like nanosheets	Wang et al., 2019b
i) Hot-air oven ii) Electrodeposition	–	2:1	90/9	536.96 μAh cm^{-2} at 2 mA cm^{-2}	Nanosheets on nanoflakes	Nagaraju et al., 2017
Co-precipitation	–	1:1	140/24	777 C g^{-1} at 1 A g^{-1}	Flower-like nanosheets	Qin et al., 2019
Hydrothermal	–	2:1	High temperature/2.5	–	Nanoflower	Wu et al., 2019b
Electrodeposition	–	4:1	–	374.7 mAh g^{-1} at 2 A g^{-1}	Nanosheets	Wu et al., 2019a
Co-precipitation	9	1:1	–	2,305 F g^{-1} at 1 A g^{-1}	Nanodisc	Cheng et al., 2013
Electrodeposition	–	1:1	–	2,200 F g^{-1} at 5 A g^{-1}	Nanotubes with nanosheets	Liu et al., 2017
Electrodeposition	–	2:1	–	1,862.4 F g^{-1} at 4 A g^{-1}	Nanosheets	Nagaraju et al., 2016
Microwave-assisted hydrothermal	–	1:1	100–140/1–3	1,580 F g^{-1} at 10 A g^{-1}	Nanocones	Liu et al., 2012
Electrodeposition	–	1:1.5	–	2,104 F g^{-1} at 1 A g^{-1}	Nanosheets	Gupta et al., 2008
Co-precipitation	–	1:4	80/6	1,030 F g^{-1} at 3 A g^{-1}	1D nanorod	Sun et al., 2013
Electrodeposition	–	1:1	–	~1,300 F g^{-1} at 1 A g^{-1}	Nanoflakes	Ge et al., 2019
Electrodeposition	–	1;2	–	~1,213 F g^{-1} at 5 mV s^{-1}	Nanoflakes	Kulkarni et al., 2013
Electrodeposition	–	1:2	–	1.536 C cm^{-2} at 2 mA cm^{-2}	Flower-like nanosheets	Yang and Li, 2019
Electrodeposition	–	1:2	–	1,200 F g^{-1} at 1 A g^{-1}	Nanosheets on nanorods	Wen et al., 2016
Solvothermal	–	1.5:1	180/24	~900 F g^{-1} at 1 A g^{-1}	Nanosheets	Cai et al., 2015
Co-precipitation	–	1:2	Room temperature/6	~550 F g^{-1} at 2 A g^{-1}	Flower-like nanosheets	Zhao et al., 2015
Electrodeposition	–	1:2	–	1.52 C cm^{-2} at 2 mA cm^{-2}	Open porous nanosheets	Nguyen et al., 2017
Hydrothermal	–	1:1	100/10	1,734 F g^{-1} at 6 A g^{-1}	Nanosheets	Pu et al., 2014
Hydrothermal	–	1:1	160/6	1,600 F g^{-1} at 1 A g^{-1}	Interconnected nanosheets	Xia et al., 2015
Co-precipitation	9	1:1	Room temperature/12	1,809 F g^{-1} at 1 A g^{-1}	Flower-like nanosheets	Hu et al., 2009
Electrodeposition	–	2:1	–	1,587.5 F g^{-1} at 0.5 A g^{-1}	Nanosheets	Wei et al., 2018
Microwave-assisted hydrothermal	–	4:1	–	1,170 F g^{-1} at 4 A g^{-1}	Hexagonal nanosheet	Chen et al., 2014a
Co-precipitation	–	2:1	–	774 F g^{-1} at 0.2 A g^{-1}	Hexagonal crimpled nanosheet	Wang et al., 2016
Hydrothermal		3:7	110/0.5	943 F g^{-1} at 20 mV s^{-1}	Interwoven fabric	Jeong et al., 2019
Hydrothermal co-deposition		1.5:1	180/24	2,682 F g^{-1} at 3 A g^{-1}	Porous nanostructure	Chen et al., 2014b

deciding factor for the morphology of LDHs. They support their arguments with a wettability study where the LDHs with high nickel contents showed superhydrophilic characteristics. Regardless of the detailed explanation given in this study, the authors missed to address the importance of cobalt in the LDHs, and how does it influence the morphology of LDHs.

The metal ion ratios also influence the crystallinity and phases of LDHs. Sun et al. (2013) have studied that when Ni-Co ratio (which varies from 0 to 1) was lowered than 0.5, mixed phases of nickel hydroxide hydrate and cobalt carbonate hydroxide were more obvious in the LDHs. Moreover, the XRD peak intensities also weaken with the decrement of nickel to cobalt ratio exhibiting the poor crystallinity of LDHs. In another study on Ni-Co metal ion ratios of 0, 0.3, 0.6,1, 3 and 1 revealed contrary crystallinity results (Kulkarni et al., 2013), in which decrease of metal ion ratios leads to sharp and intense peaks of hydrotalcite phase, showing the good crystallinity of the LDHs.

Reaction Temperature

Unlike the carbon-based materials which are very stable in any temperatures, LDHs are very delicate and sensitive, making the selection of temperature in the synthesis of LDHs is very crucial. There is no fixed value of temperature for the formation of LDHs. The selection of temperature varies with a few factors namely synthesis method, aging time, type of metal cation and metal cation ratio etc. In most cases, even the same synthesis method was applied, and different temperatures was used. For instance, Hu et al. (2009) and Zhao et al. (2015) have prepared Ni-Co LDHs with flower-like nanosheets via co-precipitation method at room temperature. While, a few other studies reported similar findings at a temperature of 55°C (Li et al., 2016c) and

140°C (Qin et al., 2019) using the same method. The selection of temperature also depends on methods. Mostly, solvothermal and hydrothermal methods use higher reaction temperatures compared to the co-precipitation method. In the formation of LDHs, former methods are more preferable due to uniform and homogenous particle size compared to co-precipitation. Moreover, these methods produced LDHs with larger particle size with high crystallinity. The reason is that the reactants are exposed to thermal treatment at pressurized conditions. In a study conducted by Oh et al. (2002), the author reported that increasing the reaction temperature in the range of 100 to 180°C via hydrothermal method yielded LDHs with a larger particle size varying from 115 to 350 nm. The authors have also manifested that differences in the temperature have profound effect on the crystallinity of the LDHs as shown by the reflection intensity in the XRD. However, it is worth to note that at high temperature (> 300°C), the structure of LDHs tend to collapse (Li et al., 2012a).

CARBON MATERIALS

In the past decades, carbon materials are designed with LDHs to deliver high specific capacitance, specific energy, specific power and remarkable stability. Looking into the history, the word "carbon" is originated from the Latin word "*Carbo*" defining coal is now taking the world by storm. Carbon is found abundantly on the earth and almost all the living and non-living things on earth are made up of carbon. In the scientific world, carbon has been the most captivating material since the introduction of graphite and diamond; the allotropes to the world. Basically, it consists only of carbon atoms, but they have intriguing physical and chemical properties due to its remarkable electronic structures to adapt *sp*, sp^2, and sp^3 configurations. There are other several carbon allotropes such as fullerenes, carbon quantum dots, onion-like carbon, graphene-family nanomaterials (GFN), and so forth. The existence of carbon materials in different dimensional and forms made it stand out from other materials.

Generally, carbon materials can be classified according to their dimensionality; zero-dimensional (0D), one-dimensional (1D), two-dimensional (2D), and three-dimensional (3D) nanostructured materials. These materials have their unique characteristics that distinguish them from one to another. Briefly, the 0D carbon nanostructures are defined as particles with spherical-like shapes and their sizes are normally in nanometric range. The 0D nanostructured can be further classified into solid, hollow and core-shell nanostructured. The solid 0D carbon nanostructures (e.g., porous carbon) are famous for their variety pore size distributions; macroporous (>50 nm), mesoporous (2–50 nm), and microporous (<2 nm) materials. On the other hand, the volume density and high surface area-to-volume ratio are the merits of the hollow 0D nanostructures (Lai et al., 2012). Additionally, by controlling the inner and outer diameter, the features of the hollow shell such as thickness and surface porosity can also be tailored according to the needs. Whereas, the uniqueness of core-shell lies in the versatility of the core-shell which can be made of different materials as core or shell and tunability of the properties by varying the shape, size, morphologies and constituent of core-shell. The core-shell 0D carbon nanostructures are often referred to as a spherical-shaped core carbon coated with a carbon shell. The core-shells can also be fabricated in the form of mesoporous nanostructures. It is also feasible to fabricate carbon nanostructures with multiple particles of core coated with a sole shell or vice versa. A hollow carbon shell with a hollow core or with a removable core is another form of core-shell nanostructures (Feng et al., 2018). Fullerenes, onion-like carbon, carbon quantum dots, graphene quantum dots, and carbon nanoparticles are examples of 0D carbon nanostructures.

Whereas, fibers or wire-like shaped nanostructures are categorized as 1D carbon materials such as carbon nanotubes, carbon nanohorns, carbon nanofibers, carbon nanowires and so forth. The 1D carbon nanostructures have a high surface area-to-volume ratio and two-dimension restraints that give superior chemical and physical properties (Weng et al., 2014). Additionally, due to their unique geometrics, the 1D carbon nanostructures have remarkable electron and ion transport pathways. This will promote better electrochemical properties and the ability to endure the volume changes and adapts to the mechanical strain. The 1D nanostructures can be assorted into three groups; (a) relative ratio between length-to-diameter is < 10 (e.g., carbon nanorods), (b) relative ratio between length-to-diameter is more than 10 (e.g., carbon nanowires) (Li et al., 2019b) and (c) structure with hollow walls (e.g., carbon nanotubes) (Pan et al., 2018).

The 2D carbon nanostructures are defined as materials with two dimensions beyond the nanometric ranges (Tiwari et al., 2012). Interestingly, the 2D materials are in a layered shape resembling a planar sheet. The GFN including graphene, few-layered graphene (FLG), graphene oxide (GO) and reduced graphene oxide (rGO) are examples of 2D carbon nanostructures. These materials are known for their extraordinary conductivity and mechanical strength making them a suitable candidate for supercapacitors. For supercapacitor applications, the higher surface area to volume ratio makes GFN the most desirable materials. As an outstanding electrode, GFN predominantly graphene has a remarkably high theoretical surface area up to > 2,500 m^2/g (Singh, 2016). Yet, a propensity for self-agglomeration due to the existence of strong van der Waal forces between the graphene sheets is the main hurdle to generate graphene-based electrodes (Wang and Liu, 2011). The 2D graphene is the building block for 3D graphite. Basically, the 3D carbon nanostructures are made of low-dimensional building blocks and carbon foam and mesoporous carbon are the most explored 3D nanostructures. They have a high surface area and large electrode-electrolyte interface which provides efficient ion pathways (Tiwari et al., 2012; Zhi et al., 2013) as supercapacitor electrodes. Other than foams and mesoporous materials, activated carbon, carbon aerogels, nanopillars, nanoflowers, and nanocoils are also under the category of 3D nanostructures.

Even though the above-mentioned carbon materials possess fascinating properties, it is still a challenging endeavor for researchers to produce high-performance carbon materials as electrodes for supercapacitors. The collaboration of carbon materials with pseudocapacitive materials is a route to augment

TABLE 3 | Comparison of carbon materials, LDHs and carbon-LDHs composites as electrode materials for supercapacitors.

Materials	Specific capacitance	Conductivity	Surface area	Stability	Cost
Carbon materials	Low	Low	High	High	Cheap
LDHs	High	High	Moderate	Low	Expensive
Carbon-LDHs composite	Can be improved significantly depending on the suitable composition of the LDHs and carbon materials in the composite				Moderate

the electrochemical properties for supercapacitors. In this article, we will focus on the carbon materials combined with LDHs as electrode materials for supercapacitors and **Table 3** compares the properties of carbon materials, LDHs and carbon-LDHs composites as electrode materials for supercapacitors.

Ni-Based LDHS Combining With Carbon-Based Materials

In this section, Ni-based LDHs composite combined with carbon materials as electrodes for supercapacitors will be discussed. Li et al. (2015a) *in-situ* grown Ni-Al LDHs nanosheets on the carbon nanotubes pre-coated by the alumina (γ-Al_2O_3) showed decent improvement in term of capacitive performances. The use of γ-Al_2O_3 is very crucial in this study as a source of Al for the formation of LDHs. γ-Al_2O_3 has better dissolution than commonly used AlOOH (Li et al., 2012b). The author studied the asymmetrical configuration of this composite with activated carbon as the negative electrode and discovered a specific capacitance of 115 F g^{-1} with a specific energy of 52 Wh kg^{-1} at a current density of 1 A g^{-1}. He deduced that the introduction of carbon nanotubes is responsible for the exquisite performances shown by this composite, where carbon nanotubes (i) hinder the restacking of LDHs during synthesis, (ii) bridge the interfacial contact, and (iii) provide a conductive surface for uniform growth of nanosheets.

While, Li et al. (2014) have developed Ni-Al LDHs/rGO composite and compared the electrochemical performance of the same composite that reduced thermally and reduced via microwave irradiation. It has been shown that the former has the highest specific capacitance of 1,208 F g^{-1} at 8 A g^{-1} and able to retain the value to 1,518 F g^{-1} at 1 A g^{-1} (about 80%). The thermal treatment is responsible for creating pores for the ion movement to the interior of the composite. This highly porous composite also displayed an excellent life cycle with above 80% over 2,000 cycles. Another similar work has been reported by Yulian et al. (2013), where Ni-Al LDHs nanoflakes anchored *in-situ* on activated graphene nanosheets. This hybrid composite has a BET surface area of 3,026 m^2 $g^{-}1$ and showed a maximum specific capacitance of 1,173 F g^{-1} at a current density of 1 F g^{-1}. Gao et al. (2011) have also fabricated Ni-Al LDHs/graphene nanosheets via the hydrothermal method. The obtained composite displayed a high specific capacitance of 781.5 F g^{-1} at 5 mV s^{-1} and excellent cycling retention in a three-electrode configuration. While, Yang et al. (2013) have included graphene nanosheets and carbon nanotubes with Ni-Al LDHs via one-step ethanol solvothermal method. The obtained 3D flower-like composite was able to overcome the limitations of 2D graphene nanosheets i.e. aggregation, low surface area and deteriorations of ion movements. In this study, the role of graphene nanosheets was expected to be as a conductive scaffold to build a 3D nanostructure. More importantly, the composite revealed to possess 1,869 F g^{-1} at 1 A g^{-1} with superior cycling stability over 1,000 cycles.

Comparative study on sandwich-like Ni-Mn LDHs/rGO, Ni-Mn LDHs/carbon black, turbostratic-structured Ni-Mn LDHs/carbon nantotubes and ternary Ni-Mn LDHs/carbon nanotubes/rGO (**Figure 7**) were carried out by Li et al. (2016b). Electrochemical study in 2 M KOH revealed ternary Ni-Mn LDHs/carbon nanotubes/rGO has higher specific capacitance (1,268 F g^{-1} at 1 A g^{-1}) and superior cycle life (79% over 2,000 cycles) than other hybrid composites. This is due to the addition of rGO and carbon nanotubes where, (i) LDHs anchored firmly on the rGO, thus preventing restacking of LDHs nanosheets, (ii) carbon nanotubes provides conductive scaffold, hence increasing the conductivity of the composite, and (iii) the co-dispersed carbon nanotubes and rGO open a conductive network pathway for the ions.

Co-based LDHs Combining With Carbon-Based Materials

Great efforts have been committed to study Co-based LDHs composite combined with carbon materials as electrodes for supercapacitors. For example, honeycomb-like Co-Fe LDHs were *in-situ* deposited on the multi-layer graphene to be for energy storage devices. They showed a high specific capacitance of 882.5 F g^{-1} at 1 A g^{-1}. However, the composite only able to withstand 39% of its initial capacitance value over 2,000 cycles due to the detachment and dissolution of active material during the charge-discharge process (Xu et al., 2018).

Co-Al LDHs have also found its potential in energy storage applications. The Co-Al LDHs/rGO composite was prepared by the co-precipitation method, which formed nanosheets grown perpendicularly on the rGO layer. The composite has lesser agglomeration compared to pure LDHs with serious agglomeration (**Figures 8a,b**). The BET surface area was found to be 47.6 m^2 g^{-1} compared to that pure LDHs (24.0 m^2 g^{-1}) (**Figures 8c,d**). In an asymmetrical configuration, this composite as the positive electrode and activated carbon as the negative electrode was able to operate at a wide potential window (0 to 1.75 V), which results in enhanced specific energy (35.5 Wh kg^{-1}) and specific power (8.75 W kg^{-1}) (**Figure 8**e). Moreover, the asymmetrical assembly displayed excellent capacitance (90% retention) after 6,000 cycles (**Figure 8f**) (Zhang et al., 2013).

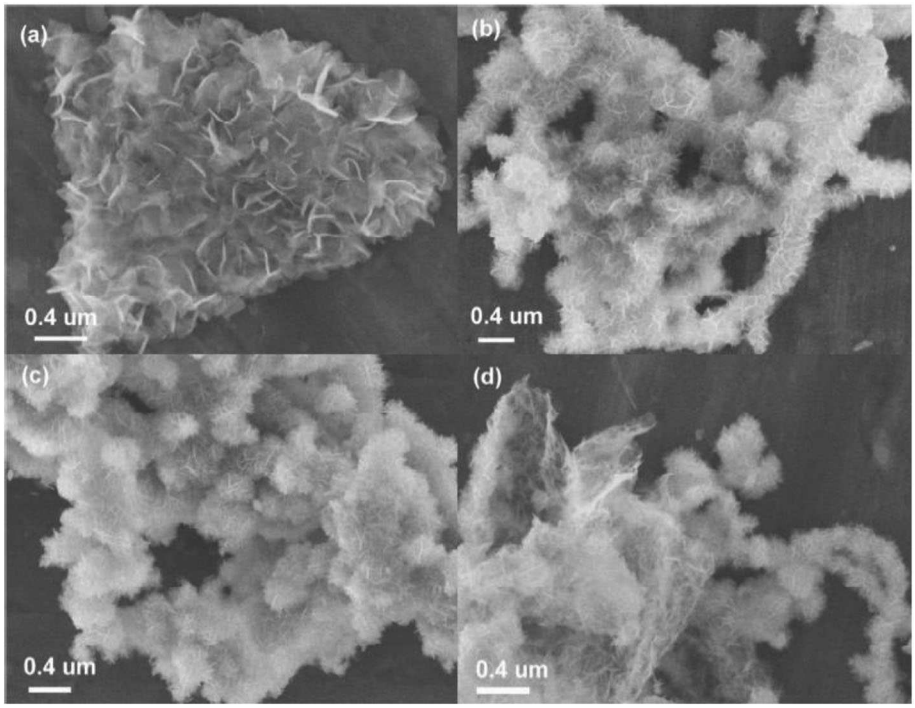

FIGURE 7 | SEM images of **(a)** Ni-Mn LDHs/rGO, **(b)** Ni-Mn LDHs/carbon nanotubes, **(c)** Ni-Mn LDHs/carbon black, and **(d)** Ni-Mn LDHs/carbon nanotubes/rGO (Li et al., 2016b).

In another study, Zhang et al. (2012) have demonstrated for the first time the fabrication of graphene nanosheets combined with Co-Al LDHs using the one-pot refluxing method. A 3D conductive network made of hexagonal flakes can be observed for this composite. The hexagonal flakes of Co-Al LDHs are covered on the surface of graphene nanosheets, preventing the re-stacking of graphene and giving rise to the surface area (23.4 m^2 $g–^1$) of the composite.

Ni-Co LDHs Combining With Carbon-Based Materials

Despite the endless effort of researchers to produce high performance Ni-Co LDHs electrode material with controlled morphologies, optimized particle sizes, enhanced surface area and broad pore size distribution, the main drawbacks including poor stability and low electrical conductivity have a profound effect on its practicability. In light of this, fabrication of composite materials, specifically the introduction of carbonaceous materials with Ni-Co LDHs could provide the right solution for this conundrum. The uniqueness and significant benefits of this combination are listed as follows (Xu et al., 2006; Li et al., 2016a; Wang et al., 2018a):

a) The severe aggregation of Ni-Co LDHs can be avoided. The charged surface of LDHs often aggregates by forming particles or irregular clusters with size ranges from 1 to 10 μm, thereby resulted in an unstable colloidal solution, which causes a serious impact on its electrochemical performances.
b) The electrical conductivity of the composite can be improved significantly by preventing the agglomeration of LDHs. Thus, electron transfer and rate of diffusion during the oxidation-reduction process will be facilitated.
c) Carbon-based materials provide large ion accessible surface areas with enhanced active sites facilitating efficient access of ions from the electrolytes and eventually shorten the ion diffusion pathway.
d) Importantly, the mechanical stability of the composite will be improved significantly. As known to all, carbon-based materials have extraordinary mechanical stability. In this instance, carbon-based materials will act as a backbone or scaffold to minimize the volume expansion of LDHs.

Thus, the introduction of carbon-based materials with Ni-Co LDHs have a considerable impact on the electrochemical performances of the composite. The studies conducted on the Ni-Co LDHs with carbon-based materials are quite encouraging (**Table 4**).

Most of the materials from carbon-based materials exhibit high surface area and good electrical conductivity. Due to these features, Ni-Co LDHs often introduced with graphene-based materials to improve the electrochemical properties of the composites. For example, Wang et al. (2019a) have directly fabricated Ni-Co LDHs/rGO grown on carbon cloth (CC) using a simple one-pot hydrothermal method. The Ni-Co LDHs uniformly grow on the CC forming hydrangea petal-like structure with 2D sheet-like morphology. While the rGO grew between the LDHs sheets were greatly improved the specific surface area of the composite. It was used directly as a binder-free electrode in a symmetrical supercapacitor. The as-prepared composite obtained specific capacitance of 151.46 F

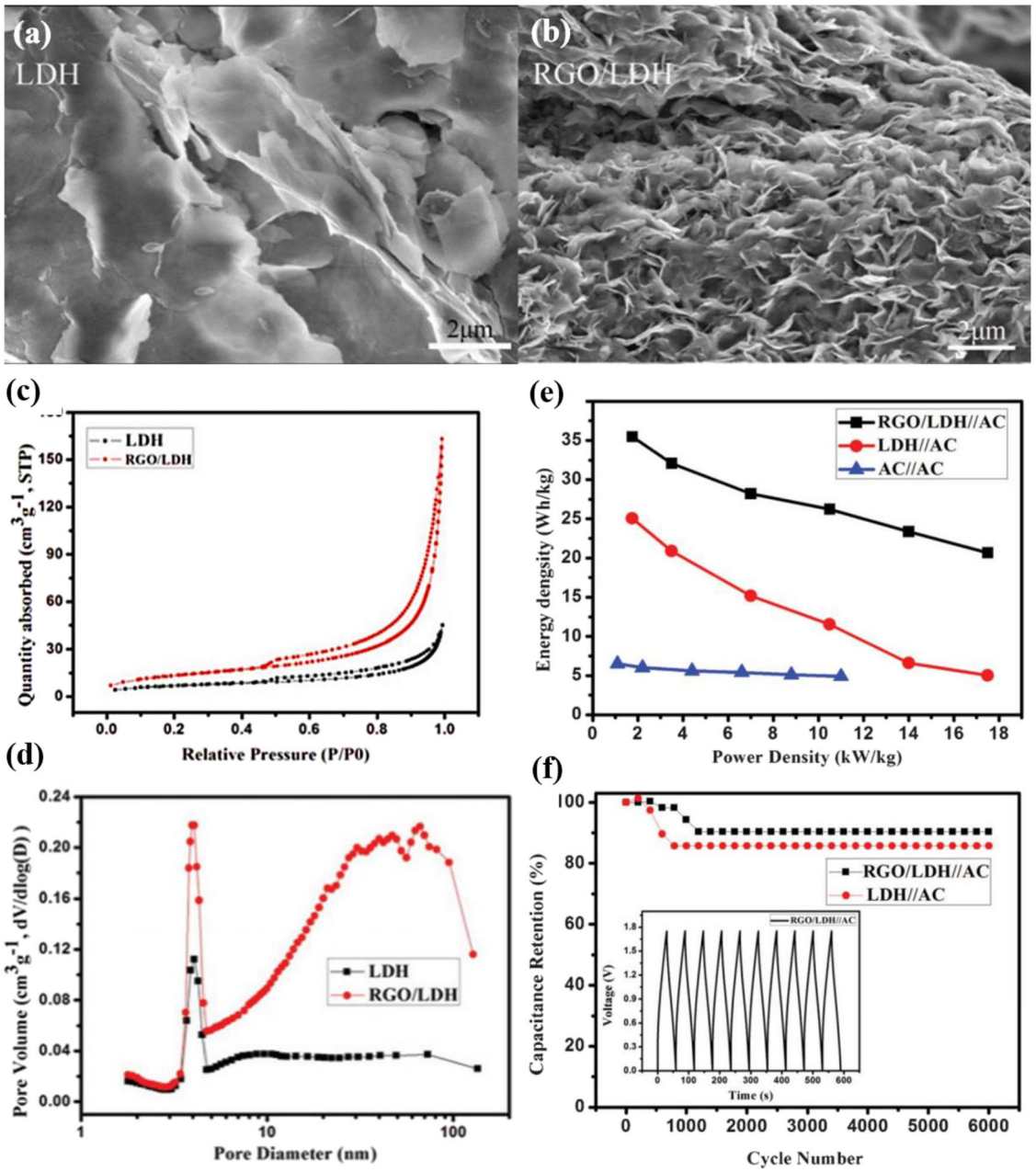

FIGURE 8 | SEM images of **(a)** LDHs, **(b)** low-magnification of rGO/LDHs, **(c)** nitrogen adsorption and desorption isotherm loops of LDHs and rGO/LDHs composite, **(d)** pore size distribution of LDHs and rGO/LDHs, **(e)** Ragone plots of LDHs//AC, rGO/LDHs//AC asymmetric ECs, and AC//AC symmetric EC, and **(f)** Cycle stability of LDHs//AC and rGO/LDHs//AC ECs during charge–discharge test at a current density of 4 A g^{-1} (Zhang et al., 2013).

g^{-1} at a current density of 2.5 A g^{-1} and prominent cycling stability of 85.6% after 3,000 cycles at 5 A g^{-1}. The author claimed that the hydrangea petal-like morphology of the Ni-Co LDHs/rGO/CC with large interlayer spacing facilitates the transport of ions between the composite and electrolyte and shorten the ion diffusion pathway endowing the electrode with a specific energy of 30.29 Wh kg^{-1} at a specific power of 1,500 W kg^{-1}. Importantly, after the continuous 3,000 cycling process, the structure of the composite does not undergo any destruction indicating the importance of the rGO in the Ni-Co LDHs and its role as the backbone for LDHs.

In another attempt to produce a binder-free supercapacitor electrode, Yang et al. (2019) developed a hierarchical Ni-Co LDH/rGO on nickel foam via a solvothermal process. The composite has various merits : (i) upon the addition of rGO in the Ni-Co LDHs the interlayer spacing increases drastically

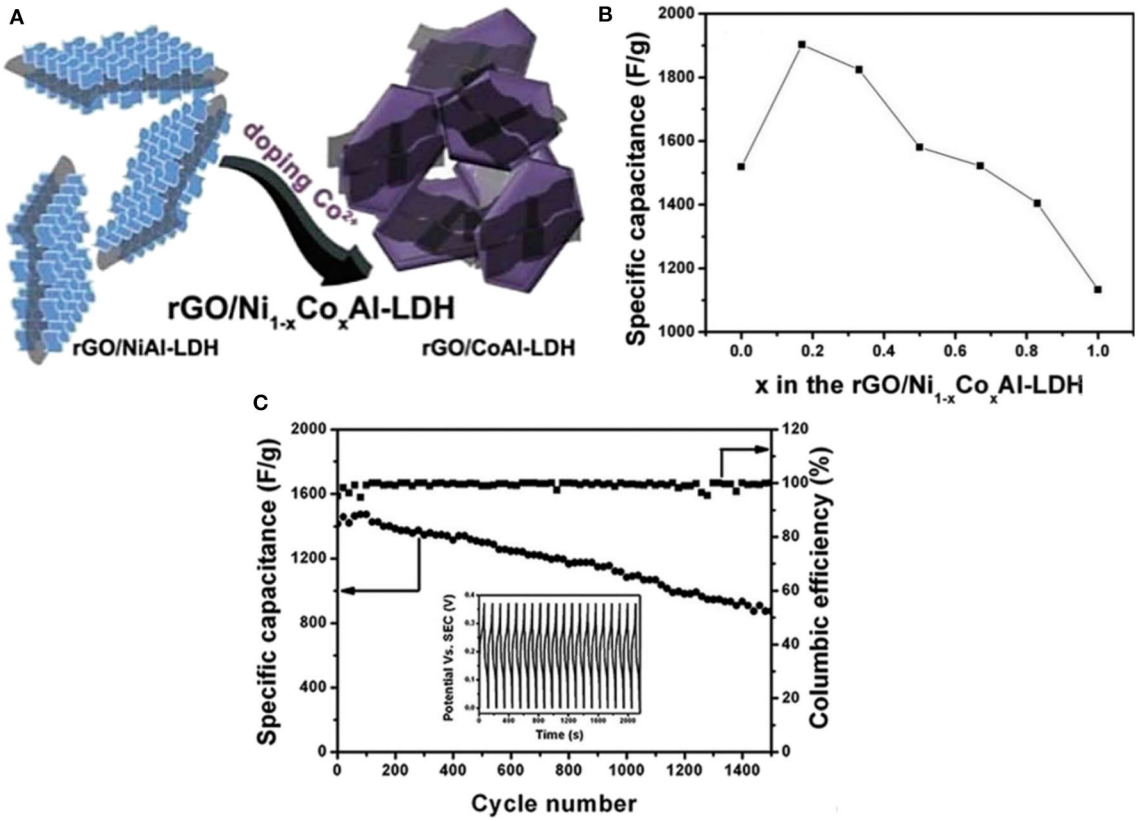

FIGURE 9 | (A) Schematic illustration for the shape conversion from rGO/NiAl-LDHs to the rGO/CoAl-LDHs composite, **(B)** Relationship between the specific capacitance and the doped Co content in rGO/$Ni_{1-x}Co_x$Al-LDHs, and **(C)** The cycling performance and corresponding Coulombic efficiency of rGO/$Ni_{0.83}Co_{0.17}$Al-LDHs at a current density of 10 A g^{-1}. The inset is the first 20 charge-discharge curves (Xu et al., 2014).

promoting the rapid movement of ions and electrons across the sheets; (ii) As the rGO sufficiently decorated within the LDHs, the agglomeration of the composite can be hindered, thereby improves the electrolyte transport to the inner part of the composite; and (iii) the flower-like structure with mesopores on the 2D interconnected nickel foam avoid the formation of "dead volume" which encourage the more active sites to involve in the electrochemical reaction, thus decreases the internal resistance of the composite. The produced asymmetrical supercapacitor device based on Ni-Co LDH/rGO/nickel foam delivered a specific capacitance of 105.62 F g^{-1} at 0.5 A g^{-1} and remarkable specific energy of 40.5 Wh kg^{-1} and a maximum specific power of 4,631 W kg^{-1}.

Another similar composite, Ni-Co LDHs/rGO was prepared via one-pot microwave-assisted synthesis (Kim et al., 2016). It was found that the reaction time, temperature, type of solvent, surfactant and precursor have a profound influence on the size, shape, pore size distribution and crystallinity of Ni-Co LDHs. The different molar ratios of nickel and cobalt also showed a significant effect on the morphology and electrochemical behavior of the composite. Among the different nickel/cobalt ratios, the 2:1 ratio shows the best capacitive performances in a three-electrode system such as the highest specific capacitance (1,622 F g^{-1} at 5 mV s^{-1}) and good cycling stability (80% retention over 5,000 cycles). The improved electrochemical performances of this composite not only originate from the bimetallic hydroxides, but rGO also played an important role in enhancing the overall specific surface area of the composites. In addition, the authors also revealed the influence of nickel and cobalt where nickel controlled the capacitive performance of the composite, while cobalt in maintaining the rate capability of the composite. Likewise, Yan et al. (2014) also reported that the addition of graphene resulted in a high specific surface area of 408.5 m^2 g^{-1} with a pore diameter of 4.75 nm. It also revealed that the basal spacing of the composites increases to 0.86 nm compared to the pristine Ni-Co LDHs, which demonstrated a high specific capacitance 1,980 F g^{-1} at 1 A g^{-1} in a three-electrode system.

Similar findings also were reported by Shahrokhian et al. (2018) in the preparation of electrode material made of Ni-Co LDHs electrodeposited on rGO/nickel foam with excellent supercapacitive performances. In this study, the effect of surfactant cetyltrimethylammonium bromide (CTAB) on the morphology also has been described in detail. The addition of CTAB showed variation in terms of the thickness of Ni-Co LDHs on the rGO/nickel foam. Ni-Co LDHs with CTAB forms thinner

TABLE 4 | Summary of nanocomposites containing carbon-based materials with Ni^{2+}/Co^{2+} LDHs.

Materials		LDH preparation method	Molar ratio of precursor salt (M^{2+}:M^{3+})	C_{sp} (F g^{-1})	SE (Wh kg^{-1})	SP (W kg^{-1})	Electrolyte	Stability	References
+ve electrode	**–ve electrode**								
Carbon nanofibers/Ni-Co-Fe LDHs	Activated carbon	Hydrothermal	Chlorides (5:1:1)	*84.9 (at 1 A g^{-1})	*30.2	*800.1	6 M KOH	*82.7% over 2,000 cycles	Wang et al., 2017a
rGO/NiCoAl LDH	–	Hydrothermal	Nitrates (1:2:1)	#1962 (at 1 A g^{-1})	–	–	6 M KOH	#96.2% over 2,000 cycles	He et al., 2015
rGO/NiCoAl LDH	–	*In-situ* growth	Nitrates (2:1:1)	#1902 (at 1 A g^{-1})	–	–	6 M KOH	#62% over 1,500 cycles	Xu et al., 2014
Graphene sheets/Ni-Co LDHs	–	Microwave heating reflux	Nitrates (2:1)	#1980 (at 1 A g^{-1})	–	–	6 M KOH	#Increase 2.9% over 1,500 cycles	Yan et al., 2014
Ni-Co LDHs/rGO	–	Hydrothermal	Nitrates (1:1)	*151.46 (at 2.5 A g^{-1})	*30.29	*1,500	PVA/KOH gel	*85.6% over 3,000 cycles	Wang et al., 2019a
Ni-Co LDHs/rGO	Activated carbon	Hydrothermal	Nitrates (3:3)	*105.62 (at 0.5 A g^{-1})	*40.54	*206.5	6 M KOH	*94.7% over 8,000 cycles	Yang et al., 2019
N-doped graphene/NiCo LDHs	Activated carbon	Microwave-assisted hydrothermal process	Nitrates (3:2)	*100 (at 0.5 A g^{-1})	*31.2	*354	6 M KOH	*83% over 10,000 cycles	Wang et al., 2019b
Ni-Co LDHs/rGO	–	One-pot microwave-assisted synthesis	Chlorides (2:1)	#1622 (at 5 mV s^{-1})	–	–	6 M KOH	#80% over 5,000 cycles	Kim et al., 2016
Ni-Co LDHs/rGO/nickel foam	rGO/nickel foam	Electrodeposition	Nitrates (1:2)	*233.3 (at 4 A g^{-1})	*68	*4,300	3 M NaOH	#90.5% over 1,000 cycles	Shahrokhian et al., 2018
Ni-Co LDHs/CNTs/nickel foam	–	Chemical bath deposition	Sulfate (1:2)	#1151.2 (at 1 A g^{-1}	–	–	2 M NaOH	#77% over 10,000 cycles	Li et al., 2015b
Ni-Co LDHs/rGO/Ni-Co LDHs/rGO	Activated carbon	Electrodeposition	Nitrates (1:1)	–	*84.9	*424	1 M KOH	*91.6% over 2,000 cycles	Li et al., 2020
Ni-Co LDHs/Ag NP/rGO	Activated carbon	Electrodeposition	Nitrates (1:1)	–	*76	*480	1 M KOH	*79.8% over 5,000 cycles	Li et al., 2019a
Ni-Co LDHs/rGO	Activated carbon	Magnetic stirring	Chlorides (3:2)	#1703 (at 0.5 A g^{-1})	*47.1	*399.9	2 M KOH	*73.3% over 10,000 cycles	Long et al., 2019

#the three-electrode system.
**the two-electrode system.*
C_{sp} is specific capacitance.
SE is a specific energy.
SP is a specific power.

nanosheets compared to hydroxides without CTAB. Moreover, CTAB prevents the formation of bubbles at the solution-electrode interface, thus allowing a uniform formation of Ni-Co LDHs with high porosity on the rGO/nickel foam. In asymmetric assembly, the composite showed good capacitive behavior with a specific energy of 68 Wh kg^{-1} at a specific power of 1,070 W kg^{-1}. The author claimed that the direct deposition of a highly porous thin layer Ni-Co LDHs on highly conductive rGO helps in enhancing the performances.

Li's group (Li et al., 2020) has developed a novel multi-layered Ni-Co LDHs|rGO|Ni-Co LDHs|rGO composite through inkjet printing and electrodeposition method. They employed rGO ink on the nickel foam to form a conductive layer for the electrodeposition of Ni-Co LDHs. Then, the process was continued to form the multi-layered composite. It has been deduced that rGO thin layer on nickel foam not only acts as a conductive scaffold but also provides an excellent charge transfer path in the composite. Moreover, as a conductive scaffold, rGO is also important in forming homogenous nanoflakes of LDHs with good adherence, which are also observed by Guo et al. (2019a). A high energy density of 84.9 Wh kg^{-1} with a maximum power density of 424 W kg^{-1} is achieved by assembling an asymmetrical supercapacitor using this multi-layered Ni-Co LDHs|rGO as the positive electrode and activated carbon as the negative electrode. A similar strategy was also reported by Li et al. (2019a) who have introduced conductive silver nanoparticles (Ag NP) on top of the rGO layer coated on carbon cloth before electrodepositing LDHs. The benefit of Ag NP is to promote conductivity of the composite as Ag NP is known for its high conductivity and excellent chemical stability. This nanocomposite has a high capacity value of 173 mA hg^{-1} at 1 A g^{-1}. The asymmetrical configuration of this nanocomposite delivered a maximum energy density of 76 Wh kg^{-1} at a power density of 480 W kg^{-1}.

With the idea of increasing the capacitive behavior of Ni-Co LDHs/rGO based system, the third transition metal, Al was included (He et al., 2015). The unique nanoflakes structure of Ni-Co-Al LDHs were grown uniformly on the 3D rGO nanosheets created intact contact between the hydroxides and rGO, and subsequently provides better ion movements. The hydroxides may undergo aggregation. However, upon the addition of rGO, such a phenomenon was avoided, resulting in better utilization of both rGO and LDHs in the composites. A study on the content of rGO nanosheets in the composites revealed that the presence of rGO is highly important to increase the specific surface area with desirable pore size distribution generating improved ion transport to the intrinsic space. In a separate study conducted by Xu et al. (2014) showed the influence of the cobalt on the electrochemical performances of Ni-Co LDHs/rGO. At optimized cobalt content of 17%, the composite was able to reach a remarkable specific capacitance of 1,902 F g^{-1} at 1 A g^{-1} in a three-electrode system (**Figure 9**). Both studies disclosed that the synergy between LDHs and rGO promotes electron transport, thus enhance the electrochemical performances. Another work reported by Long et al. (2019) which also used rGO incorporated with Ni-Co LDHs via magnetic stirring. The Ni-Co LDHs/rGO composite with uniform and loose nanostructure exhibited a high specific capacitance of 1,703 F g^{-1} at 0.5 A g^{-1}. The incorporation of rGO greatly helps in preventing aggregation of the Ni-Co hydroxides and, thus improves the supercapacitive performance of the composite. The composite was then tested as a device with activated carbon as the negative electrode. The supercapacitor device demonstrated specific energy as high as 47.1 Wh kg^{-1} and specific power of 399.9 W kg^{-1} (**Figure 10**).

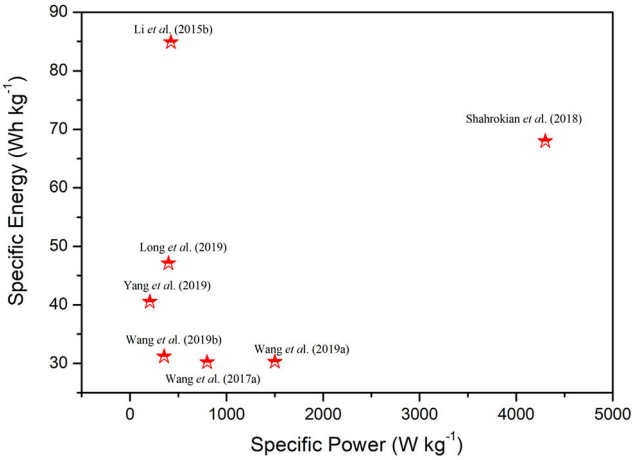

FIGURE 10 | Ragone plot summarizing specific energy and specific power of some of the reported literature on Ni-Co LDHs combining with carbon-based materials.

Instead of using rGO, another work reported on Ni-Co LDHs coated on nitrogen-doped graphene via a simple microwave-assisted hydrothermal process. Two significant improvements were noticed, (a) the good hydrophilicity nature of N-doped graphene serves as good nucleation sites for Ni-Co LDHs growth and (b) N-doped graphene with high conductivity provides large surface area improving the capacitive performance of the composite. The as-prepared composite as a positive electrode and activated carbon as a negative electrode delivers specific energy of 31.2 Wh kg^{-1} at a specific power of 354 W kg^{-1} and extraordinary cycling stability of 83% retention over 10,000 cycles.

In another attempt, Li et al. (2015b) have reported a one-step chemical bath deposition of Ni-Co LDHs nanoflakes uniformly coated on highly porous carbon nanotubes. The functionalized carbon nanotubes acted as a nucleation site for the growth of gauze-like Ni-Co LDHs nanoflakes. The author in this study varied the content of cobalt in the LDHs and found that the rate capabilities increase with the content of cobalt. Three reasons can explain this behavior; (1) the formation of highly conductive CoOOH during oxidation/reduction process, (2) Expansion of interlayer spacing and conductivity due to the presence of intercalated anions and (3) carbon nanotubes as the core in the composite ease the electron transfer in the composite whilst minimizing electrochemical polarization. This hybrid structure shows a maximum specific capacitance of 701 F g^{-1} at a current density of 10 A g^{-1} and a long life span.

SUMMARY AND PERSPECTIVES

In summary, two-dimensional layered double hydroxides, particularly nickel-cobalt layered double hydroxides (Ni-Co LDHs) and their composite with carbon materials have prompted profound research attentions. Benefitting from their unique layered structure, multiple oxidation states of Ni^{2+}/Ni^{3+} and $Co^{2+}/Co^{3+}/Co^{4+}$, exchangeability of interlayer anions and tunability of metal ion ratios, Ni-Co LDHs have gained incredible demand in the field of the supercapacitor. pH and metal ion ratio are the two most prominent factors to be considered to produce LDHs with good crystallinity and phase with desirable morphology. These factors also influence the electrochemical behavior of Ni-Co LDHs and Ni-Co LDHs/carbon-based supercapacitors. The incorporation of carbon-based material into Ni-Co LDHs can help to prevent severe aggregation of Ni-Co LDHs and enhance the supercapacitive performance of the composite due to their high surface area, high conductivity and excellent mechanical strength.

Although there are some encouraging results have been reported on Ni-Co LDHs and Ni-Co LDHs/carbon-based supercapacitors, the development of these electrodes for practical use is still in the early stage. Therefore, substantial measures and action need to be taken to promote the supercapacitor performances of these electrodes, including:

a) Detailed studies on the effects of layered structures, multiple oxidation states, exchangeability of interlayer anions, tunability of metal ion ratio and interlayer spacing of Ni-Co LDHs on the charge storage behavior are much needed. A lot of theoretical understanding of Ni-Co LDHs has been reported, however, advanced and detailed studies on the behavior and charge storage mechanism with respect to the mentioned factors are yet to be found.
b) Knowledge of widening the interlayer spacing of the Ni-Co LDHs are appreciated. Interlayer spacing plays a pivotal role in determining the capacitive behavior of supercapacitors, whereby the larger spacing facilitating the ions intercalation and de-intercalation. Compositing Ni-Co LDHs with carbon-based materials indeed reduces mechanical stress and improves capacitive behavior. However, its impact on interlayer spacing should be explored. It also will be helpful in prolonging the life span of LDHs.

AUTHOR CONTRIBUTIONS

SK wrote the manuscript with the supervision of YS. NA gathered data and organized the manuscript. YS revised the manuscript, edited, and made important supplementary. All authors reviewed the manuscript.

ACKNOWLEDGMENTS

The authors would like to thank Universiti Putra Malaysia for the funding under the research grant of GP-IPS/2017/9580500.

REFERENCES

Abellán, G., Carrasco, J. A., and Coronado, E. (2020). "Layered double hydroxide nanocomposites based on carbon nanoforms," in *Layered Double Hydroxide Polymer Nanocomposites,* eds S. Thomas and S. Daniel (Kidlington: Woodhead Publishing), 411–460.

Albiston, L., Franklin, K. R., Lee, E., and Smeulders, J. B. A. F. (1996). Rheology and microstructure of aqueous layered double hydroxide dispersions. *J. Mater. Chem.* 6, 871–877. doi: 10.1039/jm9960600871

Allmann, R. (1968). The crystal structure of pyroaurite. *Acta Crystallogr. B* 24, 972–977. doi: 10.1107/S0567740868003511

Arias, S., Eon, J. G., San Gil, R. A. S., Licea, Y. E., Palacio, L. A., and Faro, A. C. (2013). Synthesis and characterization of terephthalate-intercalated NiAl layered double hydroxides with high Al content. *Dalton Trans.* 42, 2084–2093. doi: 10.1039/C2DT31502E

Bastakoti, B. P., Huang, H.-S., Chen, L.-C., Wu, K. C. W., and Yamauchi, Y. (2012). Block copolymer assisted synthesis of porous α-Ni(OH)2 microflowers with high surface areas as electrochemical pseudocapacitor materials. *Chem. Commun.* 48, 9150–9152. doi: 10.1039/c2cc32945j

Beaudot, P., De Roy, M. E., and Besse, J. P. (2004). Intercalation of noble metal complexes in LDH compounds. *J. Solid State Chem.* 177, 2691–2698. doi: 10.1016/j.jssc.2004.03.048

Becker, H. I. (1957). *Low Voltage Electrolytic Capacitor*. United States patent application. New York, NY.

Boclair, J. W., Braterman, P. S., Brister, B. D., and Yarberry, F. (1999). Layer–anion interactions in magnesium aluminum layered double hydroxides intercalated with cobalticyanide and nitroprusside. *Chem. Mater.* 11, 2199–2204. doi: 10.1021/cm990148l

BP (2018). *BP Statistical Review of World Energy 2018*. London. Available online at: https://www.bp.com/en/global/corporate/energy-economics/statistical-review-of-world-energy.html

Cai, X., Shen, X., Ma, L., Ji, Z., Xu, C., and Yuan, A. (2015). Solvothermal synthesis of NiCo-layered double hydroxide nanosheets decorated on RGO sheets for high performance supercapacitor. *Chem. Eng. J.* 268, 251–259. doi: 10.1016/j.cej.2015.01.072

Cao, J., Mei, Q., Wu, R., and Wang, W. (2019). Flower-like nickel–cobalt layered hydroxide nanostructures for super long-life asymmetrical supercapacitors. *Electrochim. Acta* 321:134711. doi: 10.1016/j.electacta.2019.134711

Cao, L., Xu, F., Liang, Y.-Y., and Li, H.-L. (2004). Preparation of the novel nanocomposite $Co(OH)_2$/ultra-stable y zeolite and its application as a supercapacitor with high energy density. *Adv. Mater.* 16, 1853–1857. doi: 10.1002/adma.200400183

Cavani, F., Trifirò, F., and Vaccari, A. (1991). Hydrotalcite-type anionic clays: preparation, properties and applications. *Catal. Today* 11, 173–301. doi: 10.1016/0920-5861(91)80068-K

Chang, Z., Wu, C., Song, S., Kuang, Y., Lei, X., Wang, L., et al. (2013). Synthesis mechanism study of layered double hydroxides based on nanoseparation. *Inorg. Chem.* 52, 8694–8698. doi: 10.1021/ic4008763

Chen, G., Liaw, S. S., Li, B., Xu, Y., Dunwell, M., Deng, S., et al. (2014a). Microwave-assisted synthesis of hybrid $Co_xNi_{1-x}(OH)_2$ nanosheets: tuning the composition for high performance supercapacitor. *J. Power Sources* 251, 338–343. doi: 10.1016/j.jpowsour.2013.11.070

Chen, H., Hu, L., Chen, M., Yan, Y., and Wu, L. (2014b). Nickel–cobalt layered double hydroxide nanosheets for high-performance supercapacitor electrode materials. *Adv. Funct. Mater.* 24, 934–942. doi: 10.1002/adfm.201301747

Chen, J., Bradhurst, D. H., Dou, S. X., and Liu, H. K. (1999). Nickel hydroxide as an active material for the positive electrode in rechargeable alkaline batteries. *J. Electrochem. Soc.* 146, 3606–3612. doi: 10.1149/1.1392522

Chen, J.-C., Hsu, C.-T., and Hu, C.-C. (2014c). Superior capacitive performances of binary nickel–cobalt hydroxide nanonetwork prepared by cathodic deposition. *J. Power Sources* 253, 205–213. doi: 10.1016/j.jpowsour.2013.12.073

Cheng, Y., Zhang, H., Varanasi, C. V., and Liu, J. (2013). Improving the performance of cobalt–nickel hydroxide-based self-supporting electrodes

for supercapacitors using accumulative approaches. *Energy Environ. Sci.* 6, 3314–3321. doi: 10.1039/c3ee41143e

Cui, H., Zhao, Y., Ren, W., Wang, M., and Liu, Y. (2013). Large scale selective synthesis of α-$Co(OH)_2$ and β-$Co(OH)_2$ nanosheets through a fluoride ions mediated phase transformation process. *J. Alloys Compd.* 562, 33–37. doi: 10.1016/j.jallcom.2013.02.031

Cullity, B. D. (1957). Elements of X-ray diffraction. *Am. J. Phys.* 25, 394–395. doi: 10.1119/1.1934486

Daud, M., Kamal, M. S., Shehzad, F., and Al-Harthi, M. A. (2016). Graphene/layered double hydroxides nanocomposites: a review of recent progress in synthesis and applications. *Carbon N. Y.* 104, 241–252. doi: 10.1016/j.carbon.2016.03.057

Fan, Z., Yan, J., Wei, T., Zhi, L., Ning, G., Li, T., et al. (2011). Asymmetric supercapacitors based on graphene/MnO_2 and activated carbon nanofiber electrodes with high power and energy density. *Adv. Funct. Mater.* 21, 2366–2375. doi: 10.1002/adfm.201100058

Feitknecht, W., and Gerber, M. (1942). Zur Kenntnis der Doppelhydroxyde und basischen Doppelsalze III. *Über magnesium-aluminiumdoppelhydroxyd. Helvetica Chimica Acta* 25, 131–137. doi: 10.1002/hlca.19420250115

Feng, H.-P., Tang, L., Zeng, G.-M., Tang, J., Deng, Y.-C., Yan, M., et al. (2018). Carbon-based core–shell nanostructured materials for electrochemical energy storage. *J. Mater. Chem. A* 6, 7310–7337. doi: 10.1039/C8TA01257A

Forano, C., Hibino, T., Leroux, F., and Taviot-Guého, C. (2006). "Chapter 13.1 layered double hydroxides," in *Developments in Clay Science,* eds *F. Bergaya, B. K. G. Theng, and* G. Lagaly (Kidlington: Elsevier), 1021–1095.

Gao, Z., Wang, J., Li, Z., Yang, W., Wang, B., Hou, M., et al. (2011). Graphene nanosheet/Ni^{2+}/Al^{3+} layered double-hydroxide composite as a novel electrode for a supercapacitor. *Chem. Mater.* 23, 3509–3516. doi: 10.1021/cm200975x

Ge, X., He, Y., Plachy, T., Kazantseva, N., Saha, P., and Cheng, Q. (2019). Hierarchical PANI/NiCo-LDH core-shell composite networks on carbon cloth for high performance asymmetric supercapacitor. *Nanomaterials* 9:527. doi: 10.3390/nano9040527

Ghadiri, M., Chrzanowski, W., and Rohanizadeh, R. (2015). Biomedical applications of cationic clay minerals. *RSC Adv.* 5, 29467–29481. doi: 10.1039/C4RA16945J

Guo, D., Song, X., Tan, L., Ma, H., Sun, W., Pang, H., et al. (2019a). A facile dissolved and reassembled strategy towards sandwich-like rGO@NiCoAl-LDHs with excellent supercapacitor performance. *Chem. Eng. J.* 356, 955–963. doi: 10.1016/j.cej.2018.09.101

Guo, X., Feng, B., Gai, L., and Zhou, J. (2019b). Reduced graphene oxide/polymer dots-based flexible symmetric supercapacitors delivering an output potential of 1.7 V with electrochemical charge injection. *Electrochim. Acta* 293, 399–407. doi: 10.1016/j.electacta.2018.10.057

Gupta, V., Gupta, S., and Miura, N. (2008). Potentiostatically deposited nanostructured Co_xNi_{1-x} layered double hydroxides as electrode materials for redox-supercapacitors. *J. Power Sources* 175, 680–685. doi: 10.1016/j.jpowsour.2007.09.004

Haas, O., and Cairns, J. E. (1999). Chapter 6. Electrochemical energy storage. *Annu. Rep. C* 95, 163–198. doi: 10.1039/pc095163

Hai-Yan Wang, G.-Q. S. (2018). Layered double hydroxide/graphene composites and their applications for energy storage and conversion. *Acta Phys. Chim. Sin.* 34, 22–35. doi: 10.3866/PKU.WHXB201706302

He, F., Hu, Z., Liu, K., Guo, H., Zhang, S., Liu, H., et al. (2015). Facile fabrication of GNS/NiCoAl-LDH composite as an advanced electrode material for high-performance supercapacitors. *J. Solid State Electrochem.* 19, 607–617. doi: 10.1007/s10008-014-2644-3

Hochstetter, C. (1842). Untersuchung über die zusammensetzung einiger Mineralien. *J. Prakt. Chem.* 27, 375–378. doi: 10.1002/prac.18420270156

Hou, L., Du, Q., Su, L., Di, S., Ma, Z., Chen, L., et al. (2019). Ni-Co layered double hydroxide with self-assembled urchin like morphology for asymmetric supercapacitors. *Mater. Lett.* 237, 262–265. doi: 10.1016/j.matlet.2018.11.123

Hu, Z.-A., Xie, Y.-L., Wang, Y.-X., Wu, H.-Y., Yang, Y.-Y., and Zhang, Z.-Y. (2009). Synthesis and electrochemical characterization of mesoporous CoxNi1–x layered double hydroxides as electrode materials for supercapacitors. *Electrochim. Acta* 54, 2737–2741. doi: 10.1016/j.electacta.2008.11.035

Jeong, Y.-M., Son, I., and Baek, S.-H. (2019). Binder-free of NiCo-layered double hydroxides on Ni-coated textile for wearable and flexible supercapacitors. *Appl. Surf. Sci.* 467–468, 963–967. doi: 10.1016/j.apsusc.2018.10.252

Kameda, T., Saito, M., and Umetsu, Y. (2006). Preparation and characterisation of Mg, Al layered double hydroxides intercalated with 2-naphthalene sulphonate and 2,6-naphthalene disulphonate. *Mater. Trans.* 47, 923–930. doi: 10.2320/matertrans.47.923

Kim, B. K., Sy, S., Yu, A., and Zhang, J. (2015). "Electrochemical supercapacitors for energy storage and conversion," in *Handbook of Clean Energy Systems,* ed J. Yan (Waterloo, ON: John Wiley & Sons, Ltd.), 1–25.

Kim, H.-J., Lee, G. J., Choi, A.-J., Kim, T.-H., Kim, T.-I., and Oh, J.-M. (2018). Layered double hydroxide nanomaterials encapsulating angelica gigas nakai extract for potential anticancer nanomedicine. *Front. Pharmacol.* 9:723. doi: 10.3389/fphar.2018.00723

Kim, I.-H., and Kim, K.-B. (2006). Electrochemical characterization of hydrous ruthenium oxide thin-film electrodes for electrochemical capacitor applications. *J. Electrochem. Soc.* 153, A383–A389. doi: 10.1149/1.2147406

Kim, Y., Cho, E.-S., Park, S.-J., and Kim, S. (2016). One-pot microwave-assisted synthesis of reduced graphene oxide/nickel cobalt double hydroxide composites and their electrochemical behavior. *J. Ind. Eng. Chem.* 33, 108–114. doi: 10.1016/j.jiec.2015.09.023

Kulandaivalu, S., Abdul Shukur, R., and Sulaiman, Y. (2018). Improved electrochemical performance of electrochemically designed layered poly(3,4-ethylenedioxythiophene)/graphene oxide with poly(3,4-ethylenedioxythiophene)/nanocrystalline cellulose nanocomposite. *Synth. Met.* 245, 24–31. doi: 10.1016/j.synthmet.2018.08.002

Kulandaivalu, S., Hussein, M. Z., Jaafar, A. M., Mohd, M. A. A., Azman, N. H. N., and Sulaiman, Y. (2019). A simple strategy to prepare a layer-by-layer assembled composite of Ni–Co LDHs on polypyrrole/rGO for a high specific capacitance supercapacitor. *RSC Adv.* 9, 40478–40486. doi: 10.1039/C9RA08134H

Kulandaivalu, S., and Sulaiman, Y. (2019). Recent advances in layer-by-layer assembled conducting polymer based composites for supercapacitors. *Energies* 12:2107. doi: 10.3390/en12112107

Kulkarni, S. B., Jagadale, A. D., Kumbhar, V. S., Bulakhe, R. N., Joshi, S. S., and Lokhande, C. D. (2013). Potentiodynamic deposition of composition influenced $Co_{1-x}Ni_x$ LDHs thin film electrode for redox supercapacitors. *Int. J. Hydr. Energy* 38, 4046–4053. doi: 10.1016/j.ijhydene.2013.01.047

Lai, X., Halpert, J. E., and Wang, D. (2012). Recent advances in micro-/nano-structured hollow spheres for energy applications: from simple to complex systems. *Energy Environ. Sci.* 5, 5604–5618. doi: 10.1039/C1EE02426D

Largeot, C., Portet, C., Chmiola, J., Taberna, P. L., Gogotsi, Y., and Simon, P. (2008). Relation between the ion size and pore size for an electric double-layer capacitor. *J. Am. Chem. Soc.* 130, 2730–2731. doi: 10.1021/ja7106178

Li, C., Wang, G., Evans, D. G., and Duan, X. (2004). Incorporation of rare-earth ions in Mg–Al layered double hydroxides: intercalation with an [Eu(EDTA)]–chelate. *J. Solid State Chem.* 177, 4569–4575. doi: 10.1016/j.jssc.2004.09.005

Li, K., Kumada, N., Yonesaki, Y., Takei, T., Kinomura, N., Wang, H., et al. (2010). The pH effects on the formation of Ni/Al nitrate form layered double hydroxides (LDHs) by chemical precipitation and hydrothermal method. *Mater. Chem. Phys.* 121, 223–229. doi: 10.1016/j.matchemphys.2010.01.026

Li, L., Hui, K. S., Hui, K. N., and Cho, Y.-R. (2017a). Ultrathin petal-like NiAl layered double oxide/sulfide composites as an advanced electrode for high-performance asymmetric supercapacitors. *J. Mater. Chem. A* 5, 19687–19696. doi: 10.1039/C7TA06119F

Li, M., Cheng, J. P., Fang, J. H., Yang, Y., Liu, F., and Zhang, X. B. (2014). NiAl-layered double hydroxide/reduced graphene oxide composite: microwave-assisted synthesis and supercapacitive properties. *Electrochim. Acta* 134, 309–318. doi: 10.1016/j.electacta.2014.04.141

Li, M., Cheng, J. P., Wang, J., Liu, F., and Zhang, X. B. (2016a). The growth of nickel-manganese and cobalt-manganese layered double hydroxides on reduced graphene oxide for supercapacitor. *Electrochim. Acta* 206, 108–115. doi: 10.1016/j.electacta.2016.04.084

Li, M., Liu, F., Cheng, J. P., Ying, J., and Zhang, X. B. (2015a). Enhanced performance of nickel–aluminum layered double hydroxide nanosheets/carbon nanotubes composite for supercapacitor and asymmetric capacitor. *J. Alloys Compd.* 635, 225–232. doi: 10.1016/j.jallcom.2015.02.130

Li, M., Liu, F., Zhang, X. B., and Cheng, J. P. (2016b). A comparative study of Ni–Mn layered double hydroxide/carbon composites with different morphologies for supercapacitors. *Phys. Chem. Chem. Phys.* 18, 30068–30078. doi: 10.1039/C6CP05119G

Li, M., Ma, K. Y., Cheng, J. P., Lv, D., and Zhang, X. B. (2015b). Nickel–cobalt hydroxide nanoflakes conformal coating on carbon nanotubes as a supercapacitive material with high-rate capability. *J. Power Sources* 286, 438–444. doi: 10.1016/j.jpowsour.2015.04.013

Li, Q., Lu, C., Chen, C., Xie, L., Liu, Y., Li, Y., et al. (2017b). Layered $NiCo_2O_4$/reduced graphene oxide composite as an advanced electrode for supercapacitor. *Energy Storage Mater.* 8, 59–67. doi: 10.1016/j.ensm.2017.04.002

Li, S., Wang, F., Jing, X., Wang, J., Saba, J., Liu, Q., et al. (2012a). Synthesis of layered double hydroxides from eggshells. *Mater. Chem. Phys.* 132, 39–43. doi: 10.1016/j.matchemphys.2011.10.049

Li, T., Li, G. H., Li, L. H., Liu, L., Xu, Y., Ding, H. Y., et al. (2016c). Large-scale self-assembly of 3D flower-like hierarchical Ni/Co-LDHs microspheres for high-performance flexible asymmetric supercapacitors. *ACS Appl. Mater. Interfaces* 8, 2562–2572. doi: 10.1021/acsami.5b10158

Li, W., Livi, K. J. T., Xu, W., Siebecker, M. G., Wang, Y., Phillips, B. L., et al. (2012b). Formation of crystalline Zn–Al layered double hydroxide precipitates on γ-Alumina: the role of mineral dissolution. *Environ. Sci. Technol.* 46, 11670–11677. doi: 10.1021/es3018094

Li, X., Du, D., Zhang, Y., Xing, W., Xue, Q., and Yan, Z. (2017c). Layered double hydroxides toward high-performance supercapacitors. *J. Mater. Chem. A* 5, 15460–15485. doi: 10.1039/C7TA04001F

Li, X., Zhao, Y., Yu, J., Liu, Q., Chen, R., Zhang, H., et al. (2019a). Layer-by-layer inkjet printing GO film and Ag nanoparticles supported nickel cobalt layered double hydroxide as a flexible and binder-free electrode for supercapacitors. *J. Colloid Interface Sci.* 557, 691–699. doi: 10.1016/j.jcis.2019.09.063

Li, X., Zhao, Y., Yu, J., Liu, Q., Chen, R., Zhang, H., et al. (2020). Layer by layer inkjet printing reduced graphene oxide film supported nickel cobalt layered double hydroxide as a binder-free electrode for supercapacitors. *Appl. Surf. Sci.* 509:144872. doi: 10.1016/j.apsusc.2019.144872

Li, Y., Yuan, X., Yang, H., Chao, Y., Guo, S., and Wang, C. (2019b). One-step synthesis of silver nanowires with ultra-long length and thin diameter to make flexible transparent conductive films. *Materials*12:401. doi: 10.3390/ma12030401

Liu, J., Wang, J., Xu, C., Jiang, H., Li, C., Zhang, L., et al. (2018a). Advanced energy storage devices: basic principles, analytical methods, and rational materials design. *Adv. Sci.* 5:1700322. doi: 10.1002/advs.201700322

Liu, L., Niu, Z., and Chen, J. (2016). Unconventional supercapacitors from nanocarbon-based electrode materials to device configurations. *Chem. Soc. Rev.* 45, 4340–4363. doi: 10.1039/C6CS00041J

Liu, T., Zhang, L., You, W., and Yu, J. (2018b). Core–shell nitrogen-doped carbon hollow spheres/co_3o_4 nanosheets as advanced electrode for high-performance supercapacitor. *Small* 14:1702407. doi: 10.1002/smll.201702407

Liu, X., Ma, R., Bando, Y., and Sasaki, T. (2012). A general strategy to layered transition-metal hydroxide nanocones: tuning the composition for high electrochemical performance. *Adv. Mater.* 24, 2148–2153. doi: 10.1002/adma.201104753

Liu, Y., Fu, N., Zhang, G., Xu, M., Lu, W., Zhou, L., et al. (2017). Design of hierarchical Ni-Co@Ni-Co layered double hydroxide core–shell structured nanotube array for high-performance flexible all-solid-state battery-type supercapacitors. *Adv. Funct. Mater.* 27:1605307. doi: 10.1002/adfm.201605307

Lobato, B., Suárez, L., Guardia, L., and Centeno, T. A. (2017). Capacitance and surface of carbons in supercapacitors. *Carbon N. Y.* 122, 434–445. doi: 10.1016/j.carbon.2017.06.083

Long, D., Liu, H., Yuan, Y., Li, J., Li, Z., and Zhu, J. (2019). A facile and large-scale synthesis of NiCo-LDHs@rGO composite for high performance asymmetric supercapacitors. *J. Alloys Compd.* 805, 1096–1105. doi: 10.1016/j.jallcom.2019.07.161

Long, X., Li, J., Xiao, S., Yan, K., Wang, Z., Chen, H., et al. (2014). A strongly coupled graphene and feni double hydroxide hybrid as an excellent electrocatalyst for the oxygen evolution reaction. *Angew. Chem Int Ed.* 53, 7584–7588. doi: 10.1002/anie.201402822

Luan, F., Wang, G., Ling, Y., Lu, X., Wang, H., Tong, Y., et al. (2013). High energy density asymmetric supercapacitors with a nickel oxide nanoflake cathode and a 3D reduced graphene oxide anode. *Nanoscale* 5, 7984–7990. doi: 10.1039/c3nr02710d

Mahjoubi, F. Z., Khalidi, A., Abdennouri, M., and Barka, N. (2017). Zn–Al layered double hydroxides intercalated with carbonate, nitrate, chloride and sulphate ions: synthesis, characterisation and dye removal properties. *J. Taibah Univ. Sci.* 11, 90–100. doi: 10.1016/j.jtusci.2015.10.007

Mehrabimatin, B., Gilshteyn, E. P., Melandsø Buan, M. E., Sorsa, O., Jiang, H., Iraji Zad, A., et al. (2019). Flexible and mechanically durable asymmetric supercapacitor based on NiCo layered double hydroxide and nitrogen-doped graphene using a simple fabrication method. *Energy Technol.* 7:1801002. doi: 10.1002/ente.201801002

Meng, X., and Deng, D. (2016). Bio-inspired synthesis of α-$Ni(OH)_2$ nanobristles on various substrates and their applications. *J. Mater. Chem. A* 4, 6919–6925. doi: 10.1039/C5TA09329E

Miyata, S. (1975). The syntheses of hydrotalcite-likecompounds and their structures and physico-chemical properties i: the systems Mg^{2+}-Al^{3+}-NO_3^-, Mg^{2+}-Al^{3+}-Cl^-, Mg^{2+}-Al^{3+}-ClO_4^-, Ni^{2+}-Al^{3+}-Cl^- and Zn^{2+}-Al^{3+}-Cl^-. *Clays Clay Miner.* 23, 369–375. doi: 10.1346/CCMN.1975.0230508

Mohd Abdah, M. A., Mohammed Modawe Aldris Edris, N., Kulandaivalu, S., Abdul Rahman, N., and Sulaiman, Y. (2018a). Supercapacitor with superior electrochemical properties derived from symmetrical manganese oxide-carbon fiber coated with polypyrrole. *Int. J. Hydrogen Energy* 43, 17328–17337. doi: 10.1016/j.ijhydene.2018.07.093

Mohd Abdah, M. A., Mohd Razali, N. S., Lim, P. T., Kulandaivalu, S., and Sulaiman, Y. (2018b). One-step potentiostatic electrodeposition of polypyrrole/graphene oxide/multi-walled carbon nanotubes ternary nanocomposite for supercapacitor. *Mater. Chem. Phys.* 219, 120–128. doi: 10.1016/j.matchemphys.2018.08.018

Motori, A., Sandrolini, F., and Davolio, G. (1994). Electrical properties of nickel hydroxide for alkaline cell systems. *J. Power Sources* 48, 361–370. doi: 10.1016/0378-7753(94)80032-4

Nagaraju, G., Chandra Sekhar, S., Krishna Bharat, L., and Yu, J. S. (2017). Wearable fabrics with self-branched bimetallic layered double hydroxide coaxial nanostructures for hybrid supercapacitors. *ACS Nano* 11, 10860–10874. doi: 10.1021/acsnano.7b04368

Nagaraju, G., Raju, G. S. R., Ko, Y. H., and Yu, J. S. (2016). Hierarchical Ni–Co layered double hydroxide nanosheets entrapped on conductive textile fibers: a cost-effective and flexible electrode for high-performance pseudocapacitors. *Nanoscale* 8, 812–825. doi: 10.1039/C5NR05643H

Nguyen, T., Boudard, M., João Carmezim, M., and Fátima Montemor, M. (2017). $Ni_xCo_{1-x}(OH)_2$ nanosheets on carbon nanofoam paper as high areal capacity electrodes for hybrid supercapacitors. *Energy* 126, 208–216. doi: 10.1016/j.energy.2017.03.024

Oh, J.-M., Hwang, S.-H., and Choy, J.-H. (2002). The effect of synthetic conditions on tailoring the size of hydrotalcite particles. *Solid State Ionics* 151, 285–291. doi: 10.1016/S0167-2738(02)00725-7

Pan, Z., Sun, H., Pan, J., Zhang, J., Wang, B., and Peng, H. (2018). The creation of hollow walls in carbon nanotubes for high-performance lithium ion batteries. *Carbon N. Y.* 133, 384–389. doi: 10.1016/j.carbon.2018.03.021

Pandolfo, A. G., and Hollenkamp, A. F. (2006). Carbon properties and their role in supercapacitors. *J. Power Sources* 157, 11–27. doi: 10.1016/j.jpowsour.2006.02.065

Pausch, I., Lohse, H.-H., Schürmann, K., and Allmann, R. (1986). Syntheses of disordered and Al-Rich hydrotalcite-like compounds. *Clays Clay Miner.* 34, 507–510. doi: 10.1346/CCMN.1986.0340502

Pu, J., Tong, Y., Wang, S., Sheng, E., and Wang, Z. (2014). Nickel–cobalt hydroxide nanosheets arrays on Ni foam for pseudocapacitor applications. *J. Power Sources* 250, 250–256. doi: 10.1016/j.jpowsour.2013.10.108

Qin, Q., Ou, D., Ye, C., Chen, L., Lan, B., Yan, J., et al. (2019). Systematic study on hybrid supercapacitor of Ni-Co layered double hydroxide//activated carbons. *Electrochim. Acta* 305, 403–415. doi: 10.1016/j.electacta.2019.03.082

Qiu, Z., Peng, Y., He, D., Wang, Y., and Chen, S. (2018). Ternary Fe_3O_4@C@PANi nanocomposites as high-performance supercapacitor electrode materials. *J. Mater. Sci.* 53, 12322–12333. doi: 10.1007/s10853-018-2451-9

Richetta, M., Varone, A., Mattoccia, A., Medaglia, P. G., Kaciulis, S., Mezzi, A., et al. (2018). Preparation, intercalation, and characterization of nanostructured (Zn, Al) layered double hydroxides (LDHs). *Surf. Interf. Anal.* 50, 1094–1098. doi: 10.1002/sia.6468

Sarfraz, M., and Shakir, I. (2017). Recent advances in layered double hydroxides as electrode materials for high-performance electrochemical energy storage devices. *J. Energy Stor.* 13, 103–122. doi: 10.1016/j.est.2017.06.011

Shahrokhian, S., Rahimi, S., and Mohammadi, R. (2018). Nickel-cobalt layered double hydroxide ultrathin nanosheets coated on reduced graphene oxide nonosheets/nickel foam for high performance asymmetric supercapacitors. *Int. J. Hydrogen Energy* 43, 2256–2267. doi: 10.1016/j.ijhydene.2017.12.019

Shao, M., Wei, M., Evans, D. G., and Duan, X. (2015). "Layered double hydroxide materials in photocatalysis," in *Photofunctional Layered Materials,* eds *D. Yan and M. Wei (Cham: Springer International Publishing)*, 105–136.

Shen, J., Ye, S., Xu, X., Liang, J., He, G., and Chen, H. (2019). Reduced graphene oxide based NiCo layered double hydroxide nanocomposites: an efficient catalyst for epoxidation of styrene. *Inorg. Chem. Commun.* 104, 219–222. doi: 10.1016/j.inoche.2019.03.044

Shi, W., Zhu, J., Sim, D. H., Tay, Y. Y., Lu, Z., Zhang, X., et al. (2011). Achieving high specific charge capacitances in Fe_3O_4/reduced graphene oxide nanocomposites. *J. Mater. Chem.* 21, 3422–3427. doi: 10.1039/c0jm03175e

Simon, P., and Gogotsi, Y. (2008). Materials for electrochemical capacitors. *Nat. Mater.* 7, 845–854. doi: 10.1038/nmat2297

Singh, Z. (2016). Applications and toxicity of graphene family nanomaterials and their composites. *Nanotechnol. Sci. Appl.* 9, 15–28. doi: 10.2147/NSA.S101818

Sun, P., Yi, H., Peng, T., Jing, Y., Wang, R., Wang, H., et al. (2017). Ultrathin MnO_2 nanoflakes deposited on carbon nanotube networks for symmetrical supercapacitors with enhanced performance. *J. Power Sources* 341, 27–35. doi: 10.1016/j.jpowsour.2016.11.112

Sun, X., Neuperger, E., and Dey, S. K. (2015). Insights into the synthesis of layered double hydroxide (LDH) nanoparticles: part 1. *Optimization and controlled synthesis of chloride-intercalated LDH. J Colloid Interface Sci.* 459, 264–272. doi: 10.1016/j.jcis.2015.07.073

Sun, X., Wang, G., Sun, H., Lu, F., Yu, M., and Lian, J. (2013). Morphology controlled high performance supercapacitor behaviour of the Ni–Co binary hydroxide system. *J. Power Sources* 238, 150–156. doi: 10.1016/j.jpowsour.2013.03.069

Taylor, H. F. W. (2018). Segregation and cation-ordering in sjögrenite and pyroaurite. *Mineral. Mag.* 37, 338–342. doi: 10.1180/minmag.1969.037.287.04

Tiwari, J. N., Tiwari, R. N., and Kim, K. S. (2012). Zero-dimensional, one-dimensional, two-dimensional and three-dimensional nanostructured materials for advanced electrochemical energy devices. *Prog. Mater. Sci.* 57, 724–803. doi: 10.1016/j.pmatsci.2011.08.003

Vaccari, A. (1998). Preparation and catalytic properties of cationic and anionic clays. *Catal. Today* 41, 53–71. doi: 10.1016/S0920-5861(98)00038-8

Varadwaj, G. B. B., and Nyamori, V. O. (2016). Layered double hydroxide- and graphene-based hierarchical nanocomposites: synthetic strategies and promising applications in energy conversion and conservation. *Nano Res.* 9, 3598–3621. doi: 10.1007/s12274-016-1250-3

Vellacheri, R., Pillai, V. K., and Kurungot, S. (2012). Hydrous RuO_2-carbon nanofiber electrodes with high mass and electrode-specific capacitance for efficient energy storage. *Nanoscale* 4, 890–896. doi: 10.1039/C2NR11479H

Walton, R. I. (2018). "Double hydroxides: present and future," in *Clay Minerals. Cambridge University Press*, ed V. Rives (New York, NY), 139–139.

Wang, C., Zhang, X., Sun, X., and Ma, Y. (2016). Facile fabrication of ethylene glycol intercalated cobalt-nickel layered double hydroxide nanosheets supported on nickel foam as flexible binder-free electrodes for advanced electrochemical energy storage. *Electrochim. Acta* 191, 329–336. doi: 10.1016/j.electacta.2015.12.154

Wang, D., Wei, A., Tian, L., Mensah, A., Li, D., Xu, Y., et al. (2019a). Nickel-cobalt layered double hydroxide nanosheets with reduced graphene oxide grown on carbon cloth for symmetric supercapacitor. *Appl. Surf. Sci.* 483, 593–600. doi: 10.1016/j.apsusc.2019.03.345

Wang, F., Sun, S., Xu, Y., Wang, T., Yu, R., and Li, H. (2017a). High performance asymmetric supercapacitor based on cobalt nickle iron-layered double hydroxide/carbon nanofibres and activated carbon. *Sci. Rep.* 7:4707. doi: 10.1038/s41598-017-04807-1

Wang, F., Wang, T., Sun, S., Xu, Y., Yu, R., and Li, H. (2018a). One-step synthesis of nickle iron-layered double hydroxide/reduced graphene oxide/carbon nanofibres composite as electrode materials for asymmetric supercapacitor. *Sci. Rep.* 8:8908. doi: 10.1038/s41598-018-27171-0

Wang, G., Zhang, L., and Zhang, J. (2012). A review of electrode materials for electrochemical supercapacitors. *Chem. Soc. Rev.* 41, 797–828. doi: 10.1039/C1CS15060J

Wang, J., Wang, L., Chen, X., Lu, Y., and Yang, W. (2015). Chemical power source based on layered double hydroxides. *J. Solid State Electrochem.* 19, 1933–1948. doi: 10.1007/s10008-014-2723-5

Wang, Q., Gao, Y., Luo, J., Zhong, Z., Borgna, A., Guo, Z., et al. (2013a). Synthesis of nano-sized spherical Mg3Al–CO3 layered double hydroxide as a high-temperature CO_2 adsorbent. *RSC Adv.* 3, 3414–3420. doi: 10.1039/c2ra22607c

Wang, T., Liu, X., Ma, C., Liu, Y., Dong, H., Ma, W., et al. (2018b). 3D Ag/NiCo-layered double hydroxide with adsorptive and photocatalytic performance. *J. Taiwan Inst. Chem. Eng.* 93, 298–305. doi: 10.1016/j.jtice.2018.07.031

Wang, T., Zhang, S., Yan, X., Lyu, M., Wang, L., Bell, J., et al. (2017b). 2-Methylimidazole-Derived Ni–Co layered double hydroxide nanosheets as high rate capability and high energy density storage material in hybrid supercapacitors. *ACS Appl. Mater. Interfaces* 9, 15510–15524. doi: 10.1021/acsami.7b02987

Wang, W., Zhang, N., Ye, Z., Hong, Z., and Zhi, M. (2019b). Synthesis of 3D hierarchical porous Ni–Co layered double hydroxide/N-doped reduced graphene oxide composites for supercapacitor electrodes. *Inorg. Chem. Front.* 6, 407–416. doi: 10.1039/C8QI01132J

Wang, X., and Liu, T. (2011). Fabrication and characterization of ultrathin graphene oxide/Poly(vinyl alcohol) composite films via layer-by-layer assembly. *J. Macromol. Sci. B* 50, 1098–1107. doi: 10.1080/00222348.2010.497694

Wang, Y., Shang, B., Lin, F., Chen, Y., Ma, R., Peng, B., et al. (2018c). Controllable synthesis of hierarchical nickel hydroxide nanotubes for high performance supercapacitors. *Chem. Commun.* 54, 559–562. doi: 10.1039/C7CC08879E

Wang, Y., Wu, P., Li, Y., Zhu, N., and Dang, Z. (2013b). Structural and spectroscopic study of tripeptide/layered double hydroxide hybrids. *J. Colloid Interface Sci.* 394, 564–572. doi: 10.1016/j.jcis.2012.11.031

Wang, Y.-F., Wang, H.-T., Yang, S.-Y., Yue, Y., and Bian, S.-W. (2019c). Hierarchical NiCo2S4@Nickel–cobalt layered double hydroxide nanotube arrays on metallic cotton yarns for flexible supercapacitors. *ACS Appl. Mater. Interfaces* 11, 30384–30390. doi: 10.1021/acsami.9b06317

Wei, M., Huang, Q., Zhou, Y., Peng, Z., and Chu, W. (2018). Ultrathin nanosheets of cobalt-nickel hydroxides hetero-structure via electrodeposition and precursor adjustment with excellent performance for supercapacitor. *J. Energy Chem.* 27, 591–599. doi: 10.1016/j.jechem.2017.10.022

Wen, J., Li, S., Chen, T., Yue, Y., Liu, N., Gao, Y., et al. (2016). Three-dimensional hierarchical NiCo hydroxide@Ni3S2 nanorod hybrid structure as high performance positive material for asymmetric supercapacitor. *Electrochim. Acta* 222, 965–975. doi: 10.1016/j.electacta.2016.11.064

Weng, B., Liu, S., Tang, Z.-R., and Xu, Y.-J. (2014). One-dimensional nanostructure based materials for versatile photocatalytic applications. *RSC Adv.* 4, 12685–12700. doi: 10.1039/c3ra47910b

Windisch, C. F., Exarhos, G. J., Ferris, K. F., Engelhard, M. H., and Stewart, D. C. (2001). Infrared transparent spinel films with p-type conductivity. *Thin Solid Films* 398–399, 45–52. doi: 10.1016/S0040-6090(01)01302-5

Wu, S., Guo, H., Hui, K. S., and Hui, K. N. (2019a). Rational design of integrated CuO@$Co_xNi_{1-x}(OH)_2$ nanowire arrays on copper foam for high-rate and long-life supercapacitors. *Electrochim. Acta* 295, 759–768. doi: 10.1016/j.electacta.2018.10.183

Wu, X., Lian, M., and Wang, Q. (2019b). A high-performance asymmetric supercapacitors based on hydrogen bonding nanoflower-like polypyrrole and NiCo(OH)2 electrode materials. *Electrochim. Acta* 295, 655–661. doi: 10.1016/j.electacta.2018.10.199

Xia, D., Chen, H., Jiang, J., Zhang, L., Zhao, Y., Guo, D., et al. (2015). Facilely synthesized α phase nickel–cobalt bimetallic hydroxides: Tuning the composition for high pseudocapacitance. *Electrochim. Acta* 156, 108–114. doi: 10.1016/j.electacta.2015.01.018

Xie, L., Hu, Z., Lv, C., Sun, G., Wang, J., Li, Y., et al. (2012). CoxNi1–x double hydroxide nanoparticles with ultrahigh specific capacitances as supercapacitor electrode materials. *Electrochim. Acta* 78, 205–211. doi: 10.1016/j.electacta.2012.05.145

Xu, J., Gai, S., He, F., Niu, N., Gao, P., Chen, Y., et al. (2014). Reduced graphene oxide/Ni1-xCoxAl-layered double hydroxide composites: preparation

and high supercapacitor performance. *Dalton Trans.* 43, 11667–11675. doi: 10.1039/C4DT00686K

Xu, J., Liao, K., Song, K., Wu, J., Hu, X., Gao, H., et al. (2018). Fast *in situ* synthesis of CoFe layered double hydroxide onto multi-layer graphene for electrochemical capacitors. *J. Solid State Electrochem.* 22, 1037–1045. doi: 10.1007/s10008-017-3839-1

Xu, Z. P., Stevenson, G., Lu, C.-Q., and Lu, G. Q. (2006). Dispersion and size control of layered double hydroxide nanoparticles in aqueous solutions. *J. Phys. Chem. B* 110, 16923–16929. doi: 10.1021/jp062281o

Yan, A.-L., Wang, X.-C., and Cheng, J.-P. (2018). Research progress of NiMn layered double hydroxides for supercapacitors: a review. *Nanomaterials* 8:747. doi: 10.3390/nano8100747

Yan, T., Li, R., and Li, Z. (2014). Nickel–cobalt layered double hydroxide ultrathin nanoflakes decorated on graphene sheets with a 3D nanonetwork structure as supercapacitive materials. *Mater. Res. Bull.* 51, 97–104. doi: 10.1016/j.materresbull.2013.11.044

Yan, T., Li, R., Yang, T., and Li, Z. (2015). Nickel/cobalt layered double hydroxide hollow microspheres with hydrangea-like morphology for high-performance supercapacitors. *Electrochim. Acta* 152, 530–537. doi: 10.1016/j.electacta.2014.08.149

Yang, S., Zhang, Z., Zhou, J., Sui, Z., and Zhou, X. (2019). Hierarchical NiCo LDH–rGO/Ni foam composite as electrode material for high-performance supercapacitors. *Trans. Tianjin Univ.* 25, 266–275. doi: 10.1007/s12209-018-0180-4

Yang, W., Gao, Z., Wang, J., Ma, J., Zhang, M., and Liu, L. (2013). Solvothermal one-step synthesis of Ni–Al layered double hydroxide/carbon nanotube/reduced graphene oxide sheet ternary nanocomposite with ultrahigh capacitance for supercapacitors. *ACS Appl. Mater. Interfaces* 5, 5443–5454. doi: 10.1021/am4003843

Yang, Y. J., and Li, W. (2019). Hierarchical Ni–Co double hydroxide nanosheets on reduced graphene oxide self-assembled on Ni foam for high-energy hybrid supercapacitors. *J. Alloys Compd.* 776, 543–553. doi: 10.1016/j.jallcom.2018.10.344

Young, C., Lin, J., Wang, J., Ding, B., Zhang, X., Alshehri, S. M., et al. (2018). Significant effect of pore sizes on energy storage in nanoporous carbon supercapacitors. *Chem. A Eur. J.* 24, 6127–6132. doi: 10.1002/chem.201705465

Yu, Z., Tetard, L., Zhai, L., and Thomas, J. (2015). Supercapacitor electrode materials: nanostructures from 0 to 3 dimensions. *Energy Environ. Sci.* 8, 702–730. doi: 10.1039/C4EE03229B

Yulian, N., Ruiyi, L., Zaijun, L., Yinjun, F., and Junkang, L. (2013). High-performance supercapacitors materials prepared via *in situ* growth of NiAl-layered double hydroxide nanoflakes on well-activated graphene nanosheets. *Electrochim. Acta* 94, 360–366. doi: 10.1016/j.electacta.2012.09.084

Zhang, J., Zheng, Z., Wu, G., and Hua, Q. (2019). Hierarchical electrodes assembled by alternate NiCo hydroxide nanowires arrays and conductive interlayers with enhanced properties for electrochemical supercapacitors. *J. Alloys Compd.* 785, 725–731. doi: 10.1016/j.jallcom.2019.01.233

Zhang, L., Zhang, X., Shen, L., Gao, B., Hao, L., Lu, X., et al. (2012). Enhanced high-current capacitive behavior of graphene/CoAl-layered double hydroxide composites as electrode material for supercapacitors. *J. Power Sources* 199, 395–401. doi: 10.1016/j.jpowsour.2011.10.056

Zhang, W., Ma, C., Fang, J., Cheng, J., Zhang, X., Dong, S., et al. (2013). Asymmetric electrochemical capacitors with high energy and power density based on graphene/CoAl-LDH and activated carbon electrodes. *RSC Adv.* 3, 2483–2490. doi: 10.1039/c2ra23283a

Zhao, J., Xu, S., Tschulik, K., Compton, R. G., Wei, M., O'hare, D., et al. (2015). Molecular-scale hybridization of clay monolayers and conducting polymer for thin-film supercapacitors. *Adv. Funct. Mater.* 25, 2745–2753. doi: 10.1002/adfm.201500408

Zhao, M., Zhao, Q., Li, B., Xue, H., Pang, H., and Chen, C. (2017). Recent progress in layered double hydroxide based materials for electrochemical capacitors: design, synthesis and performance. *Nanoscale* 9, 15206–15225. doi: 10.1039/C7NR04752E

Zhao, Y., Xiao, F., and Jiao, Q. (2011). Hydrothermal synthesis of Ni/Al layered double hydroxide nanorods. *J. Nanotechnol* 2011: 6. doi: 10.1155/2011/646409

Zhi, M., Xiang, C., Li, J., Li, M., and Wu, N. (2013). Nanostructured carbon–metal oxide composite electrodes for supercapacitors: a review. *Nanoscale* 5, 72–88. doi: 10.1039/C2NR32040A

Zhong, C., Deng, Y., Hu, W., Qiao, J., Zhang, L., and Zhang, J. (2015). A review of electrolyte materials and compositions for electrochemical supercapacitors. *Chem. Soc. Rev.* 44, 7484–7539. doi: 10.1039/C5CS00303B

Conflict of Interest: The authors declare that the research was conducted in the absence of any commercial or financial relationships that could be construed as a potential conflict of interest.

frontiers in Materials

ORIGINAL RESEARCH
published: 07 August 2020
doi: 10.3389/fmats.2020.00263

Improving Cyclic Stability of $LiMn_2O_4$/Graphite Battery Under Elevated Temperature by Using 1, 3-Propane Sultone as Electrolyte Additive

Xinxi Li[1], Long Liu[1], Shumin Li[2], Lin Guo[3†], Bin Li[1,3] and Guoqing Zhang[1]**

[1] School of Materials and Energy, Guangdong University of Technology, Guangzhou, China, [2] School of Chemistry and Environment, South China Normal University, Guangzhou, China, [3] School of Chemistry and Materials Engineering, Huizhou University, Huizhou, China

OPEN ACCESS

Edited by:
Federico Cesano,
University of Turin, Italy

Reviewed by:
Xianwen Wu,
Jishou University, China
Renheng Wang,
Shenzhen University, China
Şaban Patat,
Erciyes University, Turkey

***Correspondence:**
Bin Li
lib120@163.com
Guoqing Zhang
pdzgq008@126.com

†Present address:
Lin Guo,
Guangdong Guangxin Holdings Group Ltd., Guangzhou, China

Specialty section:
This article was submitted to Energy Materials, a section of the journal Frontiers in Materials

Received: 26 December 2019
Accepted: 17 July 2020
Published: 07 August 2020

Citation:
Li X, Liu L, Li S, Guo L, Li B and Zhang G (2020) Improving Cyclic Stability of $LiMn_2O_4$/Graphite Battery Under Elevated Temperature by Using 1, 3-Propane Sultone as Electrolyte Additive. Front. Mater. 7:263. doi: 10.3389/fmats.2020.00263

Spinel lithium manganese oxide ($LiMn_2O_4$) based Li-ion battery (LIB) is attractive for hybrid/full electric vehicles because of its abundant resources and easy preparation. However, operation under an elevated temperature could cause severe capacity fading of the spinel cathodes. In this work, 1, 3-propane sultone (PS) is investigated as an electrolyte additive for improving the cyclability of the $LiMn_2O_4$/graphite LIB at elevated temperature. The charge and discharge measurement proves that PS can significantly enhance the cyclability of 053048-type $LiMn_2O_4$/graphite pouch cell at 60°C. Compared to the cell without additive, the capacity retention of the cell using electrolyte with 5% PS increases from 52 to 71% after 180 cycles. The improved cyclability is attributable to the modification of the solid electrolyte interface (SEI) on both positive and negative sides of the $LiMn_2O_4$/graphite cell by PS, which effectively prevents anode and cathode from structural breakdown and inhibits the electrolyte decomposition.

Keywords: 1, 3-propane sultone, solid electrolyte interphase, graphite anode, spinel cathode, lithium ion battery

INTRODUCTION

Li-ion battery (LIB) is successfully applied in portable electronic equipment and is scaled up for hybrid/full electric vehicles and grid storage for renewable energy sources (Cheng et al., 2017; Yu et al., 2020). Spinel lithium manganese oxide ($LiMn_2O_4$) is an ideal material for LIB owing to its superior properties, such as low cost, high operating voltage, good safety, and low toxicity. However, $LiMn_2O_4$ is not widely utilized in LIB commercialization due to its poor cycling performance, especially at high temperature over 55°C (Huang et al., 2018; Hai et al., 2019). Generally, the poor cycling performance is arised from the irreversible crystal phase transition (Jahn–Teller distortion) and oxygen deficiency (Xie et al., 2019), and more importantly, manganese (Mn) ion dissolving into the electrolyte and subsequently deposited on the graphite anode, which degrades the solid electrolyte interphase (SEI) on the electrode surface or deteriorates the graphite structure (Ryou et al., 2010; Liao et al., 2017; Flamme et al., 2020).

Many methods were reported to effectively improve the electrochemical performance of the $LiMn_2O_4$ cells, such as element partial substitutions (Ding et al., 2011; Piao et al., 2018) and

surface coatings (Cao et al., 2018; Li et al., 2018; Zhang et al., 2018). However, alternatives and surface coatings usually cause reversible capacity loss and involve high cost manufacture. The use of surface film-forming electrolyte additive is an effective and facile method to enhance the electrochemical behavior of lithium ion battery. This method cannot only modify the SEI layers on electrodes and prevent the dissolution/deposition of transition metal, but also can inhibit the electrolyte decomposition during the cycling.

Various SEI-film forming additives have been used for enhancing the high temperature stability of the $LiMn_2O_4$-based cells, including sulfur-containing compounds such as methylene methanedisulfonate (Zuo et al., 2014), prop-1-ene-1, 3-sultone (Li Y. et al., 2013), P-toluenesulfonyl isocyanate (Wang et al., 2015), 3, 3′–sulfonyldipropionitrile (Huang et al., 2015), and butyl sultone (Xu et al., 2007). The sulfur-containing substances generated from the additives decomposition can deactivate many catalysts (Czekaj et al., 2011). It helps to build protective surface film on the electrode and suppress decomposition of the electrolyte, which leads to the improved performance of the cell. 1, 3-propane sultone (PS) is one of the most used additives in LIBs (Guo et al., 2008). It has been used as an electrolyte additive in $LiMn_2O_4$-based battery to improve the thermal storage performance. The improvement can be ascribed to its suppression of solvent co-intercalating into graphite anode (Xu et al., 2009).

Although PS has been applied as suppress propylene carbonate (PC) co-intercalation co-solvent and additive to improve the thermal storage performance in $LiMn_2O_4$/graphite cell, the behavior of PS on the cathode reactions, modification of the anode SEI, and thermal cyclability of the cell have not been clearly investigated. Herein, we present a study focused on morphology and structure of the cathode and anode SEI films by using PS as an electrolyte additive in $LiMn_2O_4$/graphite cell. The effect of PS on the cell cyclability at high operating temperature was investigated and the morphologies and chemical compositions of the surface films of the cycled electrodes were also presented.

EXPERIMENTAL

The $LiMn_2O_4$ electrode was prepared by coating a mixture of 90 wt.% $LiMn_2O_4$ (Hunan Reshine New Material Co., Ltd.), 5 wt.% of super-p (MMM carbon, Belgium), and 5 wt.% of polyvinylidene difluoride (PVDF, Shanghai Ofluorine Chemical Technology Co., Ltd.) binder on an aluminum current collect (thickness was 16 um). The active material loading of the $LiMn_2O_4$ electrode was 340 g m^{-2} and the thickness was about 179 um. The graphite electrode was obtained by coating a mixture 95 wt.% of graphite (BTR Battery Materials Co., Ltd.), 1 wt.% of super-p, 2 wt.% carboxymethyl cellulose, and 2 wt.% of styrene butadiene rubber in deionized water on a copper foil (thickness was 8 um). The graphite material loading of the electrode was 155 g m^{-2} and the thickness was about 165 um. The full cells (053048-type) were assembled in an argon-filled dry glove box (Mbraun Unilab MB20, water and oxygen contents were lower than 0.1 ppm) with the $LiMn_2O_4$ electrode as positive electrodes (P) and graphite electrode as negative electrodes (N). The loading weight of the active material for $LiMn_2O_4$/graphite cells was controlled to the specific capacity of N/P = 1.15 (the specific capacity of N and P were 340 and 135 mA h g^{-1} for graphite and $LiMn_2O_4$, respectively). The design capacity of the punch cell was 500 mAh. The separator was a Celgard 2400 membrane. The electrolyte was composed of 1.0 M $LiPF_6$ - ethylene carbonate (EC) / ethyl methyl carbonate (EMC) with the volume ratio of 1:2 (Guangzhou Tinci Materials Technology Co. Ltd, China). 1, 3-propane sultone (PS) was purchased from Aladdin (purity: >99%). The amount of electrolyte used in the pouch cell was controlled to 2.8 g Ah^{-1}.

The electrochemical performance test of the full cell was performed using CT-4008-5V6A-S1 test system (NEWARE, Shenzhen, China) between 2.75 and 4.20 V at room temperature and 60°C, respectively. Five cells were tested with each electrolyte and the reported charge/discharge results are the average values of top three cells. The thickness of cells was tested by a micrometer caliper (Cal PRO IP67, SYLVAC, Swiss). The formula for calculating the swell value of the $LiMn_2O_4$/graphite battery is as follows:

$$\text{Swellvalue}(\%) = (T - T_0)/T_0 \times 100.$$

where T_0 and T are the thickness of the $LiMn_2O_4$/graphite cell before and after 180 cycles at 60°C, respectively.

The internal resistance of cells was measured by resistance meter (HK3561, Meifu, Shenzhen) when the cells cooled down to the room temperature. The formula for calculating the internal resistance rate of the $LiMn_2O_4$/graphite battery is as follows:

Internal resistance rate (%) = $(R\text{-}R_0)/R_0 \times 100$.

where R_0 and R are the internal resistance of the $LiMn_2O_4$/graphite cell before and after 180 cycles at 60°C, respectively.

Conductivity of the electrolyte solutions was measured using a Model DDS-307 conductometer (Shanghai Precision Scientific Instrument Co., Ltd., China). The linear sweep voltammetry (LSV) was performed in Li/Pt cell on Solartron-1408 instrument (England) at a scan rate of 0.2 mV s^{-1} in voltage range of open circuit potential to 5.0 V (vs. Li^+/Li). Cyclic voltammetry of Li/graphite cell was performed on Solartron-1470 instrument (England) in the potential range of 0.01–2.5 V (vs. Li^+/Li) at a scanning rate of 0.2 mV s^{-1}. The diameter and the thickness of Li disk were 15.6 and 0.2 mm, respectively. The graphite and $LiMn_2O_4$ electrodes were disassembled from the full cells and washed with dimethyl carbonate solvent 3 times to remove residual electrolytes. The rinsed electrodes were kept in an antechamber of the glovebox to remove the solvent before conducting surface characterization. The morphology and structure of the electrodes were obtained by a scanning electron microscope (SEM, JEOL JSM-6380) and a transmission electron microscope (TEM, JEOL JEM-2100HR). X-ray diffractometer (XRD, Rigaku Ultima IV, Japan) was used to investigate the crystal structure of the electrode. The chemical composition on the surface of the electrodes was analyzed by X-ray photoelectron spectroscopy (XPS, Kratos Axis Ultra DLD) with Al Ka line ($h\upsilon$ = 1486.6 eV) as a radiation exciting source. X-ray analysis

area for the surface was ~500 × 500 um. Pressure in the analytical chamber during spectral acquisition was less than 5×10^{-9} Torr. Pass energy for survey and detail spectra (to calculate composition) was 80 eV. The take-off angle (the angle between the sample normal and the input axis of the energy analyzer) was 0°, and the input lens was operated in hybrid mode (0° take-off angle = around 100 Å sampling depth). The binding energy was calibrated based on the C 1s level at 284.3 eV (C-C).

RESULTS AND DISCUSSION

Figure 1 depicts the cycling behavior of $LiMn_2O_4$/graphite pouch full-cells without and with variable concentrations of 1, 3-propane sultone (PS) at room temperature at a current of 500 mA. As shown in **Figure 1A**, the reversible capacity of the $LiMn_2O_4$/graphite cell without additive is only 430 mAh in the first cycle, which indicates a large amount of irreversible lithium consumption during charging owing to the decomposition of electrolyte on the anode surface. When PS additive is applied in the electrolyte, the discharge capacities increased. The first cycle capacity of the cells with 3, 5, and 7 wt.% PS addition in the electrolyte are 474, 497, and 467 mAh, respectively. Obviously, when the concentration of PS is 5 wt.%, a most effective SEI film was formed on the electrodes. The SEI film cannot only suppress the electrolyte decomposition but also can benefit the lithium insertion/de-insertion during the cycling. However, the discharge capacity decreased when the PS concentration is higher than 5 wt.%. This phenomenon suggests that excess PS might lead to the formation of a thicker SEI film on the electrode which would hinder the transport of Li^+ in the cells.

Figure 2 shows the cycling performances of $LiMn_2O_4$/graphite cells using the electrolyte without and with various concentrations of PS at 60°C. Before the cycling at high temperature, all the cells were cycling for three times under room temperature at 1C (500 mA). In the cell with additive-free electrolyte, the capacity fading becomes severe during the cycling, as shown in **Figure 2A**. The reversible capacity of the cell using the electrolyte without additive displays about 48% capacity loss at the 180th cycle (**Figure 2B**). At high temperature (60°C), the decomposition of the electrolyte becomes severe and the $LiMn_2O_4$ suffer destruction, result in the dissolution of Mn ions from spinel into the electrolyte. The Mn ions in the electrolyte can deposit on the graphite side and further catalyze

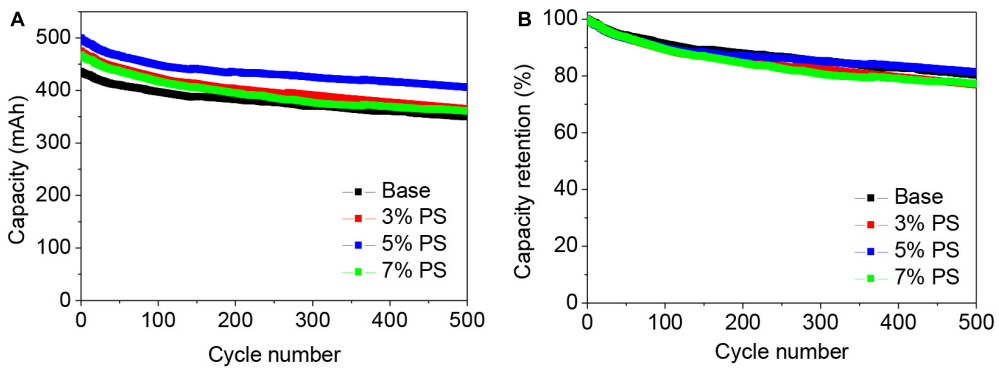

FIGURE 1 | Cyclic stability **(A)** and corresponding capacity retention **(B)** of $LiMn_2O_4$/graphite cells using the electrolyte without (Base), with 3, 5, and with 7 wt.% PS. Charge-discharge rate was 1.0 C in the potential range of 2.75–4.20 V at 25°C.

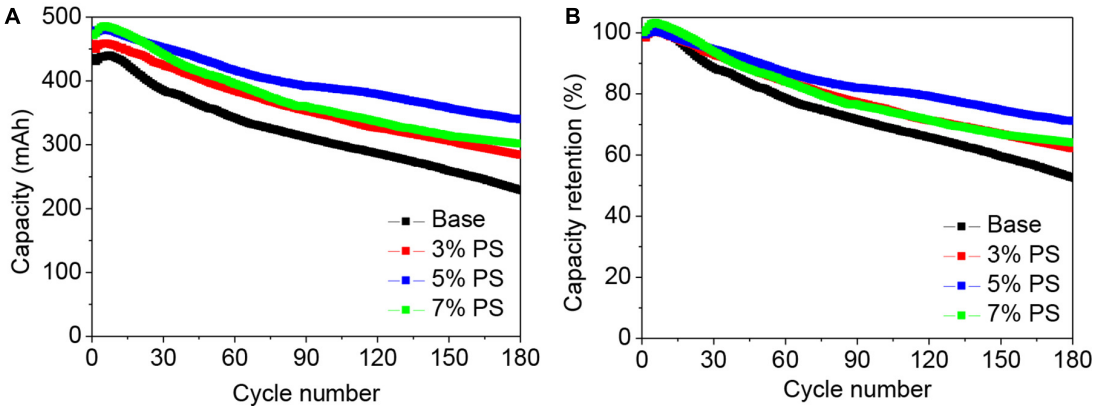

FIGURE 2 | Cycling stability **(A)** and corresponding capacity retention **(B)** of $LiMn_2O_4$/graphite cells using the electrolyte without (Base), with 3, 5, and with 7 wt.% PS. Charge-discharge rate was 1.0 C in the potential range of 2.75–4.20 V at 60°C.

the electrolyte decomposition when the cell was charging, leading to poor cycling performance (Li Y. et al., 2013). In case of the $LiMn_2O_4$/graphite cells using PS, the cycling stabilities are much higher than that of the additive-free cell. The discharge capacity retention of the $LiMn_2O_4$/graphite in the electrolyte using 3, 5, and 7 wt.% PS are 62, 71, and 64%, respectively. This indicates that an excellent SEI film can be formed on graphite with 5 wt.% PS addition. The electrochemical performance of the cell becomes worse when the content of the additive is further increased, which might be related to the over thickness of the SEI film. These results indicate the contribution of PS to the enhanced stability performance of the $LiMn_2O_4$/graphite cells.

The dimensional change and resistance growth of the cells can further confirm that PS can effectively protect the electrolyte from decomposition. **Figure 3** and **Table 1** present the thickness change and resistance growth of the cells before and after 180 cycles at 60°C. Under high temperature, the electrolyte decompositions on both anode and cathode become severe during the cycling, which result in gas generation and structural change of the SEI film and consequently increase the thickness and resistance along the electrodes. The swell value of the cells using electrolyte without, with 3, 5, and 7 wt.% PS are 35.8, 21.3, 6.5, and 7.2%, while the internal resistance rate for those cells are 78.5, 46.4, 31.8, and 38.2%, respectively. Apparently, the electrolyte decomposition in the $LiMn_2O_4$/graphite cells with PS as electrolyte additive can be significantly suppressed at high temperature.

The conductivities of electrolyte without and with different contents of PS were investigated at room temperature. Due to the high melting point of PS (30–33°C), the conductivity of the electrolyte is slightly decreased with the increase content of the additive, as shown in **Table 2**. The conductivity of electrolyte containing 5% PS can reach 8.63 mS cm^{-1}, indicating an insignificant effect on electrolyte conductivity if PS is used within certain limits.

The stability of the electrolyte was also evaluated with linear sweep voltammetry (LSV). **Figure 4** presents the LSV of Pt in the electrolyte with and without PS. The base electrolyte is decomposed at around 4.7 V (vs. Li^+/Li). When adding 5% PS into the electrolyte, oxidation current can be observed at around 4.1 V (vs. Li^+/Li). This behavior implies that the preferential oxidation of PS, suggests PS can form the modified surface film on $LiMn_2O_4$ compared to the base electrolyte.

The reduction behavior of the PS on graphite anode was also investigated by cyclic voltammograms (CV). **Figure 5** shows the CV of graphite electrodes in 1.0 M LiPF6-EC / EMC (1:2) with and without 5% PS. In the electrolyte without additive, a reduction peak located at around 0.5 V (vs. Li^+/Li) can be observed during the first cathodic potential sweep, which is attributed to the reduction of EC in the electrolyte. This reduction peak still appears in the second cycle, although it is smaller than that of the first one, as shown **Figure 5A**. It means the EC-derived SEI film does not completely suppress the further reduction of electrolyte during the second cycle. In the case of the electrolyte with PS, a small reduction peak at around 0.7 V (vs. Li^+/Li) can be observed in the first cycle, and the peak at 0.5 V (vs. Li^+/Li) disappears, as shown in **Figure 5B**. In the second cycle, the reduction peak of PS disappears. These results indicate the preferential reduction of PS and the SEI formed by PS was effective enough to suppress the further decompositions of solvents. It can be noted that the de-intercalation peak of lithium ions swifts to 0.30 V (vs. Li^+/Li) in the second cycle, which is lower than that of the base electrolyte (0.37 V vs. Li^+/Li). This suggests the SEI formed by PS on the first cycle promotes the reaction at the interface and thus leads to higher capacity of the cell than that of the base one.

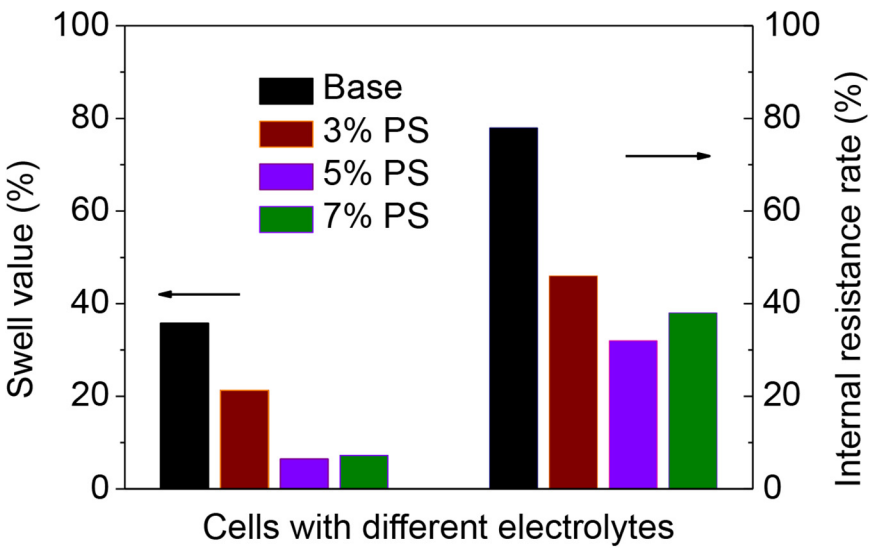

FIGURE 3 | Swell value and internal resistance rate of $LiMn_2O_4$/graphite cells using the electrolyte without (Base) and with variable concentrations of PS after 180 cycles at 60°C.

TABLE 1 | Swell value and internal resistance rate of $LiMn_2O_4$/graphite cells using different electrolytes before and after 180 cycles at 60°C.

Solvent	Additive	Swell value (%)	Internal resistance (%)
EC-EMC(1:2)	Base	35.8	78.2
	3 wt.% PS	21.3	45.9
	5 wt.% PS	6.5	32.1
	7 wt.% PS	7.2	38.4

TABLE 2 | Conductivities of 1.0 M $LiPF_6$ – EC / EMC (1:2) at different content of PS.

Electrolyte	Conductivity (mS cm^{-1})
Base	9.17
3% PS	8.91
5% PS	8.63
7% PS	8.47

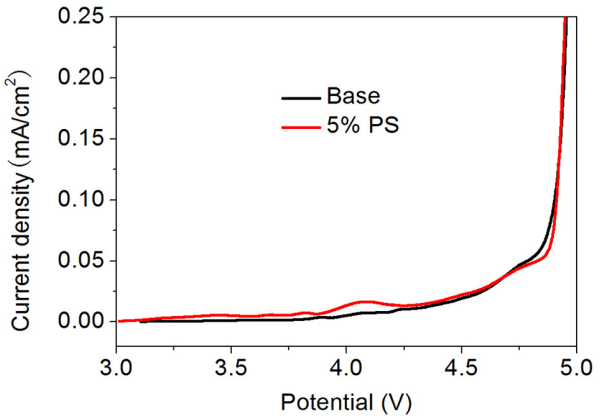

FIGURE 4 | LSV of Pt electrode in 1.0 M $LiPF_6$-EC / EMC (1:2) with and without 5% PS. The area of working electrode was 1.0 cm^2.

To investigate the effect of PS on the improved cyclability of $LiMn_2O_4$/graphite cell at elevated temperature, XRD, SEM, TEM, and XPS measurements were conducted to analyze the morphologies and compositions of the cycled electrode surface films.

The SEM images in **Figure 6** show the surface morphology of the pristine and the graphite electrodes after 180 cycles at 60°C using the electrolyte with and without 5 wt.% PS. The flake-like structure graphite particles with clean surface and sharp edges can be clearly observed in the pristine electrode (**Figures 6a,d**). After cycling in the electrolyte without additive, the electrode surface becomes rough and display a fluffy and thick morphology as shown in **Figures 6b,e**. It suggests that the electrolyte is decomposed and the graphite structure is destroyed. In contrast, the PS electrode continued to display a smooth surface and almost kept relatively similar to original shape of fresh graphite particles after cycling (**Figure 6c**). Moreover, the surface of the graphite particles is evenly covered with a dense surface film. This result indicates that a stable and robust SEI could be formed by the addition of PS, which inhibits further electrolyte decomposition and protects the graphite effectively from exfoliation. The development of sulfur-containing interfaces may allow for the use of electrolytes that are otherwise structural unstable anode materials, such as the Si-based and oxide anode (Wu et al., 2019; Fang et al., 2020).

Figure 7 reveals the SEM and TEM images of the p.ristine $LiMn_2O_4$ and the cathodes cycled with and without PS after 180 cycles. As shown in **Figures 7a,d**, the fresh $LiMn_2O_4$ particles present a typical octahedral spinel shape and the surface are smooth and clean. After cycling in the electrolyte without PS, thick and inhomogeneous deposits can be observed on the spinel particle surface (**Figures 7b,e**), and cracks appear as indicated by the arrow in **Figure 7c**. By contrast, the deposit on the $LiMn_2O_4$ particle with PS additive is uniform

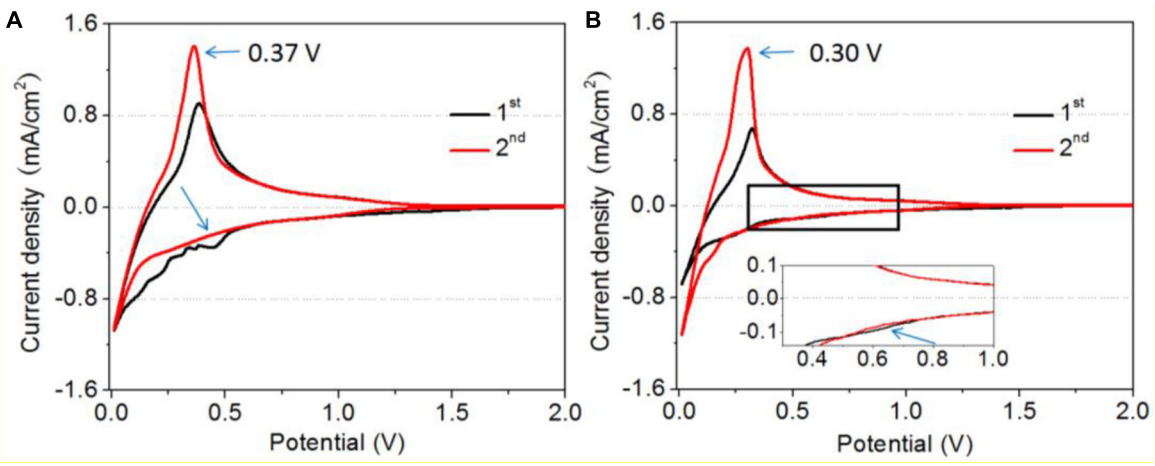

FIGURE 5 | Cyclic voltammograms of graphite electrode in 1.0 M $LiPF_6$-EC / EMC (1:2) without **(A)** and with 5% PS **(B)**. The diameter of graphite electrode was 13.0 mm.

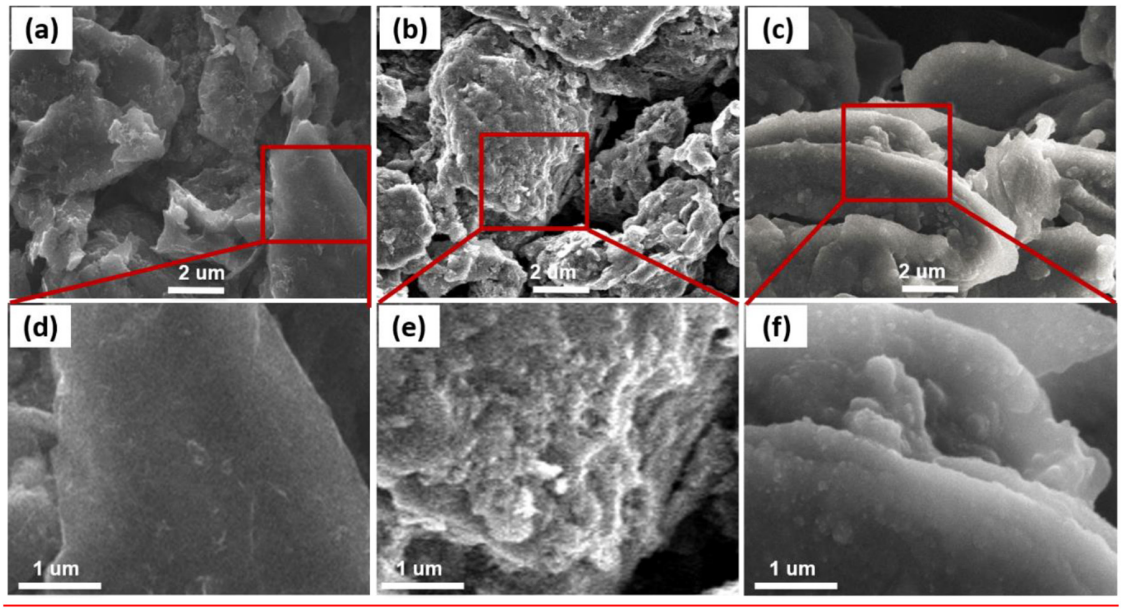

FIGURE 6 | SEM images of pristine graphite anode **(a,d)** and the anodes cycled in the electrolyte without **(b,e)**, with 5 wt.% PS **(c,f)**.

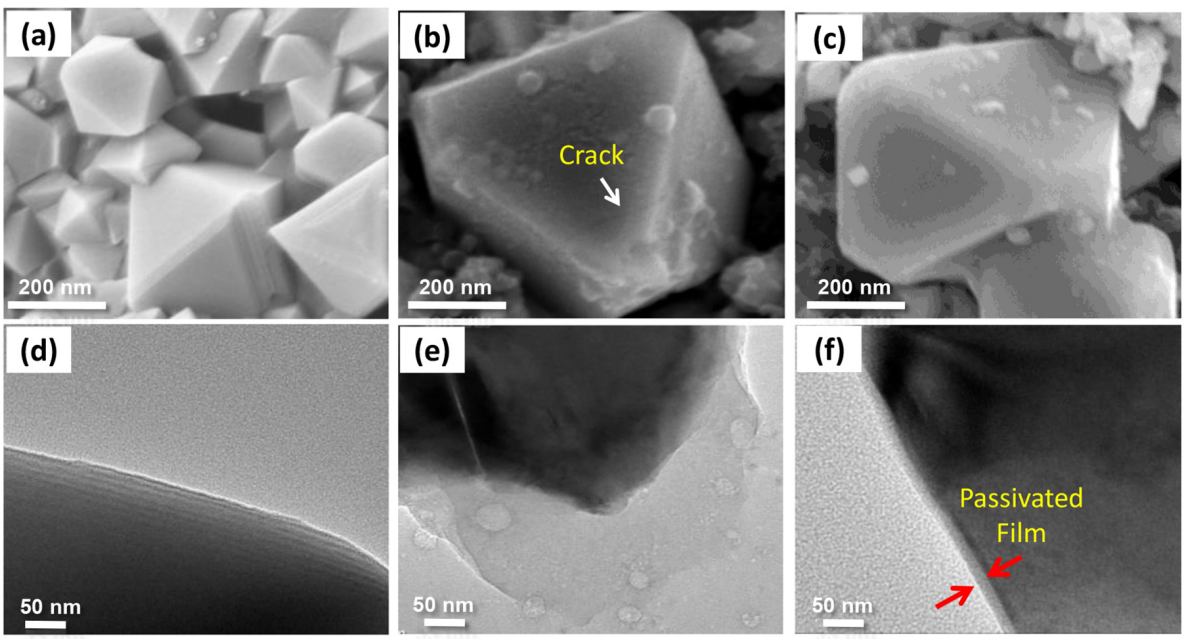

FIGURE 7 | SEM and TEM images for pristine $LiMn_2O_4$ cathode **(a,d)** and the cathode that have been cycled without **(b,e)**, with 5 wt.% PS **(c,f)**.

and thin. The TEM image (**Figure 7f**) displays that the thickness of SEI is around 30 nm. Moreover, the morphology of spinel particle maintains well after cycling. These results indicate that Mn dissolution occurs because of the deterioration of the $LiMn_2O_4$ structure when the cell operated in the base electrolyte. In case of the application of PS as an additive, a protective SEI film can be formed on the cathode surface. This SEI can protect the $LiMn_2O_4$ particles from destruction, inhibits the dissolution of manganese ions from $LiMn_2O_4$ and greatly hinders the continuous decomposition of the electrolyte.

The structural stability of the $LiMn_2O_4$ cycling in the electrolyte with PS was characterized by XRD measurements. As shown in **Figure 8**, all the major diffraction peaks in the pristine electrode and the two cycled $LiMn_2O_4$ electrodes can be indexed to the typical spinel structure for the $LiMn_2O_4$

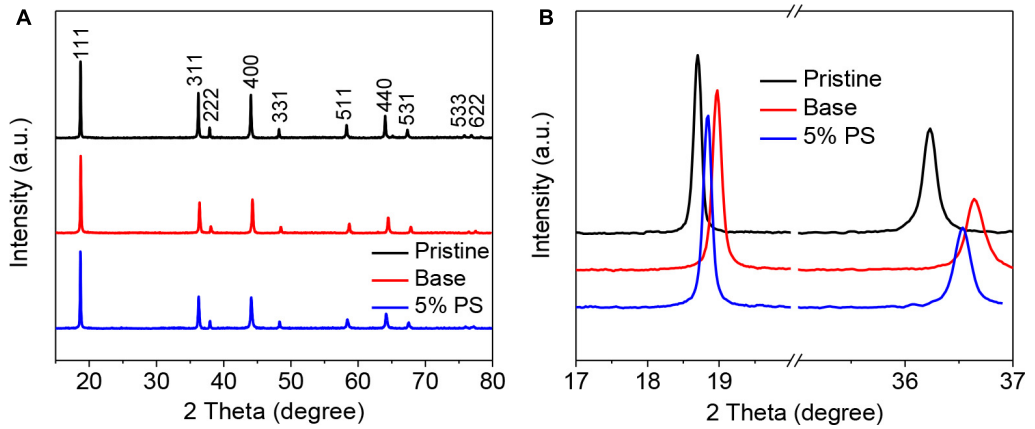

FIGURE 8 | XRD patterns **(A)** and the magnified XRD patterns in the 17–37° 2 Theta interval **(B)** of $LiMn_2O_4$ electrodes before and after cycling in the electrolyte with and without 5 wt.% PS.

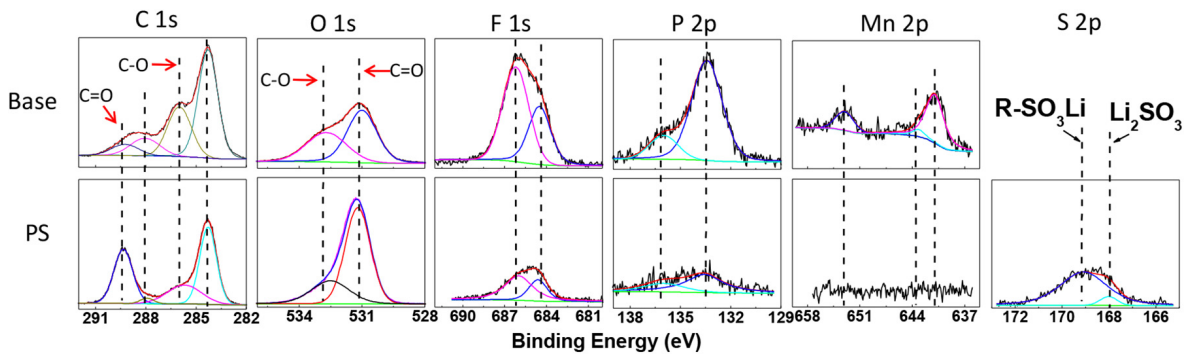

FIGURE 9 | XPS spectra of C 1s, O 1s, F 1s, P 2p, Mn 2p, and S 2p for graphite electrodes after 180 cycles at 60°C in base electrolyte and PS-containing electrolyte.

(JCPDS No. 35-0782). For the $LiMn_2O_4$ cathode cycled with the additive-free electrolyte, the overall intensity of the $LiMn_2O_4$ diffraction peaks is weaker than the pristine electrode, confirming that $LiMn_2O_4$ suffers structural deterioration. This can be ascribed to the severe transition metal (Mn^{3+}) dissolution from the crystal structure that related to the nature of $LiMn_2O_4$ itself (Amatucci et al., 1997; Huang et al., 2018). As shown in **Figure 8B**, the (111) and (311) XRD peaks of electrode cycled without additive shift to higher angles, indicating the crystal lattice shrinkage (Liu et al., 2009). By contrast, the shifting extent for the $LiMn_2O_4$ electrode in the electrolyte with PS is less than that of the electrode without additive, which indicates the SEI formed from PS provides sufficient protection for the crystal structure integrity. This result is in a good agreement with that observed by SEM and TEM. Noted that the shifting still happens while the cell using PS as the electrolyte additive. This might be the reason for the degradation in the cell performance at elevated temperature (as shown in **Figure 2**).

The *ex-situ* XPS spectra have been utilized to investigate the surface compositions of graphite and $LiMn_2O_4$ electrodes. **Figure 9** and **Table 3** reveal the XPS spectra results of graphite anodes after 180 cycles at 60°C. In the C 1s and O 1s spectra, C = O (289.4 eV, 531.2 eV) bond corresponds to lithium carbonates and polycarbonates, while C-O (286.1 and 533.2 eV) bond corresponds to ethers and carbonates (Verma et al., 2010; Zhu et al., 2018). The peak of C = O bond in electrode with PS is much stronger than that of the sample without additive, which indicates that the SEI derived from PS contains more C = O functional groups.

In F 1s spectra, the signals at 684.3 and 686.1 eV are characteristic of lithium fluoride and $Li_xPO_yF_z$ (Dedryvère et al., 2005), respectively. As for P 2p spectra, the binding energy values around 133.3 eV and 136.0 eV are belong to $Li_xPO_yF_z$ and Li_xPF_y (Zheng et al., 2018; Li et al., 2020). These compounds are ascribed to the decomposition products of lithium hexafluorophosphate

TABLE 3 | Element concentrations of the cycled anodes using base electrolyte and PS-containing electrolyte.

	C 1s (%)	O 1s (%)	F 1s (%)	P 2p (%)	Mn 2p (%)	S 2p (%)
Base	46.1	37.7	12.0	2.9	1.3	–
With PS	40.5	53.6	4.4	0.5	–	1.0

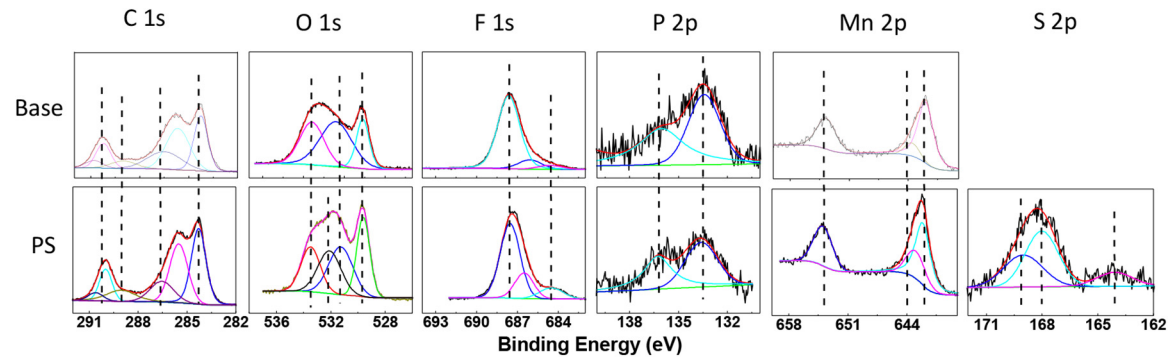

FIGURE 10 | XPS spectra of C 1s, O 1s, F 1s, P 2p, Mn 2p, and S 2p for the $LiMn_2O_4$ electrodes after 180 cycles at 60°C in base electrolyte and PS-containing electrolyte.

in the electrolyte. The concentrations of fluorine and phosphorus discernibly decreased in PS-containing electrolyte, as shown in **Table 3**. Moreover, the anode cycled with PS shows much weaker intensities of lithium fluoride, $Li_xPO_yF_z$ and Li_xPF_y than that of with base electrolyte. It suggests the SEI formed by PS can suppress the decomposition of the electrolyte. It can be noted that the Mn 2p spectrum appears in the graphite electrode, which split into $2p^{3/2}$ and $2p^{1/2}$. The binding energy at 641.1 and 643.1 eV correspond to Mn^{3+} in Mn_2O_3 and Mn^{4+} in MnO_2, while the binding energy at 653.3 eV is attributed to Mn $2p^{1/2}$ (Liu et al., 2016). It indicates that the manganese ions pass through the membrane and deposited on the anode side. On the contrary, the element manganese is hardly detected on the PS graphite electrode, which means the SEI derived from PS can suppress the deposition on the graphite and inhibit the decomposition of the electrolyte. In S 2p spectra, a broad signal around 168–169 eV can be detected in the PS-containing electrolyte, which correspond to Li_2SO_3 and $ROSO_2Li$ (Ota et al., 2003; Li M. et al., 2013), respectively, and this result also clearly indicates that the decomposition products of PS are introduced into SEI.

Figure 10 presents XPS profile of the $LiMn_2O_4$ electrodes in the electrolytes with and without PS after 180 cycles at 60°C, and the related element concentrations are also shown in **Table 4**. The C 1s spectra for $LiMn_2O_4$ cycled in both of the electrolytes mainly contain C from conductive carbon (284.3 eV) and PVDF (285.5 and 290.4 eV) (Verma et al., 2010; Cao et al., 2013), while C-O (285.5 eV), C = O (288.9 eV) and OCO_2 (290.1 eV), respectively from $ROCO_2Li$, ROLi and Li_2CO_3 species that decomposed from the electrolyte (Aurbach et al., 1996). The O1s contains three main peaks for both of the cathodes: Mn_xO_y or $LiMn_2O_4$ (529.5 eV), Li_2CO_3 (531.5 eV), and lithium alkyl carbonates (532.6 eV) (Zuo et al., 2012; Rong et al., 2014). The binding energy at 532 eV in the electrolyte with PS can be related to the decomposition product of PS. The detected peaks at 642.1/643.4 eV and the 653.9 eV correspond to Mn $2p^{3/2}$ and Mn $2p^{1/2}$. Noted that the Mn signals in Mn 2p and Mn–O in O 1s spectra of the PS-containing electrolyte are stronger than that of the electrolyte without additive, suggesting the thin SEI formed by PS on $LiMn_2O_4$ electrode in which more active material can be detected.

The F 1s spectra of **Figure 10** reveal three peaks: PVDF (687.5 eV), $Li_xPO_yF_z$ (686.4 eV), and lithium fluoride (684.6 eV) (Dedryvère et al., 2005). The signals at 133.6 and 135.9 eV in P 2p spectra can be characteristic of $Li_xPO_yF_z$ and Li_xPF_y (Zheng et al., 2018), which are considered to be the decomposition products of the lithium hexafluorophosphate. The peak intensities of $Li_xPO_yF_z$ and Li_xPF_z decreased when the $LiMn_2O_4$ cathode cycled using the electrolyte with PS. It indicates that the SEI derived from PS can reduce the decomposition of lithium hexafluorophosphate on the $LiMn_2O_4$ surface. For the cathode cycled with PS-containing electrolyte, the peak at around 168–169 eV shows the existence of sulfur-containing species (Li_2SO_3 and $ROSO_2Li$) (Ota et al., 2003). This result clearly shows the existence of PS decomposition products in the SEI, and this SEI film can protect the structure of $LiMn_2O_4$ and the dissolution of manganese from spinel particles and inhibit the decomposition of electrolyte.

TABLE 4 | Element concentrations of the cycled cathodes using base electrolyte and PS-containing electrolyte.

	C 1s (%)	O 1s (%)	F 1s (%)	P 2p (%)	Mn 2p (%)	S 2p (%)
Base	47.1	21.2	26.5	1.8	3.4	–
With PS	45.3	23.2	24.8	0.8	4.4	1.5

CONCLUSION

The cycling stability of $LiMn_2O_4$/graphite under elevated temperature can be improved by applying 1, 3-propane sultone (PS) as an electrolyte additive. The enhanced cycling performances are mainly ascribed to the PS-originated solid electrolyte interface (SEI) film on both anode and cathode surface. These SEIs are essential to inhibit the electrolyte decomposition on graphite and $LiMn_2O_4$ electrodes, and protect the spinel structure of $LiMn_2O_4$ from destruction. Moreover, the SEIs can also suppress the dissolution of manganese ions from the cathode and the deposition on the anode.

DATA AVAILABILITY STATEMENT

The raw data supporting the conclusions of this article will be made available by the authors, without undue reservation.

AUTHOR CONTRIBUTIONS

XL and BL conceived and designed the experiments. XL, LL, SL, LG, and BL performed the experiments. XL, LL, and BL analyzed the data. XL and GZ contributed reagents, materials, and analysis tools. XL, LL, BL, and GZ wrote the manuscript. All authors contributed to the article and approved the submitted version.

FUNDING

This work was financially supported by the joint project of the National Natural Science Foundation of China (Grant No. 21875046) and China Postdoctoral Science Foundation (Grant No. 2017M622625).

REFERENCES

Amatucci, C. N., Schmutz, A., Blyr, C., Sigala, A. S., Gozdz, D., Larcher, J. M., et al. (1997). Materials' effects on the elevated and room temperature performance of C/LiMn2O4 Li-ion batteries. *J. Power Sourc.* 69, 11–25.

Aurbach, I., Weissman, A., Schechter, H., and Cohen, H. (1996). X-ray photoelectron spectroscopy studies of lithium surfaces prepared in several important electrolyte solutions. A comparison with previous studies by Fourier transform infrared spectroscopy. *Langmuir* 12, 3991–4007. doi: 10.1021/la9600762

Cao, S., Guo, R., Yan, C., Zhang, J., and Guo, P. (2018). Carbon-coated single-crystalline LiMn2O4 nanowires synthesized by high-temperature solid-state reaction with high capacity for Li-ion battery. *J. Alloys Compd.* 741, 1–6. doi: 10.1016/j.jallcom.2018.01.107

Cao, Y., Li, X., Li, J., Zheng, J., Gao, Y., Gao, X., et al. (2013). Novel phosphamide additive to improve thermal stability of solid electrolyte interphase on graphite anode in lithium-ion batteries. *ACS Appl. Mater. Interf.* 5:11494. doi: 10.1021/am4024884

Cheng, R., Zhang, C. Z., Zhao, T., and Zhang, P. (2017). Toward Safe lithium metal anode in rechargeable batteries: a review. *Chem. Rev.* 117, 10403–10473. doi: 10.1021/acs.chemrev.7b00115

Czekaj, R., Struis, J., Wambach, S., and Biollaz, S. (2011). Sulphur poisoning of Ni catalysts used in the SNG production from biomass: computational studies. *Catal. Today* 176, 429–432. doi: 10.1016/j.cattod.2010.10.078

Dedryveĭre, S., Laruelle, S., Grugeon, L., Gireaud, J.-M., Tarascon, P., and Gonbeau, D. (2005). XPS identification of the organic and inorganic components of the electrode/electrolyte interface formed on a metallic cathode. *J. Electrochem. Soc.* 152, A689–A696.

Ding, J., Xie, G. S., Cao, T. J., Zhu, H. M., Yu, X. B., and Zhao, B. (2011). Enhanced elevated-temperature performance of Al-doped single-crystalline LiMn2O4 nanotubes as cathodes for lithium ion batteries. *J. Phys. Chem. C.* 115, 9821–9825. doi: 10.1021/jp201669x

Fang, C., Miao, H., Mou, W., and Xiao, M. (2020). Facile synthesis of Si@TiO2@rGO composite with sandwich-like nanostructure as superior performance anodes for lithium ion batteries. *J. Alloy Compd.* 818, 152884. doi: 10.1016/j.jallcom.2019.152884

Flamme, D. J., Yeadon, S., Phadke, S., and Anouti, M. (2020). Promising routes to a high Li+ transference number electrolyte for lithium ion batteries. *J. Energy Chem.* 52, 332–342.

Guo, Z., Yin, Z., Tao, X., Li, Z., and Wang, T. (2008). An advanced electrolyte for improving surface characteristics of LiMn2O4 electrode. *J. Power Sourc.* 184, 513–516. doi: 10.1016/j.jpowsour.2008.03.018

Hai, Z., Zhang, H., Liu, L., Liao, P., Fan, Y., Wu, G., et al. (2019). Facile controlled synthesis of spinel limn2o4 porous microspheres as cathode material for lithium ion batteries. *Front. Chem.* 7:437. doi: 10.3389/fchem.2019.00437

Huang, N., Zheng, Y., Pan, W., Wang, G., Fang, M., and Wu, R. (2015). 3, 3'-sulfonyldipropionitrile: a novel additive to improve the high temperature performance of lithium-ion battery. *Electrochim. Acta* 156, 328–335. doi: 10.1016/j.electacta.2015.01.006

Huang, X., Zheng, G., Fang, Y., Pan, W., Wang, R., and Wu, M. (2018). A novel electrolyte additive for improving the interfacial stability of LiMn2O4 cathode lithium-ion batteries at elevated temperature. *RSC Adv.* 8, 38831–38835. doi: 10.1039/c8ra08355j

Li, X., Chen, Y., Liu, Y., and Chen, W. (2018). One-time sintering process to synthesize ZrO2-coated LiMn2O4 materials for lithium-ion batteries. *RSC Adv.* 8, 16753–16761. doi: 10.1039/c8ra01421c

Li, X., Lin, H., Zhou, L., Xing, G., Lan, W., Zhang, J., et al. (2020). Stabilizing the interphasial layer of Ni-rich cathode and graphite anode for lithium ion battery with multifunctional additive. *J. Power Sources* 467, 228343. doi: 10.1016/j.jpowsour.2020.228343

Li, Y., Wang, H., Rong, Y., Wang, J., Liu, L., Xing, M., et al. (2013). A novel electrolyte with the ability to form a solid electrolyte interface on the anode and cathode of a LiMn2O4/graphite battery. *J. Mater. Chem. A* 1, 12954–12961.

Li, M., Xu, B., Li, Y., Liu, L., Yang, W., and Li, S. (2013). Properties of solid electrolyte interphase formed by prop-1-ene-1,3-sultone on graphite anode of Li-ion batteries. *Electrochim. Acta* 105, 1–6. doi: 10.1016/j.electacta.2013.04.142

Liao, H., Li, X., Wang, M., Xu, L., Xing, Y., Liao, X., et al. (2017). Significantly improved cyclability of lithium manganese oxide, simultaneously inhibiting electrochemical and thermal decomposition of the electrolyte by the use of an additive. *RSC Adv.* 7, 46594–46603. doi: 10.1039/c7ra07870f

Liu, Q. C., Zhuang, Y. L., Shi, X. D., Yan, X., Zhao, N., and Chen, X. B. (2016). Tertiary butyl hydroquinone as a novel additive for SEI film formation in lithium-ion batteries. *RSC Adv.* 6, 42885–42891. doi: 10.1039/c6ra04839k

Liu, Y. J., Li, X. H., Guo, H. J., Wang, Z. X., Hu, Q. Y., Peng, W. J., et al. (2009). Electrochemical performance and capacity fading reason of LiMn2O4/graphite batteries stored at room temperature. *J. Power Sour.* 189, 721–725. doi: 10.1016/j.jpowsour.2008.08.044

Ota, T., Akai, H., Namita, S., Yamaguchi, M., and Nomura, M. (2003). XAFS and TOF-SIMS analysis of SEI layers on electrodes. *J. Power Sourc.* 119–121, 567–571. doi: 10.1016/s0378-7753(03)00291-x

Piao, S.-Y., Duan, X.-J., Lin, X.-S., Tao, Y.-S., Xu, A.-M., Cao, L.-J., et al. (2018). Surface Zn doped LiMn2O4 for an improved high temperature performance. *Wan. Chem. Commun.* 54, 5326–5329. doi: 10.1039/c8cc01878b

Rong, M. Q., Xu, L. D., Xing, W. S., and Li, M. (2014). Enhanced cyclability of LiNi0.5*Mn*1.5O4 cathode in carbonate based electrolyte with incorporation of tris(trimethylsilyl)phosphate (TMSP). *J. Power Sourc.* 261, 148–155. doi: 10.1016/j.jpowsour.2014.03.032

Ryou, G.-B., Han, Y. M., Lee, J.-N., Lee, D. J., Lee, Y. O., Yoon, J.-K., et al. (2010). The effects of humidity on the self-discharge properties of Li(Ni1/3Co1/3Mn1/3)O2/graphite and LiCoO2/graphite lithium-ion batteries during storage. *Electrochim. Acta* 55, 2073–2077.

Verma, P., Maire, P., and Novák, P. (2010). A review of the features and analyses of the solid electrolyte interphase in Li-ion batteries. *Electrochim. Acta* 55, 6332–6341. doi: 10.1016/j.electacta.2010.05.072

Wang, R., Li, X., Wang, Z., Guo, H., and Wang, J. (2015). Electrochemical analysis for cycle performance and capacity fading of lithium manganese oxide spinel cathode at elevated temperature using p-toluenesulfonyl isocyanate as electrolyte additive. *Electrochim. Acta* 180, 815–823. doi: 10.1016/j.electacta.2015.09.019

Wu, X., Li, Y., Zhao, S., Zeng, F., Peng, X., Xiang, Y., et al. (2019). Fabrication of F-doped, C-coated NiCo2O4 nanocomposites and its electrochemical performances for lithium-ion batteries. *Solid State Ionics* 334, 48–55. doi: 10.1016/j.ssi.2019.01.039

Xie, R., Jin, Y., and Xiang, L. (2019). Tuning the nanoarea interfacial properties for the improved performance of Li-Rich polycrystalline Li-Mn-O Spinel. *ACS Appl. Mater. Interf.* 11, 14796–14802. doi: 10.1021/acsami.9b01651

Xu, W., Li, B. L., and Lucht, L. (2009). Effect of propane sultone on elevated temperature performance of anode and cathode materials in lithium-ion batteries. *J. Power Sourc.* 193, 804–809. doi: 10.1016/j.jpowsour.2009.03.067

Xu, W. S., Li, X. X., Zuo, J. S., Liu, S., and Xu, X. (2007). Performance improvement of lithium ion battery using PC as a solvent component and BS as an SEI forming additive. *J. Power Sourc.* 174, 705–710. doi: 10.1016/j.jpowsour.2007.06.112

Yu, L., Zhao, Y., Huang, Y., Hu, L., Chen, Y.-B., and He, R. (2020). Progress and perspective of constructing solid electrolyte interphase on stable lithium metal anode. *Front. Mater.* 7:71. doi: 10.3389/fmats.2020.00071

Zhang, J., Su, T., Wang, K., Yuan, C., Chen, S., Liu, T., et al. (2018). Porous polyethylene bundles with enhanced hydrophobicity and pumping oil-recovery ability via skin-peeling. *ACS Sustain. Chem. Eng.* 6, 7890–7901.

Zheng, L., Xing, X., Yang, X., Li, C., Ye, K., Wang, Q., et al. (2018). N-Allyl-N, N-Bis (trimethylsilyl) amine as a novel electrolyte additive to enhance the interfacial stability of a Ni-rich electrode for lithium-ion batteries. *ACS Appl. Mater. Interf.* 10, 16843–16851. doi: 10.1021/acsami.8b00913

Zhu, X., Luo, H., Zhi, Y., Liao, L., Xing, M., Xu, X., et al. (2018). Diethyl (thiophen-2-ylmethyl) phosphonate: a novel multifunctional electrolyte additive for high voltage batteries. *J. Mater. Chem.* 6, 10990–11004. doi: 10.1039/c8ta01236a

Zuo, C., Fan, X., Xiao, J., Liu, J., and Nan, P. (2012). High-voltage performance of LiCoO2/graphite batteries with methylene methanedisulfonate as electrolyte additive. *J. Power Sourc.* 219, 94–99. doi: 10.1016/j.jpowsour.2012.07.026

Zuo, J., Wu, C., Fan, K., Lai, J., Liu, J., and Nan, P. (2014). A novel electrolyte additive for improving the interfacial stability of LiMn2O4 cathode lithium-ion batteries at elevated temperature. *Electrochim. Acta* 130, 778–784.

Conflict of Interest: The authors declare that the research was conducted in the absence of any commercial or financial relationships that could be construed as a potential conflict of interest.

frontiers in Materials

REVIEW
published: 03 September 2020
doi: 10.3389/fmats.2020.00219

All-Carbon Conductors for Electronic and Electrical Wiring Applications

Federico Cesano[1], Mohammed Jasim Uddin[2], Karen Lozano[3], Marco Zanetti[1] and Domenica Scarano[1]*

[1] Department of Chemistry, NIS (Nanostructured Interfaces and Surfaces) Interdepartmental Centre and INSTM Centro di Riferimento, University of Turin, Turin, Italy, [2] Photonics and Energy Research Laboratory, Department of Chemistry, The University of Texas Rio Grande Valley, Edinburg, TX, United States, [3] Center for Nanotechnology, Department of Mechanical Engineering, The University of Texas Rio Grande Valley, Edinburg, TX, United States

Electrical conductors based on carbons have recently attracted a growing interest due to the prospect of replacing metals. Electrical conductors without metals could represent not only an alternative for traditional wiring, but also a step forward in the progress and advancing of technology. This result can be achieved by combining high electrical conductivity with other properties, that are dexterity, light weight, environmental stability, high strength and flexibility. As the best mechanical properties, high electrical/thermal conductivity of the assembled fibers are all generally associated with low concentration of defects in the fiber backbone and in the individual carbon "*building blocks*", a special attention is paid to an empirical relationship between morphology/structure/composition and the electrical properties. In this review, starting from the beginning, from the late 19th century, when the carbon filaments became the lights for urban streets, some of the recent developments in the field of "*all-carbon*" electrical conductors are discussed. Such conductors can be obtained by assembling nanoscale carbons (i.e., carbon nanotubes, graphene) into macroscopic fibers, yarns and ropes (hereafter fibers). In this perspective, the role played by the chemistry in particular by means of the molecular-level control and doping, is emphasized. This contribution elucidates most recent results in the field, and envisages new potential applications.

Keywords: graphene, carbon nanotubes, carbon fibers, graphene fibers, CNT fibers, yarns, doped carbon, electrical conductivity

OPEN ACCESS

Edited by:
Antonio Di Bartolomeo, University of Salerno, Italy

Reviewed by:
Jinquan Wei, Tsinghua University, China
Qingyu Peng, Harbin Institute of Technology, China

****Correspondence:***
Federico Cesano
federico.cesano@unito.it

Specialty section:
This article was submitted to Carbon-Based Materials, a section of the journal Frontiers in Materials

Received: *09 March 2020*
Accepted: *15 June 2020*
Published: *03 September 2020*

Citation:
Cesano F, Uddin MJ, Lozano K, Zanetti M and Scarano D (2020) All-Carbon Conductors for Electronic and Electrical Wiring Applications. Front. Mater. 7:219. doi: 10.3389/fmats.2020.00219

INTRODUCTION

Due to the growing interests about new electrically conductive materials with superior characteristics than the conventional conductors, a detailed knowledge of the electrical properties of carbon-based materials is mandatory. Obviously, the electrical properties are not the only element of evaluation for a possible use of alternative electrical conductors. Other characteristics, including thermal and mechanical properties, chemical and thermal resistance, low weight and density, the heat removal efficiency, and interconnections with traditional wires, reliability and durability, should also be considered.

Many carbon nanomaterials are currently prepared and used as such or are embedded in multiphase materials involving polymers (Haznedar et al., 2013; Cesano and Scarano, 2015; Cesano et al., 2016). However, highly conductive carbon conductors are available in form of assemblies, which contain nanocarbons with a small length/size compared to metal conductors

(Fang et al., 2020). The lack of progress in the fabrication of "*single domain*" continuous carbon nanotube and graphene fibers has offered the motivation for building carbon-based macroscopic assemblies with improved electrical, mechanical, thermal and electrochemical properties (Zhang et al., 2007; Lu et al., 2012, 2017, 2019; Miao, 2013; Mäder et al., 2015; Kou et al., 2017; Dhanabalan et al., 2019; Foroughi and Spinks, 2019; Yang et al., 2020; Yin et al., 2020). In analogy with conventional metal wires, carbon nanotubes and graphene-based conductors have reached electrical properties of their metal counterparts, they possess numerous advantages, such as lower weight, high mechanical properties, sensing properties, resistance to extreme conditions, thermal and electrical conductivities (Cesano et al., 2013; Cravanzola et al., 2013; Cesano and Scarano, 2018; Chowdhury et al., 2019; Harun et al., 2019). On the other hand, metals are present in nature with limited amounts and the need for an advantageous alternative solution would be of great relevance. Under these perspectives, it is important to remark that many reviews concerning the main topic of the carbon-based materials and properties are present and that a certain number of them (Chou et al., 2010; Lu et al., 2012; Cong et al., 2014; Lekawa-Raus et al., 2014b; Li and Pandey, 2015; Li et al., 2015; Xu and Gao, 2015; Kou et al., 2017; Yadav et al., 2017; Xu et al., 2019; Zhang et al., 2019; Zheng et al., 2020) should be nevertheless deemed of a great significance. Along with recent findings, Zheng et al. (2020) have recently demonstrated the ultrafast electro-thermal response (5943 K s^{-1}) of graphene fibers surpassing the record value of carbon nanotubes. The authors have shown the structural engineering of the graphene fiber assembly, where entanglements of individual graphene nanosheets is beneficial to achieve very low density (0.015–0.020 g/cm^{-3}), together with high mechanical strength (c.a. 3.9 MPa), high specific electrical conductivity (SEC) (0.95–1.67 S m^2/g) and specific thermal conductivity (STC) (42.3–100 W cm^2 K^{-1} g^{-1}) values, which are comparable to those of metals (SEC_{Cu}: 6.61 S m^2 g^{-1}; STC_{Cu}: 0.45 W cm^2 K^{-1} g^{-1}; SEC_{Ag}: 5.98 S m^2 g^{-1}; STC_{Ag}: 0.40 W cm^2 K^{-1} g^{-1}). Hills et al. (2019) have recently demonstrated that microprocessors (called 16-bit RV16X-NANO microprocessor handling 32-bit instructions of the RISC-V architecture) made of carbon nanotube FETs on Si wafers can be fabricated. Together with the validation of the microprocessor under working conditions, including instruction fetching, decoding, registering, execution units, and back writing to memory, the authors proposed a manufacturing methodology for manipulation, doping, etching and assembling of carbon nanotubes, for overcoming nanoscale imperfections at macroscopic scales and figuring out industrial standards. At the same time, Afroj et al. (2019) reported the engineering of graphene oxide and graphene flakes by means of the high-speed fiber dyeing technique to coat conventional textiles. The process has the potential to produce tons of conductive graphene-based yarn using existing textile machineries. The authors also shown that the derived textile maintains its conductivity after some washing cycles. Furthermore, a number of recent studies has demonstrated various functions of graphene and carbon nanotube-based yarns, including sensors and biosensors, actuators, energy harvesting and storage devices, catalysis (Foroughi and Spinks, 2019; Jang et al., 2019; Panwar et al., 2019; Wang et al., 2019; Fang et al., 2020). These recent examples, together with the critical investigation of the literature indicate that the scientific background on this subject is, however, plentiful and rapidly rising, but extremely various and it is nearly unattainable to afford a complete description of all the possible applications. For this reason, the purpose of the present review is to provide a selection of insights dedicated to electrical properties of micro-assembled nanocarbon fibers with no metal present (hereafter all-carbon fibers).

THE FIRST DEVELOPED CARBON CONDUCTIVE WIRES

In 1838, Marcellin Jobard was the first who experienced a "*glow lamp*" based on carbon, a vacuum bulb containing a small strip of carbon used as a conductor of a current, emitting an intense, fixed, and durable light. In the late century, Henry Woodward, Mathew Evans, Joseph W. Swan, Thomas A. Edison and Alessandro Cruto were among the first scientists pioneering on electric lighting. After the first approaches with metal filaments placed outside or inside a vacuum bulb, apart from one another they realized that low cost, high-resistance filaments of about a few hundred ohms were required for reducing the sizes of the electric lamps. Thus, pyrolyzed carbon filaments were identified as the best possible candidate materials and some of whom filed separately patents. Edison and Swan are perhaps the more famous, but not the first inventors of the electric lamp, while the most durable ones were probably obtained by Alessandro Cruto. In this context, besides the higher number of patents, Edison's contribution has been a series of requirements, characteristics and methods required to fabricate durable electrical lamps. After about 20 years, in 1904, a new revolution appeared in the light bulbs: the tungsten coiled coils in a bulb filled with inert gas soon substituted carbon filaments, due to its brighter light and better durability.

CARBON FIBERS

The fabrication of carbon fibers could be traced back to Joseph Swan, who in 1860 produced for the first time carbon fibers from cellulose filaments for light bulb applications, but the first high-performance carbon fibers were manufactured only one century later (1958) by Union Carbide. Such fibers were fabricated by heating under inert gas at a relatively high temperature rayon fibers until their carbonization. However, the method was demonstrated to be ineffective, because fibers were stiff, with low strength and contained only c.a. 20% of carbon. In the early 1960s, new processes from polyacrylonitrile (PAN) were developed to produce carbon fibers made of more than 99% carbon and in the next years new generation carbon fibers with high-tensile modulus and mechanical strength were obtained by playing with process parameters (very high temperature) and precursor types (i.e., rayon, PAN, pitch). The carbonization at high temperature was optimized to eliminate heteroatoms (N,

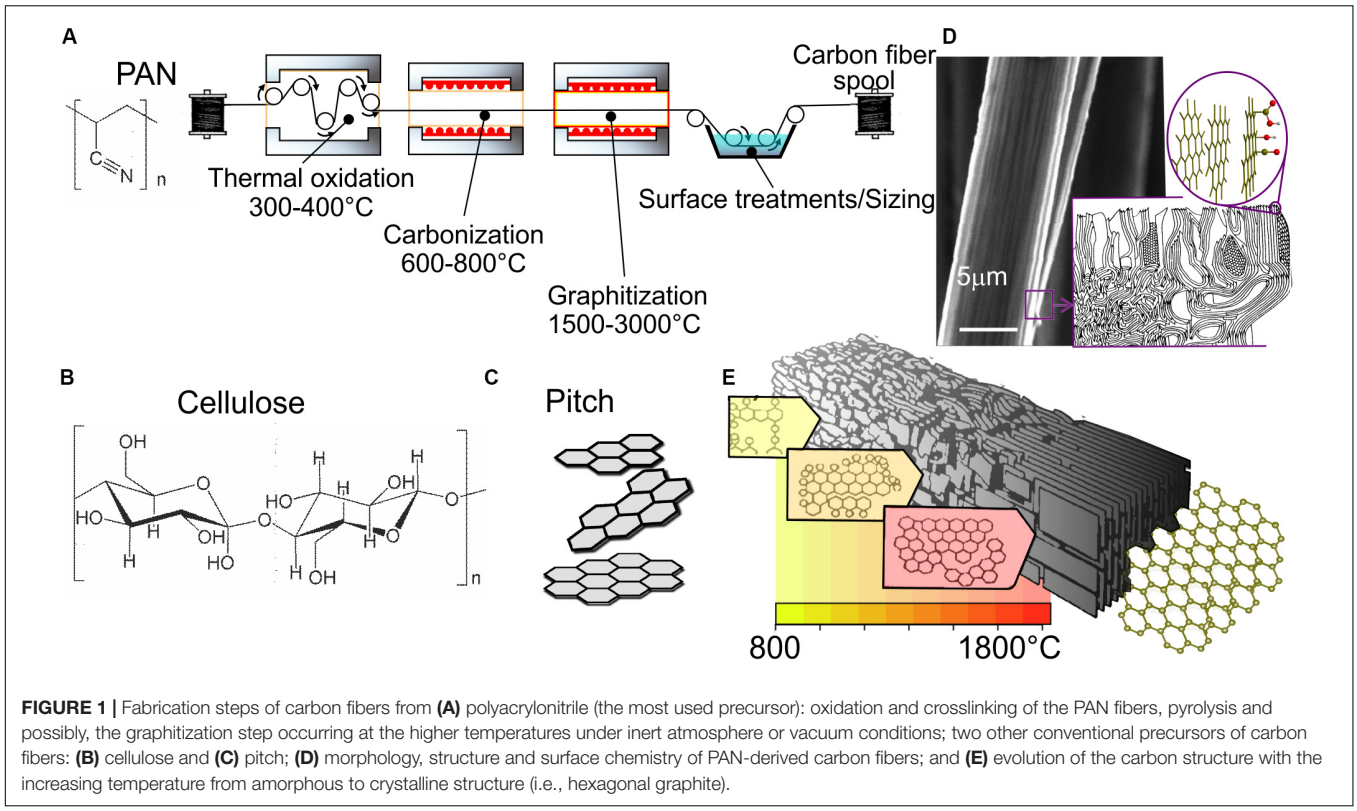

FIGURE 1 | Fabrication steps of carbon fibers from **(A)** polyacrylonitrile (the most used precursor): oxidation and crosslinking of the PAN fibers, pyrolysis and possibly, the graphitization step occurring at the higher temperatures under inert atmosphere or vacuum conditions; two other conventional precursors of carbon fibers: **(B)** cellulose and **(C)** pitch; **(D)** morphology, structure and surface chemistry of PAN-derived carbon fibers; and **(E)** evolution of the carbon structure with the increasing temperature from amorphous to crystalline structure (i.e., hexagonal graphite).

S, O, H) and to constitute a graphitic structure. PAN is by far the most used precursor of today's carbon fibers by following several steps (thermal oxidation, carbonization, graphitization and surface treatments) (**Figure 1A**), while the other precursors, the cellulose type (including Rayon) and pitch (**Figures 1B,C**), require different process routes. The morphology of a carbon fiber obtained from PAN is SEM imaged in **Figure 1D**, together with a few models of the crystalline domain arrangements and surface chemistry. Furthermore, depending on the precursor type and process, carbon fibers can be produced with a wide range of properties: when they are subjected to thermal treatments above 1500–2000°C, they exhibit a more ordered arrangements (**Figure 1E**), possess a very high elastic modulus, higher thermal and electrical conductivities and have a carbon content > 99%. Sometimes they are called graphitic fibers. Fibers obtained at lower temperature contain a lower C amount (93–95%) and possess lower mechanical properties and conductivities. Apart from the foremost use in fiber-reinforced composites, carbon fibers are used in electrode/microelectrodes (i.e., a single carbon fiber), flexible heating applications, whenever a low wear friction on the contact interface is required (e.g., brush contact).

Despite their excellent mechanical properties and some peculiarities (PAN-based fibers have a turbostratic structure: contain basal planes slipped out of their alignment, thus exhibiting high tensile strength, while pitch-derived fibers show higher Young's modulus, high stiffness) and peculiar thermal/electrical conductivities (Chung, 2017), carbon fibers do not represent the end, but the beginning of new classes of fibers. In fact, carbon fibers display a polycrystalline nature (**Figures 1D,E**), plenty of grain boundaries/defects, close voids and a rough morphology as schematized in the insets of **Figure 1D**, with consequent limitation in properties when compared to the graphite counterpart. This can be considered a straightforward consequence of the direct pyrolysis of organic precursors.

VAPOR GROWN CARBON NANOFIBERS (VGCFS), MULTI-WALLED- AND SINGLE-WALLED CARBON NANOTUBES (MWCNTS AND SWCNTS)

Since the 1950s, the formation of graphitic filaments from hydrocarbons or CO was observed as deposits, often accidentally, on various substrates inside the tube of furnaces (350–2500°C) (Bacon, 1959). However, the fabrication of carbon fibers and nanofibers became more attractive with the catalytic decomposition of hydrocarbons promoted by metal (i.e., Fe, Ni, Co, alloys) and metal oxide nanoparticles, due to the lower deposition temperature (350–800°C) (Tibbetts, 1985). There are many scientific articles, book chapters and books dedicated to this topic. For an in-depth examination of this subject the reader can refer to the specific literature (Iijima and Ichihashi, 1993; Rodriguez et al., 1995; Ajayan, 1999). Briefly, it is important to recall the fact that three different types of precursors (solid, liquid and gas) are of interest. Solid and liquid carbon precursors are attracting the interest owing to their high availability and

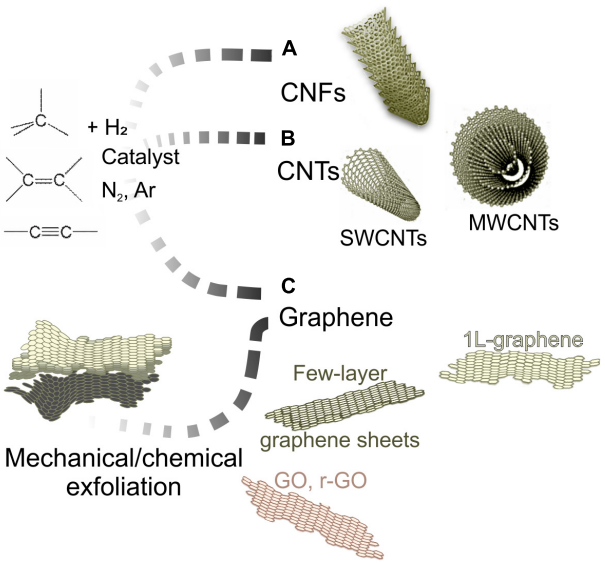

FIGURE 2 | Fabrication scheme of 1D and 2D carbons from molecular precursors (or pre-constituted CNT/graphene structures): **(A)** carbon nanofibers (CNFs), **(B)** single-walled and multi-walled carbon nanotubes (SWCNTs, MWCNTs); and **(C)** 2D carbons obtained from "*bottom-up*" and "*top-down*" approaches: graphene, graphene oxide (GO) and reduced graphene oxide (r-GO).

low cost, while hydrocarbons are the most popular ones due to the fact that, thanks to their purity, they can be considered as model systems. On this subject, it is commonly accepted that when hydrocarbons are used, the reactions proceed at the exposed surfaces of metal catalyst and carbon nanostructures under formation are shaped by metal nanoparticles (Cesano et al., 2005; Li and Pandey, 2015). The growth mechanism of carbon nanostructures is therefore governed by bulk diffusion, carbon concentration gradients and temperature of reaction (Derbyshire et al., 1975; Iijima et al., 1992; Rodriguez et al., 1995; De Jong and Geus, 2000; Kharlamova, 2017). Depending on the catalyst type, temperature of reaction, metal particle sizes and growth methods, different types of structure can be observed (Li and Pandey, 2015; Kharlamova, 2017) (**Figures 2A,B**). In this regard, carbon nanotubes (SWCNTs and MWCNTs) can be distinguished from nanofibers by the different stacking of the carbon layers, and the little metal nanoparticles are cut out for the synthesis of SWCNTs, whilst bigger catalyst particles promote the MWCNT/nanofiber formation (De Jong and Geus, 2000). In the same way, large-area graphene films can be obtained by following a bottom-up approach by using a carbon feedstock and a metal catalyst (i.e., mainly Cu, Pt, Co, but also Ni and other metals) and by controlling the hydrocarbon concentration and the cooling rate during graphene growth. The reader may refer to the dedicated literature (Li et al., 2009; Reina et al., 2009). In this manner, the uniformity and the thickness of one- and two- or a few layers can be largely controlled (Lee et al., 2017) (**Figure 2C**). Deposition at a temperature as low as 300°C has been reported by Vishwakarma et al. (2019) by using a microwave plasma CVD method by adopting ppm CO_2 during growth from CH_4 for the control over vertical graphene growth, and O_3 treatment for increasing transmittance and carrier mobility. On the other hands, 2D graphene family materials (i.e., single-layer or few-layer graphene sheets, graphene oxide and reduced-graphene oxide) with lower quality and smaller lateral sheet dimensions can be obtained by using a top-down approach by following a mechanical or a chemical exfoliation (Harun et al., 2019).

FIBER INTERCONNECTS: VAN DER WAALS INTERACTIONS AND COVALENT BONDING

It is known that mechanical properties, thermal and electrical conductivities of carbon fibers are limited by presence of defects and by the weak interactions among adjacent fibers (Lekawa-Raus et al., 2014b; Fang et al., 2020; Wang et al., 2020). Cesano et al. (2005), Veedu et al. (2006), and Anthony et al. (2018) have shown the interconnection of fibers by means of catalytically grown nanofilaments (carbon nanofibers and carbon nanotubes) by using C_2H_4 or xylene at 700 and 800°C (**Figure 3**).

The authors displayed that the metal nanoparticles (Fe, Ni) go away from the surface of the fibers where they were initially located and move on the tip of the filaments under formation, acting as independent catalytic centers (Cesano et al., 2005). Such catalytic nanoparticles transferred into the structure of the growing nanofilaments, play a big part in the ongoing formation of interconnected CNF entanglement, which connects the adjacent CFs and at later stages the densification of a more compact CNT/CFs composite can be obtained (**Figures 3A–D**). Recently, Zheng et al. (2020) have shown the 3D assembling of graphene sheets directly grown on carbon fibers by thermal CVD. The carbon nanofibers, previously obtained by electrospinning of PAN fibers, were stabilized (in air) and carbonized at 1100°C (under NH_3). The authors observed a remarkable densification of the graphene nanosheets, with the growth time and the filling of the space between composite fibers for prolonged reactions (10h) (**Figures 3E–H**). In a recent paper, Karakassides et al. (2020) have recently reported the catalyst-free growth of radially aligned graphene nanoflakes on carbon fibers by means of microwave plasma-enhanced chemical vapor deposition (PECVD) process with CH_4 and N_2 gas mixture under vacuum conditions (total pressure = 15 Torr). Together with a remarkable increment of the mechanical properties, the authors observed that both, electrical conductivity and specific capacitance (C_{sp}), resulted to be improved (from c.a. 160 S/cm to c.a. 257 S/cm and from c.a. 0.27 mF/cm^2 to c.a. 0.65 mF/cm^2, respectively), due to the reduction of the contact resistance between graphene flakes and carbon fibers.

THE ASSEMBLING OF CNTS AND GRAPHENE TO FORM FIBERS

CNTs and graphene are well known to be used in polymer matrix composite materials (i.e., bulk materials or films), while

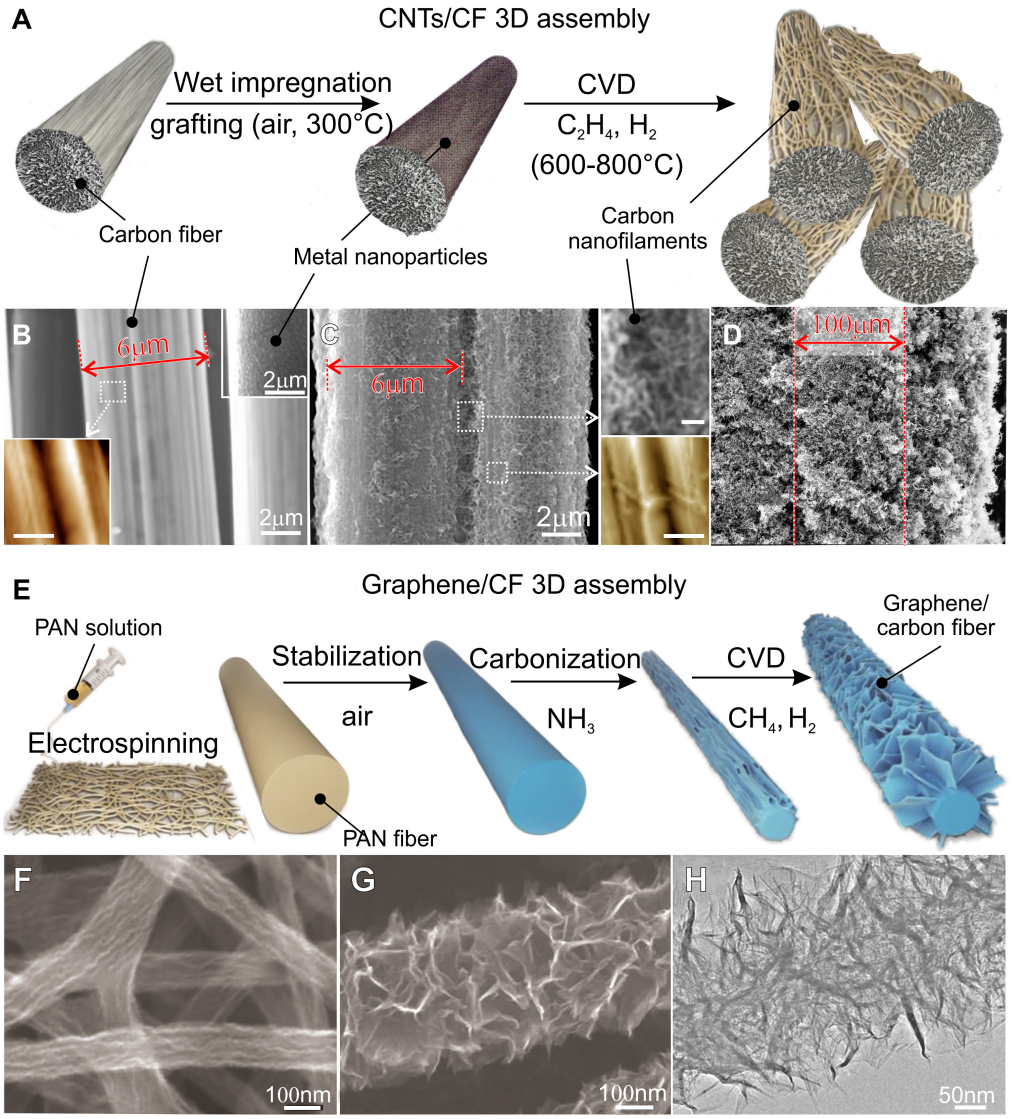

FIGURE 3 | (A) Schematic representation of carbon nanofilaments-interconnected carbon fiber assemblies as obtained by C_2H_4 catalytic decomposition at 700°C; SEM and AFM images of: **(B)** the native carbon fibers used as support; In the top and bottom insets of **(B)** the morphologies of a nickel catalyst nanoparticles supported on carbon fiber and of the wrinkled surface of the native carbon fibres; **(C)** interconnection and **(D)** densification of the carbon fiber support by carbon nanofilaments as obtained under static (700 Torr) and dynamic conditions (100 ml/min) after 1h of reaction time; **(E)** schematic representation of carbon fiber-graphene assemblies as obtained by CH_4 thermal decomposition at 700°C; **(F)** SEM images of the native PAN nanofibers; and **(G,H)** SEM and TEM images of the graphene-coated carbon fibers. AFM image scalebars are 300 nm. Panels **(B–D)** adapted from Cesano et al. (2005) with permission from American Chemistry Society. Panels **(E–H)** adapted from Zeng et al. (2018) with permission from Wiley-VCH.

in some application fields carbon-based polymer fibers find a specific use. In recent papers, Salavagione et al. (2018) and Lu et al. (2019), reviewed potentialities (and limitations) of CNT/polymer and graphene/polymer fibers, respectively. Briefly, the state of the art of polymer-based fiber shows the potential in some fields of application, including the electromagnetic shielding, wearable and smart textiles or as electrodes, but such composite fibers do not nearly reach the thermal and electrical conductivities of metals. The need to go beyond the characteristics of polymer matrix composites has stimulated the development of nanocarbons assembled into fibers, whose interest is particularly significant from the practical point of view, if they go beyond the mechanical properties of carbon fibers and provide thermal and electrical conductivities close to or beyond those of metals (i.e., Cu, Ag). Although the theme of the carbon-based yarn fabrication is much broader than that described here, it can be further examined in some recent dedicated papers (Miao, 2013; Kou et al., 2017; Zhang et al., 2019; Yin et al., 2020). The quality of CNT and graphene fibers depends on a large extent on the fabrication process, by following solid-state or liquid spinning approaches. The spinning techniques take advantage at the molecular level of

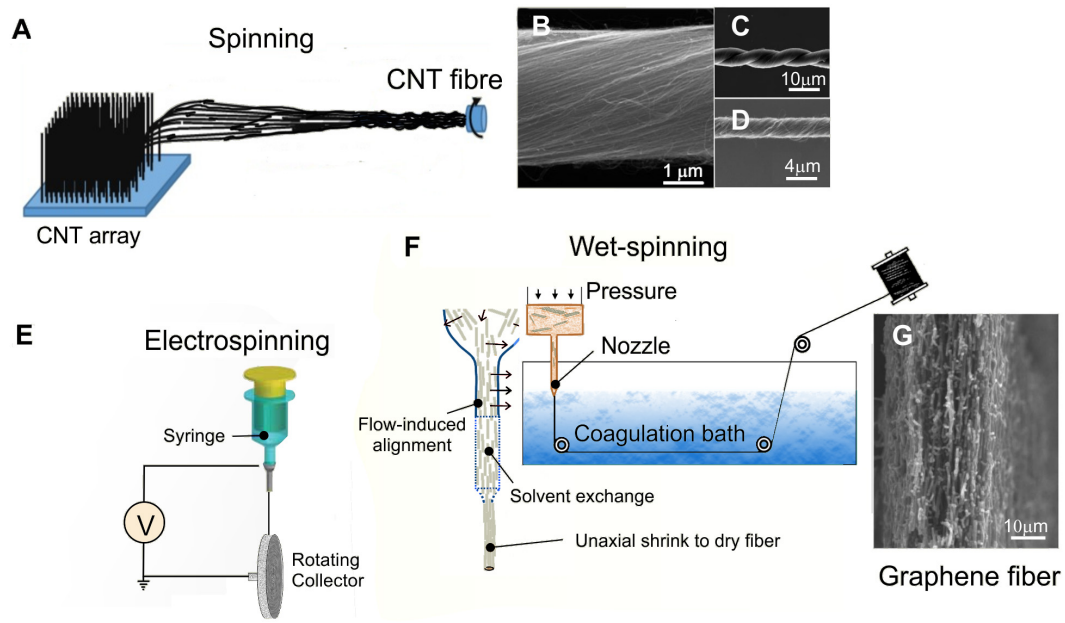

FIGURE 4 | Macroscopic assembling methods of: **(A)** CNT fibers from a forest of CNT arrays by spinning; **(B–D)** SEM images of the CNT ropes after spinning and twisting steps; **(E)** CNT/graphene fibers by electrospinning and **(F)** graphene fibers by wet-spinning/coagulation methods; and **(G)** SEM image of the graphene fiber. Panels **(B–D)** adapted from Zhang et al. (2007) with permission from Wiley-VCH. Panel **(G)** reproduced from Zeng et al. (2018) with permission from Wiley-VCH.

the polymer science (Cheng and Lee, 2016; Cecone et al., 2018; García-Mateos et al., 2019; Mohammadzadehmoghadam and Dong, 2019).

CNT yarns can be easily obtained from vertically grown CNTs by the direct dry-spinning procedure (**Figure 4A**) or twisting during spinning taking advantage of the van der Waals forces acting among the vertically grown SWCNTs and/or MWCNTs to arrange them into micro-sized ropes of an unlimited length (Jiang et al., 2002; Li et al., 2004; Zhang et al., 2004, 2005). The resulting structure could be very different depending on the spinning parameters and twisting procedure (if adopted) (**Figures 4B–D**). Otherwise, the CNT and graphene fiber can be obtained by electrospinning or wet spinning procedures (**Figures 4E,F**), which confer a peculiar morphology to the fiber (**Figure 4G**). Post treatments have been found to increase the density and the properties of the fibers.

A note can be drawn about the comparison between the different preparation methods for CNT fibers. The yarns can be fabricated by the fixed-catalyst CVD, with CNTs directly spun from a floating-catalyst CVD reactor, which is a relatively more simple and clean procedure (i.e., no solvents and acids are needed) or wet-spinning method. The last procedure can provide fibers with the best conductivity (8.5×10^4 S/cm) (Tsentalovich et al., 2017) for CNT fiber probably arising from a doping step, due to the strong acid treatment in the coagulation bath. Below electrical properties of fibers coming from the wet spinning method, the floating-catalyst CVD procedure provides better conductivity, as compared to CNT arrays (Dini et al., 2019). Furthermore, SWCNTs or DWCNTs are by far the best candidates to achieve better fiber performances. The arrangement of nanotubes into aligned CNT arrays yields fibers with much better properties, whilst more entangled arrays give poor characteristics (Kou et al., 2017). Furthermore, the long length and the large aspect ratio of individual nanotubes are known to play a relevant role in achieving good properties. Interestingly, Behabtu et al. (2013) fabricated CNT yarns after dissolving CNTs in chlorosulfonic acid by the wet spinning method, similar to the process commonly used to produce high-performance industrial fibers. Together with electrical properties that will be discussed later, such fibers were tested for mechanical and thermal properties. Briefly, tensile strength (1 GPa) and modulus (120 GPa), were determined together with an elongation at break of 1.4%. The same fibers displayed a thermal conductivity of c.a. 380 W/m K^{-1}. The same authors determined the effect of doping with iodine. As a result, the thermal conductivity was increased by 100% (635 W/m K^{-1}) even after thermal annealing at 600°C. From these, we can conclude that optimal morphology and structure (i.e., alignment of CNTs, high packing density, lack of impurities and defects) are crucial for the final properties of CNT fibers.

As far as graphene fibers are concerned, the two-dimensional structure and crystal domains with finite dimensions dictate a few considerations. First of all, layered structures are very flexible, but their structural organization in a yarn of indefinite length, implies a stacking (**Figure 5**). A full scale approach to minimize defects from atomic to macroscale levels was attempted by Xu et al. (2016). The authors used large GO liquid crystals and the wet-spinning method with continuous stretching during the process to obtain the ordered orientation of graphene sheets along the axis of fibers. The control over the concentration and nozzle

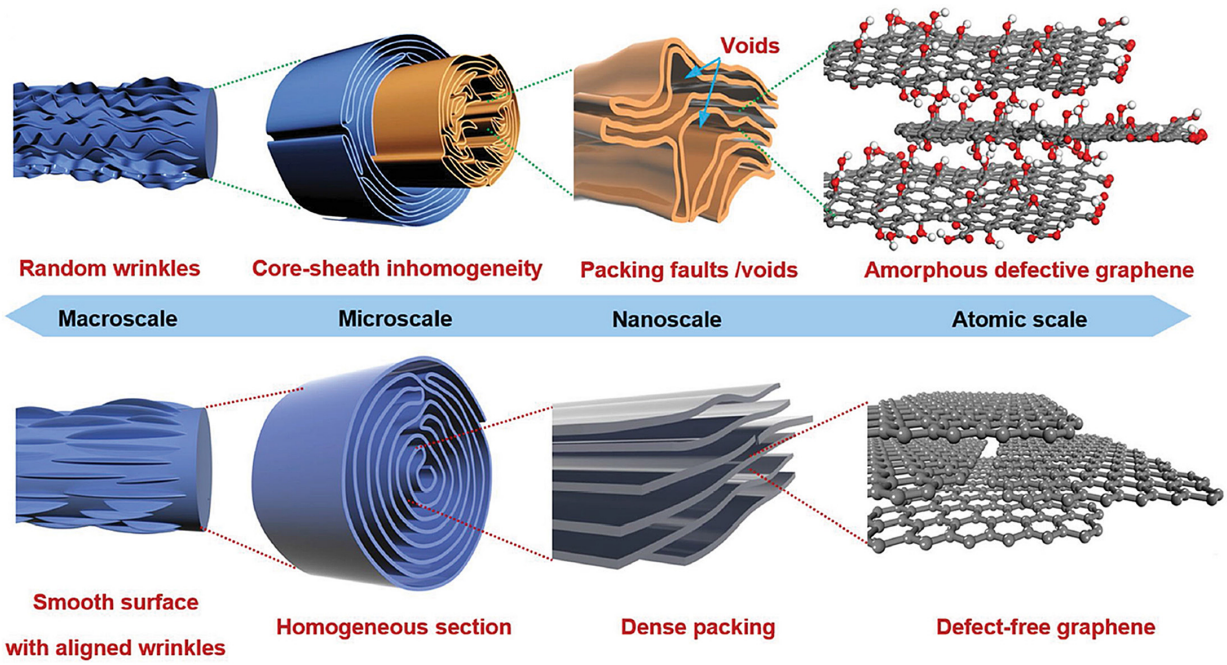

FIGURE 5 | Structural models of: defects in GFs from the macroscale to the atomic scale of chemically reduced GO (top panels); high-quality defect-free GFs (bottom panels). Adapted from Xu et al. (2016) with permission from Wiley-VCH.

diameter together with the thermal treatment at 3000°C helped to perfect the atomic structure of graphene. The obtained fibers demonstrated a series of record properties, including ultrahigh stiffness (282 GPa), tensile strength (1.45 GPa) high electrical conductivity (8×10^5 S m^{-1}) and ampacity (2.3×10^{10} A m^{-2}).

HIGHLY ELECTRICALLY CONDUCTIVE METAL-LESS CONDUCTORS

Conventional and unconventional materials for electrical wiring are listed in **Table 1**. In almost all cases, the Drude model of electrical conduction is a good approximation. Among metals, the best conductors have one electron in their outermost shell layer (metal Cu: 2, 8, 18, 1; metal Ag: 2, 8, 18, 18, 1; and Au: 2, 8, 18, 32, 18, 1). It is well known that conventional electrical conductors operating nearly room temperature are commonly based on copper (5.8×10^5 S/cm) or silver (6.4×10^5 S/cm at 25°C). Both metals require only a weak field to strip one electron as compared to other metals or elements. Graphite is a non-metallic material two orders less conductive than metals ($2–3 \times 10^3$ S/cm). Depending on the precursor type, the preparation process and the heating temperature, carbon fibers exhibit a relatively lower conductivity than graphite. The conductivity at room temperature is, for a fact, found to be unaffected by heating the material up to ≈2500°C, while above this temperature, it increases becoming closer to that of graphite (Tsukamoto et al., 1986).

In principle, an assembled carbon yarn could virtually transport electricity like a ballistic conductor and the behavior could be well interpreted in terms of electrons and holes with the Drude model of electrical conduction (Fujita and Suzuki, 2010). However, fibers made exclusively of the same metallic (armchair) SWCNT type or graphene strips, defect-free and infinitely long, are by now technologically unfeasible. Thess et al. (1996) observed the self-organization of SWCNTs into ropes of 5–20 nm in diameter. The authors measured at room temperature a resistivity of c.a. 10^{-4} Ω cm (c.a. 10^4 S/cm), a value that is two orders of magnitude higher than that of single metallic CNTs. The conductivity of individual tubes is often two orders of magnitude larger than their assemblies, thus highlighting the role played by the contact resistances at the interfaces of the single nanotubes (Li et al., 2007). As the overlap of nanoconductors make possible electrical connections and that an infinite number of junctions is present in the fiber, Xu F. et al. (2013) demonstrated that the energy gap introduced by long junctions can be overcome by small voltage (∼0.04 V) across the whole fiber. Lekawa-Raus et al. (2017) calculated that there is a theoretical conductance limit, which depends on the fiber length, and is 5.9×10^{11} S/m, 5.9×10^{13} S/m or 5.9×10^{16} S/m for a 1 cm, 1 m or 1 km long fiber of 10 μm in diameter, constituted by (metallic) (10,10) armchair SWCNTs. Interestingly, the authors have also demonstrated that the conductivity scales inversely proportionally to the CNT diameter for an ideal fiber. Barnett et al. (2019) and Lepak-Kuc et al. (2019) have shown via experimental and theoretical approaches the dependence of the electrical contact resistance at the junction regions between CNTs (SWCNTs and/or MWCNTs) and between CNTs and graphene interfaces by considering morphology, structure (i.e., chirality). Interestingly, it was shown that when there is a large

TABLE 1 | Electrical properties at room temperature of CNT/graphene-based fibers, including some reference materials.

Materials/Fibers	Electr. conductivity, S/cm (resistivity, Ω cm)	Specific conductivity, S m^2 kg^{-1}	J_{max}, A cm^{-2}	Density, g/cm^3	Surface area, m^2/g (Porosity, %)	References
Some metals/reference materials:						
Copper	5.85×10^5 (1.7×10^{-6})	6.73×10^3	2.17×10^5	8.69		Ross, 1992
Silver	6.45×10^5 (1.55×10^{-6})	6.15×10^3		10.49		Ross, 1992
Alumium	3.7×10^5 (2.7×10^{-6})	1.37×10^4		2.7		Ross, 1992
Gold	4.55×10^5 (2.2×10^{-6})	2.36×10^3		19.32		Ross, 1992
Graphite ⊥ c-axis =c-axis	1.02×10^3 (9.8×10^{-4})	4.51×10^1		2.26		Powell and Childs, 1972
PAN-based carbon fibers	$\sim 0.1-1 \times 10^3$ ($\sim 0.1-1 \times 10^{-3}$)	$\sim 0.1-10 \times 10^1$		$\sim 1.6-2$		Newcomb and Chae, 2018
Pitch-based carbon fibers	$\sim 0.1-1 \times 10^3$ ($\sim 0.1-1 \times 10^{-3}$)	$\sim 0.1-10 \times 10^1$		$\sim 1.7-2.1$		Newcomb and Chae, 2018
SWCNTs	$\sim 1 \times 10^6$ (1×10^{-6})	$\sim 7.7 \times 10^4$	$\sim 4 \times 10^9$	1.3		Hong and Myung, 2007
Radially grown GR/carbon fiber yarns	$2.6-5.9 \times 10^2$ ($1.7-3.9 \times 10^{-3}$)	$1-3 \times 10^1$		2		Karakassides et al., 2020
High T annealed GR film	1×10^4 (1×10^{-4})					Peng et al., 2017
$MoCl_5$-intercalated GR film	$1.1-1.7 \times 10^5$ ($5.8-9.1 \times 10^{-6}$)	$4.1-7.3 \times 10^3$		2.37		Liu Y. et al., 2020
K-doped GR film	$1.2-1.5 \times 10^5$ ($6.7-8.3 \times 10^{-6}$)	$6.0-9.1 \times 10^3$		1.45–1.63		Zhou et al., 2017
CNT fibers:						
Metallic-based SWCNT yarns	–	2×10^6				Sundaram et al., 2011
High aligned SWCNT and MWCNT fibers	$\sim 1 \times 10^4$ ($\sim 1 \times 10^{-4}$)	2270				Lee J. et al., 2019
DWCNT yarns	5×10^3 (2×10^{-4})	$\sim 5 \times 10^2$		~ 1.0		Zhong et al., 2010
SWCNTs or DWCNTs, wet-spinning sol. in acid	8.50×10^4 ($1{,}18 \times 10^{-5}$)	5.7×10^3		1.5		Tsentalovich et al., 2017
Thin MWCNTs, wet-spinning sol.	1.82×10^4 (5.49×10^{-5})	$\sim 1.2 \times 10^3$		1.3–1.8		Wang et al., 2014
MWCNT yarns	300 (3.3×10^{-3})	3.75×10^1				Mirfakhrai et al., 2008
MWCNT purified yarns	400–800 ($2.5-1.25 \times 10^{-3}$)	$4.4-8.9 \times 10^1$				Jakubinek et al., 2012
(2000-MWCNT purified yarns 2500°C) annealed MWCNT yarns	1.32×10^3 (7.6×10^{-4})					Dini et al., 2020
Graphene fibers:						
Hyperbranched polyglycerol-based fibers	2.51×10^1 (3.99×10^{-2})				2210	Aboutalebi et al., 2014
GR composite fibers by electrospinning/CVD/soaking sequential method	4.59×10^1 (2.18×10^{-2})				9.8	Sun et al., 2018
3D assembled GR fibers	$0.34-1.2 \times 10^3$ ($0.83-2.9 \times 10^{-3}$)	$\sim 1.3 \times 10^2$				Zeng et al., 2018
Polydopamine/GO fibers annealed @1200°C	6.6×10^2 (1.52×10^{-3})					Ma et al., 2018
Large/small GR sheets annealed @1400°C	5.5×10^2 (1.82×10^{-3})	$\sim 4.2 \times 10^1$		1.3	(42%)	Xin et al., 2019
Large/small GR sheets annealed @2000°C	1.5×10^3 (6.67×10^{-4})	$\sim 1.01 \times 10^2$		1.48	(34%)	Xin et al., 2019

(Continued)

TABLE 1 | Continued

Materials/Fibers	Electr. conductivity, S/cm (resistivity, Ω cm)	Specific conductivity, S m^2 kg^{-1}	J_{max}, A cm^{-2}	Density, g/cm^3	Surface area, m^2/g (Porosity, %)	References
Large/small GR sheets annealed @2500°C	1.6×10^3 (6.25×10^{-4})	~1.03×10^2		1.55	(31.5%)	Xin et al., 2019
Large/small GR sheets annealed @2850°C	1.79×10^3 (5.59×10^{-4})	~1.13×10^2		1.58	(30%)	Xin et al., 2019
As before, optimized GR fibers, annealed @2850°C	2.1×10^3 (4.76×10^{-4})	~1.13×10^2		1.86	(18.5%)	Xin et al., 2019
GR fibers annealed @2500°C, wet-spinned with microfluidic approach	1.04×10^4 (9.62×10^{-5})	6.5×10^2				Xin et al., 2019
GR fibers annealed @3000°C	8.3×10^3 (1.2×10^{-4})	~2.3×10^3	2.3×10^6			Xu et al., 2016
GR fibers	$8{,}0 \times 10^3$					Liu et al., 2016
GR fibers @3000°C doped with Ca	*(superconducting ≤ 11 K)*					Liu et al., 2017
Doped CNT fibers:						
H_2SO_4-doped SWCNT yarns	5×10^3 (2×10^{-4})	~5×10^2		1.11		Ericson et al., 2004
N-doped rGO/acid-oxidized SWNT composite fibers	1.02×10^3 (9.8×10^{-4})				396	Yu et al., 2014
(2000–2500°C) annealed and $PtCl_4$-doped MWCNT yarns	1×10^5 (1×10^{-5})					Dini et al., 2020
HSO_3Cl-doped coagulation bath	7.7×10^4 (1.3×10^{-5})	4.9×10^3		1.58		Headrick et al., 2018
MWCNT oxidized in HNO_3 (5M) yarns	969 (1.03×10^{-3})	–				Li et al., 2007
HSO_3Cl-doped SWCNT yarns	2.9×10^4 (3.4×10^{-5})	2.2×10^3	6.6×10^3	1.3		Behabtu et al., 2013
I-doped SWCNT yarns	5.0×10^4 (3.4×10^{-5})	~3.57×10^3		1.4		Behabtu et al., 2013
HSO_3Cl and I-doped SWCNT yarns	5×10^4 (2×10^{-5})	4.18×10^3		1.2		Behabtu et al., 2013
Thermally oxidized and chemically etched DWCNT yarns (H_2O_2 30%), $HCl_{(c)}$, then $H_2SO_{4(c)}$)	2×10^4 (5×10^{-5})	~7.1×10^3	~10^4–10^5	0.28		Zhao et al., 2011
as above additionally I-doped DWCNT yarns	6.7×10^4 (1.5×10^{-5})	1.96×10^4		0.33		Zhao et al., 2011
Doped graphene fibers:						
$FeCl_3$-doped GR fibers	0.77×10^5 (1.3×10^{-5})	4.74×10^3		~1.625		Liu et al., 2016
Br_2-doped GR fibers	$1{,}5 \times 10^5$ (6.7×10^{-6})	9.23×10^3		~1.625		Liu et al., 2016
K-doped GR fibers	2.24×10^5 (4.5×10^{-6})	1.38×10^4		~1.625		Liu et al., 2016
Au-coated GR fibers	2.86×10^2 (3.50×10^{-3})	6.81×10^2		0.42		Yun et al., 2017
Ag-doped GR fibers	9.3×10^2 (1.08×10^{-3})		7.1×10^3			Xu Z. et al., 2013
N-doped rGO fibers	6.94×10^1 (1.44×10^{-2})					Liu Q. et al., 2020
N-doped GR fibers	9.51×10^{-1} (1.05)	–	–	–		Chong et al., 2019

The ~ symbol refers to values calculated from the data provided by authors. SWCNTs: single-walled carbon nanotubes; DWCNTs: double-walled carbon nanotubes; MWCNTs: multi-walled carbon nanotubes; GR: graphene; GO: graphene oxide; rGO: reduced graphene oxide.

mismatch (i.e., alignment of the 6-member rings within adjacent CNTs) and a large diameter ratio among two intersecting carbon nanotubes, an increased resistance of three orders of magnitude was measured at the junction region (c.a. MΩ compared with c.a. kΩ measured far from the crossing point) (Barnett et al., 2019). The authors also showed that, in agreement with the unit cell dimensions (Meunier et al., 1999), a clear periodic dependence of the resistance on the periodicity of 2–3 Å was obtained. These and other concerns stimulate the realization of macroscopic assembles of nanocarbons to form fibers, even though in reality the availability of infinitely pure and selected "*building blocks*" still requires development, especially from a practical point of view. Moreover, the overall properties of the assembled fibers are determined in a large extent by composition, morphology and structure (i.e., orientation and type) of their basic units and their interconnection characteristics, which are controlled by the precursor type and preparation procedure (Fang et al., 2020).

The fibers containing carbon nanostructures can have a very wide range of electrical conductivity. In principle, both CNTs and graphene exhibit semimetal characteristics and their conductivities are few-orders of magnitude higher than that of their macroscopic assemblies, which behave as semiconductors (Li et al., 2007; Fang et al., 2020), thus suggesting that the contact resistance at the interface plays a significant role. Commonly, the temperature dependence with electrical properties indicates that the conductivity of all-carbon fibers increases from low to room temperature (semiconducting behavior) (Li et al., 2007; Dini et al., 2019, 2020; Fang et al., 2020), but with lower dependency than carbon counterparts (i.e., graphite, graphite fibers). In graphene and CNT fibers the electron transport properties are dominated by hopping mechanism (Li et al., 2007; Fujita and Suzuki, 2010; Liu et al., 2016). Electrical transport properties, investigated by Dini et al. (2019) in a large range of temperature (3–350 K), indicated that resistivity decreases exponentially below 70 K due to the prevailing intercontact effects among CNTs, while above 70 K the resistivity decreases linearly and the intrinsic CNT resistivity properties prevail. Interestingly, the same authors estimated the resistivity in their CNT bundle to be $\sim 8 \times 10^{-4}$ Ω·cm (1.25×10^{3} S/cm), which was very close to that of CNT yarns (1.1×10^{-3} Ω·cm, corresponding to 9.1×10^{2} S/cm) at room temperature and they concluded that the CNT bundle resistivity is the limiting factor in the CNT fibers. In the same experiments, it was also observed at room temperature that the electrical transport was not affected by densification of CNT fibers and the contacts between CNTs.

As reported by some authors, properties of carbon ropes made of individual CNTs or graphene sheets, can be increased by the heat treatment. Xin et al. (2019) have precisely determined the effect of thermal heating up to 2850°C for graphene fibers, but the same conclusion can be remarked for CNT fibers (Dini et al., 2020). Wang et al. (2020) reported that when fibers were subjected to Joule heating a significant enhancement of mechanical and electrical properties can be observed. The authors described the increase in properties with the formation of chemical bonding of individual CNTs by means of 1,3,5-tris(2′-bromophenyl) benzene (2TBB) acting as a cross-linking agent. Crosslinking with 2TBB increased the tensile strength of fibers by 47% and enhanced the electrical conductivity by a factor of c.a. 100 (from 160 up to about 10200 S/m) after passing a current through the fiber, with the consequent localized heating at the more resistive CNT junctions. The selective thermal dehalogenation of the organic precursor, for a fact, may lead to the covalent bonding formation. In another recent paper, Hada et al. (2019) reported that the Joule annealing (c.a. 1800°C) of CNT fibers of c.a. 20 μm in diameter, caused the interfacial amorphous carbon phase to be converted into graphene fragments between adjacent CNTs. Liu et al. (2012) described the CO_2 laser induced annealing of CNT fibers under vacuum conditions (10^{-6} Torr). The laser light absorbed from the (black) CNTs, may promote a local heating (Cesano et al., 2013) and similar to a conventional heat treatment, leads to the reduction of defects with the consequent increment of the mechanical and electrical properties.

On the other hands, the addition of graphene flakes within a CNT wire to constitute a hybrid composition has been shown to increase the electrical conductivity, current-carrying capacity (or ampacity, which can be defined as the maximum current in amperes, that a conductor can carry continuously under the conditions of use and without exceeding its temperature rating) and doping properties (Li and Pandey, 2015; Lepak-Kuc et al., 2019). Besides the remarked relevance of the graphene flake characteristics, of the fiber purity and of the solvent properties, the authors explained that graphene flakes constitute effective bridges by means of a theoretical model. Such bridges create Fermi level states inside the CNTs bands, with the consequent increase of current and electrical conductance in the system, while doping can enhance the conductance of the hybrid assembly. The doping of the carbon and the related electrical conductivity is discussed in the next section.

Along with CNT fibers, some important concepts for achieving higher electrical properties can be summarized. Firstly, metallic nanotubes may exhibit ballistic transport, but the defects and impurities (i.e., catalyst and amorphous carbon on the surface) interrupt the electron transport and promote a random scattering with the consequent increase of the contact resistance at the interface between CNTs (Lekawa-Raus et al., 2014b). Secondly, the choice of metallic SWCNTs, DWCNTs or a few walled CNTs together with the annealing at the high temperature (higher than c.a. 2000°C) of the assembled fibers play a significant role in targeting the high conductivity (Wang et al., 2014). Lastly, the control over structure and defects of fibers (i.e., voids, pores, tube misalignment) is necessary to further mitigate the contact resistance (Zhang et al., 2019). Considering the different methods of the CNT fiber preparation, we can conclude that among the best electrical conductivities of CNT yarns are obtained by the wet spinning techniques of SWCNTs and DWCNTs ($\sim 9 \times 10^{4}$ S·cm^{-1}) (Tsentalovich et al., 2017). However, in some of these preparations, CNTs are often in the presence of strong acids, raising the doubt that acid doping could be the main responsible for the high fiber conductivity. Along with the other CNT fiber preparation methods, CNT can be directly spun into fibers from floating catalyst CVD or fixed-bed CVD processes and the observed conductivity is of the order of $\approx 10^{3}$–10^{4} S·cm^{-1} (Liu et al., 2012; Lekawa-Raus et al., 2014a) with best values when the densification is optimized (e.g., rolling under pressure) (Wang et al., 2014).

As far as graphene fibers are concerned, some important concepts for achieving higher electrical properties can be summarized. Firstly, polymer based-graphene fibers exhibit a limited conductivity. Secondly, the heating temperature as high as ≈2000°C or more is necessary to have a significant effect on the conductivity (Xin et al., 2019). Lastly, due to the polycrystalline nature of the graphene domains and the three-dimensionality of the microfiber backbone, the control over the orientation of graphene sheets and concentration of defects (i.e., from the macroscale to the atomic scale: random wrinkles at the surface, core-shell and along axis inhomogeneities, voids/porosity, sp^3-C terminations at the boundaries) is necessary (Xu et al., 2016). Surprisingly, Liu et al. (2017) assembled macroscopic graphene fibers intercalated with Ca (Ca 10 wt%). At very low temperature (∼11 K) the Ca-doped fibers exhibited a superconducting transition.

All the previous considerations are valid with direct current (DC), while for the conductivity in alternating current (AC) other factors should be also considered, because the signal transport through a conductor becomes difficult at the high frequency, due to skin and proximity effects. Skin effect occurs in a conductor at high frequency with a distribution of the current density, leading to a higher resistance. The alternating flux in a conductor, caused by the current of the other near conductors, results an apparent increase in the resistance and is called proximity effect. Theoretically, a single SWCNT should be unaffected by skin effect. It is expected that the tubular nature at the nanoscale of CNTs should mitigate both the skin and proximity effects, thus enabling a high frequency transport superior to typical metals (Lekawa-Raus et al., 2014b, 2017). However, the literature on this subject is still very limited.

THE ROLE OF CHEMISTRY TO INCREASE THE CONDUCTIVITY

In a recent study, Lee J. et al. (2019) reported an optimized method, in which the wet spinning of CNTs in chlorosulfonic acid (CSA) followed by stretching of the fiber in a coagulation bath, allows to rearrange entangled CNTs and to increase the alignment of nanotubes. The authors reported that the highly packed and aligned CNTs confer high mechanical and electrical properties to the fiber (among the record observed for the undoped CNT fibers reported in **Table 1**). However, the electrical properties of the conductors seem to be limited by the multidomain structure of the assembled CNTs/graphene sheets, which are regularly and continuously aligned and reoriented along the axial direction (Xu and Gao, 2015). Molecular assembly strategies alone (Aboutalebi et al., 2014; Kou et al., 2017) would not allow to surpass the electrical conductivity of metals. On the other hand, it is generally observed that the infiltration with polymers resulted in a significant decrease in electrical conductivity (Lu et al., 2012).

Beyond the Conductivity of Carbon Yarns and Fibers: Doping and Intercalation

The doping paradigm to increase the electrical properties of carbon-based conductors is not new. Since the last century the graphite intercalation compounds (GICs) with halogens, alkali compounds were studied (Hennig, 1952; Ottmers and Rase, 1966). It was found that a remarkable variation of the free-carrier concentration allows the enhancements of the electrical, thermal and magnetic properties of the host material (Dresselhaus and Dresselhaus, 2002). Most of the recent studies on conductors based on doped carbons have examined the case of carbon nanotube fibers, while the literature on graphene fibers appears moderately more limited.

Randeniya et al. (2010) showed that metal nanoparticles (Cu, Au, Pd, Pt) doped CNTs are able to reach metal-like electrical conductivities ($2–3 \times 10^5$ S cm^{-1}) that are three orders of magnitude higher than the uncoated carbon fiber backbones. According to this, the approach to improve specific conductivity suggests that alkali metals (Li, Na, K) act as n-dopant, while halogen (Cl_2, Br_2, I_2), oxidants (HNO_3, $SOCl_2$, H_2O_2), $FeCl_3$, $PtCl_4$ and $MoCl_5$ as p-dopants (Liu et al., 2016; Liu Y. et al., 2020; Zhang et al., 2019). Other used dopants with molecular structure are H-carbazole (p-dopant) and phosphine derivatives (n-dopants) (Lee T. et al., 2019). A general result of the doping process is the change in the color close to the saturation percentages: pure all-carbon fibers are silver gray (i.e., graphite) or black (i.e., assembled CNTs), while $FeCl_3$- and Br_2-doped graphene fibers show dim luster appearance (15% and 10% of doping, respectively), while K-doped fibers evolve from silver gray to bright-golden yellow (26% of doping) (Liu et al., 2016), due to Drude plasma frequency shifting into visible range (Fischer, 2006) together with the increasing concentration of carriers and in analogy with graphite intercalation compounds (Dresselhaus and Dresselhaus, 2002) (i.e., charge transfer into the antibonding π^*-band or from the bonding π-band thus acting as donor or acceptor guests, respectively Clancy et al., 2018). The increased carrier density and the mobility in doped fibers may allow a higher electrical conductivity, which was found to show the same temperature dependency with small variation than pure all-carbon fibers. All these elements imply that the band structure evolves from a two-carrier semimetal model of graphite to one-carrier free-electron-like metal model with the increasing of the dopant concentration (Fischer and Thompson, 1978).

Recent studies suggest that the electrical properties increase with the amount of dopant due to the shifting of the Fermi level, although there is an intrinsic limit of the doping loading (Zhang et al., 2019). Zhao et al. (2011) reported the preparation of I-doped CNT fibers with electrical conductivity as high as 6.7×10^4 S/cm. With the doping with iodine, polyiodide chains are formed. Together with I_3^- and I_5^- species, the hole concentration was found to be one order of magnitude higher (from c.a. 1.65×10^{18} cm^{-3} to 2.90×10^{19} cm^{-3}) (Zhang S. et al., 2017). Together with improved carrier mobilities, a similar increased charge carrier concentrations (holes) (i.e., p-type doping) of 2.69×10^{20} cm^{-3} and 1.43×10^{20} cm^{-3} (from 3.96×10^{19} cm^{-3} of pure graphene) for Br_2- and $FeCl_3$-doped graphene, while K-doped graphene showed n-type characteristics (i.e., carrier type: electron) with a much higher carrier concentration (2.07×10^{21} cm^{-3}) that is a value closer to the carrier mobility value of metals (c.a. 10^{22} cm^{-3}), as obtained with Hall effect measurements in a van der Pauw geometry by

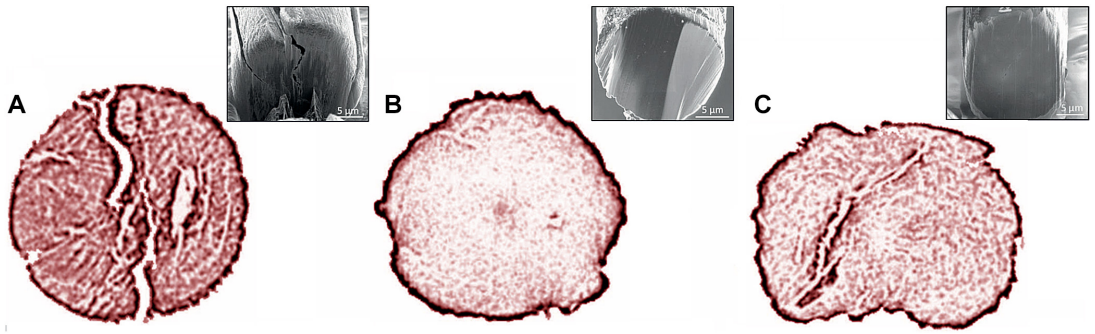

FIGURE 6 | Phase contrast X-ray computed tomography images of CNT fiber cross-sections for three type of fibers prepared by twisting **(A)** thick, **(B)** thin, or **(C)** by solution-spinning from coagulation bath. SEM images of the same fibers are reported in the insets. Adapted from Headrick et al. (2018) with permission from Wiley-VCH.

Liu et al. (2016), Liu Y. et al. (2020). In another paper, Zhang and Fahrenthold (2019) reported the highest doping density with K atoms on the graphene surface as obtained by adding one dopant per two carbon hexagons, thus giving a structure corresponding to KC_8 (Zhang and Fahrenthold, 2019), while 15% and 10% are nearly the saturation doping percentages for $FeCl_3$ and Br_2, respectively (Liu et al., 2016). Along the dopant series, K and I appear to be the most promising, but they have been also found somehow instable in air and the fiber structure may undergo an immediate degradation by moderate temperature exposures. The preparation of iodine-doped DWCNT cables with electrical resistivity achieving 10^{-5} Ω·cm (6.7×10^4 S/cm) has been reported by Zhao et al. (2011). The authors reported that cables of different diameters ranging from 4 to 45 μm display high current carrying capacity (10^9–10^{10} A/cm^2), which is of three orders of magnitude larger than those of metals. In the paper, DWCNT yarns with smaller diameter were found to have larger resistivity compared to larger diameter fibers, thus indicating the role played by voids, other defects and skin effects on the conductivity. The electrical conductivity boosted to a metallic level has been observed for doped-graphene and carbon nanotube fibers (Xu and Gao, 2015; Fang et al., 2020). In a recent paper, Lee T. et al. (2019) have shown the fabrication of flexible thermoelectric generators based on CNT fibers. Interestingly, the authors reported that by optimizing the alignment degree of CNTs and doping the nanotubes with H-carbazole and phosphine derivatives (p- and n-dopant, respectively) the carrier mobility increased with an improvement of the power factor of the generator. In another recent paper, Hada et al. (2019) reported the thermoelectric application of Joule annealed CNT yarns undoped and doped with polyethylenimine (PEI). Surprisingly, Joule annealed undoped and PEI doped CNT fibers exhibit remarkable Seebeck coefficients (+ 100 μV/K and −100 μV/K, respectively), which are values close to those of inorganic thermoelectric materials. Furthermore, Joule heating of the CNT yarns after PEI doping (n-dopant) was found to increase the conductivity of the yarns of about three times (10^5 S/m). Liu Y. et al. (2020) have recently reported the intercalation of graphene films by means of $MoCl_5$. The room temperature conductivity of the film reached the record value for the graphene series of 1.7×10^{-5} S cm^{-1}. Interestingly, the authors reported a significative dependence of the conductivity with the doping amount together with a long-term stability under environmental conditions (> 1 year), thermal (140°C) and chemical resistance against some $MoCl_5$ solvents (acetone, carbon tetrachloride, ethanol and H_2O).

In summary, the chemical doping has the potential to improve the thermal and electrical conductivities of CNT and graphene fibers. Notwithstanding the increase observed for doped systems, the electrical conductivity of carbon yarns becomes comparable or higher than that of metal filaments. Another advantage of carbon-based filaments over metallic filaments is that they allow a remarkable chemical resistance. However, the temperature and time stability under working conditions still needs further investigations and improvements.

A-Few Characterization Techniques

3D X-ray tomography (3D XRT) is a non-destructive method, which now offers a spatial resolution down to ∼10 and 50 nm in synchrotron and lab facilities, respectively. The method could be applied to examine structure, porosity, cracks phase distribution, external habit of fibers (**Figure 6**), thus highlighting also interfaces within the structure of the assembled fiber (Headrick et al., 2018).

X-ray scattering techniques can provide useful insights of the fiber scaffold and of its components. Although, from X-ray diffraction (XRD) patterns, the structure of CNTs appears close to those of graphitic materials due to their intrinsic nature, 3D XRD analysis can further provide the fiber crystallite sizes along both, longitudinal and transversal directions (Xin et al., 2019). In addition, XRD measurements can be also utilized to study the nature of intercalated compounds (e.g., doping) with the appearance of peaks corresponding to the d-spacings larger than 0.334 nm (002) peak of graphite. For example, Zhou et al. (2017) reported the occurrence of a series of peaks indexed as (00*l*) with d-spacings of 0.53 nm and of 0.43 nm in K-doped graphene film intercalation compounds. The same (00*l*) peak series was identified together with a shifting toward lower 2θ values (Liu et al., 2016) (**Figure 7A**). The same authors reported also interlayer spacings of 0.34 nm and of 0.49 nm for Br_2- and $FeCl_3$-doped graphene fibers, respectively. Ca-doped

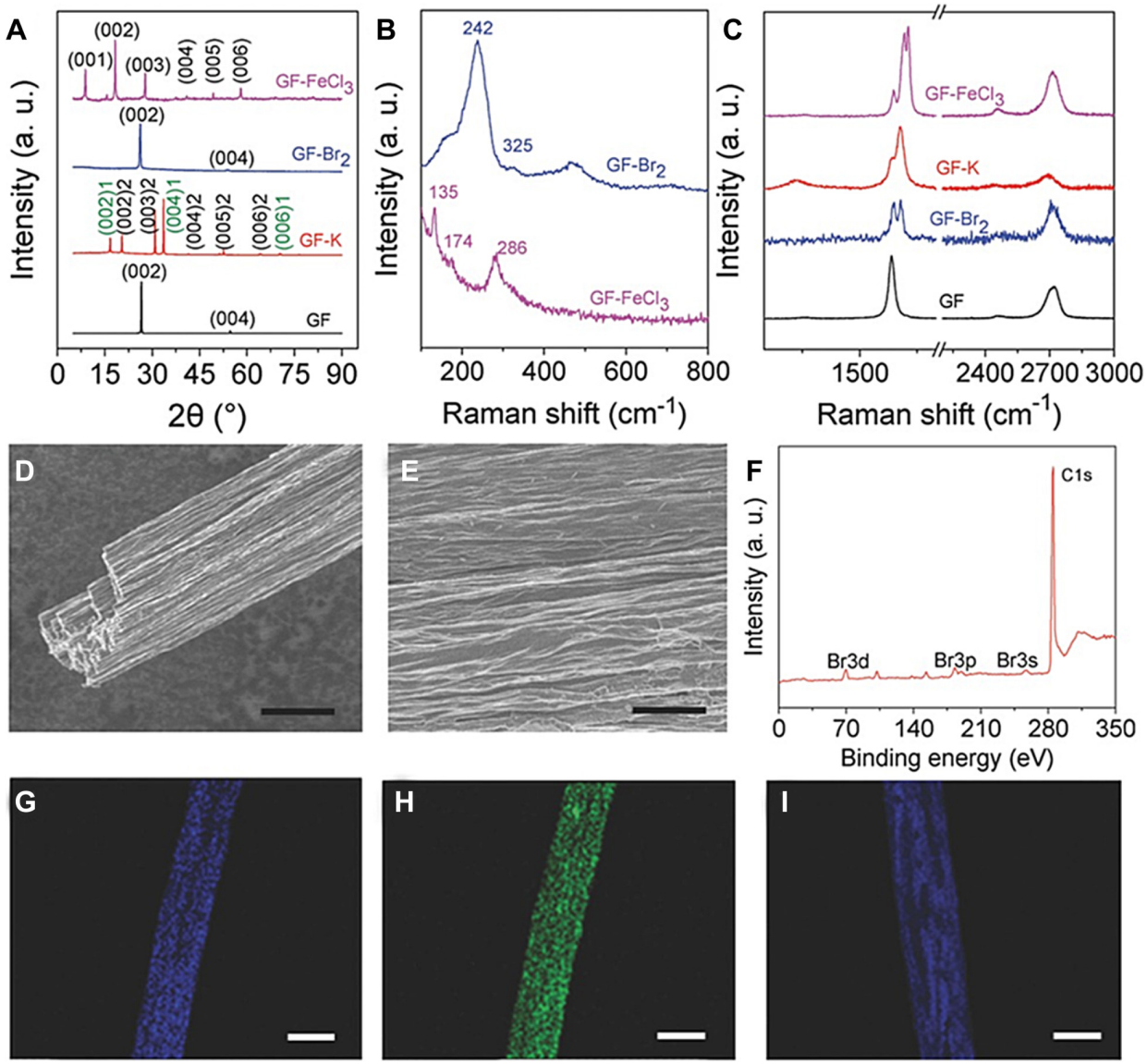

FIGURE 7 | (A) XRD patterns of the pure and doped graphene fibers. Raman spectra of: **(B)** doped graphene fibers in the lower wavenumber region and **(C)** pure and doped graphene fibers in the higher wavenumber region; **(D,E)** SEM images of the graphene fibers obtained at different magnification (Scalebars: 20 μm in **D** and 5 μm in **E**); **(F)** XPS spectrum of the Br-doped graphene fibers; and **(G–I)** Elemental mapping images of iron, chlorine, and potassium doped graphene fibers (Scalebars are 50 μm). Reproduced from Liu et al. (2016) with permission from Wiley-VCH.

carbon-assembled fibers was reported to show a series of (00*l*) reflections with d-spacings of 0.45 nm, 0.34 nm, and 0.23 nm indexed as (003), (002), and (006) (Liu et al., 2017). Wide-angle X-ray scattering (WAXS) technique can be informative about the structure and orientation degree along the fiber axis (Xu et al., 2012, 2016; Alemán et al., 2015). Small-angle X-ray scattering (SAXS) was performed by Xu et al. (2012, 2019) to investigate the size and shape confinements in the fiber of the carbon building blocks and optimize the fluid dynamics in the wet-spinning of the graphene fiber fabrication (2D SAXS configuration). Lamellar structural information is of particular interest when GO or liquid crystals are used in presence of nematic, lamellar and chiral compounds (Kumar et al., 2017; Clancy et al., 2018; Fang et al., 2020). This fact is however not surprisingly, due to the familiar concept in polymer science.

Raman spectroscopy is one of the main analytical techniques that provide a detailed picture about chemical structure, phase, crystallinity and molecular interactions, not only of the CNTs and graphene sheets, but also of the final assembled fiber. A detailed description of CNT and graphene Raman features goes beyond the scope of this review and can be found elsewhere (Dresselhaus et al., 2010; Saito et al., 2011; Eckmann et al., 2012; Jain et al., 2017; Groppo et al., 2018). Among all fingerprints,

the presence of the D-band at about 1350 cm^{-1} comes from double resonance Raman effect corresponding to disordered carbon structure, while the G-band (c.a. 1580–1600 cm^{-1}) is associated with stretching modes of the C-C bonds in graphitic materials commonly found in all sp^2 carbons. This spectral feature associated with the curvature and appearing similar for nanotubes and graphene, reveals distinct characteristics allowing to distinguish a carbon structure from another one (i.e., multiple peaks in SWCNTs, a strong peak at c.a. 1582 cm^{-2} in graphene, etc.). A D-band overtone centered at about 2700 cm^{-1} and called 2D band can be found. The evolution of the 2D/D intensity ratio can be used to determine the number of the stacked graphene layers (Papageorgiou et al., 2017). Furthermore, an additional feature is found in SWCNTs known as radial breathing mode (RBM) of SWCNTs. This fingerprint can also provide a detailed description of the type, structure and diameters of the nanotubes. Interestingly and very recently, Park Y. et al. (2019) reported a reinterpretation of SWCNTs' Raman fingerprints considering also opened tubular graphene structures (c.a. 2 nm in diameter). The authors associated the observed RBM band with a convolution of "localized RBM" (c.a. 170 cm^{-1}) and RTM (radial–tangential mode) (c.a.190 cm^{-1}), together with the D mode (c.a. 1350 cm^{-1}), originated from the edge defects of graphene and the G^- mode (c.a. 1570 cm^{-1}) appearing red shifted from the G^+ peak (c.a. 1590 cm^{-1}) and with a different shape (due to a curvature effect). Notably, the alignment of CNT fibers can be assessed by polarized Raman measurements (Kou et al., 2017; Lee J. et al., 2019; Xin et al., 2019; Zhang et al., 2019). An increased $I_{G\,||}/I_{G\,\perp}$ (G-peak intensity ratio obtained for the polarization parallel to that of the polarization perpendicular to the fiber axis, respectively) is an indication of the increased domain alignment. Raman spectroscopy is also worth of a special mention in the case of doped systems. As a matter of fact, the G band upshift is usually observed in doped CNTs and graphene also when the structural integrity of the structure is preserved. The reason is that G-band position, very sensitive to charge doping, shifts the Fermi level left from the neutrality point (Liu et al., 2016). Liu et al. (2016) have shown a double peaks (c.a. 1616 cm^{-1} and 1626 cm^{-1}) of the G-band for $FeCl_3$-doped graphene fibers. The author observed a similar G-band upshifting of c.a. 23 cm^{-1} and 25 cm^{-1} for K- and Br_2-doped graphene fibers, respectively. Liu et al. (2016) showed Raman spectra with upshifted G peaks, together with an additional peak at c.a. 242 cm^{-1}, which corresponds to bromine anions. Additional peaks at 135 cm^{-1}, 174 cm^{-1}, and 286 cm^{-1} can be found to verify the successful doping with $FeCl_3$ (Liu et al., 2016) (**Figures 7B,C**). 2D band downshifting can be observed after doping. This fact arises from the not negligible lattice expansion occurred after doping.

Electron microscopies (scanning and transmission electron microscopy: SEM and TEM, respectively) are typically adopted techniques to investigate the morphology, structure and twisting properties of the assembled fibers (Aboutalebi et al., 2014; Zeng et al., 2018). Visual inspections of the fiber backbone, allows to identify multiscale defects, which include rough surface with wrinkles, degree of homogeneity of the structure, presence of larger pores and boundary regions at lower resolution (SEM), crystallinity and defects of CNTs and of graphene sheets, including vacancy defects, dislocation edges, stacking faults, grain boundaries and other features (HR-TEM), as well documented in some papers (Behabtu et al., 2013; Kou et al., 2014, 2017; Liu et al., 2016; Papageorgiou et al., 2017; Zeng et al., 2018; Fang et al., 2020; Yin et al., 2020) (**Figures 7D–I**). Furthermore, elemental mapping images can demonstrate not only the doping, but also the element distributions along the fiber. Focused ion beam (FIB) milling can be used to cut down a fiber with sections perpendicular and parallel to the axis of the fiber. Such sections can be directly SEM imaged to reveal the yarn structure and correlate changes in morphology and structure with properties (Sears et al., 2010).

X-ray photoelectron spectroscopy (XPS) measurements can be informative of the chemical state, and of the electronic state composition of the elements at the surface of fibers. Together with the characteristic peaks of both graphene and CNTs at 284.5 eV (C–C bonds) and 285.7 eV (C=C bonds), minor peaks at c.a. 286.2 eV, c.a. 287.8 eV, and c.a. 289.0 eV can be observed, due to the presence of C–O, C=O, and O–C=O functional groups, respectively. It is also observed that the intensities of oxygen-reach peaks increased with the oxidation time (Park H. et al., 2019). The incorporation of other dopants into CNT and graphene fibers can be also determined by XPS. The high-resolution spectra indicated C–N sp^2 and sp^3 bonding at 286.1 eV and 288.2 eV, respectively (Ryu et al., 2015), C–Br at 286.9 eV together with peaks at 257.2 eV, 182.9 eV, and 69.6 eV corresponding to Br 3s, Br 3p, and Br 3d.

Often the assembled fibers contain pores among nanotubes or sheets due to the microcrystalline nature of the carbon building blocks. A porosity would be beneficial for electrochemical and sensing applications (Xu et al., 2012; Cai et al., 2015; Fan et al., 2016; Park H. et al., 2019), but can limit the properties for electrical transport applications (Miao, 2011). For this reason, it would be convenient to investigate the porosity of the fiber by means of sorption techniques. Zeng et al. (2018) have obtained microporous CNFs with variable surface area (from c.a. 850 $m^2\ g^{-1}$ to c.a. 7 $m^2\ g^{-1}$ depending on the duration of the CVD process), due to the highly defective nature caused by NH_3 etching. The authors observed an increase of the electrical conductivity with the densification of the fiber of one order of magnitude.

Contact angle measurements can provide important findings on the fiber-liquid interactions (Zhang L. et al., 2017; Zeng et al., 2018). The non-polar and polar surface energy components can be obtained and other wetting parameters (work of adhesion, spreading coefficient and wetting tension) can be predicted.

In most of the synthesis methods to obtain nanocarbons a material with a large variety of properties is produced. Such material contains also catalyst nanoparticles, amorphous carbon and other side-products. There are several methods to investigate carbon yarns, before/after fiber production and after the doping step. Among all, termogravimetric analysis (TGA) can be used to verify purity and thermal stability of the fibers (Lepak-Kuc et al., 2018; Lee J. et al., 2019). Due to the higher chemical reactivity in air, a decrease in weight in the 250–400°C range may be related to amorphous carbon elimination (i.e., from CNTs). The oxidation

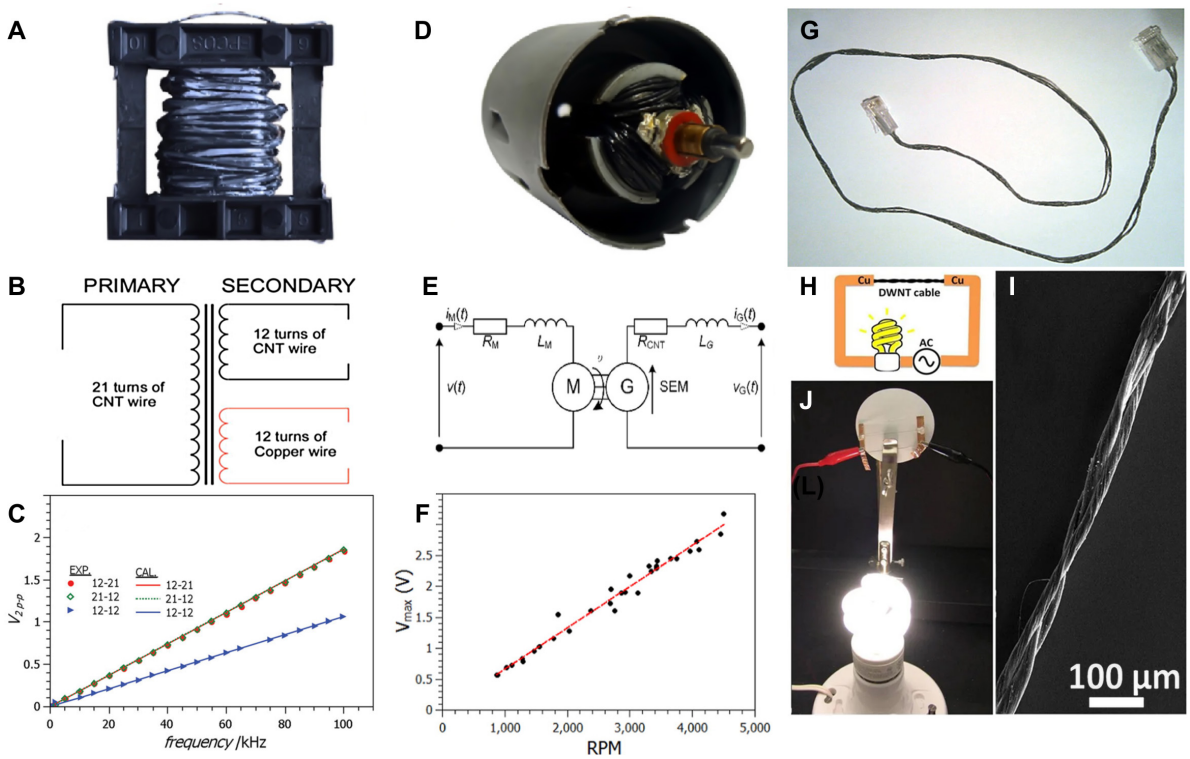

FIGURE 8 | (A) Photo, **(B)** characteristics of the primary and of the secondary windings, and **(C)** electrical performances of the CNT-fiber transformer. **(D)** Photo, **(E)** schematics of the circuit, and **(F)** electrical performances of the CNT-fiber shunt generator. **(G)** image of the ethernet cable made of CNT wires, **(H)** scheme, **(I)** SEM image, and **(J)** image of an I-doped CNT cables exceeding the specific electrical conductivity of metals. **A,D,E,F**: reproduced from Lekawa-Raus et al. (2017) with permission from Elsevier. **B,C**: reproduced from Kurzepa et al. (2014) with permission from Wiley-VCH. Panel **(G)** adapted from Lekawa-Raus et al. (2014b). Panels **(H-J)** adapted from Zhao et al. (2011) under the Creative Commons CC BY license.

of more graphitized structures is, for a fact, expected to occur above 500°C in air. The loading of metal catalyst and of the inorganic supports (Al_2O_3, SiO_2) of the initial carbon materials and/or their presence in the final fibers can be determined. If the fiber is undoped, the residue of the thermal treatment performed in air can be easily associated with the inorganic content of the catalyst and of the metal oxide support. A decrease in the stability of materials with a reduction of the oxidation temperature can be also observed after an acid treatment (e.g., H_2SO_4, $HClO_4$) of purification or doping. Notice that, in general the strongly oxidized carbon materials are more reactive to the thermal treatments (Cravotto et al., 2011).

FRONTIERS OF THE CURRENT TECHNOLOGY

Behabtu et al. (2013) have demonstrated several applications of CNT fibers. Interestingly, the authors showed a light-emitting diode (LED) suspended and electrically contacted by two CNT fibers (24 nm in diameter) loaded with 30 mA current (6.6×10^3 A/cm^2 as a current density). More interestingly, the same authors illustrated a field-emitting device fabricated with a CNT fiber working as a cathode. An emitted current density of 5.8×10^3 A/cm^2 was reported (3.6 mA from a CNT fiber with a diameter of 9 µm) at 0.86 V/µm placed at 1 mm from the anode. Surprisingly, Kim et al. (2017) presented an energy harvester, made of two twisted carbon nanotube yarns, which converts electrical from mechanical energy, both torsional and tensile motions, without the need of an external bias voltage. By stretching the coiled yarns 250 W/kg can be generated when cycled up to 30 hertz. These kinds of devices could be used perhaps in the sea to harvest wave energy, as well as with thermally driven artificial muscles to convert temperature fluctuations to electrical energy. In other papers, Uddin et al. (2014) and Yan et al. (2014) have shown a three-dimensional dye-sensitized solar cell (DSSC) wire by using 50 µm diameter CNT yarns as working electrodes. Beside other advantages (flexibility, mechanical resistance, electrically and catalytically active), the authors reported a photovoltaic efficiency from the sunlight raising about the 7.4%.

Koziol and colleagues (Lekawa-Raus et al., 2017) have shown a few prototypes based on CNT fibers (**Figure 8**), including a small transformer and a DC generator containing CNT rope windings (substituting copper windings of the primary transformer and of a generator rotor, respectively) (**Figures 8A,B**). The authors found the characteristics of the transformer to be perfectly linear and are not dependent on the material in agreement with the classical theory (Kurzepa et al., 2014) being 10 mA (p–p) applied

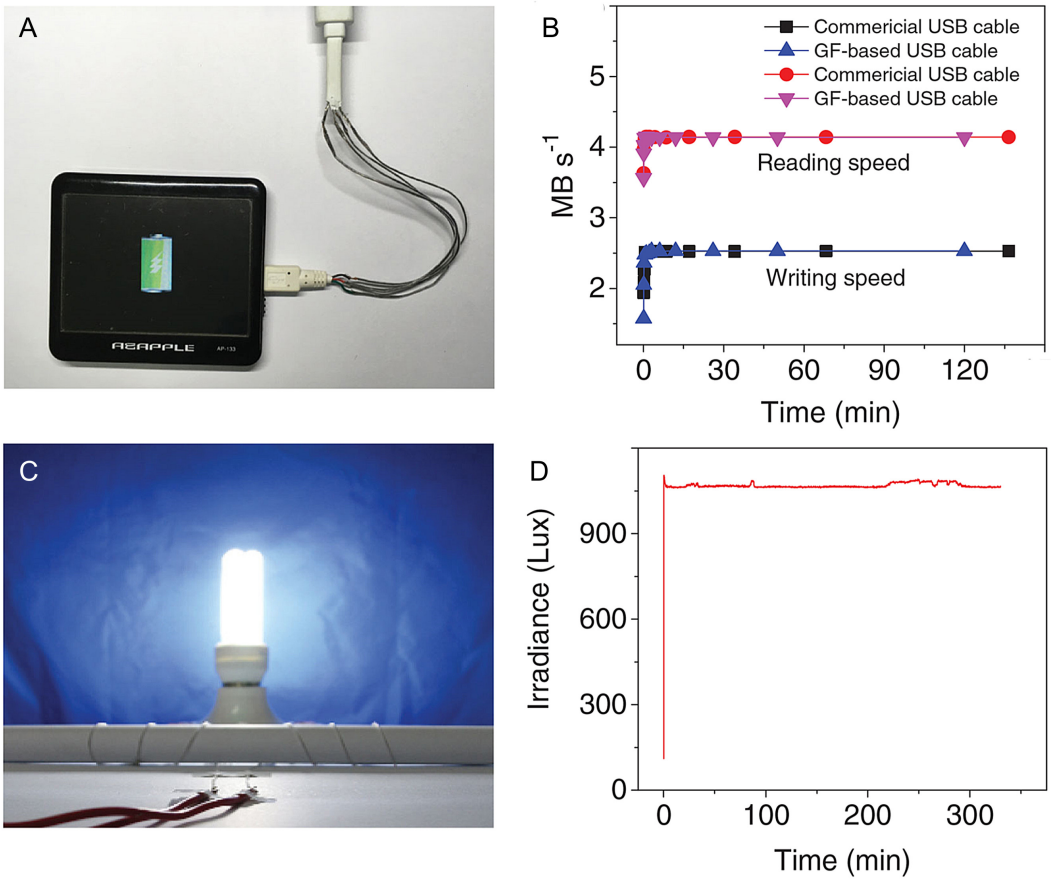

FIGURE 9 | (A) Picture of the USB cable fabricated with graphene fibers. **(B)** Reading/writing performances of the graphene cable as compared with traditional Cu wires. **(C,D)** picture showing a 9W working lamp (220 V) connected with a one meter long Br-doped graphene cable and the irradiance intensity tested along the time. Reproduced from Liu et al. (2016) with permission from Wiley-VCH.

to the primary winding of the transformer in the frequency range of 1–100 kHz (**Figure 8C**). The same authors found also a linear dependence of the maximum generated voltage (V) with the angular velocity (RPM, revolutions per minute) in the 1000–5000 rpm range for a shunt generator based on a CNT fiber (**Figures 8D–F**). It is however expected that both devices were close to their operational limits, but still limited if compared with the copper-based counterparts. A CNT fiber conductors was fabricated to demonstrate the feasibility as a standard electrical wire (Kurzepa et al., 2014). The home-built cable was successfully tested in sending 10 MB s^{-1} (**Figure 8G**). Zhao et al. (2011) reported the fabrication and properties of DWCNT twisted rope, used as a conducting cable loaded with 9 watts, 0.15A, 120V of a household bulb (**Figures 8H–J**) public power.

Liu et al. (2016) reported the preparation of $FeCl_3$-, Br_2- and K-doped GFs with excellent electrical conductivity by using a two-zone vapor transport method starting from high-purity GFs. Interestingly, the authors fabricated a graphene fiber-based USB cable, which was tested in reading and writing operation speeds as compared with a conventional USB cable (**Figures 9A,B**). In the same paper, the long-term durability in electrical properties of one-meter long Br-doped graphene cable (60 μm in diameter) connected with a 9W lamp (220V) was demonstrated (**Figures 9C,D**). In the test, a stable irradiance intensity of the lamp was obtained (1060 Lux), which was similar to what obtained by copper wires. The potential uses under practical conditions seems to be limited by the stability of doped graphene (i.e., K, $FeCl_3$, Br_2, I_2) when exposed to air, due to the absorption of oxygen and water (Zhang et al., 2019). For example, a fast modification of the color from yellow to black of the K- and $FeCl_3$-doped was observed after a few minutes in air, indicating an irreversible modification. In general terms, the instability could be verified by comparing electrical performance of doped graphene fibers with spectroscopic methods (UV-Vis, Raman and XPS techniques), which are very sensitive to the change in the optical, electronic, elemental and structure properties (Liu et al., 2016).

Though the shielding with metal films, composites and fiber mats is much more popular (Zhou et al., 2017; Ramírez-Herrera et al., 2019), the flexibility and the relatively high electrical conductivity of the assembled fibers make possible shielding characteristics. In fact, by considering the continuously interconnected network realized by the fibers and by the interwoven fibers the application in electromagnetic interference (EMI) shielding is expected, but studies on interference shielding with CNT and graphene yarns are only just beginning and few

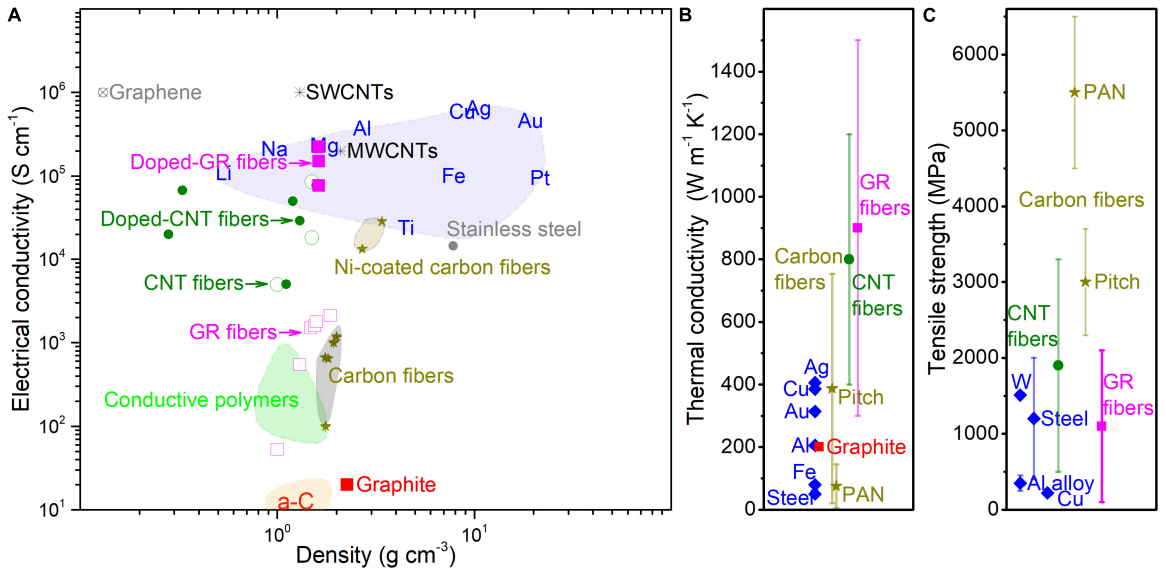

FIGURE 10 | (A) Electrical, **(B)** thermal conductivities, and **(C)** tensile strength of CNT- and graphene-fibers (dark green and magenta colors, respectively) as compared to carbon fibers, some metals (brown and blue colors, respectively), and other reference materials.

studies are reported so far. Zeng et al. (2018) fabricated stacked layers with 3D assembled graphene fibers to form thicknesses in the 3.0–26 μm range and measured the EMI shielding properties in the X-band frequency range (8–12 GHz). The authors achieved a record value of shielding effectiveness normalized by density and thickness ($SEE_{/t}$) of about 60000 dB cm^2 g^{-1}, which is higher than that of conventional materials (Cu and Al foils), of CNT/graphene core-shell foams (51000 dB cm^2 g^{-1}) (Song et al., 2017) and of $Ti_3C_2T_x$ MXene film (~31000 dB cm^2 g^{-1}) (Shahzad et al., 2016). The authors ascribed the high shielding with the porous structure and with the continuously interconnected network that generate an expanded interface and high electrical conductivity. In another recent paper Li et al. (2020) have fabricated a wool-coated CNT coiled yarn fabric with good shielding characteristics and washing durability for wearable E-textile applications.

Electrical/thermal conductivities and tensile strength of the assembled carbon fibers compared to those of other materials (metals, commercial PAN and pitch-derived carbon fibers) are compared (**Figures 10A–C**). It can be seen from this figure that CNT- and graphene fibers may exhibit properties equivalent or superior to those of metals. However, a wide range of values is observed for the assembled carbon fibers. Such data dispersion is largely determined by several factors. First of all, the basic unit type (SWCNT, MWCNT, graphene) and its main characteristics (aspect ratio, diameter, length, local and structural defect content, purity, presence of impurities and eventually amorphous carbon phases) certainly play a key role, at least at the molecular level. In addition, the structure, morphology and characteristics at the interface between building blocks in forming the fiber scaffold, including chemical bonds, presence of voids and structural defects of the fiber, twisting and wrapping properties are definitely decisive to regulate the fiber properties. Moreover, the doping strategy of CNT and graphene fibers has shown to be crucial for boosting the electrical and thermal properties to record values. However, the stability over time and temperature should be deeply verified and improved to have such fibers as a practical alternative to metals (and commercial carbon fibers). Most importantly, CNTs, graphene and graphene derivatives are becoming cheaper and the ability to control their purity and characteristics, as well as the prospect to assemble the fibers in continuous processes according to industrially viable methods, gives the chance to rapid progress in the field, although it is still difficult to replicate the properties of individual CNT and graphene units to macroscopic fibers.

In conclusion, the carbon-based fiber preparation technology is mature and allows to operate with continuous processes and with industrial equipments, while the fiber doping strategy allows to reach and overcome the electrical/thermal conductivity of metals and with excellent mechanical characteristics. CNTs and graphene are excellent conductors, albeit directionally. At present, they can be used effectively in conductive cables, but not as direct metal replacements. In order to replace traditional cables, there are some issues that need to be deeply investigated, such as stability over time and temperature (in the case of doping). Two final aspects deserve to be mentioned. First of all, the electrical cable insulation, which appears to be relatively simple (Lekawa-Raus et al., 2014a) with polymer coating the carbon cable. Moreover, the connection of CNT and graphene fibers with traditional cables is more difficult and represent a non-secondary standpoint to be solved. In the laboratory practice electrodes and electrical connections are made with Au film, silver, other metals (e.g. In), alloys or carbon paste, but who tried to build interconnections with traditional electronics realized the difficulty of the conventional

joints (i.e., soldering, crimping, etc.), which have no durability and are quite inappropriate to the pure carbon assemblies. The topic has not received so far all the attention it deserves and very few studies have been targeted at this issue (Burda et al., 2015; Ebrahimian and Kokabi, 2017; Kim et al., 2018; Milowska et al., 2019; Fu et al., 2020).

SUMMARY AND OUTLOOK

The review summarizes the scientific progress in the field of carbon-based fibers to be used as electrical conductors, from the origin to the most recent findings. From graphite and first developed pyrolyzed fibers to carbon fibers and assembled nanocarbons (carbon nanotubes and graphene sheets) into fibers/yarns/ropes the issue has been progressively renewed to translate the carbon attributes into materials at the frontier. The main addressed theme is about the most recent innovations concerning the doping paradigm of all-carbon fibers/based on carbon nanotubes and/or graphene, emphasizing the role played by the chemistry. Taking advantage of the doping with metal and with non-metal compounds unprecedented electrical properties are observed achieving the metal counterpart values. Along this line, the conductivity record values have been found much higher than those of metals, thus demonstrating the potential to substitute them in some prototypes reported in the recent literature. Moreover, the other advantages provided by all-carbon fibers over conventional metals are manifold, including low weight, environmental and chemical stability, flexibility and mechanical properties. Despite the great advancement in the field, some problems should be addressed, including long-term stability, high-performance electrical properties, scalable and cost-effective production methods and interconnection with traditional cables. CNTs and graphene are excellent conductors, albeit directionally. At present, they can be used effectively in conductive cables, but not as direct metal replacements. We can expect a great development in the next years in particular in the flexible and wearable electronics, such as multifunctional fabrics, power cables, energy harvesting and storage and sensing device fields.

AUTHOR CONTRIBUTIONS

FC wrote and organized the manuscript. MU, KL, MZ, and DS provided a substantial contribution to the work. All authors approved it for publication.

FUNDING

This work was supported by MIUR (Ministero dell'Istruzione, dell'Università e della Ricerca), INSTM Consorzio and NIS (Nanostructured Interfaces and Surfaces) Inter-Departmental Centre of University of Turin.

REFERENCES

Aboutalebi, S. H., Jalili, R., Esrafilzadeh, D., Salari, M., Gholamvand, Z., Aminorroaya Yamini, S., et al. (2014). High-performance multifunctional graphene yarns: toward wearable all-carbon energy storage textiles. *ACS Nano* 8, 2456–2466. doi: 10.1021/nn406026z

Afroj, S., Karim, N., Wang, Z., Tan, S., He, P., Holwill, M., et al. (2019). Engineering graphene flakes for wearable textile sensors via highly scalable and ultrafast yarn dyeing technique. *ACS Nano* 13, 3847–3857. doi: 10.1021/acsnano.9b00319

Ajayan, P. M. (1999). Nanotubes from carbon. *Chem. Rev.* 99, 1787–1800. doi: 10.1021/cr970102g

Alemán, B., Reguero, V., Mas, B., and Vilatela, J. J. (2015). Strong carbon nanotube fibers by drawing inspiration from polymer fiber spinning. *ACS Nano* 9, 7392–7398. doi: 10.1021/acsnano.5b02408

Anthony, D. B., Sui, X. M., Kellersztein, I., De Luca, H. G., White, E. R., Wagner, H. D., et al. (2018). Continuous carbon nanotube synthesis on charged carbon fibers. *Comp. Part A Appl. Sci. Manufact.* 112, 525–538.

Bacon, R. (1959). Growth, structure, and properties of graphite whiskers. *J. Appl. Phys.* 31, 283–290. doi: 10.1063/1.1735559

Barnett, C. J., Evans, C., Mccormack, J. E., Gowenlock, C. E., Dunstan, P., Adams, W., et al. (2019). Experimental measurement of angular and overlap dependence of conduction between carbon nanotubes of identical chirality and diameter. *Nano Lett.* 19, 4861–4865. doi: 10.1021/acs.nanolett.9b00025

Behabtu, N., Young, C. C., Tsentalovich, D. E., Kleinerman, O., Wang, X., Ma, A. W. K., et al. (2013). Strong, light, multifunctional fibers of carbon nanotubes with ultrahigh conductivity. *Science* 339, 182–186. doi: 10.1126/science.1228061

Burda, M., Lekawa-Raus, A., Gruszczyk, A., and Koziol, K. K. K. (2015). Soldering of carbon materials using transition metal rich alloys. *ACS Nano* 9, 8099–8107. doi: 10.1021/acsnano.5b02176

Cai, W., Lai, T., and Ye, J. (2015). A spinneret as the key component for surface-porous graphene fibers in high energy density micro-supercapacitors. *J. Mater. Chem. A* 3, 5060–5066. doi: 10.1039/C5TA00365B

Cecone, C., Caldera, F., Anceschi, A., Scalarone, D., Trotta, F., Bracco, P., et al. (2018). One-step facile process to obtain insoluble polysaccharides fibrous mats from electrospinning of water-soluble PMDA/cyclodextrin polymer. *J. Appl. Polym. Sci.* 135:46490. doi: 10.1002/app.46490

Cesano, F., Bertarione, S., Scarano, D., and Zecchina, A. (2005). Connecting carbon fibers by means of catalytically grown nanofilaments: formation of carbon-carbon composites. *Chem. Mater.* 17, 5119–5123. doi: 10.1021/cm050427a

Cesano, F., Rattalino, I., Bardelli, F., Sanginario, A., Gianturco, A., Veca, A., et al. (2013). Structure and properties of metal-free conductive tracks on polyethylene/multiwalled carbon nanotube composites as obtained by laser stimulated percolation. *Carbon* 61, 63–71. doi: 10.1016/j.carbon.2013.04.066

Cesano, F., and Scarano, D. (2015). "Dispersion of carbon-based materials (CNTs, Graphene) in polymer matrices," in *Carbon for Sensing Devices*, eds D. Demarchi and A. Tagliaferro (Heidelberg: Springer International Publishing), 43–75. doi: 10.1007/978-3-319-08648-4_3

Cesano, F., and Scarano, D. (2018). Graphene and other 2D layered hybrid nanomaterial-based films: synthesis, properties, and applications. *Coatings* 8:419. doi: 10.3390/coatings8120419

Cesano, F., Zaccone, M., Armentano, I., Cravanzola, S., Muscuso, L., Torre, L., et al. (2016). Relationship between morphology and electrical properties in PP/MWCNT composites: processing-induced anisotropic percolation threshold. *Mater. Chem. Phys.* 180, 284–290. doi: 10.1016/j.matchemphys.2016.06.009

Cheng, J., and Lee, S.-H. (2016). Development of new smart materials and spinning systems inspired by natural silks and their applications. *Front. Mater.* 2:74. doi: 10.3389/fmats.2015.00074

Chong, W. G., Xiao, F., Yao, S., Cui, J., Sadighi, Z., Wu, J., et al. (2019). Nitrogen-doped graphene fiber webs for multi-battery energy storage. *Nanoscale* 11, 6334–6342. doi: 10.1039/C8NR10025J

Chou, T. W., Gao, L., Thostenson, E. T., Zhang, Z., and Byun, J. H. (2010). An assessment of the science and technology of carbon nanotube-based fibers and composites. *Comp. Sci. Technol.* 70, 1–19. doi: 10.1016/j.compscitech.2009.10.004

Chowdhury, A. R., Jaksik, J., Hussain, I., Longoria, R., Faruque, O., Cesano, F., et al. (2019). Multicomponent nanostructured materials and interfaces for efficient piezoelectricity. *Nano-Struct. Nano-Objects* 17, 148–184. doi: 10.1016/j.nanoso.2018.12.002

Chung, D. D. L. (2017). "1 – Carbon fibers, nanofibers, and nanotubes," in *Carbon Composites*, 2nd Edn, ed. D. D. L. Chung (Oxford: Butterworth-Heinemann), 1–87. doi: 10.1016/b978-0-12-804459-9.00001-4

Clancy, A. J., Bayazit, M. K., Hodge, S. A., Skipper, N. T., Howard, C. A., and Shaffer, M. S. P. (2018). Charged carbon nanomaterials: redox chemistries of fullerenes, carbon nanotubes, and graphenes. *Chem. Rev.* 118, 7363–7408. doi: 10.1021/acs.chemrev.8b00128

Cong, H. P., Chen, J. F., and Yu, S. H. (2014). Graphene-based macroscopic assemblies and architectures: an emerging material system. *Chem Soc. Rev.* 43, 7295–7325. doi: 10.1039/c4cs00181h

Cravanzola, S., Haznedar, G., Scarano, D., Zecchina, A., and Cesano, F. (2013). Carbon-based piezoresistive polymer composites: structure and electrical properties. *Carbon* 62, 270–277. doi: 10.1016/j.carbon.2013.05.064

Cravotto, G., Garella, D., Calcio Gaudino, E., Turci, F., Bertarione, S., Agostini, G., et al. (2011). Rapid purification/oxidation of multi-walled carbon nanotubes under 300 kHz-ultrasound and microwave irradiation. *New J. Chem.* 35, 915–919. doi: 10.1039/c0nj00892c

De Jong, K. P., and Geus, J. W. (2000). Carbon nanofibers: catalytic synthesis and applications. *Cat. Rev. Sci. Engin.* 42, 481–510. doi: 10.1081/CR-100101954

Derbyshire, F. J., Presland, A. E. B., and Trimm, D. L. (1975). Graphite formation by the dissolution-precipitation of carbon in cobalt, nickel and iron. *Carbon* 13, 111–113. doi: 10.1016/0008-6223(75)90267-5

Dhanabalan, S. C., Dhanabalan, B., Chen, X., Ponraj, J. S., and Zhang, H. (2019). Hybrid carbon nanostructured fibers: stepping stone for intelligent textile-based electronics. *Nanoscale* 11, 3046–3101. doi: 10.1039/C8NR07554A

Dini, Y., Faure-Vincent, J., and Dijon, J. (2019). How to overcome the electrical conductivity limitation of carbon nanotube yarns drawn from carbon nanotube arrays. *Carbon* 144, 301–311. doi: 10.1016/j.carbon.2018.12.041

Dini, Y., Rouchon, D., Faure-Vincent, J., and Dijon, J. (2020). Large improvement of CNT yarn electrical conductivity by varying chemical doping and annealing treatment. *Carbon* 156, 38–48. doi: 10.1016/j.carbon.2019.09.022

Dresselhaus, M. S., and Dresselhaus, G. (2002). Intercalation compounds of graphite. *Adv. Phys.* 51, 1–186. doi: 10.1080/00018730110113644

Dresselhaus, M. S., Jorio, A., Hofmann, M., Dresselhaus, G., and Saito, R. (2010). Perspectives on carbon nanotubes and graphene Raman spectroscopy. *Nano Lett.* 10, 751–758. doi: 10.1021/nl904286r

Ebrahimian, A., and Kokabi, A. H. (2017). Friction stir soldering: a novel route to produce graphite-copper dissimilar joints. *Mater. Des.* 116, 599–608. doi: 10.1016/j.matdes.2016.12.057

Eckmann, A., Felten, A., Mishchenko, A., Britnell, L., Krupke, R., Novoselov, K. S., et al. (2012). Probing the nature of defects in graphene by Raman spectroscopy. *Nano Lett.* 12, 3925–3930. doi: 10.1021/nl300901a

Ericson, L. M., Fan, H., Peng, H., Davis, V. A., Zhou, W., Sulpizio, J., et al. (2004). Macroscopic, neat, single-walled carbon nanotube fibers. *Science* 305, 1447–1450. doi: 10.1126/science.1101398

Fan, T., Zhao, C., Xiao, Z., Guo, F., Cai, K., Lin, H., et al. (2016). Fabricating of high-performance functional graphene fibers for micro-capacitive energy storage. *Sci. Rep.* 6:29534. doi: 10.1038/srep29534

Fang, B., Chang, D., Xu, Z., and Gao, C. (2020). Review on graphene fibers: expectations, advances, and prospects. *Adv. Mater.* 32:1902664. doi: 10.1002/adma.201902664

Fischer, J. E. (2006). "Ch 2: Carbon nanotubes: structure and properties," in *Carbon Nanomaterials* ed Y. Gogotsi (Boca Raton, FL: Taylor & Francis).

Fischer, J. E., and Thompson, T. E. (1978). Graphite intercalation compounds. *Phys. Today* 31, 36–45. doi: 10.1063/1.2995104

Foroughi, J., and Spinks, G. (2019). Carbon nanotube and graphene fiber artificial muscles. *Nanoscale Adv.* 1, 4592–4614. doi: 10.1039/C9NA00038K

Fu, H., Xiao, Y., Song, R., Wang, Z., Ji, H., and He, D. (2020). Rapid soldering of flexible graphene assembled films at low temperature in air with ultrasonic assistance. *Carbon* 158, 55–62. doi: 10.1016/j.carbon.2019.11.089

Fujita, S., and Suzuki, A. (2010). Theory of temperature dependence of the conductivity in carbon nanotubes. *J. Appl. Phys.* 107:013711. doi: 10.1063/1.3280035

García-Mateos, F. J., Ruiz-Rosas, R., Rosas, J. M., Rodríguez-Mirasol, J., and Cordero, T. (2019). Controlling the composition, morphology, porosity, and surface chemistry of lignin-based electrospun carbon materials. *Front. Mater.* 6:114. doi: 10.3389/fmats.2019.00114

Groppo, E., Bonino, F., Cesano, F., Damin, A., and Manzoli, M. (2018). "Raman, IR and INS characterization of functionalized carbon materials," in *Metal-free Functionalized Carbons in Catalysis: Synthesis, Characterization and Applications*, eds A. Villa and N. Dimitratos (London: Royal Society of Chemistry), 103–137. doi: 10.1039/9781788013116-00103

Hada, M., Hasegawa, T., Inoue, H., Takagi, M., Omoto, K., Chujo, D., et al. (2019). One-minute Joule annealing enhances the thermoelectric properties of carbon nanotube yarns via the formation of graphene at the interface. *ACS Appl. Ener. Mater.* 2, 7700–7708. doi: 10.1021/acsaem.9b01736

Harun, S. W., Stauber, T., Ozkan, C., Celasco, E., Chaika, A. N., Zhang, M., et al. (eds) (2019). *Handbook of Graphene*, Vol. 1-8. Hoboken, NJ: Wiley.

Haznedar, G., Cravanzola, S., Zanetti, M., Scarano, D., Zecchina, A., and Cesano, F. (2013). Graphite nanoplatelets and carbon nanotubes based polyethylene composites: electrical conductivity and morphology. *Mater. Chem. Phys.* 143, 47–52. doi: 10.1016/j.matchemphys.2013.08.008

Headrick, R. J., Tsentalovich, D. E., Berdegué, J., Bengio, E. A., Liberman, L., Kleinerman, O., et al. (2018). Structure–property relations in carbon nanotube fibers by downscaling solution processing. *Adv. Mater.* 30:1704482. doi: 10.1002/adma.201704482

Hennig, G. (1952). The properties of the interstitial compounds of graphite. III. The electrical properties of the halogen compounds of graphite. *J. Chem. Phys.* 20, 1443–1447. doi: 10.1063/1.1700778

Hills, G., Lau, C., Wright, A., Fuller, S., Bishop, M. D., Srimani, T., et al. (2019). Modern microprocessor built from complementary carbon nanotube transistors. *Nature* 572, 595–602. doi: 10.1038/s41586-019-1493-8

Hong, S., and Myung, S. (2007). A flexible approach to mobility. *Nat. Nanotechnol.* 2, 207–208. doi: 10.1038/nnano.2007.89

Iijima, S., Ajayan, P. M., and Ichihashi, T. (1992). Growth model for carbon nanotubes. *PRL* 69, 3100–3103. doi: 10.1103/PhysRevLett.69.3100

Iijima, S., and Ichihashi, T. (1993). Single-shell carbon nanotubes of 1-nm diameter. *Nature* 363, 603–605. doi: 10.1038/363603a0

Jain, S. M., Cesano, F., Scarano, D., and Edvinsson, T. (2017). Resonance raman and IR spectroscopy of aligned carbon nanotube arrays with extremely narrow diameters prepared with molecular catalysts on steel substrates. *PCCP* 19, 30667–30674. doi: 10.1039/C7CP06973A

Jakubinek, M. B., Johnson, M. B., White, M. A., Jayasinghe, C., Li, G., Cho, W., et al. (2012). Thermal and electrical conductivity of array-spun multi-walled carbon nanotube yarns. *Carbon* 50, 244–248. doi: 10.1016/j.carbon.2011.08.041

Jang, Y., Kim, S. M., Spinks, G. M., and Kim, S. J. (2019). Carbon nanotube yarn for fiber-shaped electrical sensors, actuators, and energy storage for smart systems. *Adv. Mater.* 32:1902670. doi: 10.1002/adma.201902670

Jiang, K., Li, Q., and Fan, S. (2002). Spinning continuous carbon nanotube yarns. *Nature* 419:801. doi: 10.1038/419801a

Karakassides, A., Ganguly, A., Tsirka, K., Paipetis, A. S., and Papakonstantinou, P. (2020). Radially grown graphene nanoflakes on carbon fibers as reinforcing interface for polymer composites. *ACS Appl. Nano Mater.* 3, 2402–2413. doi: 10.1021/acsanm.9b02536

Kharlamova, M. V. (2017). Investigation of growth dynamics of carbon nanotubes. *Beilstein J. Nanotechnol.* 8, 826–856. doi: 10.3762/bjnano.8.85

Kim, S. H., Choi, J.-P., Eom, Y.-S., Nam, Y., Baek, S., and Aranas, C. (2018). A phenomenological study of a Sn–Ag–Al composite solder reinforced with Mg–MWCNT: improved electrical conductivity and thermo-physical performance. *Mater. Des.* 140, 196–208. doi: 10.1016/j.matdes.2017.11.073

Kim, S. H., Haines, C. S., Li, N., Kim, K. J., Mun, T. J., Choi, C., et al. (2017). Harvesting electrical energy from carbon nanotube yarn twist. *Science* 357, 773–778. doi: 10.1126/science.aam8771

Kou, L., Huang, T., Zheng, B., Han, Y., Zhao, X., Gopalsamy, K., et al. (2014). Coaxial wet-spun yarn supercapacitors for high-energy density and safe wearable electronics. *Nat. Commun.* 5:3754. doi: 10.1038/ncomms4754

Kou, L., Liu, Y., Zhang, C., Shao, L., Tian, Z., Deng, Z., et al. (2017). A mini review on nanocarbon-based 1D macroscopic fibers: assembly strategies and mechanical properties. *Nano-Micro Lett.* 9:51. doi: 10.1007/s40820-017-0151-7

Kumar, M., Gowda, A., and Kumar, S. (2017). Discotic liquid crystals with graphene: supramolecular self-assembly to applications. *Part. Part. Syst. Charact.* 34:1700003. doi: 10.1002/ppsc.201700003

Kurzepa, L., Lekawa-Raus, A., Patmore, J., and Koziol, K. (2014). Replacing Copper wires with carbon nanotube wires in electrical transformers. *Adv. Func. Mater.* 24, 619–624. doi: 10.1002/adfm.201302497

Lee, C. H., Liu, W.-W., Chai, S.-P., Mohamed, A. R., Aziz, A., Khe, C.-S., et al. (2017). Review of the synthesis, transfer, characterization and growth mechanisms of single and multilayer graphene. *Adv. Mater.* 7, 15644–15693. doi: 10.1039/C7RA00392G

Lee, J., Lee, D.-M., Jung, Y., Park, J., Lee, H. S., Kim, Y.-K., et al. (2019a). Direct spinning and densification method for high-performance carbon nanotube fibers. *Nat. Commun.* 10:2962. doi: 10.1038/s41467-019-10998-0

Lee, T., Park, K. T., Ku, B. C., and Kim, H. (2019b). Carbon nanotube fibers with enhanced longitudinal carrier mobility for high-performance all-carbon thermoelectric generators. *Nanoscale* 11, 16919–16927. doi: 10.1039/C9NR05757A

Lekawa-Raus, A., Gizewski, T., Patmored, J., Kurzepa, L., and Koziol, K. K. (2017). Electrical transport in carbon nanotube fibres. *Scripta Mater.* 131, 112–118. doi: 10.1016/j.scriptamat.2016.11.027

Lekawa-Raus, A., Kurzepa, L., Peng, X., and Koziol, K. (2014a). Towards the development of carbon nanotube based wires. *Carbon* 68, 597–609. doi: 10.1016/j.carbon.2013.11.039

Lekawa-Raus, A., Patmore, J., Kurzepa, L., Bulmer, J., and Koziol, K. (2014b). Electrical properties of carbon nanotube based fibers and their future use in electrical wiring. *Adv. Funct. Mater.* 24, 3661–3682. doi: 10.1002/adfm.201303716

Lepak-Kuc, S., Boncel, S., Szybowicz, M., Nowicka, A. B., Jozwik, I., Orlinski, K., et al. (2018). The operational window of carbon nanotube electrical wires treated with strong acids and oxidants. *Sci. Rep.* 8:14332. doi: 10.1038/s41598-018-32663-0

Lepak-Kuc, S., Milowska, K. Z., Boncel, S., Szybowicz, M., Dychalska, A., Jozwik, I., et al. (2019). Highly conductive doped hybrid carbon nanotube-graphene wires. *ACS Appl. Mater. Interf.* 11, 33207–33220. doi: 10.1021/acsami.9b08198

Li, J., and Pandey, G. P. (2015). Advanced physical chemistry of carbon nanotubes. *Ann. Rev. Phys. Chem.* 66, 331–356. doi: 10.1146/annurev-physchem-040214-121535

Li, Q., Li, Y., Zhang, X., Chikkannanavar, S. B., Zhao, Y., Dangelewicz, A. M., et al. (2007). Structure-dependent electrical properties of carbon nanotube fibers. *Adv. Mater.* 19:3358. doi: 10.1002/adma.200602966

Li, W., Xu, C., Ren, X., Xue, Y., Zhao, J., Li, Q., et al. (2020). Anti-fatigue and multifunctional core-spun yarns based on carbon nanotube springs. *Comp. Commun.* 19, 127–133. doi: 10.1016/j.coco.2020.03.008

Li, X., Cai, W., An, J., Kim, S., Nah, J., Yang, D., et al. (2009). Large-area synthesis of high-quality and uniform graphene films on copper foils. *Science* 324, 1312–1314. doi: 10.1126/science.1171245

Li, Y. L., Kinloch, I. A., and Windle, A. H. (2004). Direct spinning of carbon nanotube fibers from chemical vapor deposition synthesis. *Science* 304, 276–278. doi: 10.1126/science.1094982

Li, Z., Liu, Z., Sun, H., and Gao, C. (2015). Superstructured assembly of nanocarbons: fullerenes, nanotubes, and graphene. *Chem. Rev.* 115, 7046–1117. doi: 10.1021/acs.chemrev.5b00102

Liu, K., Zhu, F., Liu, L., Sun, Y., Fan, S., and Jian, K. (2012). Fabrication and processing of high-strength densely packed carbon nanotubeyarns without solution processes. *Nanoscale* 4, 3389–3393. doi: 10.1039/c2nr30226h

Liu, Q., Zhou, J., Song, C., Li, X., Wang, Z., Yang, J., et al. (2020a). 2.2V high performance symmetrical fiber-shaped aqueous supercapacitors enabled by "water-in-salt" gel electrolyte and N-Doped graphene fiber. *En. Stor. Mater.* 24, 495–503. doi: 10.1016/j.ensm.2019.07.008

Liu, Y., Yang, M., Pang, K., Wang, F., Xu, Z., Gao, W., et al. (2020b). Environmentally stable macroscopic graphene films with specific electrical conductivity exceeding metals. *Carbon* 156, 205–211. doi: 10.1016/j.carbon.2019.09.066

Liu, Y., Liang, H., Xu, Z., Xi, J., Chen, G., Gao, W., et al. (2017). Superconducting continuous graphene fibers via calcium intercalation. *ACS Nano* 11, 4301–4306. doi: 10.1021/acsnano.7b01491

Liu, Y., Xu, Z., Zhan, J., Li, P., and Gao, C. (2016). Superb electrically conductive graphene fibers via doping strategy. *Adv. Mater.* 28, 7941–7947. doi: 10.1002/adma.201602444

Lu, W., Zu, M., Byun, J. H., Kim, B. S., and Chou, T. W. (2012). State of the art of carbon nanotube fibers: opportunities and challenges. *Adv. Mater.* 24, 1805–1833. doi: 10.1002/adma.201104672

Lu, Z., Foroughi, J., Wang, C., Long, H., and Wallace, G. G. (2017). Superelastic hybrid CNT/graphene fibers for wearable energy storage. *Adv. Ener. Mater.* 8:1702047. doi: 10.1002/aenm.201702047

Lu, Z., Raad, R., Safaei, F., Xi, J., Liu, Z., and Foroughi, J. (2019). Carbon nanotube based fiber supercapacitor as wearable energy storage. *Front. Mater.* 6:138. doi: 10.3389/fmats.2019.00138

Ma, T., Gao, H.-L., Cong, H.-P., Yao, H.-B., Wu, L., Yu, Z.-Y., et al. (2018). A bioinspired interface design for improving the strength and electrical conductivity of graphene-based fibers. *Adv. Mater.* 30:1706435. doi: 10.1002/adma.201706435

Mäder, E., Liu, J., Hiller, J., Lu, W., Li, Q., Zhandarov, S., et al. (2015). Coating of carbon nanotube fibers: variation of tensile properties, failure behavior, and adhesion strength. *Front. Mater.* 2:53. doi: 10.3389/fmats.2015.00053

Meunier, V., Senet, P., and Lambin, P. (1999). Scanning tunneling spectroscopy signature of finite-size and connected nanotubes: a tight-binding study. *Phys. Rev. B* 60:7792. doi: 10.1103/PhysRevB.60.7792

Miao, M. (2011). Electrical conductivity of pure carbon nanotube yarns. *Carbon* 49, 3755–3761. doi: 10.1016/j.carbon.2011.05.008

Miao, M. (2013). Yarn spun from carbon nanotube forests: production, structure, properties and applications. *Particuology* 11, 378–393. doi: 10.1016/j.partic.2012.06.017

Milowska, K. Z., Burda, M., Wolanicka, L., Bristowe, P. D., and Koziol, K. K. K. (2019). Carbon nanotube functionalization as a route to enhancing the electrical and mechanical properties of Cu–CNT composites. *Nanoscale* 11, 145–157. doi: 10.1039/C8NR07521B

Mirfakhrai, T., Kozlov, M., Fang, S., Zhang, M., Baughman, R. H., and Madden, J. D. (2008). "Carbon nanotube yarns: sensors, actuators and current carriers," in *Proceedings of SPIE – The International Society for Optical Engineering*, Texas, TX.

Mohammadzadehmoghadam, S., and Dong, Y. (2019). Fabrication and characterization of electrospun silk fibroin/gelatin scaffolds crosslinked with glutaraldehyde vapor. *Front. Mater.* 6:91. doi: 10.3389/fmats.2019.00091

Newcomb, B. A., and Chae, H. G. (2018). "Ch 21: The properties of carbon fibers," in *Handbook of Properties of Textile and Technical Fibres*, 2nd Edn, ed. A. R. Bunsell (Cambridge: Woodhead Publishing).

Ottmers, D. M., and Rase, H. F. (1966). Potassium graphites prepared by mixed-reaction technique. *Carbon* 4, 125–127. doi: 10.1016/0008-6223(66)90017-0

Panwar, N., Soehartono, A. M., Chan, K. K., Zeng, S., Xu, G., Qu, J., et al. (2019). Nanocarbons for biology and medicine: sensing, imaging, and drug delivery. *Chem. Rev.* 119, 9559–9656. doi: 10.1021/acs.chemrev.9b00099

Papageorgiou, D. G., Kinloch, I. A., and Young, R. J. (2017). Mechanical properties of graphene and graphene-based nanocomposites. *Progr. Mat. Sci.* 90, 75–127. doi: 10.1016/j.pmatsci.2017.07.004

Park, H., Ambade, R. B., Noh, S. H., Eom, W., Koh, K. H., Ambade, S. B., et al. (2019a). Porous graphene-carbon nanotube scaffolds for fiber supercapacitors. *ACS Appl. Mater. Interf.* 11, 9011–9022. doi: 10.1021/acsami.8b17908

Park, Y., Hembram, K. P. S. S., Yoo, R., Jang, B., Lee, W., Lee, S. G., et al. (2019b). Reinterpretation of single-wall carbon nanotubes by Raman spectroscopy. *J. Phys. Chem. C* 123, 14003–14009. doi: 10.1021/acs.jpcc.9b02174

Peng, L., Xu, Z., Liu, Z., Guo, Y., Li, P., and Gao, C. (2017). Ultrahigh thermal conductive yet superflexible graphene films. *Adv. Mater.* 29:1700589. doi: 10.1002/adma.201700589

Powell, R. L., and Childs, G. E. (1972). *American Institute of Physics Handbook*, 3rd Edn. New York, NY: McGraw-Hill, 4–160.

Ramírez-Herrera, C. A., Gonzalez, H., De La Torre, F., Benitez, L., Cabañas-Moreno, J. G., and Lozano, K. (2019). Electrical properties and electromagnetic interference shielding effectiveness of interlayered systems composed by carbon nanotube filled carbon nanofiber mats and polymer composites. *Nanomaterials* 9:238. doi: 10.3390/nano9020238

Randeniya, L. K., Bendavid, A., Martin, P. J., and Tran, C. D. (2010). Composite yarns of multiwalled carbon nanotubes with metallic electrical conductivity. *Small* 6, 1806–1811. doi: 10.1002/smll.201000493

Reina, A., Jia, X., Ho, J., Nezich, D., Son, H., Bulovic, V., et al. (2009). Large area, few-layer graphene films on arbitrary substrates by chemical vapor deposition. *Nano Lett.* 9, 30–35. doi: 10.1021/nl801827v

Rodriguez, N. M., Chambers, A., and Baker, R. T. K. (1995). Catalytic engineering of carbon nanostructures. *Langmuir* 11, 3862–3866. doi: 10.1021/la00010a042

Ross, R. B. (1992). *Metallic Materials Specification Handbook*, 4th Edn. London: Chapman & Hall.

Ryu, S., Chou, J. B., Lee, K., Lee, D., Hong, S. H., Zhao, R., et al. (2015). Direct insulation-to-conduction transformation of adhesive catecholamine for simultaneous increases of electrical conductivity and mechanical strength of CNT fibers. *Adv. Mater.* 27, 3250–3255. doi: 10.1002/adma.201500914

Saito, R., Hofmann, M., Dresselhaus, G., Jorio, A., and Dresselhaus, M. S. (2011). Raman spectroscopy of graphene and carbon nanotubes. *Adv. Phys.* 60, 413–550. doi: 10.1080/00018732.2011.582251

Salavagione, H. J., Gómez-Fatou, M. A., Shuttleworth, P. S., and Ellis, G. J. (2018). New perspectives on graphene/polymer fibers and fabrics for smart textiles: the relevance of the polymer/graphene interphase. *Front. Mater.* 5:18. doi: 10.3389/fmats.2018.00018

Sears, K., Skourtis, C., Atkinson, K., Finn, N., and Humphries, W. (2010). Focused ion beam milling of carbon nanotube yarns to study the relationship between structure and strength. *Carbon* 48, 4450–4456. doi: 10.1016/j.carbon.2010.08.004

Shahzad, F., Alhabeb, M., Hatter, C. B., Anasori, B., Man Hong, S., Koo, C. M., et al. (2016). Electromagnetic interference shielding with 2D transition metal carbides (MXenes). *Science* 353:1137. doi: 10.1126/science.aag2421

Song, Q., Ye, F., Yin, X., Li, W., Li, H., Liu, Y., et al. (2017). Carbon nanotube–multilayered graphene edge plane core–shell hybrid foams for ultrahigh-performance electromagnetic-interference shielding. *Adv. Mater.* 29:1701583. doi: 10.1002/adma.201701583

Sun, H., Fu, C., Gao, Y., Guo, P., Wang, C., Yang, W., et al. (2018). Electrical property of macroscopic graphene composite fibers prepared by chemical vapor deposition. *Nanotechnol.* 29:305601. doi: 10.1088/1361-6528/aac260

Sundaram, R. M., Koziol, K. K. K., and Windle, A. H. (2011). Continuous direct spinning of fibers of single-walled carbon nanotubes with metallic chirality. *Adv. Mater.* 23, 5064–5068. doi: 10.1002/adma.201102754

Thess, A., Lee, R., Nikolaev, P., Dai, H., Petit, P., Robert, J., et al. (1996). Crystalline ropes of metallic carbon nanotubes. *Science* 273, 483–487. doi: 10.1126/science.273.5274.483

Tibbetts, G. G. (1985). Lengths of carbon filaments grown from iron catalyst particles in natural gas. *J. Cryst. Growth* 73, 431–438. doi: 10.1016/0022-0248(85)90005-3

Tsentalovich, D. E., Headrick, R. J., Mirri, F., Hao, J., Behabtu, N., Young, C. C., et al. (2017). Influence of carbon nanotube characteristics on macroscopic fiber properties. *ACS Appl. Mater. Interf.* 9, 36189–36198. doi: 10.1021/acsami.7b10968

Tsukamoto, J., Matsumura, K., Takahashi, T., and Sakoda, K. (1986). Structure and conductivity of graphite fibres prepared by pyrolysis of cyanoacetylene. *Synth. Metals* 13, 255–264. doi: 10.1016/0379-6779(86)90075-5

Uddin, M. J., Daramola, D. E., Velasquez, E., Dickens, T. J., Yan, J., Hammel, E., et al. (2014). A high efficiency 3D photovoltaic microwire with carbon nanotubes (CNT)-quantum dot (QD) hybrid interface. *Phys. Status Solidi. RRL* 8, 898–903. doi: 10.1002/pssr.201409392

Veedu, V. P., Cao, A. Y., Li, X. S., Ma, K. G., Soldano, C., Kar, S., et al. (2006). Multifunctional composites using reinforced laminae with carbon-nanotube forests. *Nat. Mater.* 5, 457–462. doi: 10.1038/nmat1650

Vishwakarma, R., Zhu, R., Abuelwafa, A. A., Mabuchi, Y., Adhikari, S., Ichimura, S., et al. (2019). Direct synthesis of large-area graphene on insulating substrates at low temperature using microwave plasma CVD. *ACS Omega* 4, 11263–11270. doi: 10.1021/acsomega.9b00988

Wang, G., Kim, S. K., Wang, M. C., Zhai, T., Munukutla, S., Girolami, G. S., et al. (2020). Enhanced electrical and mechanical properties of chemically cross-linked carbon-nanotube-based fibers and their application in high-performance supercapacitors. *ACS Nano* 14, 632–639. doi: 10.1021/acsnano.9b07244

Wang, J. N., Luo, X. G., Wu, T., and Chen, Y. (2014). High-strength carbon nanotube fibre-like ribbon with high ductility and high electrical conductivity. *Nat. Commun.* 5:3848. doi: 10.1038/ncomms4848

Wang, K., Frewin, C. L., Esrafilzadeh, D., Yu, C., Wang, C., Pancrazio, J. J., et al. (2019). High-performance graphene-fiber-based neural recording microelectrodes. *Adv. Mater.* 31:1805867. doi: 10.1002/adma.201805867

Xin, G., Zhu, W., Deng, Y., Cheng, J., Zhang, L. T., Chung, A. J., et al. (2019). Microfluidics-enabled orientation and microstructure control of macroscopic graphene fibres. *Nat. Nanotechnol.* 14, 168–175. doi: 10.1038/s41565-018-0330-9

Xu, F., Sadrzadeh, A., Xu, Z., and Yakobson, B. I. (2013a). Can carbon nanotube fibers achieve the ultimate conductivity? – Coupled-mode analysis for electron transport through the carbon nanotube contact. *J. Appl. Phys.* 114:063714. doi: 10.1063/1.4818308

Xu, Z., Liu, Z., Sun, H., and Gao, C. (2013b). Highly electrically conductive ag-doped graphene fibers as stretchable conductors. *Adv. Mater.* 25, 3249–3253. doi: 10.1002/adma.201300774

Xu, T., Zhang, Z. P., and Qu, L. T. (2019). Graphene-based fibers: recent advances in preparation and application. *Adv. Mater.* 32:1901979. doi: 10.1002/adma.201901979

Xu, Z., and Gao, C. (2015). Graphene fiber: a new trend in carbon fibers. *Mater. Today* 18, 480–492. doi: 10.1016/j.mattod.2015.06.009

Xu, Z., Liu, Y., Zhao, X., Peng, L., Sun, H., Xu, Y., et al. (2016). Ultrastiff and strong graphene fibers via full-scale synergetic defect engineering. *Adv. Mater.* 28, 6449–6456. doi: 10.1002/adma.201506426

Xu, Z., Zhang, Y., Li, P., and Gao, C. (2012). Strong, conductive, lightweight, neat graphene aerogel fibers with aligned pores. *ACS Nano* 6, 7103–7113. doi: 10.1021/nn3021772

Yadav, M. D., Dasgupta, K., Patwardhan, A. W., and Joshi, J. B. (2017). High performance fibers from carbon nanotubes: synthesis, characterization, and applications in composites – a review. *Ind. Eng. Chem. Res.* 56, 12407–12437. doi: 10.1021/acs.iecr.7b02269

Yan, J., Uddin, M. J., Dickens, T. J., Daramola, D. E., and Okoli, O. I. (2014). 3D wire-shaped dye-sensitized solar cells in solid state using carbon nanotube yarns with hybrid photovoltaic structure. *Adv. Mater. Interf.* 1:1400075. doi: 10.1002/admi.201400075

Yang, Z., Jia, Y., Niu, Y., Zhang, Y., Zhang, C., Li, P., et al. (2020). One-step wet-spinning assembly of twisting-structured graphene/carbon nanotube fiber supercapacitor. *J. En. Chem.* doi: 10.1016/j.jechem.2020.02.023

Yin, F., Hu, J., Hong, Z., Wang, H., Liu, G., Shen, J., et al. (2020). A review on strategies for the fabrication of graphene fibres with graphene oxide. *RSC Adv.* 10, 5722–5733. doi: 10.1039/C9RA10823H

Yu, D., Goh, K., Wang, H., Wei, L., Jiang, W., Zhang, Q., et al. (2014). Scalable synthesis of hierarchically structured carbon nanotube-graphene fibres for capacitive energy storage. *Nat. Nanotechnol.* 9, 555–562. doi: 10.1038/nnano.2014.93

Yun, Y. J., Ah, C. S., Hong, W. G., Kim, H. J., Shin, J.-H., and Jun, Y. (2017). Highly conductive and environmentally stable gold/graphene yarns for flexible and wearable electronics. *Nanoscale* 9, 11439–11445. doi: 10.1039/C7NR04384H

Zeng, J., Ji, X., Ma, Y., Zhang, Z., Wang, S., Ren, Z., et al. (2018). 3D graphene fibers grown by thermal chemical vapor deposition. *Adv. Mater.* 30:1705380. doi: 10.1002/adma.201705380

Zhang, J., and Fahrenthold, E. P. (2019). Potassium-doped graphene nanoribbons for high-specific conductivity wiring. *ACS Appl. Nano Mater.* 2, 2873–2880. doi: 10.1021/acsanm.9b00327

Zhang, L., Wang, J., Fuentes, C. A., Zhang, D., Van Vuure, A. W., Seo, W. J., et al. (2017a). Wettability of carbon nanotube fibers. *Carbon* 122, 128–140. doi: 10.1016/j.carbon.2017.06.027

Zhang, S., Park, G. J., Nguyen, N., Jolowsky, C., Hao, A., and Liang, R. (2017b). Ultra-high conductivity and metallic conduction mechanism of scale-up continuous carbon nanotube sheets by mechanical stretching and stable chemical doping. *Carbon* 125, 649–658. doi: 10.1016/j.carbon.2017.09.089

Zhang, M., Atkinson, K. R., and Baughman, R. H. (2004). Multifunctional carbon nanotube yarns by downsizing an ancient technology. *Science* 306, 1358–1361. doi: 10.1126/science.1104276

Zhang, M., Fang, S., Zakhidov, A. A., Lee, S. B., Aliev, A. E., Williams, C. D., et al. (2005). Strong, transparent, multifunctional, carbon nanotube sheets. *Science* 309, 1215–1219. doi: 10.1126/science.1115311

Zhang, S., Nguyen, N., Leonhardt, B., Jolowsky, C., Hao, A., Park, J. G., et al. (2019). Carbon-nanotube-based electrical conductors: fabrication, optimization, and applications. *Adv. Ener. Mater.* 5:1800811. doi: 10.1002/aelm.201800811

Zhang, X., Li, Q., Holesinger, T. G., Arendt, P. N., Huang, J., Kirven, P. D., et al. (2007). Ultrastrong, stiff, and lightweight carbon-nanotube fibers. *Adv. Mater.* 19, 4198–4201. doi: 10.1002/adma.200700776

Zhao, Y., Wei, J., Vajtai, R., Ajayan, P. M., and Barrera, E. V. (2011). Iodine doped carbon nanotube cables exceeding specific electrical conductivity of metals. *Sci. Rep.* 1:83. doi: 10.1038/srep00083

Zheng, B., Gao, W., Liu, Y., Wang, R., Li, Z., Xu, Z., et al. (2020). Twist-spinning assembly of robust ultralight graphene fibers with hierarchical structure and multi-functions. *Carbon* 158, 157–162. doi: 10.1016/j.carbon.2019.11.072

Zhong, X. H., Li, Y. L., Liu, Y. K., Qiao, X. H., Feng, Y., Liang, J., et al. (2010). Continuous multilayered carbon nanotube yarns. *Adv. Mater.* 22, 692–696. doi: 10.1002/adma.200902943

Zhou, E., Xi, J., Liu, Y., Xu, Z., Guo, Y., Peng, L., et al. (2017). Large-area potassium-doped highly conductive graphene films for electromagnetic interference shielding. *Nanoscale* 9, 18613–18618. doi: 10.1039/c7nr07030f

Conflict of Interest: The authors declare that the research was conducted in the absence of any commercial or financial relationships that could be construed as a potential conflict of interest.

GLOSSARY

AC, alternating current; AFM, atomic force microscopy; CFs, carbon fibers; CNFs, carbon nanofibers; CNT fibers, carbon nanotube fibers; CNTs, carbon nanotubes; C_{sp}, specific capacitance; CVD, chemical vapor deposition; DC, direct current; DSSC, dye sensitized solar cell; DWCNTs, double-walled carbon nanotubes; EMI, electromagnetic interference (shielding); FET, field-effect transistor; FIB, focused ion beam, GFs, graphene fibers; GICs, graphite intercalation compounds; GO, graphene oxide; GR, graphene; I_D, D-band Raman intensity of graphitic materials; I_G, G-band Raman intensity of graphitic materials; LED, light-emitting diode; MWCNTs, multi-walled carbon nanotubes; PAN, Polyacrylonitrile; PECVD, plasma-enhanced chemical vapor deposition; RBM, radial breathing mode; rGO, reduced graphene oxide; RTM, radial tangential mode; SAXS, small-angle X-ray scattering; SEC, specific electrical conductivity; SEM, scanning electron microscopy; STC, specific thermal conductivity; SWCNTs, single-walled carbon nanotubes; TEM, transmission electron microscopy; TGA, termogravimetric analysis; UV-Vis (spectroscopy), UV-visible (spectroscopy) VGCFs, vapor grown carbon fibers; WAXS, wide-angle X-ray scattering; XPS (spectroscopy), X-ray photoelectron (spectroscopy); XRD, X-ray diffraction; XRT, X-ray tomography.

frontiers in Materials

ORIGINAL RESEARCH
published: 22 September 2020
doi: 10.3389/fmats.2020.00259

Molten Salt Synthesized Submicron Perovskite $La_{1-x}Sr_xCoO_3$ Particles as Efficient Electrocatalyst for Water Electrolysis

*Swati Mohan[1] and Yuanbing Mao[2]**

[1] Department of Chemistry, University of Texas at Rio Grande Valley, Edinburg, TX, United States, [2] Department of Chemistry, Illinois Institute of Technology, Chicago, IL, United States

Perovskite oxides are an important and effective class of mixed oxides which play a significant role in the fields of energy storage and conversion systems. Here we present a series of cobaltite perovskite $LaCoO_3$ particles which have been doped with 0, 5, 10, 20, and 30% of Sr^{2+} and have been synthesized by a combined sol–gel and molten-salt synthesis procedure, which provides a regular morphology of the particles. These Sr^{2+}-doped $LaCoO_3$ particles have been characterized by powder X-ray diffraction, Raman spectroscopy, infrared spectroscopy, X-ray photoelectron spectroscopy, and scanning electron microscopy. Moreover, these Sr^{2+} doped $LaCoO_3$ particles have been demonstrated as efficient catalysts for oxygen evolution reaction (OER) based on the measured specific capacitance, total charge, most accessible charge, electrochemically active surface area, and roughness factor using rotating disk and rotating ring-disk electrode techniques. The 30% Sr^{2+}-doped $LaCoO_3$ sample shows enhanced electrocatalytic OER activity in 0.5 M H_2SO_4 media compared to the $LaCoO_3$ samples doped with 0, 5, 10, and 20% Sr^{2+}. Among all five $LaCoO_3$ samples, the doped $LaCoO_3$ samples demonstrate better OER activity than the undoped sample.

Keywords: $LaCoO_3$, sol-gel, molten-salt synthesis, electrocatalysis, OER, Sr^{2+}-doped

OPEN ACCESS

Edited by:
Zhenhai Xia,
University of North Texas,
United States

Reviewed by:
Tianhua Zhou,
Fujian Institute of Research on the Structure of Matter (CAS), China
Sajib K. Barman,
University of Texas at Arlington,
United States

****Correspondence:***
Yuanbing Mao
ymao17@iit.edu

Specialty section:
This article was submitted to Energy Materials, a section of the journal Frontiers in Materials

Received: *08 January 2020*
Accepted: *15 July 2020*
Published: *22 September 2020*

Citation:
Mohan S and Mao Y (2020) Molten Salt Synthesized Submicron Perovskite $La_{1-x}Sr_xCoO_3$ Particles as Efficient Electrocatalyst for Water Electrolysis. Front. Mater. 7:259. doi: 10.3389/fmats.2020.00259

INTRODUCTION

Growing environmental and geopolitical problems have been arising from the shortage of fossil fuel, promoting efforts to develop cheap, ample, and eco-friendly materials for advanced energy conversion and storage systems. In water electrolysis, the overpotential requirement is a serious issue at which oxygen evolution reaction (OER) occurs (Huynh and Meyer, 2007; Yeo and Bell, 2011). Therefore, it is a significant challenge to design active electrocatalysts for water electrolysis to meet the demands of the sustainable energy-powered economy (Loi and Hummelen, 2013). On the other hand, the global use of noble metal oxides like ruthenium and iridium oxides, especially in the field of catalysis, requires us to minimize the use of these noble metal oxides and to introduce new types of materials, e.g., perovskite oxides. Perovskites are fascinating alternatives to noble metals because of their catalytic activity and cost-effectiveness (Gasteiger et al., 2005; Jörissen, 2006; Neburchilov et al., 2010).

Perovskite oxides have the general formula of ABO_3, where A is lanthanide, alkaline-earth, or alkaline cations, and B is transition metal cations such as Fe, Mn, Co, Cr, or Ti. Perovskite

oxides can be customized with chemical and physical properties due to the exceptional tunability of their structure and composition. They are a type of mixed oxide and are a class of materials that show a remarkable electronic structure, redox behavior, ionic and electronic activity, and thermal stability (Pena and Fierro, 2001; Schaak and Mallouk, 2002; Royer et al., 2014; Zhu et al., 2014). Perovskites with multiple A or B cations of difference sizes and valences have distortion in their crystal structure. Doping of A or B cations of perovskite with elements of Ce, Ba, or Sr creates oxygen vacancies and increases oxygen mobility (Nitadori and Misono, 1985; Nitadori et al., 1986; de la Cruz et al., 2001; Mefford et al., 2014). In perovskites, the cations present on A and B sites play a crucial role in altering its electronic structure and tuning catalytic properties (JO'M et al., 1983; Bockris and Otagawa, 1984; Vojvodic and Nørskov, 2011; Mueller et al., 2015).

Due to their slow reaction kinetics, both OER and oxygen reduction reaction (ORR) need electrocatalysts. Pt and Pt-alloys are the most essential catalysts for ORR while the Ir and Ru-based materials are good OER catalysts (Gupta et al., 2009; Slanac et al., 2012; Cui et al., 2013; Mefford et al., 2016). Many research studies based on perovskites for OER and ORR have been focused on structural and electronic properties of the surface or bulk (Otagawa and Bockris, 1983; Bockris and Otagawa, 1984; Matsumoto and Sato, 1986). Over the past 40 years, $La_{0.8}Sr_{0.2}CoO_3$ has been studied to give different mechanistic theories as an active catalyst for ORR (Meadowcroft, 1970). For example, Hong et al. (2015) summarized the OER activity by showing correlations between the surface and bulk properties of metal oxides and their electrocatalytic activities. This study showed that the substitution of La^{2+} by Sr^{2+} to maintain the perovskite structure following the effects of vacancy defects, covalency, and oxygen exchange on the electrode surface during the electrocatalysis of OER. LSCO ($LaSrCoO_3$) electrocatalysis in alkaline media showed good structural stability, electrolytic corrosion resistance, and high activities for ORR and OER (Jasem and Tseung, 1979; Gorlin and Jaramillo, 2010; McCrory et al., 2013).

There are several procedures to synthesize Sr^{2+}-doped $LaCoO_3$, such as solid-state synthesis (Li et al., 2002), sol–gel (Patel and Patel, 2012), chemical vapor deposition (CVD; Armelao et al., 2005), spray-freeze drying (Lee et al., 2006), aqueous gel-casting technique (Cheng et al., 2008), thermal decompositions (Kaituo et al., 2014), precipitation (Singh and Rakesh, 2009), combustion (Luo and Liu, 2007), low pressure plasma synthesis (Rousseau et al., 2007), etc. In terms of morphology control of products, many of these methods are not sufficient, including the solid-state route and sol–gel method. Molten-salt synthesis method is a simple, reliable, eco-friendly, and cost-effective method when compared to the methods mentioned above. To obtain undoped and Sr^{2+}-doped $LaCoO_3$ particles with a controlled and regular morphology, we introduced a new combination of sol-gel and molten-salt synthesis procedure in this work. Furthermore, we studied their catalytic applications of OER.

Specifically, we successfully synthesized uniform $LaCoO_3$ particles with 0, 5, 10, 20, and 30% Sr^{2+} nominal doping levels using our facile and reliable method. We characterized their composition, morphology, and structure by powder X-ray diffraction (XRD), Raman spectroscopy, infrared spectroscopy, X-ray photoelectron spectroscopy, X-ray energy dispersive spectroscopy, and scanning electron microscopy. More importantly, their electrocatalytic performance for OER in acidic 0.5 M H_2SO_4 media was investigated systematically using rotating disk and rotating ring-disk electrode techniques in terms of specific capacitance, total charge, most accessible charge, electrochemically active surface area, and roughness factor. The 30% Sr^{2+}-doped $LaCoO_3$ sample showed the highest electrocatalytic OER activity compared to the $LaCoO_3$ samples doped with 0, 5, 10, and 20% Sr^{2+}. Among all five $LaCoO_3$ samples, the doped $LaCoO_3$ samples demonstrate a better OER activity than the undoped sample. Therefore, this study proves that the combined sol–gel and molten-salt synthesis method is a novel and desirable method to prepare $LaCoO_3$ particles with a uniform morphology and enhanced OER activity in acidic media.

EXPERIMENTAL SECTION

Materials and Synthesis

The Sr^{2+}-doped $LaCoO_3$ samples were prepared as follows using the combined sol–gel and molten-salt method synthesis process. Specifically, in a representative synthesis, a stoichiometric amount of $La(NO_3)_3{\cdot}6H_2O$, $Sr(NO_3)_3$ and $Co(NO_3)_2{\cdot}6H_2O$ on a 1 mM scale were added into 10 ml distilled water. After stirring for 2 h at room temperature, polyvinyl alcohol (PVA) aqueous solution (20 wt%) was added. After further stirring, the obtained sol was dried in an oven at 80°C for 2 h, followed by 120°C on a hot plate overnight. During the molten-salt synthesis step, 0.23 g dried gel of each of the five samples was first mixed with 60 mM of $NaNO_3 + KNO_3$ mixture (1:1) and then ground together in a mortar and pestle for 20 min (Zuniga et al., 2018). The resulting mixture was transferred into a crucible and kept at 700°C for 6 h with a ramp-up rate of 15° min^{-1} and cooling-down rate of 10°C min^{-1}. In the final step, the annealed products were washed with deionized water several times and dried in an oven at 60°C overnight. The prepared $LaCoO_3$ samples doped with 0, 5, 10, 20, and 30% Sr^{2+} were denoted as LSCO0%, LSCO5%, LSCO10%, LSCO20%, and LSCO30%, respectively.

Materials Characterization

The samples were characterized by powder XRD on a Rigaku-Miniflex^{TM} II X-ray diffractometer with Cu $K_{\alpha 1}$ radiation (λ = 0.15406 nm). The XRD data were collected using a scanning mode in the 2θ range from 20° to 80° with a scanning step size of 0.04° and a scanning rate of 4.0° min^{-1}. Raman scattering data was recorded by employing the back-scattering geometries on a Bruker SENTERRA RAMAN microscope with an objective of 20× of an optical microscope. The excitation line (785 nm) of an Ar+ laser beam was focused to a spot size of 5 μm with a laser power of 25 mW. The spectral resolution range used was 3–5 cm^{-1} with an integration time of 100 s. Infrared spectra were recorded on a Thermal Nicolet Nexus 470 spectrometer. The morphology of the LSCO samples was observed by a field

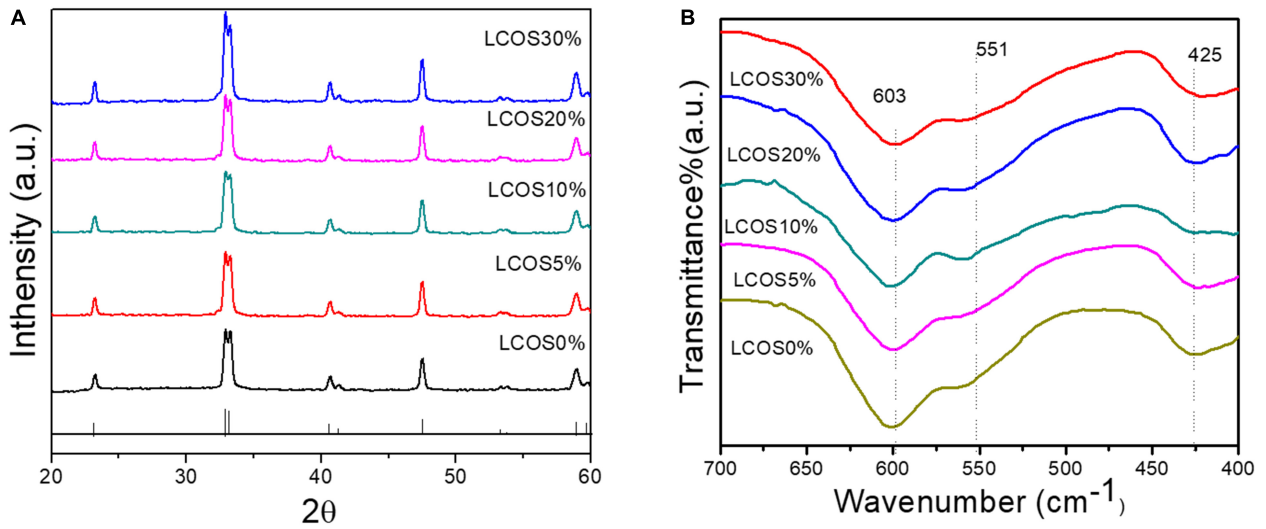

FIGURE 1 | (A) Powder XRD patterns and **(B)** FTIR spectra of the LSCO0%, LSCO5%, LSCO10%, LSCO20%, and LSCO30% samples. The pattern shown at the bottom of **(A)** is the standard pattern (JCPDS # 251060) of LCO with a tetragonal crystal structure.

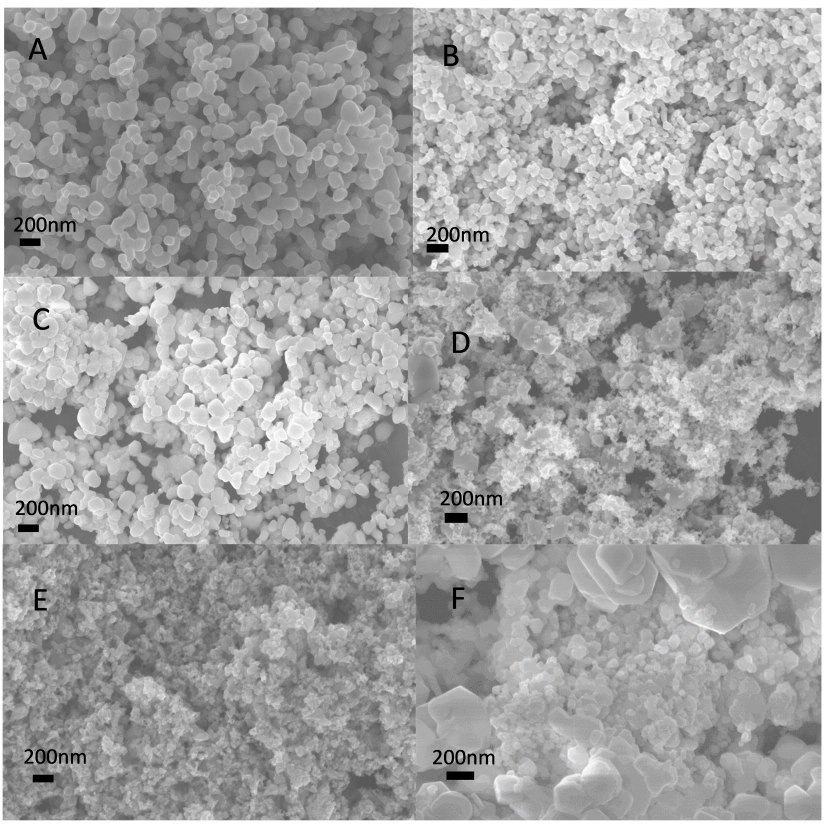

FIGURE 2 | SEM images of the LSCO samples: **(A)** LSCO0%, **(B)** LSCO5%, **(C)** LSCO10%, **(D)** LSCO20%, and **(E)** LSCO30% synthesized via the combined sol–gel and molten-salt procedure, and **(F)** LSCO0% via the conventional sol–gel process with direct calcination.

emission scanning electron microscope (SEM, Carl Zeiss Sigma VP FESEM) equipped with a field emission gun operated at 5 kV.

Electrode Preparation and Electrochemical Measurement

Three-electrode electrochemical cell configuration was used (Mohan and Mao, 2018; Mao et al., 2019). The working electrode was the catalyst-coated glassy carbon electrode with an area of 0.5024 cm^2; a platinum wire was used as the counter electrode and the Ag/AgCl electrode as the reference electrode. To prepare the working electrode, we first prepared the catalyst ink by dispersing 1 mg of the LSCO catalyst powder as active material in 362 μL water and 57 μL Nafion solution by sonication for 20 min. In the next step, we took 42 μL of the prepared catalyst ink, cast it onto the surface of the glassy carbon electrode which corresponds to 0.38 mg/cm^2, and dried it in a vacuum oven overnight. The electrochemical measurements, including cyclic voltammogram (CV) and linear sweep voltammogram (LSV), were performed in 0.5 N H_2SO_4(aq) electrolyte which was purged with nitrogen gas for 10 min prior to the electrochemical measurements to remove the dissolved air from the electrolyte toward the OER using an Autolab potentiostat/galvanostat (PGSTAT302) with Nova 10.11 software. Current density was evaluated as a function of applied voltage from the range of 0.4–1 V versus the Ag/AgCl at scan rates of 5, 10, 20, 50, 70, and 100 mV/s for CV characterization. Linear sweep voltammogram was done at a scan rate of 5 mV/s for all five catalysts in terms of OER.

RESULTS AND DISCUSSION

Materials Characterization

Figure 1A shows the XRD patterns of the synthesized samples of LSCO0%, LSCO5%, LSCO10%, LSCO20%, and LSCO30%. The observed reflections could be perfectly indexed with the peaks of (0 1 2), (1 1 0), (1 0 4), (2 0 2), (0 0 6) (0 2 4), (1 2 2), and (2 1 4) on the basis of tetragonal crystal structure (JCPDS file #251060). The XRD of all five catalysts were found to be crystalline in nature. In addition to XRD data, evidence regarding the chemical composition of the synthesized products was obtained from IR spectra (**Figure 1B**). The observed FTIR absorption band at ∼603 cm^{-1} could be assigned to the vibration of the Co–O bond in an octahedral coordination while the band observed at ∼551 cm^{-1} for La(Sr)–O bond stretching. Furthermore, the vibration of the La–O bond in a dodecahedral coordination was confirmed by the presence of a strong peak at 425 cm^{-1} (Khalil, 2003; Mahmood et al., 2013; Agilandeswari and Ruban Kumar, 2014).

SEM images of the as-synthesized LSCO samples show the formation of submicron globules as first reported for LSCO (**Figures 2A–E**). We also prepared a LSCO0% sample by

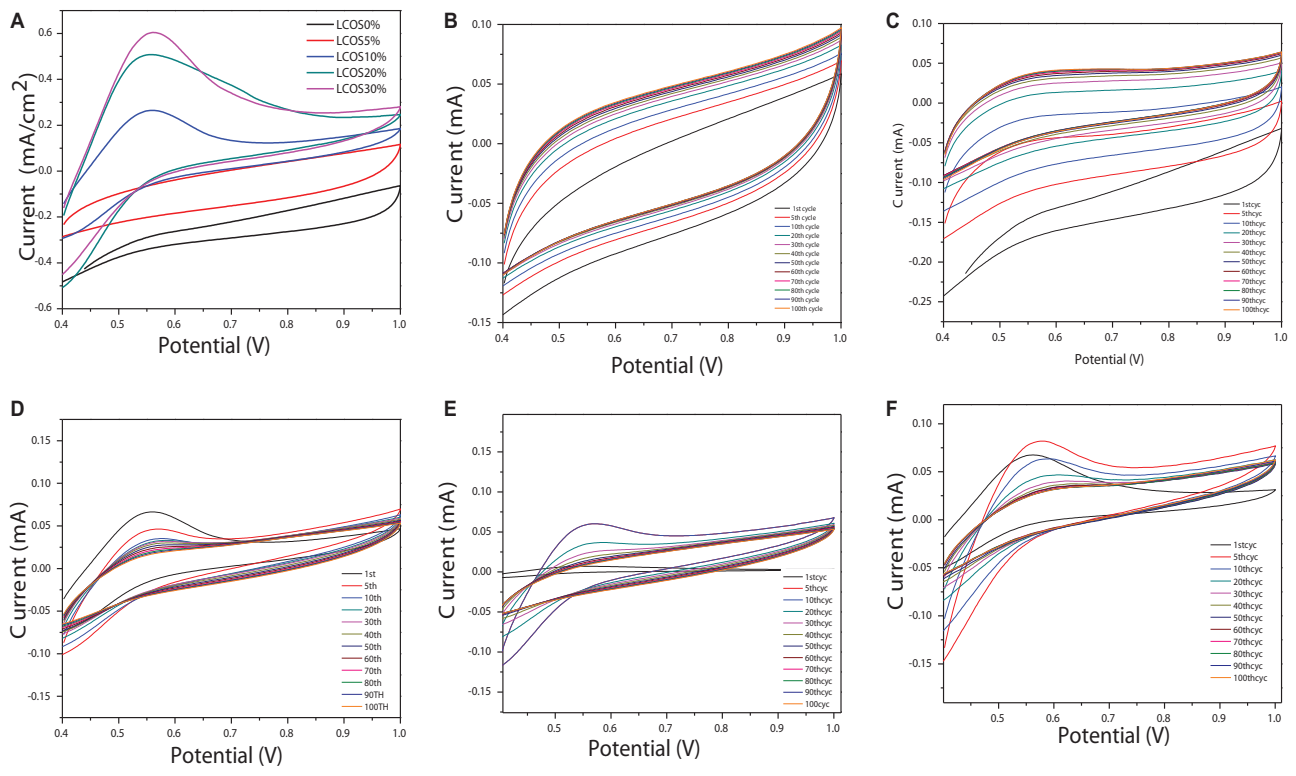

FIGURE 3 | (A) CV plots versus RHE of the LSCO-coated electrodes in 0.5 M H_2SO_4 electrolyte recorded at 50 mV/s and 25°C and normalized to the geometric area of the electrode. Overlay CV plots of the 1st, 5th, 10th, 20th, 30th, 40th, 50th, 60th, 70th, 80th, 90th, and 100th cycles of the **(B)** LSCO0%, **(C)** LSCO5%, **(D)** LSCO10%, **(E)** LSCO20%, and **(F)** LSCO30% at 0.5 M H_2SO_4 electrolyte during repetitive potential cycles at 20 mV/s and 25°C.

TABLE 1 | Calculated specific capacitance of the LSCO0%, LSCO5%, LSCO10%, LSCO20%, and LSCO30% samples at scan rates of 5, 10, 20, 50, 70, and 100 mV/s.

Scan rate (mV/s)	Specific capacitance (F/g)				
	LSCO0%	**LSCO5%**	**LSCO10%**	**LSCO20%**	**LSCO30%**
5	0.013285	0.096237	0.202794	0.216114	0.153646
10	0.113586	0.756654	1.054873	1.077412	0.809768
20	0.095984	0.455375	0.562605	0.555099	0.425452
50	0.054455	0.215751	0.257138	0.235581	0.186782
70	0.040588	0.165006	0.193801	0.174456	0.122107
100	0.036369	0.127018	0.143689	0.130235	0.074329

TABLE 2 | Voltammetry charges (q^*) of the LSCO0%, LSCO5%, LSCO10%, LSCO20%, and LSCO30% samples at scan rates of 5, 10, 20, 50, 70, and 100 mV/s.

Scan rate (mV/s)	q^*				
	LSCO0%	**LSCO5%**	**LSCO10%**	**LSCO20%**	**LSCO30%**
5	0.010637	0.115024	0.242383	0.258304	0.18364
10	0.013576	0.090437	0.12608	0.128774	0.096785
20	0.011472	0.054427	0.067244	0.066346	0.050851
50	0.006509	0.025787	0.030734	0.028157	0.022325
70	0.004851	0.019722	0.023164	0.020851	0.014594
100	0.010637	0.015181	0.017174	0.015566	0.008884

TABLE 3 | Comparison between the total charge, outer charge, and charge accessibility of the LSCO0%, LSCO5%, LSCO10%, LSCO20%, and LSCO30% samples.

Catalyst	q^*_{total} (mC)	q^*_{outer} (mC)	Accessibility (q^*_{outer}/q^*_{total})
LSCO0%	33.6	0.002625	0.000078
LSCO5%	5.474	0.0057	0.00104
LSCO10%	4.68	0.01567	0.0033
LSCO20%	1.4160	0.0206	0.0145
LSCO30%	0.765	0.00932	0.0128

direct calcination of the sol-gel precursor (i.e., the dry gel was not treated with the molten-salt process) for comparison. As commonly observed from samples synthesized by the sol–gel process, the obtained LSCO0% product shows an irregular morphology and larger particles (**Figure 2F**). Therefore, in terms of product morphology, these SEM images confirm that our combined sol–gel and molten-salt synthesis process is better than the conventional sol–gel process.

Electrochemical Characterization

The CV curves of all LSCO catalysts modified as working electrodes (**Figure 3A**) exhibits a characteristic shape with the presence of the anodic and cathodic peak at a potential range of 0.4–1 V vs reversible hydrogen electrode (RHE), indicating a nonreversible reaction (Mohan and Mao, 2018; Mao et al., 2019). Also, the LSCO30% sample showed the highest current density and the LSCO0% showed the lowest current density among the five samples.

To find out charge accumulation at the electrode/catalyst interface and to evaluate electrode capacity, capacitance measurements were conducted. The two electrochemical contribution faradic and proton adsorption processes are not integrated at the chosen potential range from 0.4 to 1 V. To avoid faradic contribution, we calculated specific capacitance (C, F/g) here for all LSCO catalysts by integrating the CV curves between 0.4 and 1 V vs RHE at scan rates of 5, 10, 20, 50, 70, and 100 mV/s using Eq. 1:

$$C = \frac{1}{\gamma m(E_2 - E_1)} \int_{E_1}^{E_2} i\,(E)\,\mathrm{d}E \tag{1}$$

where γ is the scan rate (V/s), m is the mass in grams of the catalyst deposited on the working electrode, E_1 and E_2 are limits of potentials of the integration curves, and $\int_{E_1}^{E_2} i\,(E)\,\mathrm{d}E$ is the integration of the CV curve. From the calculated specific capacitance values tabulated in **Table 1**, we can see that the capacitance values decrease for all five LSCO catalysts with an increasing scan rate. This observation indicates that the double layer formation is more consistent in a quasi-stationary mode (Sugimoto et al., 2006; Devadas et al., 2011). The diffusion of active species can occur even in miniature pores, thereby all of the active sites of the LSCO samples contribute to the double layer formation. However, at a high scan rate, the charge accumulation occurs only on the active surface sites. The diffusion effect limits the migration of electrolytic ions and causes some active surface areas to be inaccessible for charge storage.

The calculated specific capacitance values of the LSCO0% and LSCO5% samples are lower than those obtained for the LSCO10% and LSCO30% samples, while those from the LSCO20% sample showed the highest values. Overall, the specific capacitance values of our LSCO samples are in the order of LSCO20% > LSCO30% > LSCO10% > LSCO5% > LSCO0%. Specific capacitance indicates the stability of the catalysts

on the electrode surface or due to morphology change making the catalysts less accessible to charges (Ardizzone et al., 1990). The increase of capacitance can also be correlated to the higher oxidation state of metallic ions in metal oxides (Ardizzone and Trasatti, 1996). Therefore, to improve the charge accumulation, it is important to increase the number of active sites and their accessibilities. For our LSCO samples, the presence of a well-defined morphology and he miniature size of the formed submicron particles refers to the high concentration of active sites at the electrolyte/catalyst interface with a large oxidation state change, and therefore improved capacitive properties (Mohan and Mao, 2018).

Generally, the number of catalyst active sites or active surface areas are considered proportional to voltammetry charges q^* (Ardizzone et al., 1990; Wu et al., 2011). Calculation of q^* is determined following Eq. 2 as reported by Audichon et al. (2014), Mohan and Mao (2018), Mao et al. (2019).

$$q* = \frac{1}{\gamma ms} \int_{E_1}^{E_2} i\,(E)\,\mathrm{d}E \tag{2}$$

Briefly, q^* value is the average of anodic and cathodic charges measured between 0.4 and 1 V vs RHE. The calculated q^* values for the LSCO0%, LSCO5%, LSCO10%, LSCO20%, and LSCO30% samples are summarized in **Table 2**.

Ardizzone and co-workers established two relations as following Eqs 3 and 4 which depend on the basis of diffusion species phenomena at the interface of the electrode/electrolyte depending on the scan rate (Ardizzone et al., 1990).

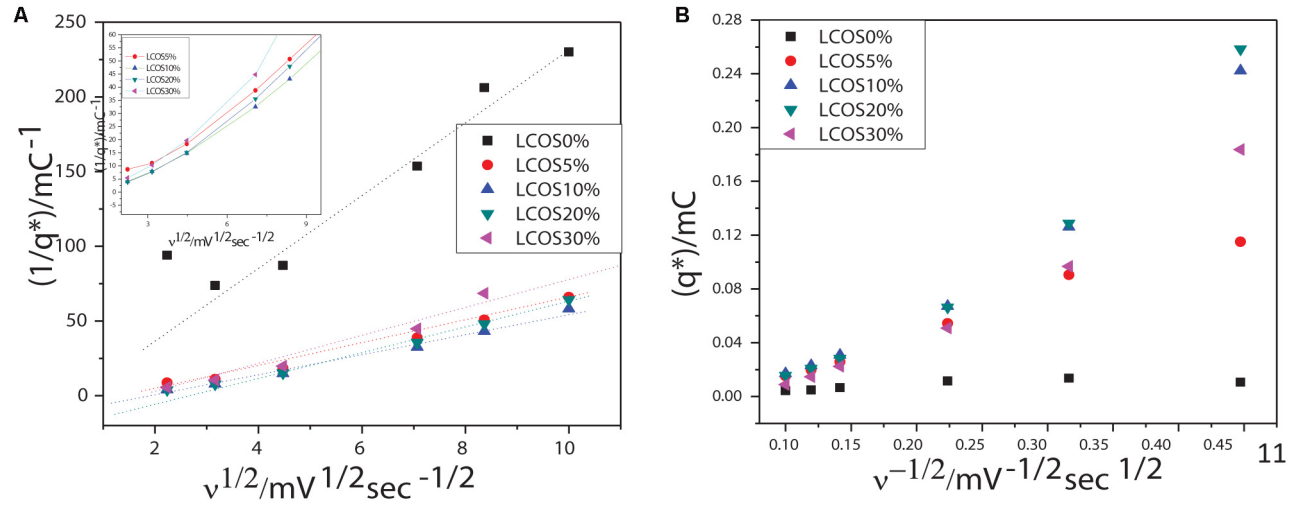

FIGURE 4 | Scan rate dependency of voltammetric charges: extrapolations of **(A)** the total charges (q^*_{total}) and **(B)** the most accessible charges (q^*_{outer}) of the LSCO0%, LSCO5%, LSCO10%, LSCO20%, and LSCO30% samples.

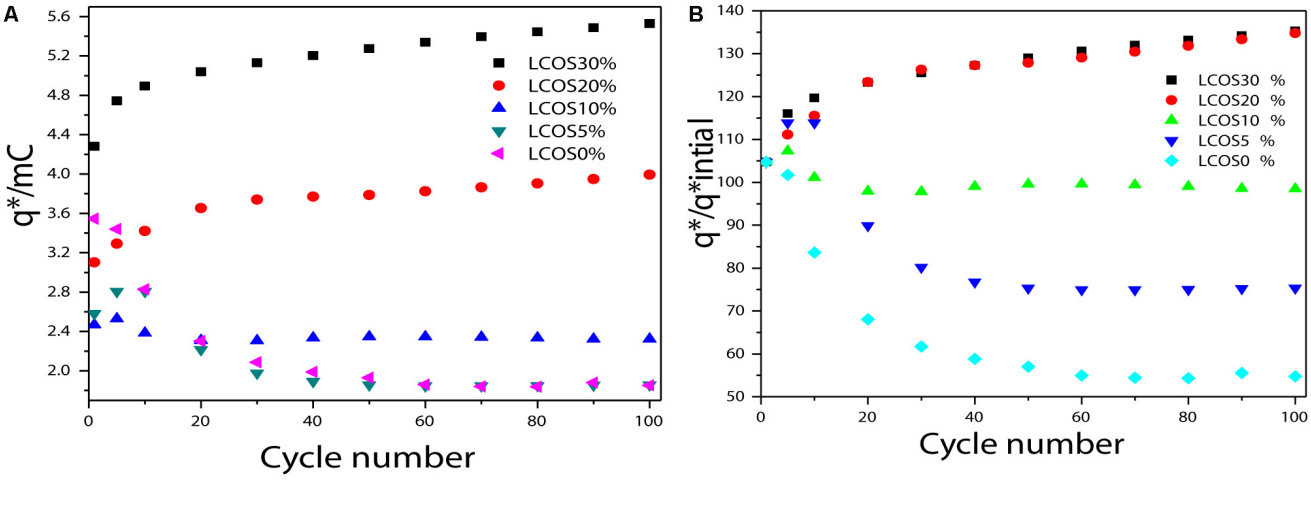

FIGURE 5 | (A) Charge (q^*) evolution and **(B)** $q^*/q^*_{initial}$ ratio of the LSCO0%, LSCO5%, LSCO10%, LSCO20%, and LSCO30% electrocatalysts during a stability test measurement.

Following Eqs 3 and 4, the total charges (q^*_{total}) and the most accessible charges (q^*_{outer}) were determined when the scan rate values tend to 0 and ∞, respectively (Cheng et al., 2009).

$$q* = q*_{\text{outer}} + C1\frac{1}{\sqrt{\gamma}}. \quad (3)$$

$$\frac{1}{q*} = \frac{1}{q*_{\text{total}}} + C2\sqrt{\gamma}. \quad (4)$$

where C_1 and C_2 are constants, v is the scan rate, and q^* are the average charges calculated for different scan rates included between 5 to 100 mV/s. The q^*_{total} and q^*_{outer} values

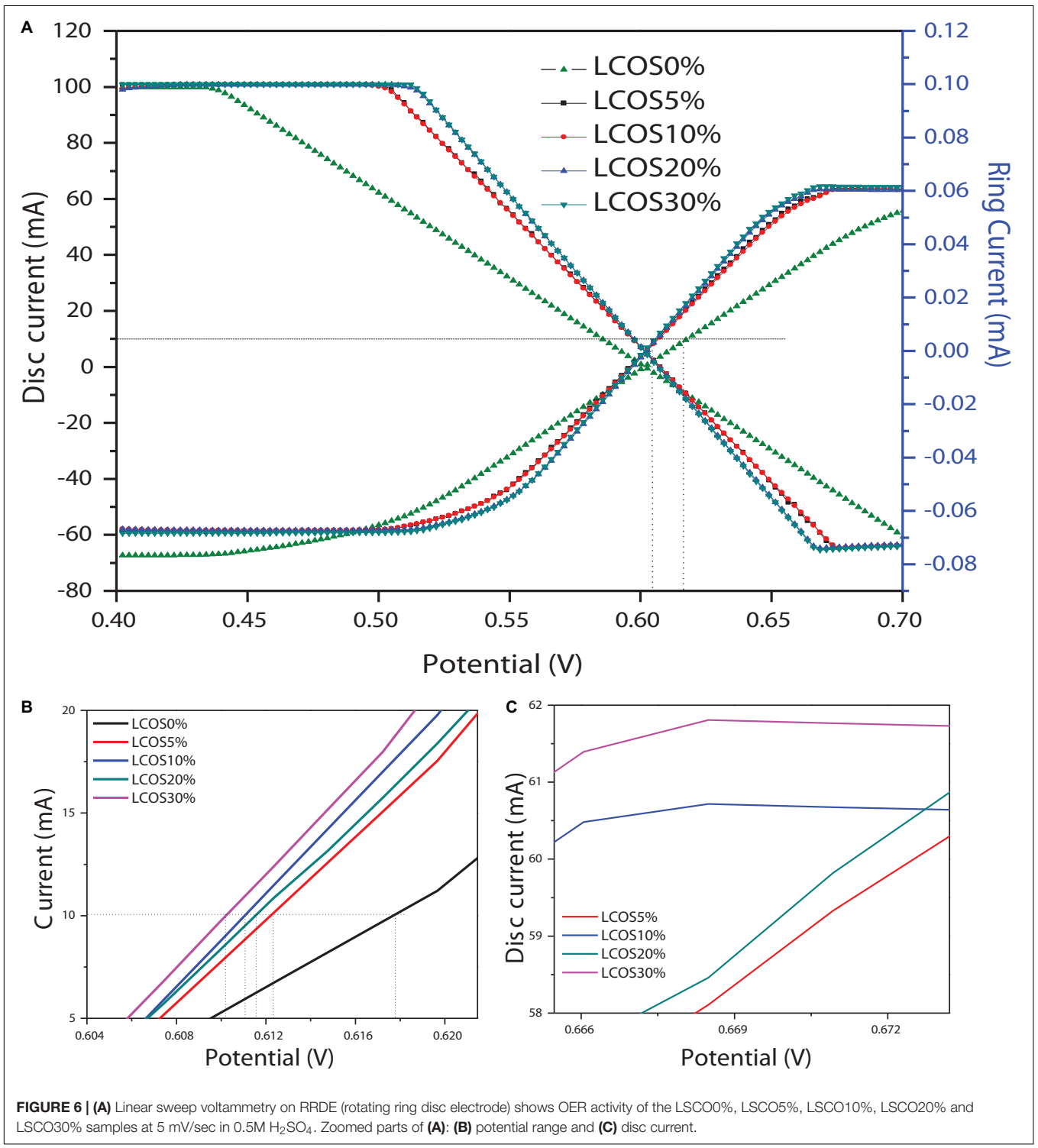

FIGURE 6 | (A) Linear sweep voltammetry on RRDE (rotating ring disc electrode) shows OER activity of the LSCO0%, LSCO5%, LSCO10%, LSCO20% and LSCO30% samples at 5 mV/sec in 0.5M H_2SO_4. Zoomed parts of **(A)**: **(B)** potential range and **(C)** disc current.

for crystalline oxides samples are obtained by linear part extrapolations of the curves presented in **Figure 4** and are summarized in **Table 3**.

The calculated total charges q^*_{total} of the LSCO30% (0.765 mC) and LSCO20% (1.416 mC) samples synthesized by the combined sol–gel and molten-salt process are the lowest compared with the LSCO0% (33.6 mC), LSCO5% (5.47 mC), and LSCO10% (4.68 mC) samples. The supposition established from the capacitance measurements therefore confirms that the number of active sites increases and promotes the charge accumulation properties of the catalyst when the mean crystallite size decreases. The highest value for the most accessible charge q^*_{outer} was obtained for the LSCO20% sample (0.0206 mC), followed by the LSCO10% (0.0156 mC), LSCO30% (0.009 mC), LSCO5% (0.005 mC) samples, and then the LSCO0% sample (0.0026 mC). The synthesized LSCO20% sample has allowed one to obtain a higher number of accessible active sites in the catalytic layer, which is probably due to the higher concentration of active sites on the surface and the stability of the catalyst at the electrode surface. Moreover, from the obtained charge values, the active site's accessibility was evaluated by the ratio q^*_{outer}/q^*_{total} (**Table 2**). The highest active site's accessibility was obtained from the LSCO20% sample (0.0145) and followed by the LSCO30% (0.0128), LSCO10% (0.0033), and LSCO5% (0.00104) samples, whereas the one with the lowest q^*_{outer}/q^*_{total} ratio was measured from the LSCO0% sample (0.000078).

Stability Test

Repetitive CV measurement was achieved to assess these oxide samples' electrochemical activity and stability (Cheng et al., 2009). As shown in **Figure 3**, **100** voltammetric cycles were carried out between 0.4 and 1 V vs RHE in 0.5 mol l^{-1} H_2SO_4 at 20 mV s^{-1} with the aim of evaluating these catalysts' aging during a long-term test through their current density evolution.

For the five LSCO catalyst samples (**Figure 3**) no modification of the CV shapes appears during the long term 100 cycle test. This observation indicates that no alteration of the particles' structure, which composed the catalytic layer, occurs during the test. However, the current densities decrease during the first cycles and finally tend to stabilize. The fact that the cathodic and anodic current densities do not evolve drastically and no extra peaks appear reveals a high stability of the obtained LSCO oxide samples after heat treatment under variable transient conditions. The corresponding CVs of the synthesized LSCO samples overlap between the 5th and 10th cycles (**Figure 5**). The evolution of the current during the test could arise from a slight loss of active sites in the catalytic layer, which could contribute to a small catalytic performance decrease.

For different cycles of this stability test, the charge values (q^*) were measured to quantify the active-sites losses and the degradation of the electrocatalytic performances (**Figure 5**). According to the agreement with the CV observations, the calculated charges decrease in the first activation time (first 5–10 cycles). For the LSCO30%, LSCO20% and LSCO10% samples, the decrease takes place until the 10th cycle whereas for the LSCO5% and LSCO0% catalysts, it is less significant and occurs only for the first five cycles.

As the charges are considered to be proportional to the number of active sites, the $q^*/q^*_{initial}$ ratio as a function of the number of cycles may be used to evaluate the active site losses (**Figure 5**). The remaining active sites after 50 cycles for the LSCO0%, LSCO5%, LSCO10%, LSCO20%, and LSCO30% samples are 84, 93, 92, 86, and 92% of the initial charges, respectively. As the CV shapes remain the same along the durability test, the charge ratio evolution could be attributed to the degradation of the catalytic layers, due to a slight erosion of the catalyst at the interface with the electrolyte (Da Silva et al., 1997).

Catalyst Used for OER Measurement

The OER activity of the LSCO samples was evaluated primarily by rotating ring disk electrode voltammetry (RRDE) at a 0.05 mV/s scan rate and 1600 rpm rotation rate. This scan rate is slow enough for steady-state behavior at the electrode surface, and the rotation rate is sufficiently fast to aid in product removal and limit bubble formation from evolved O_2 at the electrode surface. As shown in **Figure 6A**, the horizontal dashed line at 10 mA cm^{-2} per geometric area is a significant figure of merit for the electroactive catalyst (Weber and Dignam, 1984; Matsumoto and Sato, 1986; Gorlin and Jaramillo, 2010; Walter et al., 2010). To evaluate the electrocatalytic properties of the oxide materials toward the OER as well as their behavior during this reaction, linear sweep voltammetry measurements were performed. For our LSCO samples (**Figure 6A**), current was first normalized to the geometric surface area of the working electrode to compare the catalytic performance of the LSCO samples as the same masses were deposited on the electrode. It demonstrated that the LSCO20% and LSCO30% samples have better electrocatalytic efficiency for OER than the LSCO0%, LSCO5%, and LSCO10% samples. Specifically, the obtained current densities of the LSCO0%, LSCO5%, LSCO 10%, LSCO20%, and LSCO30% samples are 55.28, 60.29, 60.6, 60.8, and 61.7 mA, respectively. The zoom parts of overpotential (**Figure 6B**) and disk current (**Figure 6C**) give a clearer demonstration of the trend.

Electrochemically Active Surface Area

The electrochemically active surface area (ECSA) of the LSCO samples was estimated from the electrochemical double-layer capacitance of the catalytic surface (Trasatti and Petrii, 1991). The electrochemical capacitance was determined by measuring the non-Faradaic capacitive current associated with double-layer charging from the scan-rate dependence of CVs shown in **Figure 3** (Trasatti and Petrii, 1991; Benck et al., 2012;

TABLE 4 | Comparison between ECSA and RF values of the LSCO0%, LSCO5%, LSCO10%, LSCO20%, and LSCO30% samples.

Catalyst	ECSA (cm^2)	RF
LSCO0%	0.4538	0.0903
LSCO5%	0.0426	0.0849
LSCO10%	0.0717	0.1428
LSCO20%	0.0903	0.1799
LSCO30%	0.0791	0.1576

Ouyang et al., 2019; Wang et al., 2020). Ideal catalysts for OER should have low overpotentials, be stable over time, and have high specific activity (or low surface area) (Mahmood et al., 2013). Electrochemically active surface area was calculated based on ECSA = C_{dl}/C_s where C_{dl} and C_s are double layer capacitance and specific capacitance, respectively.

The roughness factor (RF) is calculated by dividing the estimated ECSA by the geometric area of the electrode, 0.5024 cm^2. **Table 4** shows the obtained ECSA and roughness factor values for all five LSCO catalyst samples. Electrochemically active surface area value of the LSCO20% sample is 0.0903 cm^2, which is higher than the LSCO10% (0.0717 cm^2), LSCO30% (0.791 cm^2), LSCO5% (0.0426 cm^2), and LSCO0% (0.4538 cm^2) samples. Roughness factor values of the LSCO0% (0.0903) and LSCO5% (0.0849) are lower than the LSCO10% (0.1428), LSCO20% (0.1799), and LSCO30% (0.1576) samples.

CONCLUSION

In this paper, we report a combined sol–gel and molten salt synthesis (MSS) procedure to synthesize LSCO0%, LSCO5%, LSCO10%, LSCO20%, and LSCO30% samples. Moreover, we have demonstrated the electrocatalytic comparisons between the LSCO samples as electrode materials in terms of specific capacitance, total charge, and charge accessibility. Cyclic voltammetry and a LSV on rotation ring disk electrode measurements show the enhanced electrocatalytic activity of LSCO. The resulting current density could be a function of both the surface area and the morphology of the LSCO samples used and a combination of both faradaic and non-faradaic procedure.

DATA AVAILABILITY STATEMENT

All datasets generated for this study are included in the article/supplementary material.

AUTHOR CONTRIBUTIONS

SM conducted the experiments. YM initiated the ideas and led the effort. Both authors contributed to the article and approved the submitted version.

ACKNOWLEDGMENTS

YM would like to thank the financial support by the National Science Foundation under CHE (award #1710160 and #1952803) and the IIT start-up funds.

REFERENCES

Agilandeswari, K., and Ruban Kumar, A. (2014). Synthesis, characterization, microstructure, optical and magnetic properties of strontium cobalt carbonate precursor and $Sr_2Co_2O_5$ oxide material. *Superl. Microstruct.* 68, 27–37. doi: 10.1016/j.spmi.2014.01.002

Ardizzone, S., Fregonara, G., and Trasatti, S. (1990). "Inner" and "Outer" Active Surface of RuO_2 Electrodes. *Electrochim. Acta* 35, 263–267. doi: 10.1016/0013-4686(90)85068-x

Ardizzone, S., and Trasatti, S. (1996). Interfacial Properties of Oxides with Technological Impact in Electrochemistry. *Adv. Colloid Interf. Sci.* 64, 173–251. doi: 10.1016/0001-8686(95)00286-3

Armelao, L., Barreca, D., Bottaro, G., and Gasparotto, A. (2005). Hybrid Chemical Vapor Deposition/Sol-Gel Route in the Preparation of Nanophasic LaCoO3 Films Chem. *Mater* 17, 427–433. doi: 10.1021/cm0489643

Audichon, T., Mayousse, E., Morisset, S., Morais, C., Comminges, C., Napporn, T. W., et al. (2014). Electroactivity of RuO_2-IrO_2 mixed nanocatalysts toward the oxygen evolution reaction in a water electrolyzer supplied by a solar profile. *Int. J. Hydrogen Energy* 39, 16785–16796. doi: 10.1016/j.ijhydene.2014.07.170

Benck, J. D., Chen, Z., Kuritzky, L. Y., Forman, A. J., and Jaramillo, T. F. (2012). Amorphous molybdenum sulfide catalysts for electrochemical hydrogen production: insights into the origin of their catalytic activity. *Acs Catalysis* 2, 1916–1923. doi: 10.1021/cs300451q

Bockris, J. O. M., and Otagawa, T. (1984). The electrocatalysis of oxygen evolution on perovskites. *J. Electrochem. Soc.* 131, 290–302. doi: 10.1149/1.2115565

Cheng, C., Zhang, L., Zhang, Y., and Jiang, S. (2008). Synthesis of LaCoO3 nano-powders by aqueous gel-casting for intermediate temperature solid oxide fuel cells. *Solid State Ionics* 179, 282–289. doi: 10.1016/j.ssi.2008.01.080

Cheng, J., Zhang, H., Chen, G., and Zhang, Y. (2009). Study of $Ir_xRu_{1-x}O_2$ oxides as anodic electrocatalysts for solid polymer electrolyte water electrolysis. *Electrochim. Acta* 54, 6250–6256. doi: 10.1016/j.electacta.2009.05.090

Cui, C., Gan, L., Heggen, M., Rudi, S., and Strasser, P. (2013). Compositional segregation in shaped Pt alloy nanoparticles and their structural behaviour during electrocatalysis. *Nat. Mater.* 12, 765–711.

Da Silva, L. A., Alves, V. A., Trasatti, S., and Boodts, J. F. C. (1997). Surface and Electrocatalytic Properties of Ternary Oxides $Ir_{0.3}Ti_{(0.7-x)}Pt_xO_2$. Oxygen Evolution from Acidic Solution. *J. Electroanal. Chem.* 427, 97–104. doi: 10.1016/s0022-0728(97)83088-4

de la Cruz, , R. G., Falcon, H., Pena, M., and Fierro, J. (2001). Role of bulk and surface structures of La1-xSrxNiO3 perovskite-type oxides in methane combustion. *Appl. Cataly. B Environ.* 33, 45–55. doi: 10.1016/s0926-3373(01)00157-6

Devadas, A., Baranton, S., Napporn, T. W., and Coutanceau, C. (2011). Tailoring of RuO2 nanoparticles by microwave assisted "Instant method" for energy storage applications. *Power Sourc.* 196, 4044–4053. doi: 10.1016/j.jpowsour.2010.11.149

Gasteiger, H. A., Kocha, S. S., Sompalli, B., and Wagner, F. T. (2005). Activity benchmarks and requirements for Pt, Pt-alloy, and non-Pt oxygen reduction catalysts for PEMFCs. *Appl. Cataly. B Environ.* 56, 9–35. doi: 10.1016/j.apcatb.2004.06.021

Gorlin, Y., and Jaramillo, T. F. (2010). A bifunctional nonprecious metal catalyst for oxygen reduction and water oxidation. *J. Am. Chem. Soc.* 132, 13612–13614. doi: 10.1021/ja104587v

Gupta, G., Slanac, D. A., Kumar, P., Wiggins-Camacho, J. D., Wang, X., Swinnea, S., et al. (2009). Highly stable and active Pt-Cu oxygen reduction electrocatalysts based on mesoporous graphitic carbon supports. *Chem. Mater.* 21, 4515–4526. doi: 10.1021/cm901203n

Hong, W. T., Risch, M., Stoerzinger, K. A., Grimaud, A., Suntivich, J., and Shao-Horn, Y. (2015). Toward the rational design of non-precious transition metal oxides for oxygen electrocatalysis. *Energy Environ. Sci.* 8, 1404–1427. doi: 10.1039/c4ee03869j

Huynh, M. H. V., and Meyer, T. J. (2007). Proton-coupled electron transfer. *Chem. Rev.* 107, 5004–5064.

Jasem, S. M., and Tseung, A. C. C. (1979). A potentiostatic pulse study of oxygen evolution on Teflon-bonded nickel-cobalt oxide electrodes. *J. Electrochem. Soc* 126, 1353–1360. doi: 10.1149/1.2129276

JO'M, B., Otagawa, T., and Young, V. (1983). Solid state surface studies of the electrocatalysis of oxygen evolution on perovskites. *J. Electroanaly.*

Chem. Interf. Electrochem. 150, 633–643. doi: 10.1016/s0022-0728(83)80243-5

Jörissen, L. (2006). Bifunctional oxygen/air electrodes. *J. Power Sourc.* 155, 23–32. doi: 10.1016/j.jpowsour.2005.07.038

Kaituo, W., Wu, X., Wu, W., and Li, Y. (2014). Synthesis of perovskite LaCoO3 by thermal decomposition of oxalates: Phase evolution and kinetics of the thermal transformation of the precursor. *Ceramics Int.* 40, 5997–6004. doi: 10.1016/j.ceramint.2013.11.048

Khalil, M. S. (2003). Synthesis, X-ray, infrared spectra and electrical conductivity of La/Ba-CoO3 systems. *Mater. Sci. Eng. A* 352, 64–70. doi: 10.1016/s0921-5093(02)00557-9

Lee, S. H., Lee, J. Y., and Park, Y. M. (2006). Complete oxidation of methane and CO at low temperature over LaCoO3 prepared by spray-freezing/ freeze-drying method. *Catal. Today* 117, 376–381. doi: 10.1016/j.cattod.2006.05.035

Li, F., Xianghua, Y., Liying, C., Hongjun, P., and Xinquan, X. (2002). Solid-State Synthesis of LaCoO3 Perovskite Nanocrystals. *J. Am. Ceram. Soc.* 85, 2177–2180.

Loi, M. A., and Hummelen, J. C. (2013). Hybrid solar cells: perovskites under the sun. *Nat. Mater.* 12, 1087–1089.

Luo, W.-L., and Liu, W. (2007). Combustion synthesis and characterization of porous perovskite catalysts. *J. Chem. Sci.* 119, 237–241. doi: 10.1007/s12039-007-0031-7

Mahmood, M. F., Warsi, M. N., and Ashiq, M. (2013). Ishaq, Substitution of La and Fe with Dy and Mn in multiferroic La1-xDyxFe1-yMnyO3 nanocrystallites. *J. Magn. Magn. Mater.* 327, 64–70. doi: 10.1016/j.jmmm.2012.09.033

Mao, L., Mohan, S., and Mao, Y. (2019). Delafossite CuMnO2 as an Efficient Bifunctional Oxygen and Hydrogen Evolution Reaction Electrocatalyst for Water Splitting. *J. Electrochem. Soc.* 166, H233–H242.

Matsumoto, Y., and Sato, E. (1986). Electrocatalytic properties of transition metal oxides for oxygen evolution reaction. *Mater. Chem. Phys.* 14, 397–426. doi: 10.1016/0254-0584(86)90045-3

McCrory, C. C. L., Jung, S., Peters, J. C., and Jaramillo, T. F. (2013). Benchmarking heterogeneous electrocatalysts for the oxygen evolution reaction. *J. Am. Chem. Soc.* 135, 16977–16987. doi: 10.1021/ja407115p

Meadowcroft, D. (1970). Low-cost oxygen electrode material. *Nature* 226, 847–848. doi: 10.1038/226847a0

Mefford, J. T., Hardin, W. G., Dai, S., Johnston, K. P., and Stevenson, K. J. (2014). Anion charge storage through oxygen intercalation in LaMnO3 perovskite pseudocapacitor electrodes. *Nat. Mater.* 13, 726–732. doi: 10.1038/nmat4000

Mefford, J. T., Rong, X., Abakumov, A. M., Hardin, W. G., Dai, S., Kolpak, A. M., et al. (2016). Water electrolysis on La1-xSrxCoO3-δ perovskite electrocatalysts. *Nat. Commun.* 7:11053.

Mohan, S., and Mao, Y. (2018). Dependence of (photo)electrochemical properties on geometry factors of hydrothermally synthesized delafossite copper gallium oxide CuGaO2 toward oxygen evolution reaction. *J. Electrochem. Soc.* 165, H607–H613.

Mueller, D. N., Machala, M. L., Bluhm, H., and Chueh, W. C. (2015). Redox activity of surface oxygen anions in oxygen-deficient perovskite oxides during electrochemical reactions. *Nat. Commun.* 6:6097.

Neburchilov, V., Wang, H., Martin, J. J., and Qu, W. (2010). A review on air cathodes for zinc-air fuel cells. *J. Power Sourc.* 195, 1271–1291. doi: 10.1016/j.jpowsour.2009.08.100

Nitadori, T., Kurihara, S., and Misono, M. (1986). Catalytic properties of La1-xA'xMnO3 (A' = Sr, Ce, Hf). *J. Cataly.* 98, 221–228. doi: 10.1016/0021-9517(86)90310-6

Nitadori, T., and Misono, M. (1985). Catalytic Properties of La1-xA'xFeO3 (A' = Sr, Ce) and La1-xCexCoO3. *J. Catalys.* 93, 459–466. doi: 10.1016/0021-9517(85)90193-9

Otagawa, T., and Bockris, J. (1983). Oxygen evolution on perovskites. *J. Phys. Chem* 87, 2960–2971.

Ouyang, T., Ye, Y., Wu, C., Xiao, K., and Liu, Z. (2019). Heterostructures Composed of N-Doped Carbon Nanotubes Encapsulating Cobalt and β-Mo2C Nanoparticles as Bifunctional Electrodes for Water Splitting. *Angew. Chem. Int. Ed. Engl.* 58, 4923–4928. doi: 10.1002/anie.201814262

Patel, F., and Patel, S. (2012). Carbon monoxide oxidation on LaCoO3 perovskite type catalysts prepared by reactive grinding. *Res. J. Recent Sci.* 1, 152–159.

Pena, M., and Fierro, J. (2001). Chemical structures and performance of perovskite oxides. *Chem. Rev.* 101, 1981–2018. doi: 10.1021/cr980129f

Rousseau, F., Nikravech, M., Benabdelmoumène, L., and Guyon, C. (2007). Electrochemical studies on Sr doped LaMnO3 and LaCoO3 layers synthesized in a low-pressure plasma reactor equipped with a convergent nozzle. *J. Appl. Electrochem.* 37, 95–101. doi: 10.1007/s10800-006-9214-z

Royer, S., Duprez, D., Can, F., Courtois, X., Batiot-Dupeyrat, C., Laassiri, S., et al. (2014). Perovskites as substitutes of noble metals for heterogeneous catalysis: dream or reality. *Chem. Rev.* 114, 10292–10368. doi: 10.1021/cr500032a

Schaak, R. E., and Mallouk, T. E. (2002). Perovskites by design: a toolbox of solid-state reactions. *Chem. Mater.* 14, 1455–1471. doi: 10.1021/cm010689m

Singh, C., and Rakesh, M. (2009). Preparation and characterization of nickel doped, A and B site LaCoO3 perovskite. *Indian J. Eng. Mater. Sci.* 16, 288–290.

Slanac, D. A., Hardin, W. G., Johnston, K. P., and Stevenson, K. J. (2012). Atomic ensemble and electronic effects in Ag-rich AgPd nanoalloy catalysts for oxygen reduction in alkaline media. *J. Am. Chem. Soc.* 134, 9812–9819. doi: 10.1021/ja303580b

Sugimoto, W., Yokoshima, K., Murakami, Y., and Takasu, Y. (2006). Charge Storage Mechanism of Nanostructured Anhydrous and Hydrous Ruthenium-Based Oxides. *Electrochim. Acta* 52, 1742–1748. doi: 10.1016/j.electacta.2006.02.054

Trasatti, S., and Petrii, O. (1991). Real surface area measurements in electrochemistry. *Pure Appl. Chem.* 63, 711–734. doi: 10.1351/pac199163050711

Vojvodic, A., and Nørskov, J. K. (2011). Optimizing perovskites for the water-splitting reaction. *Science* 334, 1355–1356. doi: 10.1126/science.1215081

Walter, M. G., Warren, E. L., McKone, J. R., Boettcher, S. W., Mi, Q., Santori, E. A., et al. (2010). Solar water splitting cells. *Chem. Rev.* 110, 6446–6473.

Wang, X., Ouyang, T., Wang, L., Zhong, J., and Liu, Z. (2020). Surface Reorganization on Electrochemically-Induced Zn-Ni-Co Spinel Oxides for Enhanced Oxygen Electrocatalysis. *Angew. Chem. Int. Ed. Engl.* 59, 6492–6499. doi: 10.1002/anie.202000690

Weber, M. F., and Dignam, M. J. (1984). Efficiency of splitting water with semiconducting photoelectrodes. *J. Electrochem. Soc.* 131, 1258–1265. doi: 10.1149/1.2115797

Wu, X., Tayal, J., Basu, S., and Scott, K. (2011). Nano-Crystalline RuxSn1-xO2 Powder Catalysts for Oxygen Evolution Reaction in Proton Exchange Membrane Water Electrolysers. *Int. J. Hydrogen Energy* 36, 14796–14804. doi: 10.1016/j.ijhydene.2011.01.067

Yeo, B. S., and Bell, A. T. (2011). Enhanced activity of gold-supported cobalt oxide for the electrochemical evolution of oxygen. *J. Am. Chem. Soc.* 133, 5587–5593. doi: 10.1021/ja200559j

Zhu, J., Li, H., Zhong, L., Xiao, P., Xu, X., Yang, X., et al. (2014). Perovskite oxides: preparation, characterizations, and applications in heterogeneous catalysis. *ACS Catal* 4, 2917–2940.

Zuniga, J., Abdou, M., Gupta, S. K., and Yuanbing, M. (2018). Molten-Salt Synthesis of Complex Metal Oxide Nanoparticles. *J. Visual. Exp.* 140:e58482. doi: 10.3791/58482

Conflict of Interest: The authors declare that the research was conducted in the absence of any commercial or financial relationships that could be construed as a potential conflict of interest.

Advantages of publishing in Frontiers

OPEN ACCESS
Articles are free to read for greatest visibility and readership

FAST PUBLICATION
Around 90 days from submission to decision

HIGH QUALITY PEER-REVIEW
Rigorous, collaborative, and constructive peer-review

TRANSPARENT PEER-REVIEW
Editors and reviewers acknowledged by name on published articles

Frontiers
Avenue du Tribunal-Fédéral 34
1005 Lausanne | Switzerland

Visit us: www.frontiersin.org
Contact us: info@frontiersin.org | +41 21 510 17 00

REPRODUCIBILITY OF RESEARCH
Support open data and methods to enhance research reproducibility

DIGITAL PUBLISHING
Articles designed for optimal readership across devices

FOLLOW US
@frontiersin

IMPACT METRICS
Advanced article metrics track visibility across digital media

EXTENSIVE PROMOTION
Marketing and promotion of impactful research

LOOP RESEARCH NETWORK
Our network increases your article's readership